Focalisation d'une onde de forte puissance par retournement temporel

Henri Vallon

université PARIS-SACLAY

CentraleSupélec

NNT : 2016SACLC006

THÈSE DE DOCTORAT

DE

L'UNIVERSITÉ PARIS-SACLAY

Préparée à

CentraleSupélec

ÉCOLE DOCTORALE N° 575 : Electrical, Optical, Bio-Physics and Engineering

DISCIPLINE : Physique

présentée et soutenue le **04/03/2016** à **Gif-sur-Yvette**

par

Henri VALLON

FOCUSING HIGH-POWER ELECTROMAGNETIC WAVES USING TIME-REVERSAL

FOCALISATION D'UNE ONDE DE FORTE-PUISSANCE PAR RETOURNEMENT TEMPOREL

Directeur de Thèse : Andrea COZZA
Encadrants : Florian MONSEF et Anne-Sophie CHAUCHAT

Composition du jury :

Président :	Frédéric ANIEL	Professeur (Université Paris-Sud, France)
Rapporteurs :	Philippe BESNIER	Directeur de Recherche (IETR-INSA de Rennes, France)
	Odile PICON	Professeur Émérite (Laboratoire ESYCOM - Université de PARIS-EST Marne-la-Vallée, France)
Examinateurs :	Sun K. HONG	Assistant Professor (Department of Electrical and Computer Engineering, Rose-Hulman Institute of Technology, USA)
	Andrea COZZA	Full-Professor (Centrale-Supélec, GeePs, France)
	Florian MONSEF	Maître de Conférence (Université Paris-Saclay, GeePs, France)
Membres invités :	Christian CAREL	Dr-Ingénieur (THALES Communications & Security - SEE Emerite Member, France)
	Anne-Sophie CHAUCHAT	Dr-Ingénieure (THALES Communications & Security)

"A Man's a Man for A' That", (1795) - Robert Burns

Is there for honest poverty
is there anybody honest but poor
That hings his head, an' a' that;
that cringes because of his poverty
The coward slave - we pass him by,
coward slave=slave of his own pride
We dare be poor for a' that!
For a' that, an' a' that,
Our toils obscure an' a' that,
Our toils obscure= We dare toil obscurely
The rank is but the guinea's stamp,
The rank=Aristocratic rank
guinea=a gold coin
stamp=stamped on the face of the coin
The man's the gowd for a' that.

What though on hamely fare we dine,
Wear hoddin grey, an' a' that?
hodden=coarse wool
Gie fools their silks, and knaves their wine,
A man's a man for a' that.
For a' that, an' a' that,
Their tinsel show, an' a' that,
The honest man, tho' e'er sae poor,
Is king o' men for a' that.

Ye see yon birkie ca'd a lord,
birkie=grand fellow
Wha struts, an' stares, an' a' that;
Tho' hundreds worship at his word,
He's but a coof for a' that.
coof=fool

For a' that, an' a' that,
His ribband, star, an' a' that,
riband=ribbon worn across the chest denoting an honor
star=a medal in the shape of a star
The man o' independent mind
He looks an' laughs at a' that.

A prince can mak a belted knight,
belt=belt around a sash that is wrapped around the waist and shoulder, part of Scottish military dress
A marquise, duke, an' a' that;
But an honest man's aboon his might,
Gude faith, he maunna fa' that!
fault that=fault being above the might of aristocratic rank
For a' that, an' a' that,
Their dignities an' a' that,
The pith o' sense, an' pride o' worth,
Are higher rank than a' that.

Then let us pray that come it may,
As come it will for a' that,
That Sense and Worth, o'er a' the earth,
Shall bear the gree, an' a' that.
bear the gree=take the prize
For a' that, an' a' that,
It's comin yet for a' that
That man to man, the world o'er,
Shall brithers be for a' that.

I would like to dedicate this thesis to my love Karen CHAVEZ TAIRA, my parents and my sister and to all the people who inspire me to be a better person day after day after day…

"Time is the worst place, so to speak, to get lost in, as Arthur Dent could testify, having been lost in both time and space a good deal. At least being lost in space kept you busy."

Life, the Universe and Everything - Douglas ADAMS

Acknowledgements

The completion of this manuscript, and of this PhD comes as an ending to a chapter of my life. And like all chapters in life, I have many people to thank. My first acknowledgements go to my director Andrea Cozza for his guidance on this project. His attention to detail and scholarship have set an example for me that I will carry with me for the rest of my days. I would also like to to express my gratitude towards my academic supervisor during these three years Florian Monsef for his contribution and his advice since the beginning of this thesis. I would also like to express my sincerest thanks to Guillaume Defrance who helped me and guided me during the first half of this PhD.

I would also like to thank the L2S, the Geeps and Centrale-Supélec for welcoming me in their laboratories and without which none of this would have been possible.

I would like to thank all the members of the jury for coming to my defense and for the time they have taken in order to evaluate and give feedback to my manuscript. Your suggestions and conversations than ensued were very constructive. M Aniel thank you for being president during my defense. M Besnier, Mme Picon thank you for having accepted to be reporters for my PhD and M Hong thank you for having accepted to be an examiner and to have travelled all the way to France for this occasion as well as giving a very interesting seminar on your work during your short stay.

I would like express special thanks to Anne-Sophie Chauchat and Jean-Pierre Brasile for trusting me with this project, part of a collaboration between THALES Communications & Security and Centrale-Supélec. I would like to dedicate these few lines to the team with which I had the opportunity to work with at THALES. I would like to thank them all and especially Anne-Sophie Chauchat, Christian Carel and Christian Douchin for acknowledging the potential of this project and for helping to finance part of my travels to conferences and most importantly the prototype without which most of the experimental validations here would not have been possible. I hope my future in the team will be as pleasant as it has already been. I would like to address special thanks to Quentin Kassab, Dominique Fasse, Dimitri Girard, Frederic Authier that have invested a lot of their time and work along with Anne-Sophie during the complete design of the prototype and for taking part in the measurements.

I would also like to thank my fellow PhD students from the laboratory for helping me and advising me many times during these three years : Phillippe Meton, Changyou Li, Pierre-Luc Mignot,

Mohamed Farouk, Mouad Djedidi, Giacomo Rodeghiero & Panagiotis Piteros (the dynamic duo), Ashish Rojatkar, Hidayet Zaimaga, Safaa al Ali, Xi Cheng, Moussa Kafal...

I would like to give a big thank you to the people working at the laboratory that have made these three years special and with who I shared a great deal of my life: Christophe Connessa for listening to me and his concern during these years, Marc Lambert for his jokes, sarcasm and his advise, Israël Hinoztroza our discussions will not be forgotten (Viva el Perú carajo!), Vincent Lescarret, Antoine Diet, Frederic Desprez, Dominique Picard, Mohammed Sehrir, Laurence Frémy, Vincent Polledri, Bernard Duchêne, Alain Joisel (thank you so much for the pictures and videos during my defense), Lionel Pichon...

Last but not least these words go to my friends and family I don't even think you can realise how much your presence was important to me during this part of my life.

Abstract

Time-reversal has already shown its focusing ability and the possibility of generating pulses with peak-powers greater than the injected signal. During this thesis, we were interested in studying the focusing properties offered by a time-reversal system in order to obtain medium to high-power microwaves using medium power sources named Time-Reversal Amplification System (TRAS). This system offers significant advantages over current systems. A Time-Reversal Amplification System allows pushing-back the operation limitation of the solid-state amplifiers thanks to a compression gain in diffuse-field media. We managed to obtain analytical models predicting the amplification properties offered by time reversal, we were also interested in the expected variations of this amplification. To take into account the random properties of diffuse media, the various models are decomposed into deterministic and random parts. Three metrics have been at the heart of the studies conducted during this thesis: the effectiveness of a reverberation chamber, the ratio between the transmitted pulse and the impulse response, and the actual amplification gain offered by time reversal. In order to validate the models, a prototype was developed allowing a maximum gain on the desired frequency band. A good match between measurements and models have been found for the random and deterministic part when comparing them to experimental results. Several important parameters were isolated and modelled analytically and verified by measurements. The importance of the volume and geometry of the chamber amongst other metrics was determined. In parallel, various measurement campaigns were conducted to characterize several reverberation chambers and their quality factor. We gave a beginning of explanation that could justify the differences between theoretical models and measurements. Certain limitations have also been isolated, the amplification gain depends on the frequency, the number of antennas and the effectiveness of the propagation medium.

Résumé

Le retournement temporel a déjà montré ses capacités de focalisation et la possibilité de générer des impulsions ayant des puissances supérieures à celles des signaux injectés. Dans le cadre de ces travaux de thèse, on s'intéresse à l'étude des propriétés de focalisation offertes par un système à retournement temporel ayant pour finalité l'obtention de fortes puissances à partir de sources de puissances moyennes nommé Time-Reversal Amplification System (TRAS). Ce système offre des avantages significatifs par rapport aux systèmes actuels. Un des avantages d'un système d'amplification à retournement temporel est que la limitation de fonctionnement des amplificateurs à semi-conducteurs est repoussée grâce au gain de compression dans les milieux à champs diffus. La flexibilité offerte sur l'impulsion refocalisée est aussi particulièrement intéressante. Nous sommes parvenus à obtenir des modèles analytiques permettant de prévoir les possibilités d'amplification du retournement temporel. Afin de prendre en compte le caractère aléatoire des cavités réverbérantes, les différents paramètres sont décomposés en parties déterministes et aléatoires. Trois paramètres ont particulièrement été étudiées durant cette thèse : l'efficacité d'une chambre réverbérante, le rapport entre l'impulsion émise et la réponse impulsionnelle et le gain réel d'amplification offert par le retournement temporel. Afin de valider les modèles, un prototype a été développé permettant l'obtention d'un gain maximal sur la bande de fréquence désirée. Une bonne adéquation entre les mesures et les modèles a pu être montré pour la partie aléatoire ainsi que pour la partie déterministe. Plusieurs paramètres importants ont pu être isolés et modélisés analytiquement puis vérifiés par les mesures. L'importance du volume et de la géométrie de la chambre a ainsi pu être déterminé. En parallèle, différentes campagnes de mesures ont été menées afin de caractériser dans plusieurs chambres réverbérantes le facteur de qualité. Nous avons donné un début d'explication pouvant expliquer les divergences avec les modèles. Certaines limitations ont aussi été isolées, le gain d'amplification dépend de la fréquence, du nombre d'antennes et de l'efficacité du milieu.

Résumé en Français de la Thèse - Summary in French of the Thesis

Introduction Générale

Les travaux dans ce manuscrit présentent les activités de recherche menées au sein du Laboratoire Geeps (UMR 8507), CentraleSupélec, Université Paris-Sud et au sein de la société Thales Communications & Security sur les capacités de focalisation du retournement temporel. Plus précisément, les travaux décrits ici ont pour objectifs de développer des modèles permettant d'évaluer les possibilités d'obtenir des champs électromagnétiques de forte puissance grâce à la technique de retournement temporel.

Ces travaux ont abouti au développement d'un concept nommé TRAS (Time-Reversal Amplification System) introduisant une nouvelle approche de synthèse d'un signal de forte puissance et de forme d'onde contrôlable. Le système TRAS permet en particulier de repousser les limites en puissance de certains amplificateurs notamment ceux à état solide et d'obtenir des puissances crêtes bien supérieures. Une des emplois de ce type de source est le tests de susceptibilité fort niveau d'équipements. Le concept du TRAS repose sur deux phases:

- Une première durant laquelle l'énergie d'un signa de type impulsionnel de bas niveau est étalé dans le temps dans un milieu diffus (comme par exemple une chambre réverbérante).

- Une deuxième phase de compression spatio-temporelle permise par le processus de retournement temporel.

L'étalement temporel de l'énergie permet d'obtenir une marge d'amplification. Nous nous sommes donc consacrés ici à la description de ce système et aux différents paramètres dimensionnant du retournement temporel dans le cadre des fortes puissances. De nouveaux modèles statistiques et analytiques prédictifs ont été développés et validés sur un prototype.

Ce manuscrit est divisé en 4 chapitres. Le premier chapitre s'intéresse au contexte de la thèse et définit la position d'une source à retournement temporel dans l'état de l'art actuel. Dans le deuxième chapitre, une étude plus approfondie des chambres réverbérantes et de leurs statistiques est menée. Dans une première partie, une analyse des mécanismes de pertes des chambres par le biais de mesures facteurs de qualité est conduite puis dans une seconde partie, nous analysons la statistique du rapport entre le maximum et la valeur moyennes des réponses impulsionnel en milieu complexe. Le troisième chapitre est consacré à la description des propriétés du retournement temporel en environnement réverbérant. Les performances de la refocalisation spatiale et temporelle du retournement temporel sont étudiées. Le dernier chapitre est essentiellement consacré à l'analyse et à l'étude du prototype et du potentiel de la technique de retournement temporel appliqué à la génération de forte puissance.

Les Sources Micro-Ondes de Forte Puissance - Contextes et Objectifs

Le premier chapitre est consacré à la présentation du contexte de la thèse, à l'état de l'art des sources de forte puissance micro-ondes ainsi qu'aux différents moyens d'amplifications disponibles afin de les comparer aux possibilités offertes par le retournement temporel.

Les sources Micro-Ondes de Forte Puissance (MFP) peuvent être utilisées dans différents contextes. Elles diffèrent de par leurs natures et de par les forme d'ondes qu'elles peuvent génèrer qui sont soit de forte puissance et d'énergie modérée soit de forte énergie et de puissance modérée.

- Dans le premier cas, le signal possède un caractère impulsionnel de courte durée et la susceptibilité de la cible correspond à un seuil d'énergie déposée (régime adiabatique).
- Dans le second cas, le signal correspond à une impulsion de plus grande durée, compatible avec les constantes de temps de diffusion thermique [1, 2].

Pour des impulsions de durées supérieures à 10 μs l'élévation de température est directement proportionnelle à l'apport de puissance. La répétition à fréquence élevée d'impulsions de courtes durées peut entrainer une accumulation d'énergie suffisante permettant la dégradation de la cible. En fonction des puissances mises en jeu et de la forme d'onde, ces dispositifs à rayonnement micro-onde peuvent être employés comme brouilleurs ou armes à énergie dirigée (AED).

Dans le cadre de cette thèse, la bande de fréquence d'intérêt est située entre $0,5$ GHz et 3 GHz à des puissances de l'ordre de quelques dizaines de kW.

Plusieurs types de sources sont considérées pour délivrer les signaux nécessaires au fonctionnement du TRAS. Les sources à base de tubes à vide délivrent des signaux à bande étroite et de très forte

puissance, elles sont cependant très peu flexibles quant à la forme d'onde délivrée. Les générateurs de Marx délivrent quant à eux des impulsions très brèves et de très forte puissance, mais ne peuvent pas non plus être contrôlées. Par contre les sources à état solide sont, quant à elles, contrôlables en terme de forme d'ondes et peuvent délivrer quelques kW. De plus, ces sources sont bien plus compactes que les tubes à vide ou que les générateurs de Marx.

Le véritable objectif de ces travaux a été d'utiliser le retournement temporel comme artifice permettant de focaliser une impulsion de forte puissance à partir d'un système d'amplification de puissance modérée. Cette technique permet donc d'obtenir un système dans une gamme de puissances intermédiaires comprise entre les technologies à état solide et de celles à tube. On tire profit dans un premier temps de l'étalement temporel considérable du signal pour dégager une marge d'amplification. La réponse impulsionnelle du milieu diffus est utilisée à l'entrée de l'amplificateur en chronologie inversée pour refocaliser l'impulsion de forte puissance sur la cible.

Analyse des Contributions des Différents Éléments au Facteur de Qualité

Afin de maximiser l'étalement dans le temps présenté au chapitre précédent notre choix s'est porté sur une Chambre Réverbérante (CR). En théorie, une CR est un système parfaitement diffus défini par un champ isotrope et homogène dans tout le volume de la cavité. Le champ peut alors être considéré comme constitué d'une infinité d'ondes planes se propageant dans toutes les directions de l'espace avec la même probabilité [3]. Dans le cas où la chambre est surmodée, un nombre important de modes va être excité et leurs contributions vont s'ajouter. Une chambre est dite surmodée lorsque la séparation entre les modes n'est plus perceptible. Les Chambres Réverbérantes présentent des propriétés particulièrement intéressantes pour les mesures de Compatibilité ElectroMagnétique (CEM) :

- Elles permettent d'exciter un objet selon un grand nombre de directions d'incidence et de polarisations sans avoir à déplacer l'objet sous test [4] ;
- De plus, les CR présentent la possibilité de générer des champs de forte intensité à partir de sources harmoniques de puissances relativement faibles [5].

Les CR sont principalement utilisées dans le cadre de mesures d'antennes et de CEM [6]. Dans le cas du régime diffus il est impossible d'obtenir un modèle analytique complet. Une approche statistique est alors souvent préférable lorsque l'on veut décrire certains phénomènes. Par exemple, la décomposition en spectre d'ondes planes basée sur l'hypothèse d'un champ diffus ou idéalement désordonné permet d'établir les statistiques du champ électromagnétique sous la forme de combinaison de distributions gaussiennes indépendantes.

Une importante partie du deuxième chapitre a été consacrée à l'étude des différentes contributions aux pertes dans une chambre réverbérante (CR) en régime diffus. Cette analyse s'est faite par le biais de campagnes de mesures expérimentales et de la confrontation des résultats obtenus aux modèles

analytiques existants. Cette analyse est importante car la qualité de refocalisation du signal après retournement temporel et donc l'amplification qui va être possible par le TRAS dépend directement du milieu physique dans lequel l'onde va se propager. L'étude expérimentale vise à évaluer et à séparer par la mesure les différents mécanismes de pertes ayant lieu dans une chambre réverbérante. Afin de quantifier ces pertes, nous avons analysé les composantes du facteur de qualité qui sont pour l'essentiel le facteur de qualité associé aux pertes dans les parois et le facteur de qualité associé aux pertes dans les antennes. L'approche consiste à mesurer le coefficient de qualité global avec N_1 puis N_2 antennes dans la chambre. Il en résulte un système de deux équations où les deux inconnues sont les deux composantes recherchées du coefficient de qualité. Cette démarche a nécessité de quantifier les incertitudes de mesures. En effet, la mesure du coefficient de qualité n'est elle-même qu'une estimation empirique de l'espérance d'une variable aléatoire. L'analyse des incertitudes conduite permet ainsi d'isoler la bande de fréquence basse pour laquelle les différences de mesures entre les deux situations sont statistiquement significatives de sorte que le coefficient de qualité d'une antenne soit observable. Une des observations de ces mesures est que le comportement haute fréquence du coefficient de qualité des parois semble croître (pour deux cages en acier) proportionnellement à la fréquence et non pas en raison de la racine de la fréquence comme théoriquement attendu. Ce résultat pourrait correspondre à la non prise en compte de la caractéristique réelle de la perméabilité magnétique de l'acier. Ainsi, une mesure dans une chambre réverbérante en aluminium a été entreprise.

Une deuxième partie de ce chapitre concerne une approche probabiliste de la description de la réponse impulsionnelle $h(t)$ dans une chambre réverbérante et notamment de son maximum. L'estimation du niveau maximum de la réponse impulsionnelle est nécessaire afin d'utiliser l'amplificateur de puissance en-dessous de son niveau de saturation. Pour ce faire, nous utilisons la description modale du signal et les propriétés statistiques du milieu diffus. L'enveloppe moyenne ou RMS de la réponse impulsionnelle h_0 suit une décroissance exponentielle dont l'amplitude à l'origine est proportionnelle à la racine carrée du nombre de modes excités sur la bande-passante de l'impulsion B_T. Afin d'évaluer les valeurs extrêmes des fluctuations autour de cette enveloppe, nous avons ensuite évalué la fonction de répartition (cdf) de la réponse impulsionnelle autour de cette enveloppe RMS défini par (1). La probabilité que le maximum de la réponse impulsionnelle soit inférieur à un seuil fixé est égale au produit des probabilités que cela soit vérifié à chaque instant pris en valeur discrète (kT_c).

$$F_K(x) = \prod_{k=0}^{N} \mathrm{erf}\left[x\frac{\exp(kT_c/\tau)}{\sqrt{2}}\right] \tag{1}$$

Un choix approprié du pas d'échantillonnage temporel T_c, temps nécessaire à la décorrélation temporelle a été identifié par $1/(4B_T)$. Deux résultats pratiques découlent de cette étude théorique. D'une part, plus la bande passante B_T de l'impulsion est grande et plus le niveau maximal du rapport

$K = |h(t)/h_0|$ de la réponse impulsionnelle est élevée. D'autre part cela s'accompagne d'une moins grande dispersion statistique de ce niveau maximal.

Performances et Efficacité du Retournement Temporel

Ce chapitre est consacré à la description des propriétés du retournement temporel en environnement réverbérant. Les performances de la refocalisation spatiale et temporelle du retournement temporel sont entreprises. Ces performances sont reliées théoriquement aux paramètres physiques de cet environnement et à la nature du signal impulsionnel initial. La première partie de ce chapitre est un rappel bibliographique des travaux importants dans le cadre du sujet de la thèse des performances du retournement temporel [7]. La seconde partie de ce chapitre est consacrée à l'amélioration des performances d'une chambre réverbérante grâce au retournement temporel.

Le retournement temporel repose sur la linéarité du milieu de propagation des ondes, sur les propriétés de réciprocité de ce milieu et de symétrie temporelle des solutions de l'équation d'ondes. En théorie, il est possible de disposer d'un miroir à retournement temporel entourant la source dans un milieu ouvert. En pratique cela s'avère être impossible car le nombre d'antennes nécessaires pour le miroir à retournement temporel serait alors trop important. Les chambres réverbérantes à brassage de modes, compte tenu du confinement du champ et de leur faculté à générer des sources images permettent de réaliser un miroir à retournement temporel avec seulement une ou quelques antennes.

Afin de caractériser la performance du retournement temporel, nous introduisons la notion d'efficacité d'une chambre réverbérante qui n'est autre que le rapport entre la puissance reçue par une antenne en réception et la puissance délivrée par l'antenne d'émission. Cette métrique caractérise la performance de la transmission d'énergie directe entre plusieurs antennes situées dans la chambre. Celui-ci dépend du rapport du coefficient de qualité d'antenne au coefficient de qualité des parois. Ce gain, si on admet une dépendance en racine carrée de la fréquence des pertes dans les parois, évolue selon l'inverse de la fréquence élevée à la puissance $5/2$:

$$G_{ant} = \frac{1}{2 + \frac{4}{3}\sqrt{\frac{2\mu_r}{\mu_0\sigma}}\frac{S}{c^3\pi}\omega^{2.5}} \tag{2}$$

Un autre paramètre important du retournement temporel est le contraste qui mesure le rapport entre le carré de la valeur moyenne de la valeur crête du signal focalisé et la variance de cette valeur crête (3).

$$\Lambda_p = \frac{\langle z(0)\rangle^2}{\sigma_z^2(0)} \tag{3}$$

Dans le cas où le champ peut être considéré comme diffus le contraste est proportionnel au nombre de degrés de liberté produit par le rapport de la bande passante de l'impulsion B_T à la bande de cohérence de la chambre B_C et dépend du facteur de forme de l'impulsion que l'on souhaite refocaliser (4).

$$\Lambda_p = \Lambda_{G_i} \frac{B_t}{B_c} \kappa^2 \tag{4}$$

La bande de cohérence B_C correspond à la bande de fréquence entre deux états indépendants de la chambre. Plus l'impulsion est courte meilleure sera la focalisation. Ce paramètre ne caractérise que le signal reçu au temps $t = 0$ de la refocalisation.

L'énergie associée à la partie cohérente du signal refocalisé rapportée à l'énergie non-cohérente correspondant aux fluctuations inhérentes au processus du retournement temporel est défini. Dans le cas d'un processus de retournement temporel sans modifications du signal injecté (le signal envoyé dans la CR n'est autre que la réponse impulsionnelle dans l'ordre chronologique inversé), l'énergie des fluctuations est exponentiellement décroissante et la constante de temps de ce profil correspond à celui de la cavité. En milieu diffus, l'énergie cohérente est au mieux égale à l'énergie des fluctuations. Le contraste est donc égal au produit du nombre de degrés de liberté par le contraste d'énergie (5).

$$\Lambda_p \simeq \Lambda \frac{T_n}{T_x} \simeq \Lambda \frac{B_T}{B_c} \tag{5}$$

Une configuration multi-sources permet d'améliorer le contraste d'énergie mais pour un nombre d'antenne trop important c'est en pratique irréaliste d'espérer que le contraste soit proportionnel au nombre d'antennes compte tenu de la corrélation spatiale entre les différentes sources. La focalisation vers plusieurs antennes aboutit dans une situation idéalisée à un contraste multiplié par le rapport du nombre total d'antennes au nombre d'antennes en réception.

Dans la seconde partie de ce chapitre nous nous consacrons plus précisément aux travaux menés durant la thèse. L'objectif est de vérifier les apports du retournement temporel en milieu reverbérant par rapport à l'utilisation classique en continue (CW) de ces dernières. Pour ce faire, nous étudions l'efficacité de conversion de signaux harmoniques ou de signaux retourné dans le temps (RT) de même puissance crête. Cette efficacité de conversion correspond au rapport entre la puissance crête présenté au récepteur (ou équipement sous test) et la puissance crête injectée en émission. Pour un signal d'excitation de type CW cette conversion est très variable car elle dépend du processus aléatoire gaussien associé au milieu diffus (6).

$$\eta_{CW} = \frac{C_r}{C_i} \left|\Phi(f_c)\right|^2 = \frac{C_r}{C_i} W(\nu) \tag{6}$$

Le résultat final dépend en pratique dans ce cas du processus de brassage utilisé. Dans le cas d'un signal RT, l'efficacité de conversion est proportionnelle au nombre de degrés de liberté (B_T/B_C) mais inversement proportionnelle au carré du facteur K défini lors du chapitre précédent traduisant le niveau maximal de la réponse impulsionnelle (7).

$$\eta_{TR} = \frac{C_r}{C_i}\frac{B_T}{B_C}\frac{\bar{W}\kappa^2}{K^2} \tag{7}$$

Afin de comparer les deux processus, le rapport entre les efficacités de conversions permet d'étudier le gain entre les deux méthodes. Dans un premier temps, le gain moyen de l'efficacité de conversion associé au retournement temporel est donné par l'équation (8).

$$G_{av}^{P} \leq \frac{B_T Q}{3\pi f_c} \tag{8}$$

De part la grande dissymétrie de la statistique de K, il est cependant préférable d'étudier le rapport des modes des efficacités de conversions. Ainsi, nous définissons un modèle statistique du maximum du champ dans le cas CW lors d'un processus de brassage de mode à N position indépendantes (9).

$$p_N(x) = N(1 - e^{-x})^{N-1}e^{-x} \tag{9}$$

Le rapport des modes statistiques devient alors (10) qui intègre une expression dépendant de K et du facteur de forme.

$$G_p^N = \frac{B_T}{B_C}\frac{\kappa^2}{\ln N}\left[a\ln^b\left(\frac{4B_T}{B_C}\right)\right]^{-2} \tag{10}$$

Un des résultats dérivant de ce rapport est qu'il serait nécessaire d'engendrer un très grand nombre de réalisations indépendantes en régime CW pour atteindre la performance du RT avec une bande passante de quelques dizaines de fois la bande de cohérence. Ces résultats théoriques ont ensuite été prouvés expérimentalement. Les mesures ont été conduites à l'aide d'une sonde électro-optique très faiblement invasive sur 3431 positions et sur une bande de fréquence comprise entre $1,8$ et $2,2$ GHz.

Ces expériences ont permis de valider les modèles théoriques développés jusqu'ici. La distribution empirique de la puissance maximale de la réponse impulsionnelle en fonction de la bande passante considérée pour l'impulsion est confirmée. L'évolution de l'efficacité de conversion pour le cas RT ainsi que sa densité de probabilité en fonction de B_T est également validée. Le gain de puissance suit également la courbe théorique.

Performances du TRAS et Potentialités du Retournement Temporel en tant que Source Micro-ondes de Forte Puissance (MFP)

Le dernier chapitre est essentiellement consacré à l'analyse et à l'étude du prototype et du potentiel de la technique de retournement temporel appliqué à la génération de forte puissance. Dans un premier temps, une analyse théorique des derniers paramètres importants permettant la modélisation de la compression est menée. Le modèle de la marge M, de l'efficacité de transmission η et du gain obtenu G_r sont ainsi développés.

L'efficacité de transmission est d'abord définie pour des signaux de type CW par le rapport de puissance de sortie sur la puissance injectée dans la chambre. L'expression de l'efficacité de transmission dépend uniquement des coefficients de qualité des deux antennes et des parois (11).

$$\eta(\nu) = \frac{Q_{walls}(\nu)}{2Q_{walls}(\nu) + Q_{ant}(\nu)} \tag{11}$$

La marge M est définie par le rapport du niveau maximum de l'impulsion initial sur le niveau maximal de la réponse impulsionnelle. Le modèle de la marge M s'appui sur la distribution de l'amplitude crête relative K telle définie au chapitre 2 et est donné par (12). Un des résultat intéressant de ce manuscrit est que la marge M ne dépend intrinsèquement que du coefficient de qualité des antennes. Plus particulièrement la marge M est inversement proportionnelle au carré de l'amplitude crête relative K, proportionnelle au temps de relaxation de l'antenne et inversement proportionnelle au support temporel T_p de l'impulsion.

$$M = \frac{Q_{ant} B_T \kappa^2}{K^2 \pi f_c} = \kappa^2 K^{-2} \, \frac{B_T V \omega^2}{m \pi c^3} \tag{12}$$

Il est alors possible d'obtenir un modèle du gain réalisé G_r en considérant que la réponse impulsionnelle retournée temporellement sera virtuellement amplifiée du facteur M. Ce gain réalisé est de l'ordre de grandeur de M. L'expression du gain réalisé peut s'exprimer en fonction de la marge telle que $G_r = M/(2 + \tau_a/\tau_d)$ où τ_a représente le temps de relaxation des antennes et τ_d celui associé aux pertes dans les parois. Le rapport de ces deux composantes du coefficient de qualité joue donc un rôle essentiel d'où l'importance des mesures conduites lors du chapitre 2.

$$G_r \sim K^{-2} \frac{\tau_a/T_p}{(2 + \tau_a/\tau_d)^2} \sim \frac{M}{(2 + \tau_a/\tau_d)^2}. \tag{13}$$

Deux régimes apparaissent. D'une part, il existe potentiellement, si le régime diffus est encore possible à ces fréquences, un régime basse fréquence pour lequel le support temporel de l'impulsion doit être très petit devant le temps de relaxation de l'antenne. D'autre part, il apparaît un régime haute fréquence, pour lequel le support temporel de l'impulsion doit être très petit devant le temps de relaxation des parois.

Une expérimentation est menée dans une chambre en aluminium de THALES. Elle confirme que M ne dépend que de τ_a et non de τ_d. La marge expérimentale mesurée suit bien la prédiction théorique (loi en f^2) sauf en-dessous d'une fréquence seuil de 800 MHz où le champ ne peut plus être considéré comme diffus. Le gain réalisé évalué expérimentalement dans cette cavité suit également très correctement le gain réalisé théorique après extraction préalable du coefficient de qualité des parois pour un meilleur ajustement.

Ce gain varie fortement avec la fréquence et il apparaît un point de fonctionnement optimal entre $1,2$ GHz et $1,5$ GHz dans cette chambre où un gain variant entre 3 et 8 dB est alors possible à partir d'un retournement temporel classique.

Afin d'améliorer les performances du TRAS, le signal inversé de la réponse impulsionnelle est modifié avant d'être retransmis à l'entrée de l'amplificateur. Deux types de traitements sont étudiés, la compensation de la décroissance exponentielle de l'enveloppe de la réponse impulsionnelle et le retournement temporel « 1-bit ».

Le gain additionnel en cas de compensation de la décroissance de l'enveloppe sature pour des durées de signaux supérieurs à trois fois la constante de temps de la cavité. La corrélation du signal obtenue avec l'impulsion de départ décroît cependant lentement avec cette durée. Un modèle permettant de prédire le gain additionnel que l'on peut obtenir grâce à ce traitement a été developpé.

La technique du retournement temporel « 1-bit » apporte une amélioration importante des performances. Le gain de performance par rapport à l'égalisation est important en termes de gain réalisé au détriment du bruit de refocalisation. Le retournement temporel « 1-bit » peut être interprété comme un cas limite d'une compensation d'enveloppe multiplié par un facteur d'amplification après troncature. Une distorsion plus importante du signal augmente l'énergie du bruit qui possède cependant une constante de temps bien plus importante que la durée de l'impulsion initiale. Ainsi, la progression d'un signal égalisé vers un pseudo-signal « 1-bit », permet bien d'augmenter le gain réalisé qui tend vers les performances du vrai signal « 1-bit ». Le contraste, en revanche est plus important que pour le vrai signal « 1-bit », ce qui est lié à sa plus grande durée. Un modèle permettant de prédire le gain additionnel que l'on peut obtenir grâce à ce traitement a aussi été developpé. Contrastes et gains saturent pour des valeurs d'amplification faibles. Ainsi, la valeur rms de l'impulsion doit être privilégiée comme valeur maximale admise à l'entrée de l'amplificateur.

Pour terminer ce chapitre, nous montrons les différentes étapes de développement du prototype du TRAS basé sur une enceinte réverbérante et la réalisation d'une source de puissance pulsée à étages parallèles dont les sorties sont combinées au sein d'un guide d'onde radial large bande. Le système complet a permis de valider expérimentalement les modèles théoriques de cette thèse.

Conclusions

Les travaux menés au cours de cette thèse ont permis d'obtenir des résultats dans plusieurs domaines complémentaires. Les apports théoriques portent sur les propriétés du retournement temporel associées aux chambre réverbérantes. Ces travaux ont permis d'obtenir des critères qui permettent de quantifier le gain effectivement réalisé en recourant à cette technique pour la production de signaux de forte puissance. Ces éléments de quantification ont permis de dimensionner le TRAS (Time Reversal Amplification System). Ces travaux sont allés jusqu'à la réalisation d'un prototype associant un amplificateur et une cavité.

Références

[1] J. Benford, J.A. Swegle, and E. Schamiloglu. *High Power Microwaves, Second Edition*. Series in Plasma Physics. Taylor & Francis, 2007.

[2] D.C. Wunsch and R.R. Bell. "Determination of Threshold Failure Levels of Semiconductor Diodes and Transistors Due to Pulse Voltages". In: *Nuclear Science, IEEE Transactions on* 15.6 (1968), pp. 244–259.

[3] D.A. Hill. "Plane wave integral representation for fields in reverberation chambers". In: *IEEE Transactions on Electromagnetic Compatibility* 40.3 (1998), pp. 209–217.

[4] IEC. *Standard 61000-4-21: Electromagnetic Compatibility (EMC) Part 4: Testing and Measurement Techniques, Sec. 21: Reverberation Chambers*. 2011.

[5] T. H. Lehman and G. J. Freyer. "Characterization of the maximum test level in a reverberation chamber". In: *Electromagnetic Compatibility, 1997. IEEE 1997 International Symposium on*. 1997, pp. 44–47.

[6] B. Démoulin and P. Besnier. *Les Chambres réverbérantes en électromagnétisme*. Collection Télécom. Hermes Science Publications, 2010.

[7] A. Cozza. *Stochastic modelling of large cavities - Random and coherent field applications*. Université Paris-Sud, Habilitation à Diriger la Recherche, 2012.

Contents

List of Symbols Abbreviations

Acronyms

AC	Anechoic Chamber
ASC	Accessibility, Susceptibility and Consequence
DEW	Directed Energy Weapons
DORT	Decomposition of the Time Reversal Operator
EA	Electronic Attack
ECCM	Electronic Counter-Counter Measures
ECM	Electronic Counter Measures
EMC	ElectroMagnetic Compatibility
EP	Electronic Protection
ES	Electronic Support
EUT	Element Under Test
EW	Electronic Warfare
GaN	Gallium Nitride
HEMP	High-Altitude ElectroMagnetic Pulse
HPEM	High-Power Electromagnetics
HPM	High-Power Microwaves
IED	Improvised Explosive Devices

IEMI	Intentional ElectroMagnetic Interference
M-SC	Mode-Stirred Chamber
MPM	Medium Power Microwaves
MSI	Medium-Scale Integration
MSRC	Mode-Stirred Reverberating Chamber
MVED	Microwave Vacuum Electronic Device
OATS	Open Area Test Site
RC	Reverberation Chamber
RF	Radio Frequency
RMS	Root Mean Square
RST	Radiated Susceptibility Test
SNR	Signal-to-Noise Ratio
SSI	Small-Scale Integration
SSPA	Solid-State Power Amplifiers
TR	Time Reversal
TRAS	Time-Reversal Amplification System
TREC	Time Reversal ESlectromagnetic Chamber
TRM	Time Reversal Mirrors
TWT	Travelling-Wave Tubes
UWB	Ultra WideBand
VLSI	Very-Large-Scale Integration
VNA	Vector Network Analyser

Electromagnetic and Electronic Symbols

μ_0	Vacuum Permeability	$4\pi \times 10^{-7}$ H/m
μ_r	Relative Permeability	

σ	Conductivity		S/m
c_0	Speed of Light in Vacuum	299 792 458	m/s
P_f	Dissipated Power		

Statistic Symbols

μ_x	Mean Value of a random variable x	
σ_x	Standard Deviation of arandom variable x	

Other Symbols

S	S parameters	

Introduction

Modern electronic systems are becoming increasingly dependent on sophisticated components. Their vulnerability to radiation hence becomes an important parameter to ensure proper operation under all circumstances. This vulnerability is quantified during susceptibility testing.

Susceptibility measurements aim to validate the correct operation of a device when subjected to an electromagnetic field. During a susceptibility test, the experimental protocol is to generate a field which will impact on the element under test. In this context, it is interesting to generate high-power waves while being able to maintain a good control of the waveform. The source generating the disturbance is thus a key element of the protocol. Indeed, it should generate signals that evaluates the performance of the system under test.

Current state of the art allows either a good control of the waveform or to generate high power, but not both at once. Moreover, this is only true for limited frequency bands.

In this work, we investigate the possibility of obtaining a source allowing both a good control of the waveform, while reaching power levels high-enough as part of EMC and hardening measurements.

The proposed solution adds two steps to a direct amplification chain. The first step consists in spreading the energy of any type of signal using a reverberant cavity. The impulse will be reflected on the cavity walls causing the signal to spread in time. The resulting signal is time-reversed before being amplified with solid-state amplifiers. The time-reversed signal will then refocus into the original impulse. With this system, it is possible to recover an amplified version of the emitted signal during the first stage without having to change the amplification module. The system proposed within this thesis allows new stress modes not necessitating High-Powers levels at the input of the cavity and allowing high repetition frequencies and by controlling the beam-direction and its waveform. The system is also adaptable to any environment and is UWB (Ultra WideBand).

The subject of this thesis is concerned with the amplification possibilities offered by such a system. We are particularly interested in defining the parameters in order to avoid saturation of the amplifiers. This approach necessarily involves consideration of the randomness of wave propagation in a reverberation room. The effects of signal processing are quantified and shed some new light onto the physics properties of modified time-reversal processes such as 1-bit time-reversal.

In what follows, we also study the efficiency of the energy and peak-power spread in a reverberation chamber. To do this, analytical and probabilist models were developed and compared to measurements. The purposes of this study only applies if the field is diffused in the room. Knowing that a perfectly diffuse system is defined by an isotropic and homogeneous field in the entire volume of the cavity. A statistical approach is preferable in order to establish valid models. A criterion on the amplification of the system taking into account the statistical nature of the response of the room was found to avoid saturation of the amplifier. The amplification gain or the refocusing efficiency of a time-reversal process is also modelled and confronted to experimental data.

In the first part, we compare the proposed system with current generation high-power microwave technology to show the interest of reverberation chambers and spatio-temporal focusing capabilities of time-reversal.

Subsequently, we are interested in describing the theoretical and statistical models derived during the course of this work. A brief introduction to reverberation chambers is then conducted. Specifically, a description of statistics of the rooms in the case of diffuse field is presented. Detailed experimental measurements assessing the effects of loading a chamber with antennas are presented.

In the last part of this work, the amplification properties of a time-reversal system are modelled and validated with experimental measurements. In particular, an analytical model evaluating the average amplification margin and refocusing gain but also their variations around this value was developed. A comparison between the numerical model and the analytical model for the random part is established. It is therefore possible to give a mean value of the amplification made possible by the system proposed according to the used chamber and the injected signal. The variations around this value are also taken into account by the models developed. We conclude on the various possibilities offered by such a system and by the attained levels using the prototype.

Chapter 1

High-Power Electromagnetic Sources - Context and Objectives

1.1 Applications of High-Power Microwave Sources

1.1.1 Introduction

Modern technologies depend on increasingly miniaturised complex technologies. The generalisation of these high-tech devices and the constant increase of their number in our everyday life have led to a more complex electromagnetic environment requiring thorough studies in order to guarantee appropriate simultaneous functioning of these various technologies. A hardening stage is thus necessary in order to mitigate, or even neutralise dysfunctions of systems and their electronics in all circumstances.

Electromagnetic Compatibility (EMC) is the branch of electromagnetism that is concerned with the correct operation of a system in an electromagnetic environment without itself causing interference with its surroundings. EMC is thus the study of unintentional or intentional generation, propagation and reception of unwanted electromagnetic energy. Electromagnetic disturbances designate all electromagnetic phenomenas, including noise and undesired signals susceptible of creating operational disturbances of a device or a system (cf. Figure 1.1) Whichever the physical process (radiated or conducted), two generic type of coupling can be found:

- Frontdoor : coupling through intentional receptors for electromagnetic energy such as antennas and sensors; power flows through transmission lines designed for that purpose and terminates in a detector or receiver.
- Backdoor : coupling through apertures intended for other purposes or incidental to the construction of the target system.

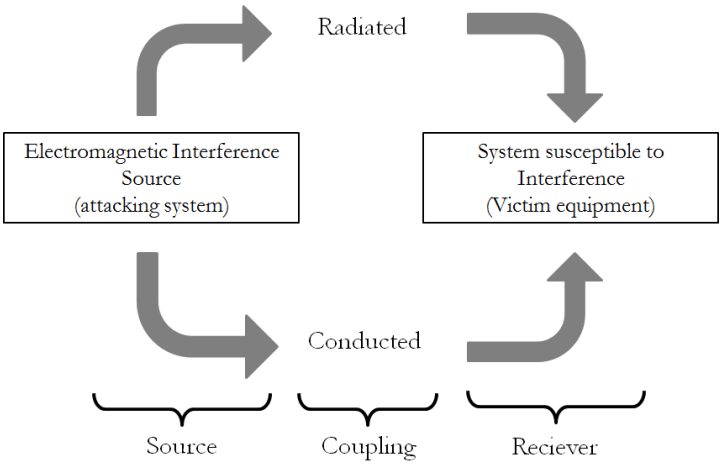

Figure 1.1 The three components of a EMC problem : source, coupling, receiver

EMC is therefore the study of the causes, effects, means of detection and protection of electromagnetic perturbations [8], to summarize, the aims of EMC studies are :

- to describe the interfering source and determine the interference fields it radiates
- to consider all the possible coupling modes between the “disturbing”source and the “disturbed” system on both qualitative and quantitative levels
- to simulate and test in order develop adapted protective techniques

The behaviour of systems when they are subjected to fields is studied during susceptibility testing. In practice, in order to study this behaviour, the device or equipment under test (EUT) is placed in an anechoic chamber or a mode-stirred reverberation chamber (MSRC). In this chamber is placed a transmitting antenna, connected to a power amplifier, itself supplied by an RF signal generator. Part of the spectrum is then swept in frequency with the field strength and the modulation required to meet test standards. The equipment under test must function normally when subjected to electromagnetic radiation defined by standards [8].

The source causing the disturbance on the desired object is a key element of the analysis. This source must generate the maximum stress on the system under test. This should enable to generate the expected field strengths on a wide enough bandwidth to ensure proper operation of the device in all circumstances. Being able to generate high-power fields over tunable bandwidths is therefore a crucial point for hardening devices.

Generating High-Powers or Controlling Waveforms?

In the context of susceptibility measurements, the generating sources are essential. According to the levels of incident fields, the effects on electronic systems can be categorised as follows [9, 10]:

1. Creating Noise (Front door)
    - These signals upset, perturb sensitive receivers placed on a system.
    - These perturbations do not need a high-field level on the system. Signal efficiency depends more on the type (intelligence) of the incident signal on the object than its power. A good waveform control is thus necessary [9].
2. False information implementation (Front door)
    - The objective is to override the normal signal of the target with another and to feed it false information.
    - These effects appear for incident field levels of decade V/m. A good control of waveform is also necessary.
3. Transient upset to loss of power [9]
    - Field level on target need to be narrowband and between decade and hundreds of V/m. The objective of such signals is to induce enough power to disrupt the logic state of an electronic component. In order to obtain critical error or failure of the device, the repetition frequency and number injected pulses must be well adapted to the system.

4. Permanent damage or Burnout (Back door)

    - Physical damage to electronic system. The system cannot function anymore after having been submitted to such high-level fields. These damages are mostly caused by transient that cause over-voltages in junctions and require 100 to 1000 or over V/m fields.

Two important effects can be found in the second category: *Jamming* and *Deception*. These two effects are most common in EW (Electronic Warfare) systems but similar effects are obtainable using HPEM. Jamming is the blinding of microwave or RF receivers or radars and Deception consists in spoofing of a system into mission failure.

Two parameters are therefore important when considering perturbation sources: generating high-level fields and waveform control. In order to ensure the correct operation of a device in all circumstances, it may be necessary to generate high-powers but also enable good control of the shape of the incident signal on the element under test.

Assessing Vulnerability and Threat to HPEM

The main type of threat considered during this work are IEMI (Intentional ElectroMagnetic Interference). An IEMI is a man-made threat specifically designed to cause interference or damage to electrical and electronic components of a system. Threat assessment to IEMI of a system is necessary in order to determine which type of signal could impact a system as well as their likeliness to happen. A classification of civilian facilities to IEMI threat is proposed in [11]. Three characteristics of a facility (Accessibility, Susceptibility and Consequence-ASC) are proposed for evaluating vulnerability to IEMI. This methodology is also called the IEMI threat cube cf. Figure 1.2. Accessibility is defined by the ability of gaining access to the different elements of the facility or its critical components. The consequence of an IEMI depends on the complexity and interdependencies of the system and characterizes how badly this system is disturbed by the attack. Susceptibility is defined as the inability of a device, equipment or system to perform without degradation in the presence of an electromagnetic disturbance in [10]. It can be subdivided into [12]:

- Receptivity, the degree of the facility's ability to mitigate disturbances between and within electromagnetic topological zones.
- Sensitivity, the different upset threshold levels of the equipment and subsystems inside the facility.
- Redundancy, the availability of backup systems and ability to "degrade gracefully".

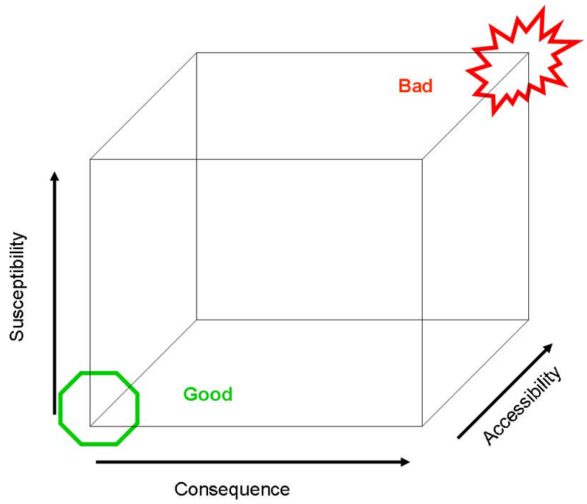

Figure 1.2 Three quantities that can be used for an IEMI vulnerability or hardness analyses of facilities and large distributed systems. The desired region is marked ("Good") along with the case of a system that is critically vulnerable ("Bad") [11].

This classification is very useful when considering hardening issues. To each axis corresponds one ASC measure. The origin is located at the bottom left. Assessing the ASC parameters allows to form a vector that can be considered as a vulnerability vector spanning within the threat-cube. Systems near the origin have good hardening against IEMI, and systems near the farthest corner to the origin are highly vulnerable against IEMI. A system should also be considered vulnerable even though the consequences of an attack are low but the accessibility and susceptibility factors are high. The upper farthest right corner of the ASC cube describes a system that is denoted critically vulnerable.

A classification of effects on electronics is also possible. Depending on the pulse width general trends of electronic thresholds can be found corresponding to the different predominating effects on electronics cf Figure 1.3, [13, 14]. Three regimes exist depending on the pulse width. The main physical process explaining these three regimes is thermal energy diffusion within the targeted electronic components. Failures in semiconductor devices due to thermal effects (4^{th} category of the list - Permanent damages or burnout) generally occur when the temperature at the critical junctions is raised above 600 to 800^{o} K [15], resulting in changes in the semiconductor up to and including melting.

For pulses of less than 100 ns, timescale is short compared to thermal diffusion times and can thus be neglected, semiconductor junction damage depends only on the energy deposited on the target components. Therefore, in this regime the threshold power for damage varies as t^{-1}, as shown in Figure 1.3. t here corresponds to time-to-failure. This is called the adiabatic region and corresponds to the regime of interest when talking of HPM-MPM UWB.

For pulses greater than 100 ns, thermal diffusion carries energy away from the junction. The general result is the Wunsch–Bell [2] relation for the power to induce failure. The Wunsch–Bell

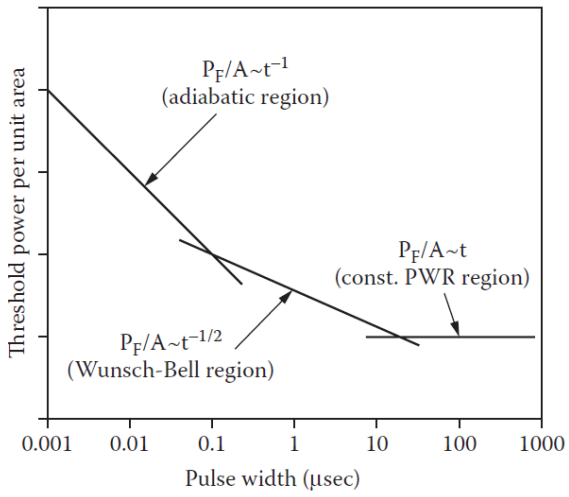

Figure 1.3 Power density for burnout vs. pulse width. UWB HPM sources operate in the adiabatic region and narrowband sources in the Wunsch–Bell or constant power regions [1, 2]

relation is a rule-of-thumb for estimating the temperature induced failure of silicon devices with constant dissipated power P_f :

$$P_f = K_1 t^{-1/2} \tag{1.1}$$

where K_1 is a device-specific constant equal to:

$$K_1 = A\sqrt{\pi\kappa\rho C_p}\,[T_m - T_i] \tag{1.2}$$

with A is the junction area, κ the thermal conductivity, ρ the density, C_p the specific heat, T_m the failure temperature and T_i the initial temperature. This relation is generally applicable because, even though thermal conductivity and specific heat vary with temperature, these effects cancel out. Therefore, in the domain between $\sim$ 100 ns and $\sim$ 10 μs, the energy required to cause semiconductor junction failure scales as $t^{1/2}$ and the power requirement scales at $t^{-1/2}$.

For pulses longer than $\sim$ 10 μs, a steady state of the component is attained and the rate of thermal diffusion is equal to the rate of energy deposition. Therefore, the temperature is proportional to power, resulting in a constant power requirement for failure. The energy requirement then scales as t.

The consequence of these scaling relations is that the shortest pulses require the highest powers but the least energy. Conversely, the highest energy and lowest power are required for long pulses.

UWB HPM-MPM sources operate in the adiabatic, narrowband sources in the Wunsch–Bell or constant power regions.

If energy is to be minimized in deployed weapons, the shorter pulses will be used, and if power is the limiting requirement, then longer pulse durations are indicated. The above relations apply to single-pulse damage. If there is insufficient time between successive pulses for heat to diffuse, then accumulation of energy or thermal stacking will occur. In order to obtain more efficient sources, there is also the possibility to have short pulses repeated fast enough (faster than thermal diffusion) to build up energy inside the target. In this case, power can be reduced. The required value of repetition rate for thermal stacking will vary with specific targets but a typical value is 1 ms.

Although the classifications presented here give rules of thumbs no easy access to the needed data exists in order to model threat assessment and time to failure without measurement especially for complex systems. Moreover, as we will see in the next section, the effects presented here are enhanced by the generalisation of small, vulnerable electronics, confirming the recent interest of such sources for vulnerability and hardening testing but as well for military purposes.

However gradual degradation seem to occur even at repetition rates much lower than the rate required for thermal stacking. This might be caused by incremental damage. This effect may allow reductions in the threshold power requirement for electronic damage. Hundreds to thousands of pulses might be sufficient to reduce the damage threshold by an order of magnitude. Such effects have not been quantified sufficiently. The repetition rate requirement can be relaxed, relative to thermal stacking, and will be determined by mission constraints, such as time on target. In any case, repetitive operation is required for any real engagement, and therefore accumulating damage effects may be inherent to HPM Directed Energy Weapons in the future.

1.1.2 Applications of HPEM sources

HPEM or HPM domain regroups all technologies enabling generation of high peak-power. HPM sources are used for electromagnetic compatibility measurements, system interference, jamming, hardening and electromagnetic weapons. One of the main proposed applications for high power microwaves are electromagnetic weapons or Directed Energy Weapons (DEW) that are at the point of deployment. The usage of powerful microwave pulses as weapons dates as far back as British radar studies during World War II. Nowadays, HPM and more particularly DEW generally fall into three categories [1], Microwave or radio frequency (RF) energy weapons, lasers, particle beam weapons. Energy weapons have two potential advantages compared to existing weapons:

- They use a power supply and not explosive munitions.
- The time (speed) of an attack is limited only by the propagation time which is the speed of light.

Avoiding such an attack is impossible and the number of shots is only limited by a power supply that does not always need to be portable. The only way of mitigating or countering such attacks is to harden the system appropriately. RF DEWs or HPEM (High Power ElectroMagnetics) have an advantage over Lasers which have difficulties propagating in the atmosphere especially through rain or humidity and electron beams that cannot propagate in space. Moreover, both lasers and electron beams are pinpoint weapons and require high accuracy to hit the target. HPEM have a spot size large enough to accommodate some lack of precision. Also, they are more electrically efficient, less complex and therefore less costly than Lasers or Particle Beams.

Some features of HPM attacks are [16]:

- Electronic attacks produce little or no collateral damages.
- To counter such an attack, entire systems must be hardened. An HPM weapon made effective against a deployed system requires modification over the complete system and can be quite long and cost full.
- Entry points can be by front door or back door.
- Attacking areas with many targets inside is possible.
- Little sensitivity to atmospheric conditions such as fog and rain.
- Relative cost per target is quite low when compared to conventional munitions.
- Repair requires high level of expertise and probably cannot be done rapidly.

Most DEW scenarios for HPM are soft-kill missions similar to radar jamming and electronic warfare. Soft kill consists in disabling critical components while the target body remains largely undamaged as opposed to hard kill, where large-scale physical destruction is inflicted on the target. Two important technology developments have led to an increase interest towards HPEM and MPM sources:

1. The development of sources capable of producing peak powers in excess of a gigawatt and now of miniaturized kilowatt sources using SSPA (Solid-State Power Amplifiers).
2. The increasing miniaturization of, and dependence on, electronic components in military and consumer electronics.

The small scale of today's electronic components makes them vulnerable to small amounts of microwave energy — thus the emergence of the "chip gun" and "E-bomb" concepts, a transmitter designed to upset or burn out integrated circuits in the electronic brains of modern systems. The continuous trend toward miniaturization and lower operating voltages has made HPEM but also MPEM weapons more attractive. Vulnerability will probably increase because of recent trends where unhardened commercial equipment at lower cost have replaced metal packaging by plastic and composite materials (cf Figure 1.4).

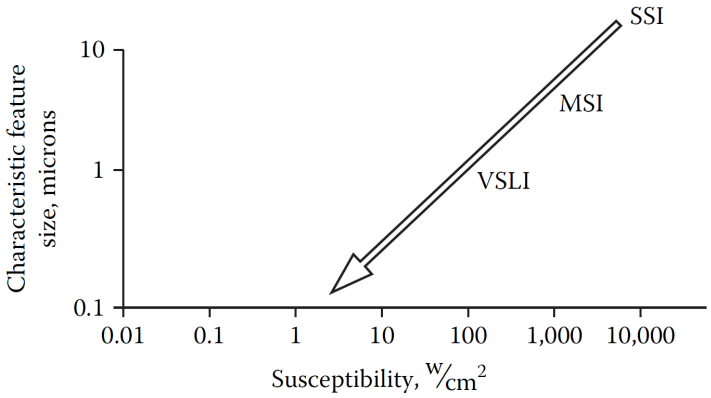

Figure 1.4 Feature size of chip technologies falls, lowering the threshold for HPM effects VLSI (Very-Large-Scale Integration), MSI (Medium-Scale Integration) and SSI (Small-Scale Integration)[17].

A limitation of electromagnetic weapons is the difficulty of kill assessment. Absence of emissions does not necessarily mean that an attack has been successful. Targets successfully attacked may appear to still operate. Radiating targets such as radars or communications equipment may continue to radiate after an HPEM attack, even if their receivers and data processing have been damaged or destroyed. A deceptive response for a system coming under attack is to shut down. This has led to two interdependent fields of research ECM (Electronic Counter Measure) and ECCM (Electronic Counter-Counter Measure). In the following, a proper definition of HPEM and MPEM will be given shedding some light on the new possibilities offered by time-reversal techniques.

1.2 State of the Art

Now that we have presented the applications as well as the effects on electronics of HPEM and MPEM two parameters were shown to be of crucial importance: waveform control and power. In this section we shall determine if there exists a source that allows both properties at present. As we have shown in the previous section a wide variety of applications exist for HPEM and MPEM sources. In this section, we show the limitations of current HPM technologies then describe the proposed solution and its location within existing MPM/HPM technologies.

Historically, HPM microwave sources define sources characterized by peak-powers over 100 MW for frequencies ranging from 200 MHz to 300 GHz [9, 18, 19]. However, with the arrival of new more vulnerable electronics presented in the previous section, a new category defined as MPM (Medium Power Microwaves) sources have emerged. These sources are not able to attain such high powers but allow a greater flexibility of attack which can be particularly interesting for testing or on the field. These sources usually work from the hundreds of watts to the hundreds of kW region. The frequency band of interest during this PhD ranges from 0.5 to 3 GHz and the peak-power levels to

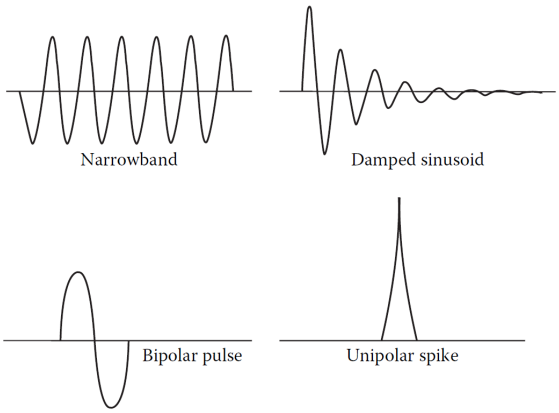

Figure 1.5 Electric fields of classes of pulses. As the number of cycles increases, the bandwidth decreases. (a) Narrowband; (b) damped sinusoid; (c) bipolar pulse; (d) unipolar spike (which does not radiate as a spike, but as a cycle). [1]

attain of tens of kW. This peak-power mostly depends on the amplification technology used. Similar results can be obtained using MPEM and the classifications presented before still hold.

1.2.1 State of the Art in HPEM for MVEDs and SSPAs

HPEM sources usually generate one of the following waveforms [9] cf. Figure 1.5:

- A single pulse with many cycles of a single frequency (an intense narrowband signal that may have some frequency agility).
- A burst containing many pulses, with each pulse containing many cycles of a single frequency.
- An ultra-wideband transient pulse (spectral content from 100s of MHz to several GHz).
- A burst of many ultra-wideband transient pulses.

As we have seen in the previous section the type of waveform is important when considering applications and power levels for burnout. These few waveforms however are not sufficient anymore when considering hardening since more intelligent lower power sources can be used. Figure 1.6 presents field spectral density with frequency for existing HPEM technologies. It also allows a qualitative comparison between HPEM that are range dependant and HEMP (High-Altitute ElectroMagnetic Pulse) waveforms that are not. If spectral domains vary according to the technology, most HPEM sources with high spectral density are very narrow-band which also represents a serious limitation.

The majority of sources with high spectral density and a very narrow band are vacuum technologies. These technologies (klystrons, magnetrons ...) require high power to operate and remain difficult to transport [18, 20]. In addition, their ignition may be complex (need to generate a plasma in some cases) and have ionised radiation. Some vacuum technologies can have their frequency tuned by varying the geometry of the vacuum cavity. Nevertheless, it is not possible with these technologies

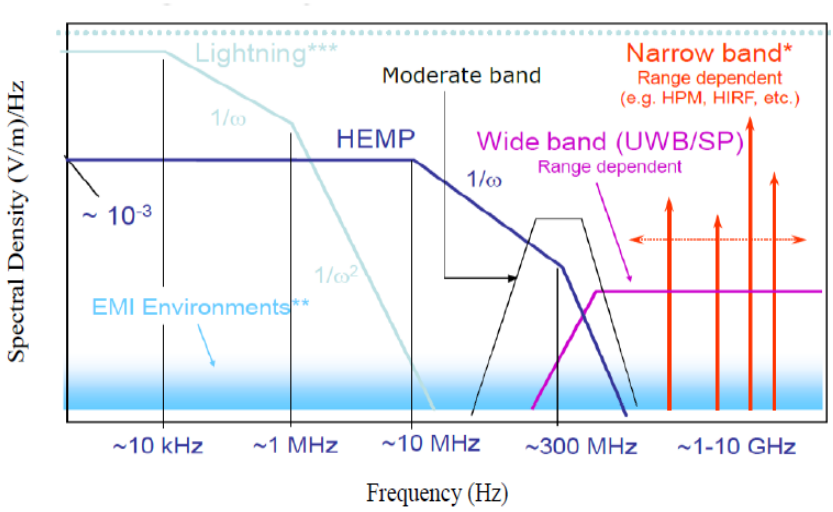

Figure 1.6 Schematic summary of some microwave power sources. HEMP (High-Altitude Electromagnetic Impulse), EMI (Electromagnetic Interference), HIRF (High Intensity Radiated Fields) [21]

to generate signals on several frequencies at the same time while controlling the waveform. Marx Generators allow the generation of an ultra-high power on ultra-wide frequency bands. These generators store and release a very high amount of energy over a very short time [18]. Even if they are more transportable, these wideband technologies use bursts techniques and do not allow any flexibility on the waveform since the bandwidth only depends on the time the generator takes to release its energy and the geometry of the antenna.

At present, in order to harden a system over wideband and waveforms for relatively high powers the system must go through extensive testing using various sources which can represent important costs and delays.

Current state of the art of microwave solid-state devices and microwave tubes is shown in Figure1.7. Figure 1.7 represents peak-powers as a function of the frequency for most microwave sources and their domain of application. Solid-state devices present the advantage of being much more flexible and are easy to use. However, solid state technologies do not, at present, allow power levels that can be categorized as HPM. In Appendix A, more graphics categorizing the different existing technologies based on their peak powers and their frequencies are available. As indicated, on the figure solid-state devices produce RF power levels at about 100 W and operate with reasonable RF output power to frequencies of about 100 GHz. This RF performance status is for single device operation and does not necessarily represent a true comparison of the RF output power capability of a system. Power-combining and phased-array technology allows the outputs of many solid-state devices to be combined, thereby producing significantly improved RF output power and solid-state systems can, in practice, compete in terms of RF output power with some tube-based systems. Combining

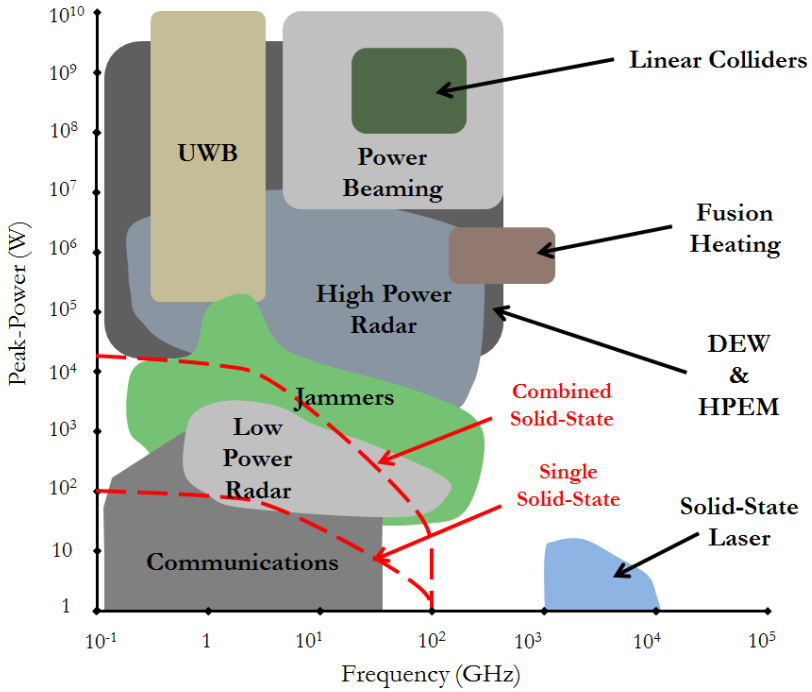

Figure 1.7 Peak-power as a function of frequency and the various sources of HPM.[26, 27]

technology can raise microwave RF output power into the kW range, at least through S band and into K_u band [22–25] and theoretically to much higher power levels. However, such multi-device concepts are increasingly difficult to apply as operating frequency increases and cannot extend the upper frequency limit beyond the present state of the art. Moreover, combining many solid-state devices in order to obtain more power may necessitate an important number of power sources or a high power source and complex electronics to power all the devices at once especially in pulsed mode. This complexity may reveal deterrent when considering a solid-state solution over a single vacuum tube. Moreover, even by combining many solid-state power amplifiers, the power levels obtained are still below the definition for HPEM.

In order to obtain improved HPM devices for electronic attack, the need is for higher power in a relatively modest band of frequencies, i.e., between 1 and 10 GHz. A simple estimate shows how this becomes a challenge in managing high power densities for MVEDs (Microwave Vacuum Electronic Device) showing their present limitations. In this frequency range, the typical device's circuit cross-sectional dimensions is more or less determined by the free space wavelength λ_0 of the radiation, will be on the order of $\sim$ 10 cm $\times$10 cm, or $\sim$ 100 cm^2. For power levels in excess of 100 MW, it becomes necessary to be able to manage power densities in excess of 1 MW/cm. For such powers, life expectancy of the sources are reduced, parasitic modes can be excited and radio frequency breakdowns become likely.

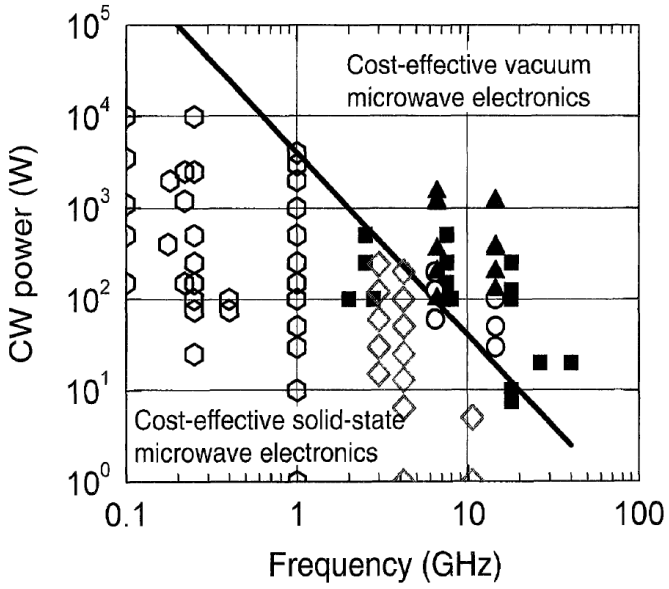

Figure 1.8 Log-log plot of CW power versus frequency of a selection of commercially available power amplifiers for communications and testing applications. Solid symbols represent vacuum electronic devices, while open data symbols represent solid-state microwave power amplifier products. In this example, "cost-effective" is an empirical characterization determined by vendors that offer both solid-state and vacuum electronic satcom and testing transmitter products. As discussed in the text, critical functionality requirements will override cost competitiveness in some applications [28].

Figure 1.8 provides a good guideline to select the appropriate technology with regards to cost. This graphic represents solid-state and MVEDs technology repartition over frequency and CW power. It is possible to fit an inverse-squared curve separating both technologies assessing cost effectiveness limits of MVEDs and solid-state in regards of frequency. This curve shows that for frequencies below 3 GHz, solid-state technologies are more cost-effective than vacuum electronics.

There are several reasons that motivate selecting an inverse squared scaling for that curve [28, 29], and that choice is also consistent with a similar analysis in [30]. Van Fleteren's curve of cost-effective power versus frequency has been plotted in Figure 1.8, along with the power and frequency specifications for commercially sold solid-state and vacuum CW amplifiers.

The data in Figure 1.8 include communications, instrumentation, and test power amplifier products. Below the line, the technology choices are almost exclusively solid state. Above the line, the options are almost exclusively vacuum. In the vicinity of the dividing line, one can find both technology choices offered on a cost-competitive basis.

Of course, it is only one measure for making a selection, and a decision should include other factors. For example, Figure 1.8 does not address the issues of size and weight differences. However, it would be interesting to obtain such a graphic with a third axis corresponding to the instantaneous

bandwidth attainable in regards of technology when considering cost effectiveness. Is it possible to improve solid-state amplification in order to come closer power levels offered by MVEDs?

1.2.2 Solid State vs Tubes

Compactness is a commonly mentioned problem for military applications of HPM. The size and weight limitations of military platforms require squeezing as much power into a specific volume as possible, and HPM systems to date have not been designed with this as a criterion, their purpose being HPM effects testing. In recent years, improvements have been made in compactness of capacitive energy storage. The specific microwave technology used for the source also has a big impact on size and weight.

It should be understood however, that MVEDs and SSPA have complementary roles [28] and it is highly unlikely that SSPA will replace MVEDs in the near future, especially after the progress that have been accomplished for compact (capacitive) Marx generators. Another particularly interesting factor when considering field applications where only small or no interventions/reparations are possible is reliability. Since MVEDs have been used for such applications for a longer period of time, there have been many improvements notably for space TWTs that can be used for more than 10^7 hours. However, even if solid-state electronics may require more regular periodic replacement than MVEDs, maintenance and the replacement non-functional parts requires less training. In most cases however solid-state technologies are more reliable. Recent improvements have shown that techniques used for low-power and low-noise amplifiers can be transposed to SSPAs but have also led to innovations in MVEDs fabrication processes. Therefore, it is really important to weigh every factor before choosing a technology.

Solid-state devices have replaced vacuum electronics in a vast majority of microwave electronic systems over the past 30 years, however for high power amplification applications the best solution depends on the required specifications and evolve with the emergence of new technologies. In particular, the areas of high radio-frequency (RF) power for microwave and millimetre-wave radar and communications transmitter applications, the ability to produce adequate RF power levels at frequencies greater than 100 GHz, and the ability of devices to operate at high temperatures greater than about 250 °C remain dominated by microwave tubes. Further, solid-state material and device development in these areas are among the last frontiers for semiconductor electronics. In these areas, solid-state devices have not been able to compete with vacuum tube devices, and most systems that must deliver kilowatt to megawatt levels of power are designed using various types of microwave tubes.

Thermal dissipation and electric field breakdown play a central role in HPM and represent a major issue for SSPA. Indeed, the size of a solid-state device is more determined by its cooling technology than by the components' sizes themselves. A solution to this heating problem is to use solid state devices in pulsed mode so they do not heat so much and therefore reduce the size and complexity

of the cooling system. Moreover, using SSPA in pulsed mode allows components to be used in non-conventional manners and higher gains can be obtained compared to continuous power supply. The trade-off is a more complex power supply system that allows a good synchronization between the RF signal and DC power. Particular attention must be given to pulse time in order to not overheat and break the semiconductor device.

However, Homeland security and military defence technology considerations have stimulated intense interest in mobile, high power sources of millimeter-wave (mmw) to terahertz (THz) regime electromagnetic radiation, from 0.1 to 10 THz. Vacuum electronic sources are still a natural choice for high power, the challenges have yet to be completely met for applications including non-invasive sensing of concealed weapons and dangerous agents, high-data-rate communications, high resolution radar, next generation acceleration drivers, and analysis of fluids and condensed matter.

For high-power applications in most cases the most suitable solution are MVEDs technologies. However for MPM applications, solid-state is becoming increasingly interesting with higher duty cycles and flexibility and can compare in reliability and efficiency to MVEDs in most frequency domains. Recent improvements have pushed these frequencies to higher levels and have opened the way to new applications. MWs sources using solid-state devices at single frequency are currently in development thanks to recent findings in semi-conductors. Ultimately, the physical advantages of one technology will manifest in the final cost, efficiency and total system size, or weight difference between the vacuum ans solid-state options for a given power-level.

The proposed system uses SSPA and not MVEDs (Microwave Vacuum Electronic Device) as amplification modules. This technology is both compact and allows to amplify a wide variety of signals with high-repetition rates on large frequency bands. The idea is to obtain a source that can be used for a wide variety of tests without having to change the system or to move the EUT. The need to have a very large instantaneous band with the same technology also determined our choice. Modern SSPAs are more efficient than before and are also very large band and for our applications do not need a sophisticated power supply in order to function [29, 31, 32]. However, is it possible to improve amplification gains of solid-state devices in order for them to be evermore competitive? This question has revealed being the main concern of this work.

Since solid-state devices do not allow HPEM levels a comparison between jammers and MPEM sources will be presented in the following section proving that MPEM sources are in fact adapted to real world constraints.

1.2.3 MPM between Jammers in EW and HPM

The distinctions between HPEM directed energy and jammers can be viewed in terms of the trade-off between the sophistication and power level of an attack, as shown in Figure 1.9 [33]. Most jammer attacks intend to implement false information on target or to obtain transient upset to loss of power. This entails overpowering enemy systems in the same manner as contemporary battlefield

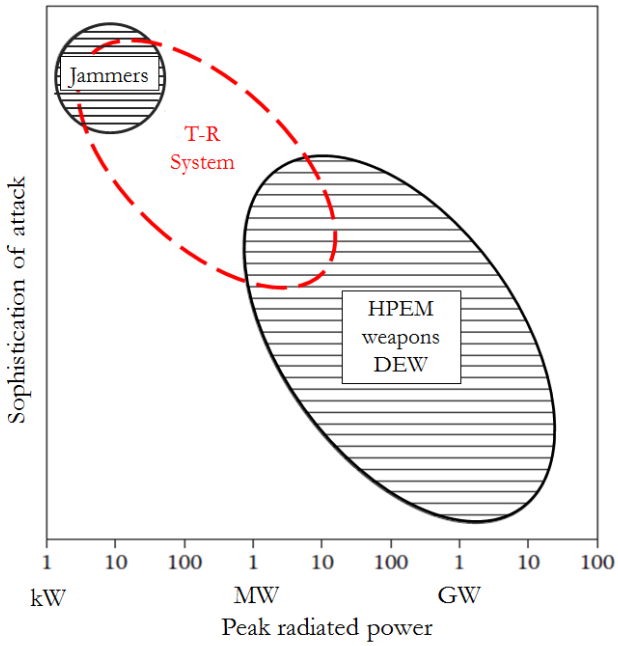

Figure 1.9 Domains and trends of HPM and jamming in electronic warfare[1]

jamming systems. HPEM-based system attacks are in the same way capable of totally dominating the EW battlefield, allowing no chance for "burnthrough" of their jamming signal. Between high power jammers and burnout devices lies a middle ground where electronics can be upset, e.g., lose information in digital systems so that a missile may become disoriented (break lock) or its tactical communications can get confused. It is this middle ground that is of interest in this work. The line between jammers and HPEM directed energy weapons has been fairly sharply drawn within the context of EW, at least in the West.

Jammers use sophisticated techniques at lower order of magnitude powers ($\sim$ 1 kW) to deny an opponent effective use of communications and weapon systems, while protecting one's own use of the electromagnetic spectrum. Electronic warfare has emerged as a vital element of military strategy, an effective way of neutralizing enemy forces and enhancing the power of friendly forces. It has also become expensive in its increasing sophistication because of the diversity of threats and a continuing race between the techniques of generating electronic countermeasures (ECMs) also known as Electronic Attacks (EA) and countering such interference with electronic counter-countermeasures (ECCMs) also called Electronic Protection (EP). The major divisions and domain of application of EW systems are presented in Appendix A. Hardening thus becomes an important aspect for every system of an operation.

In the early years, HPM DEWs were seen as the means of attacking a multitude of targets, using simple pulses from a generic weapon at $<$ 1 GW to provide higher cost effectiveness than jammers.

Then efforts turned to developing intermediate alternatives, combining features of HPM and jammers, known as smart microwaves, or medium power microwaves (MPM). The emphasis rests on employing more sophisticated waveforms at a reduced power relative to HPM. Whereas some applications of HPM have envisioned burnout of the target in a single pulse, smart microwave attacks use repetitive pulsing or amplitude and frequency modulation and other forms of pulse shaping to lower the damage level of electronics. Two types of attack modes against electronics have been proposed: point weapons and area weapons. Point weapons, fire intense pulses to disable a specific target at substantial range and area weapons aim to protect a surface by disrupting any object entering a given volume. When, a high power density is produced on that target by the weapon an upset or burnout is obtained.

Research and Development in EW (Electronic Warfare) systems are driven by ECCM (Electronic Counter-Counter Measures) and the multiplicity of threats. Most EW system are threat-specific and rely mostly on spoofing or deception attacks/effects. Increasing power of EW systems allows new more generic attack modes. Moreover, new attack modes reduce power and size requirements making MPM (Medium Power Microwaves) compatible with real world constraints.

Figure 1.9 is qualitative and shows no numerical values for sophistication of attack since there seems to be no metrics to evaluate such a quantity. The aim of the figure is to qualitatively locate the source conceived during this PhD within existing technologies based on sophistication (intelligence) of attack and the output power of the system. A time-reversal system would allow to refocus relatively high powers with a good control on the shape, bandwidth polarisation of the refocused pulse and allowing high repetition-rates for multiple test configuration without having to move the EUT. This Figure is intended to allow a good comprehension of the multiple possibilities offered by time-reversal depending application.

In this section we presented a state of the art but also limitations of current technologies. Solid-state are still very limited in power whereas MVED's seem to face compactness issues as well as facing high risks of breakdown due to the very high powers within the tubes. Moreover vacuum devices require important primary power supplies, are rarely wideband and almost no flexibility on pulse shape is possible since they depend on geometrical characteristics of the cavities of the tubes. Some MVED's create ionizing radiation and can only be used in well controlled environments.

With current technologies, it is possible either to generate high power over very-large bands or narrow frequency bands. A technology that allows to control the waveform while still obtaining high power levels is non-existent. Electronic miniaturization has led to somewhat higher susceptibility of components and systems implying that hardening "along the way" during every conception phase will be the next step in EMC testing. A general rule of thumb shows that hardening during the design stage will increase cost of roughly 1% whereas by doing it afterwards, it may cost over 30% [34]. These trends in electronics systems have led to the need to rapidly and effectively assess the susceptibility of complex systems under high/medium stress over a wide range of frequencies, waveform and directions. No single system is able to do such a wide variety of tests without having to move the

EUT. The refocusing properties of time-reversal technique allows such flexibility of usage and have initiated this work.

The proposed solution is to add a two-steps to a direct amplification system using solid state amplifiers. More graphics classifying different technologies based on their peak-powers and their frequencies are available in the appendix of the thesis. The system proposed within this thesis would allow new attack modes without the need for substantially High-Powers but instead using high repetition rates and controlling the beam-direction and waveform. The system would also be adaptable to the environment by being UWB (Ultra WideBand). This system would therefore have a wide variety of applications in both jamming and HPEM as seen in Figure 1.9.

1.3 A new amplification system using Time-Reversal and Objective of this work.

1.3.1 Concept and Working Principle of the Amplification System

One conventional approach for amplifying an arbitrary waveform is to place a solid state amplifier to the output of an Arbitrary Waveform Generator or AWG before exciting an antenna as presented at the bottom Figure 1.10. This direct amplification method is limited by the saturation of the amplifier.

To improve the amplification capabilities of a direct amplification system, we propose to add two-steps (stages) to the amplification chain (Figure 1.10). A first stage or Calibration phase at the left of Figure 1.10, before the amplifier allows the energy of the signal to spread in time. A second stage or Refocusing phase at the right of Figure 1.10, after the amplifier allows the compression of the signal. This procedure enables the refocusing of the desired signal amplified at the input of the antenna and is the basics of a time-reversal process. A more thorough presentation of time-reversal will be presented in Chapter 3. The addition of these two steps allows to obtain a gain compared to the direct amplification chain. The spreading of the signal energy can increase the capacity of the amplifier, preventing its saturation.

Spreading over time of the emitted signal (an impulse) is accomplished by taking advantage of the multiple reflections taking place in a reverberation chamber. When a signal is injected in a reverberation chamber, it undergoes numerous reflections, the energy of the signal is diffused uniformly in all the chamber for very long periods of times. This property of reverberation chambers allows to obtain an effective spreading over time of the injected signal.

Signal compression is obtained by using a time-reversal technique. The principle of the time-reversal is based on the reversibility of the propagation of waves. When a source (acoustic or electromagnetic) emits a wave, the generated signal is measured and digitized on a network of antennas then re-emitted in inverse chronology. A convergent wave focuses then, spatially as well as

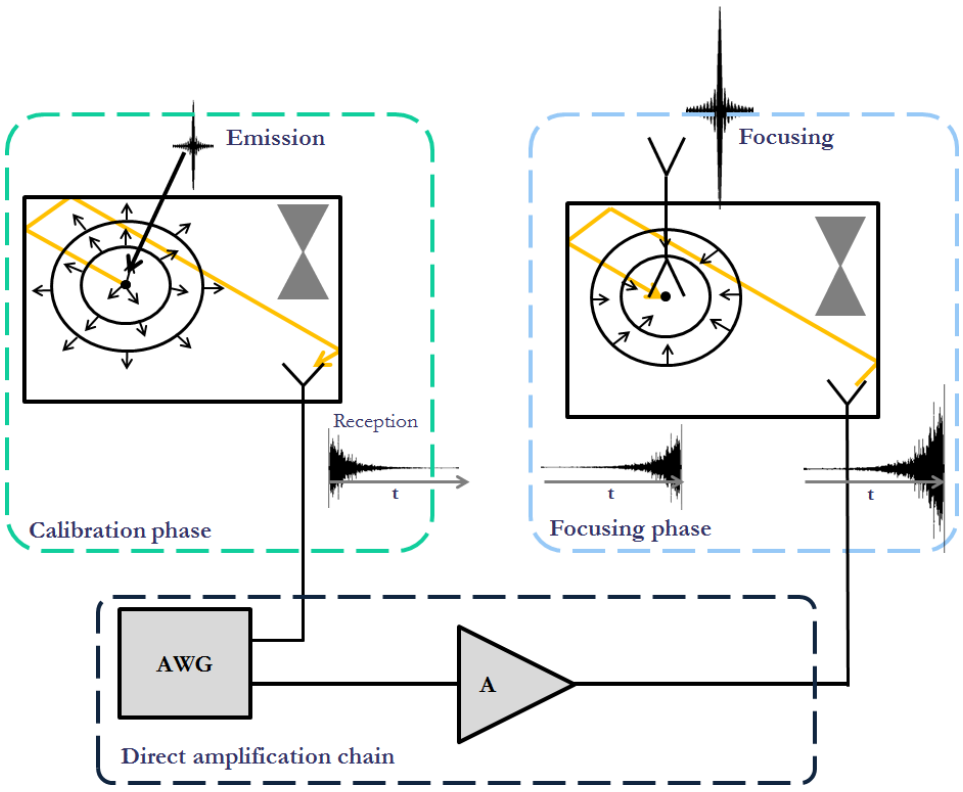

Figure 1.10 Classic amplification chain and modified with TR

temporarily, on the original (initial) source point. A more detailed presentation of the time-reversal technique will be presented in Chapter 3.

The objective of the studies presented herein is to estimate analytically and by means of simulations, the possibilities of amplification offered by a time-reversal system. To do so, various parameters and coefficient are of prime interest. We were particularly interested in the efficiency of time-reversal amplification in multipath environments such as but not limited to reverberating chambers. Statistical models related to the different parameters obtained were also necessary in order to fully encompass the possible variations of the efficiencies. A particular interest was given to the maximum-value statistics of the different signals obtained during a time-reversal process, especially the impulse response and the refocused signal. One of these parameters corresponds to the amplification margin obtained during the spread in time of the signal. It corresponds to the efficiency of the spreading of the waves in a reverberating environment.

The results obtained during this phase (calibration phase) led to a better understanding of which parameters must be considered when developing a time-reversed system so as to obtain the highest efficiency. In particular, conditions on the RC dimensioning, the effect of the number of antennas and positioning were found to be very important in order to build a prototype. Physical understanding of 1-bit time-reversal is presented and an analytical model of the added gain was found.

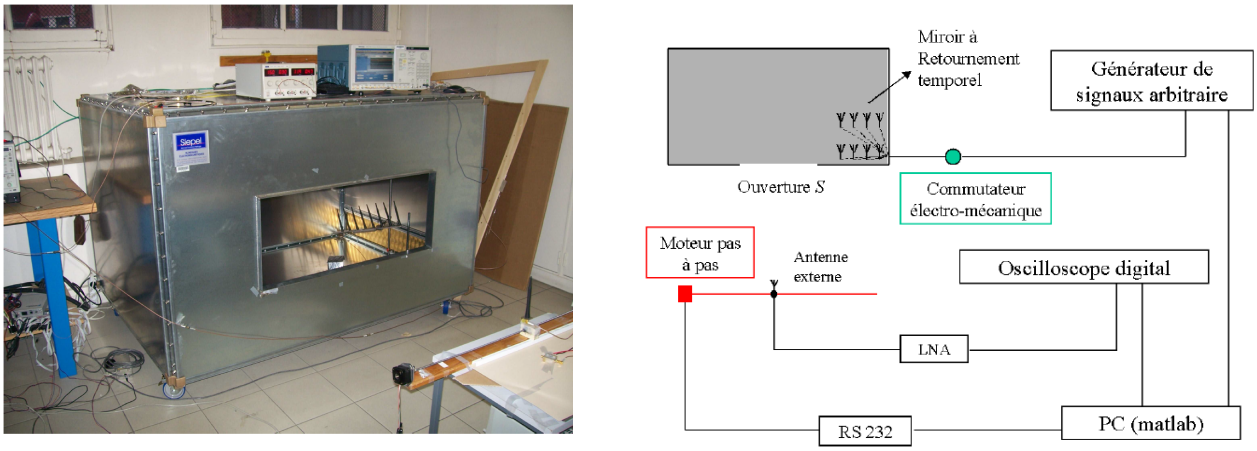

(a) Picture of the reverberation cavity (b) Schematic view of the experimental setup

Figure 1.11 Set-up using an antenna array and a reverberation chamber with an aperture to focus outside the volume [38].

1.3.2 Previous Works Using Time-Reversal

Previous works have considered the use of time-reversal focusing properties in order to achieve higher power levels [35, 36]. It was also shown that it was possible to use a cavity with an aperture to choose the focusing area [37]. The basic concept of the experimental work undertaken is presented in Figure 1.11.

A particularly interesting part of Davys' and Hongs' works is to use a leaky reverberating chamber in order to focus outside the chamber as can be seen in Figure 1.11. Amplification was obtained by using antenna arrays to receive and emit the signals arriving in the chamber and a 1-bit signal codage of the time-reversed signal. Refocusing is thus obtained on an element that would have radiated a pulse outside of the chamber. By using this technique high power gains were obtained. A model was developed in order to compare the mean and variance of the signal refocused using such a technique [36]. However the maximum value of the impulse response is taken. Here in chapter 2 we propose a model that evaluates the repartition of the maximum level of the impulse response. This allows a better assessment of the amplification allowed with 1-bit time-reversal.

This technique has its limitations. First, the efficiency of such chamber is not optimal due to big aperture of the chamber and the contrast levels decreases compared to classical time-reversal. The distance between antennas of the array in the chamber is small thus they are correlated and the gain obtained during measurements is not optimal. Moreover, a model was developed for the most optimal aperture with regards to frequency. Consequently, for every frequency a different aperture size has to be set up.

Recent works have also shown for SIMO (Single-Input Multiple-Ouput) for radar and imaging applications [39–43] using two or three dimensional cavities. The basic concepts of these type of

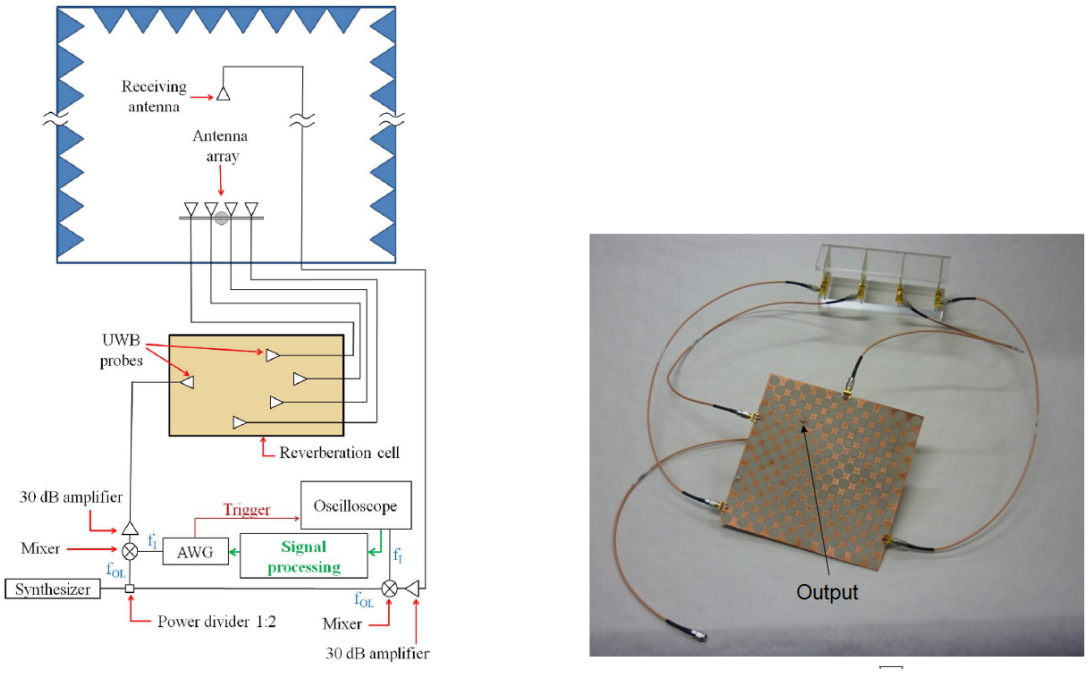

(a) Picture of the reverberation cavity (b) Schematic view of the experimental setup

Figure 1.12 Cavity and set-up used for SIMO applications [41]

application is shown in Figure 1.12. In a similar way than previously an impulse propagates using an antenna on the device or object that needs to be located. The signal is then received by an antenna array connected to the RC. If the antennas are not correlated the signal that is recorded via another antenna inside the RC will be composed of the different impulse responses within the chamber. Each impulse response being orthogonal, it is possible to focus on the different antennas with a certain desired delay and thus obtain beam forming [41, 42]. Some modifications have allowed to improve this technique in order to obtain better performances [44].

However, there have been no studies done on the energy and power efficiency of refocusing on various antennas at the same time mainly because the objective of the studies was to modify the signals recorded so as to obtain clearer images and better beamforming. In this thesis we also propose a simple model evaluating the efficiency of SIMO refocusing in reverberating chambers. These models are also adaptable to complex propagation system as only diffuse field considerations are needed.

1.3.3 Structure of the thesis

A main aspect of this work has been to develop analytical and statistical models of the power efficiency of a time-reversal amplification system (TRAS). First, since most of the theory presented here is only valid under the assumption of diffused fields a precise definition is first presented in Chapter 2 with a general presentation of mode-stirred chambers.

It is also important to evaluate the efficiency of a reverberation chamber. This allows to quantify the power received by one or more antennas when the reverberation chamber is excited. This factor is important when considering the construction of the most efficient chamber for time-reversal amplification.

Measurements assessing the loading effect of antennas in reverberation chambers when the field can be considered diffused were also undertaken and are presented in Chapter 2. The study focuses on the evaluation of the varying quality factor when adding loaded antennas in the chamber. Some unexpected results were found and are showed in this work. An attempt to explain the difference between the theoretical model and experimental results is presented.

Another focus of this work is to evaluate the ratios between signals during calibration and focusing phase. An important aspect of the studies presented in what follows concern evaluation of the maximum value of the impulse response in a complex propagation system. This model and the statistical aspects of the maximum level of an impulse response in a complex propagation system is also presented in Chapter 2.

In Chapter 3 a more precise description of the time-reversal technique and its focusing properties will be shown. The wide variety of current applications of such a technique are also presented. Theoretical models and experimental validation showing the power efficiency and gain of a time-reversal process will also be presented.

The last part of the Chapter 3, will present the power gain of time-reversal techniques and its statistical advantages compared to a classic use of a reverberation chamber and will use part of the theory developed in Chapter 2. The main focus of Chapter 4 is to present the theoretical possibilities of a time-reversal system for amplification purposes and especially as a MPM power source. The models are compared to experimental results obtained with a small RC used for the prototype. The last part of the chapter is dedicated to the description of the prototype, its functioning and the confirmation of the experimental values found in frequency domain using a VNA when compared to time domain. Values of the field and of the output received power will also be presented.

Conclusion

In this section a state-of-the-art of High-Power and Medium-Power Microwaves was presented. The different parameters measured during EMC testing were introduced. A comparison between Microwave Vacuum Electronic Devices and Solid-States amplifiers was undertaken. It was shown that both technologies go hand in hand even if solid-state devices have been slowly replacing tube technologies for the last decades. The limitations of present technologies and the novel perspectives allowed by time-reversal were then presented. Time-reversal seems especially interesting for amplification considerations because of the high energy efficiency of reverberation chambers. The limit of their theoretical derivations was then presented. Theoretical work that assesses and quantifies the power-efficiency of time-reversal is at the core of this work. The aim of a Time- Reversal Amplification System is to produce Ultra-short Wideband pulses using medium to low-power wideband sources. The objective of this PhD is to show the possibilities offered by time-reversal refocusing properties in order to produce kW power pulses using only 15 W solid-state amplifiers. A typical signal bandwidth for TRAS application will be $B_T = 100$ MHz. For such bandwidths, the pulse duration lasts less than 100 ns and looking at Figure 1.3 we can see that we are in the adiabatic region when considering vulnerability tests.

In the following chapter a more detailed presentation of reverberation chambers is assumed and the important parameters necessary to dimension an RC for amplification purposes are analyzed. Special attention was granted to the quality factor and the assessment of the effects of loading the RC with antennas.

Chapter 2

Reverberation Chambers and Quality Factor

2.1 Mode-Stirred Chambers as test facilities

Electromagnetic mode-stirred or Reverberation Chambers (M-SC or RC) have become of common use for immunity [5, 45] and emissions tests [46–48]. They were first introduced by H.A. Mendes and P. Corona in 1968 [49, 50]. A mode-stirred chamber usually consists of a rectangular test chamber with metal walls and a stirrer that allows one to smooth out the sharp nulls of the field i.e. Figure 2.1. These test facilities allow a large field to build up inside. During immunity tests, the average response of the object to the field is found by integrating the response over multiple stirrer positions . The Element Under Test (E.U.T.) is thus exposed to high field levels consisting of several different polarizations. These characteristics allow robust immunity testing without having to move the equipment under test.

Figure 2.1 Photography of an empty Reverberation Chamber.On the left side is the vertical Mode Stirrer (or Tuner), that changes the electromagnetic boundaries ensuring a (statistically) homogeneous field distribution.

The framework of our study and the theoretical models presented hereafter limit themselves to the case where the field can be considered diffuse inside the chamber. In diffuse state, a reverberation chamber is defined as an electromagnetic enclosure with faradised walls within which it is possible to greatly modify the distribution of the electromagnetic field using various mixing techniques. The behaviour of a "reverberation chamber" resides solely in its ability to generate an important number of independent propagation environments. This is possible by modifying the conditions of the field inside the surrounding walls (modification of the polarization, the position or the frequency of the transmitter) or by partially modifying the boundary conditions of the chamber using metallic mode

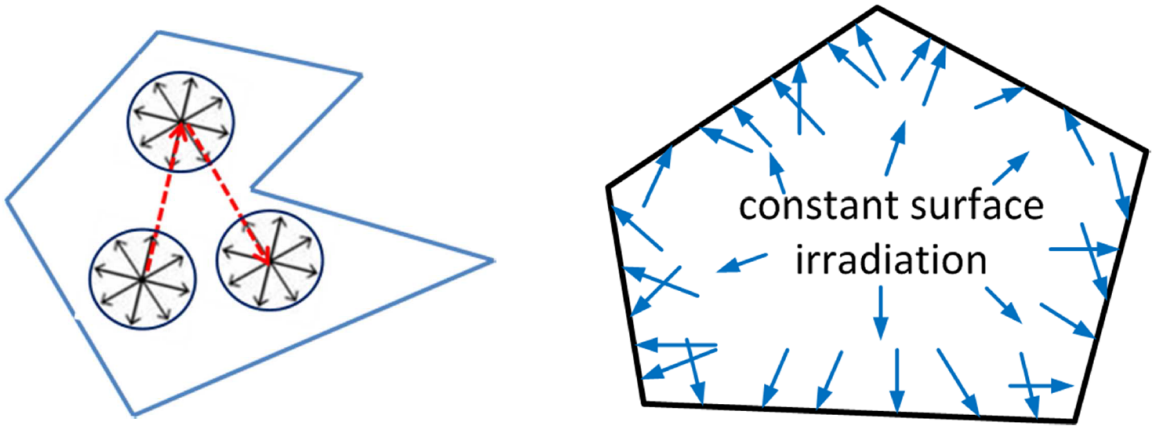

(a) Isotropy and homogeneity (same arrow lengths in every direction everywhere, at every "array-cluster")

(b) Constant irradiation of all surfaces following homogeneity

Figure 2.2 Isotropy and homogeneity conditions defining a diffuse field inside a bounded medium

stirrers. The majority of mode stirrers are made of metallic blades directed according to diverse directions turning around an axis Figure 2.1, stirring can also be electronic [51, 52].

In theory, a bounded medium or cavity is said to be a perfectly diffuse system when the field inside can be considered **isotropic** and **homogeneous** in the entire cavity's volume i.e. Figure 2.2. The field can then be considered at every point of the room as coming from an infinite number of plane-waves propagating in every direction with the same probability. Properties ensuing from such a definition will be presented in the following section.

The emergence of reverberation chambers to measure electromagnetic radiations appeared in 1974 [6]. The two main characteristics of this kind of device are its ability to generate intense electromagnetic fields and its capacity to measure radiated fields efficiently. The elaboration of standards for the measures in M-SC lead to a generalised use of this test equipment. Recent trends in research have shown an increase interest for reverberating chambers especially for antenna radiation measurement purposes [53, 54]. Due to its reverberating character, wave propagation within a RC opposes that in anechoic chamber. The almost complete absence of reflections in an anechoic chamber insures a high control of the desired signal on the object under test. Antenna measurement can then be realized for precise directions, this is particularly interesting when characterising radiation patterns. However, these properties may not be suitable when carrying out immunity measurements for ElectroMagnetic Compatibility (EMC) purposes. Indeed, the absence of reflections and the strong absorption of the energy by the walls imposes to turn the object as well as using powerful amplifiers. Within the framework of immunity tests, the advantages of reverberating chambers are (Figure 2.3):

- For a given configuration by the transmitter and by the object under test, the various positions of the stirrer allow to excite the object over a significant number of directions and polarizations.

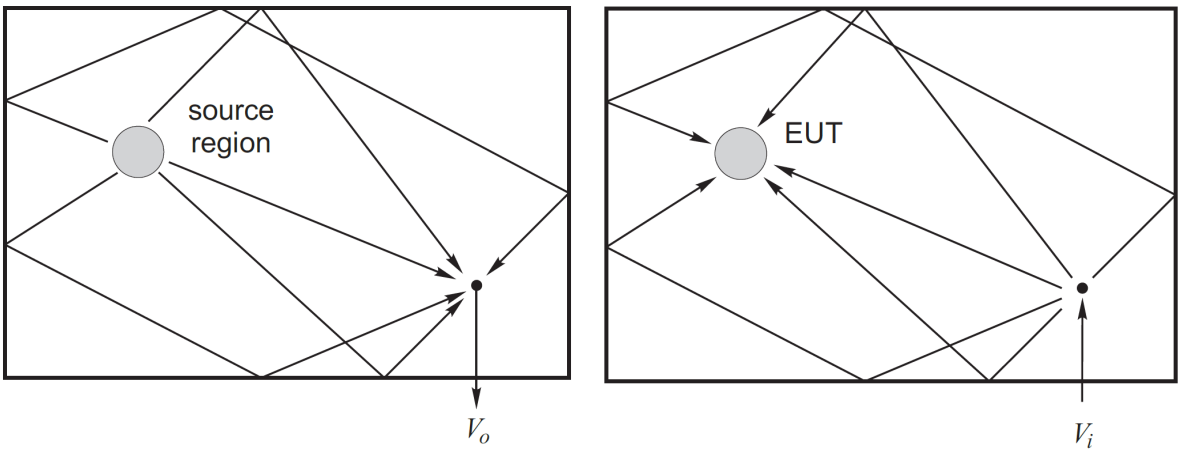

Figure 2.3 Wave diffusion in a cavity, exploited to : (a) collect data about the radiation of a source along all possible directions; (b) simultaneously excite an EUT along a large number of directions.

- During the test phase, it is not necessary to move the object under test.
- The experimental protocol is cheaper and faster than in anechoic chambers.

The average power over the EUT can be determined: it is therefore possible, from simple computations based on power conservation, to assess the power absorbed by the EUT [55]. This further application is important in room acoustics (e.g., assessing the performance of absorbers for phonic insulation, but also the amount of power lost in comfortable seats), as well as in the characterization of any material [56]. In the following sections, a description of the propagation environment as well as a certain number of modelling tools will be presented.

2.2 Wave-Propagation Modelling in large cavities

The models used to represent the propagation of waves within cavities depend on the application context. As a result, a number of methods have been proposed independently in each field of application, leading to a collection of techniques that depend on specific needs. In what follows, we will present a sum-up of propagation models obtained for temporal, frequency and statistical representation of the field within the chamber.

2.2.1 Reflections and Image Theory

The propagation within a cavity is dominated by two phenomenons: diffraction and reflections on the walls. The combination of these two phenomenons is the main reason for field diffusion.

A geometrical analysis allows to study in a simple way the propagation of a wave in a reverberation chamber. It is based on the equivalent reflection laws for electromagnetic waves and light. This

representation is only possible when the reflections are considered specular. However, diffused reflections play an important role in obtaining a diffuse fields. This shows an important limitation of this representation. However, it is very useful because of its simplicity and the properties of the field in an enclosed domain that can be derived [57–59].

This approach allows a practical graphical representation of EM wave propagation in such a medium. The dual representation of ray tracing is the image source representation. In this case, each reflection is associated to an image source located outside of the room cf Figure 2.4b. Attenuation due to spherical divergence is directly taken into account by this model since at every reflection the image-source gets further of the room. It is then possible to obtain an equivalent model with an increasing number of equivalent sources. Each equivalent source contributes at different times to the impulse-response of the room. However, this model does not take into account diffraction and diffusion phenomena thus limiting its utility to cases where the reflection surfaces are large enough and that the asperities on the surfaces are small compared to the wavelength which is in practice never the case for RCs.

The source-image contributions at a distance R have an intensity proportional to $1/R^2$ and the number of virtual sources increases proportionally to R^2 in a rectangular room. The impulse response is expected to present an increasing number $N(t)$ of echoes with decreasing intensity and a reverberant coda cf. Figure 2.5. The impulse response can be decomposed into a superposition of pulses coming from an important number of virtual transducers, images of the single real transducer, which then acts as a real cavity: this is the "kaleidoscope" effect [60]. This phenomena is used to limit the number of antennas in a cavity during a time-reversal process.

Impulse response of a room

For rectangular rooms in which an omnidirectional source is placed, waves propagate uniformly in all directions of space. In cases where the walls have infinite impedance, it is possible to identify a number of propagation paths and to identify arrival times also called echoes (see Figure 2.4b). An echo is a sound or EM wave that has experienced at least one reflection on its path between the source and the receiver.

The source S emits at time $t = 0$ a pulse in a room of volume V. An omnidirectional receiver is placed at the point M cf. Figure 2.4a. Arrive successively:

- The direct wave attenuated by the spherical divergence. This signal reaches the point M at time $t_d = \frac{SM}{c_0}$ (c_0 being the speed of light in the medium)
- The first echo from a ray having followed the quickest path between points S and M and that underwent a reflection. This signal is attenuated by the spherical divergence, and by the absorption of the wall encountered. It reaches point M at time $t_1 = (SR + RM)/c_0$.
- Echoes undergoing reflections on a wall (first order reflections), echoes that underwent reflections on two walls (second order reflections), etc. These signals constitute a series of pulses

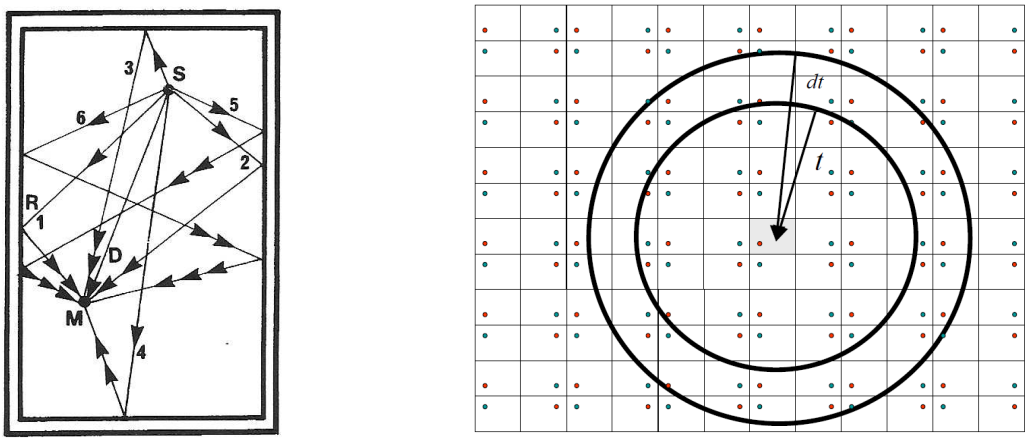

(a) (b)

Figure 2.4 Reflections and its dual representation the image-source. (a) Two-dimensional representation of the direct wave and of the first echoes (returns) in the parallelepipedic room with walls of infinite impedance. M is the point of reception, S is source, D is the direct path of the wave between S and M, $R1$ is a beam undergoing only one reflection [61]. (b) Two-dimensional representation of a density of sources-images. It is then possible to trace all the virtual beams and to define the number of returns of the sources between separate circles of dt [62].

whose density increases with time, while their amplitude decreases with distance, the number of reflections and dissipation.

Very simply, the impulse response $h(t)$ can be expressed as:

$$h(t) = A_0\delta(t - t_0) + \sum_{k=1}^{\infty} A_k\delta(t - t_k) \tag{2.1}$$

The A_k correspond to the amplitudes of the echoes arriving at time $\delta(t - t_k)$. A_0 and $\delta(t - t_0)$ correspond to the direct field component. The model is simplified by taking arrival times as a distribution of dirac peaks. The representation of the equation above will be useful when considering time-reversal focusing properties in time. For any high-order random multiple-scattering process, the majority of the signal is composed of a diffuse wave that is the result of interference of a large number of multiple-scattering paths. Since the scattering is random (e.g., random variations in the impedance of the medium) the arrival time from each path can be described as a series of Poisson impulses. For an impulse sent through the medium, the output can be described by the convolution of the electrical impulse response (IR) with the Poisson impulses corresponding to every path.

The impulse response is then a sum of echoes having intensities becoming weaker with time. When the echo density becomes large, it is no longer possible to differentiate between signal components. The signal obtained at point M is then called diffuse field. The diffuse-field can be considered

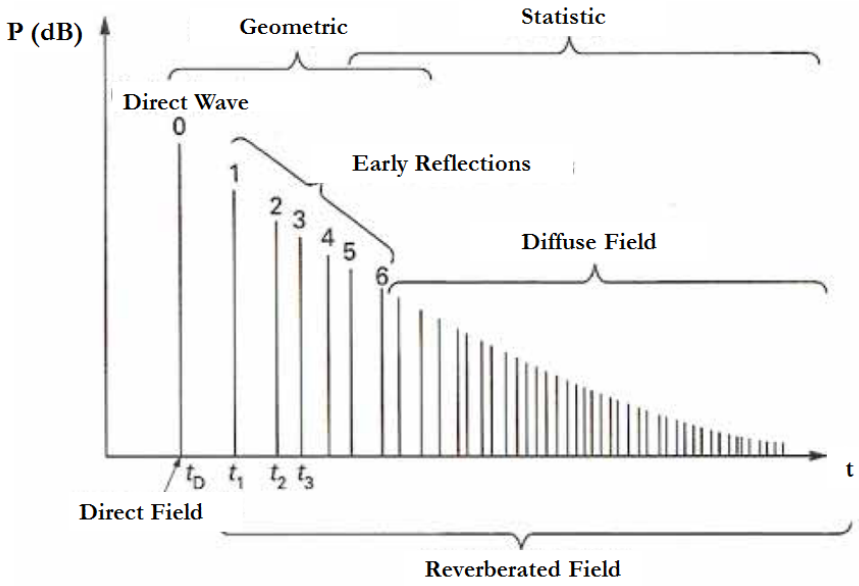

Figure 2.5 Reverberating Chamber [61].

homogeneous and isotropic this is to say consists of an infinity of plane-waves propagating in all directions of space. Figure 2.5 shows the distribution in time of pulses arriving at the reception point M. The time of arrivals depend on the characteristics of the radiation source, the distance between the source and the receiver and their position relative to the walls and therefore the volume of the cavity.

Reverberation is the consequence of the multiplication of the reflected and diffused signals by the walls. Reverberation is mainly divided into “early reflections” and “diffuse field”. Early reflections are the reflected waves that arrive at the reception point shortly after the emission. Time arrival of these echoes remain quite distinct. The diffuse field is composed of multiple reflections and diffusion. It is generally considered that apart from close to the walls, the diffuse field is homogeneous in the space. It is therefore possible to characterize the case of the diffuse-field using the source-image representation. There exists a time corresponding to a transition between two states of the room called mixing-time. In this case it may be considered that the field consists of an infinite number of plane-waves propagating in all directions of space with the same probability. This corresponds to the limiting case of the geometric representation when the number of source-image is important and in average homogeneously distributed in space. If all source-image homogeneously cover space then the cavity also has ergodic properties. It is important to note that rectangular cavities such as the one

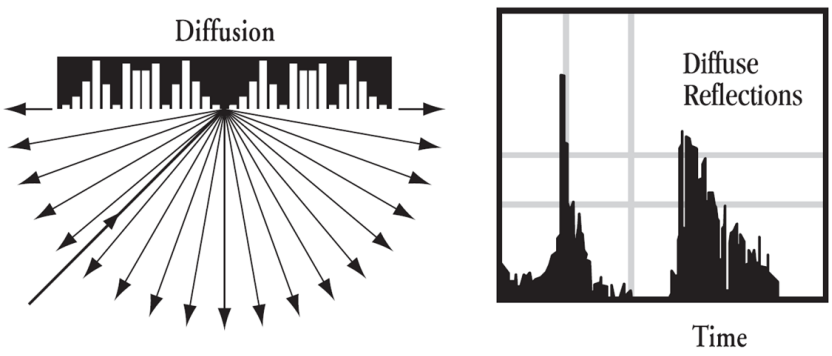

Figure 2.6 Temporal and spatial characteristics of a diffusing surface [65].

presented here are not ergodic, however they are very useful in practice for their simplicity. In the case where a large number of sources-image exist, the average number of echoes is then given by [63]

$$N(t) = \left\lfloor \frac{4}{3}\pi \left(\frac{t}{t^*}\right)^3 \right\rfloor \tag{2.2}$$

and the average time between two reflections is $t^* = V^{1/3}/c_0$.

In the practice, echoes as shown in Figure 2.5 will never be observable. Indeed, the model presented above does not take into account dissipation nor diffuse reflections on the walls. A diffuse reflection is represented in Figure 2.6, in this case an incoming beam scatters when reflected on a wall and part of the energy is also absorbed by the surface. The original impulse will therefore be distorted by the walls and the original spectrum will will be modified. Moreover, focusing phenomenons of echoes are sometimes observable. The observed diffuse field will correspond more to the case represented in the graphic on the right in Figure 2.6. In such a case, reflections on the walls do not generate image-point sources but extended or diffused images. This property is however essential when the desired field should be diffuse. Indeed, in [64] it was shown that reverberation takes place when absorption is introduced in a room: the EM field, built by superposition of all the arrivals simultaneously issued from the source and gradually reaching the receiver, decays at a rate proportional to the amount of absorption introduced in the room.

In the following we shall present the frequency representation of RCs as well as their modelling of cavities using Greens functions.

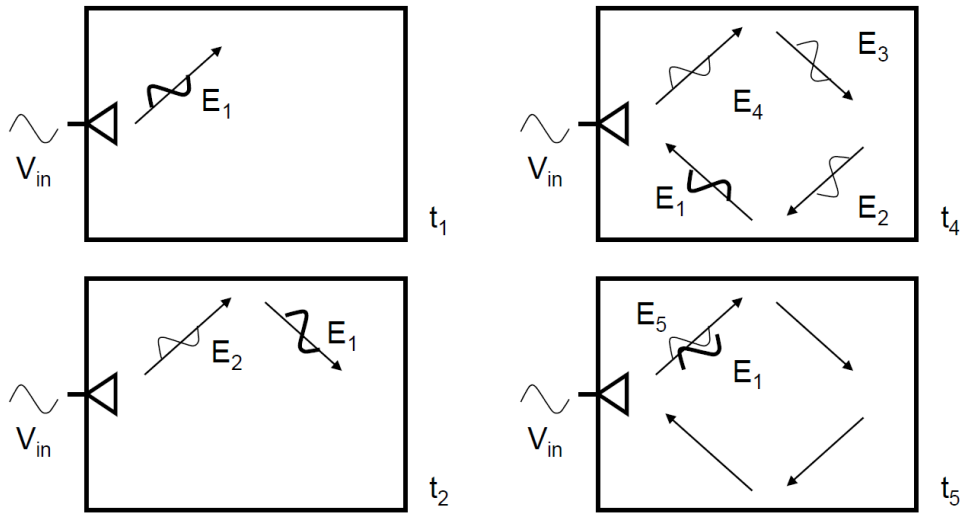

Figure 2.7 Two-dimensional representation of the wave propagation in a bounded medium during the first instants. In the last graphic we can see the field is in phase with the injected field. A periodic orbit thus exist for this frequency and direction corresponding to a mode in the frequency domain [62].

2.2.2 Modal Density and Modal Overlap

In the case the room is excited with an harmonic and the steady state is reached, to each period of the signal corresponds a wavefront propagating in the cavity. Since the cavity is a closed space where walls are reflective, closed paths of propagation appear (see Figure 2.7). The initial field will then interfere with itself (see t_5 Figure 2.7). In most cases, the phase difference on a loop will not allow constructive interference. All contributions will sum with random phases and cancel out eachother for an important number of travels. But for certain directions and frequency, the waves will interfere constructively ($2m\pi$ phase shift on a closed path also called periodic orbit) and a resonance will appear. A resonance corresponds to periodic orbits for which the interference is constructive. These resonances are self-sustained in the case chamber is lossless. However, in practice, losses exist in the middle and phase shifts are created, a self-sustaining system is impossible. For these resonances, a relatively small excitation power provides a much greater field strength. These periodic orbits appear only at certain frequencies and according to a limited number of direction. Each periodic orbit corresponds to a mode in frequency.

Figure 2.8 shows the field energy in function of frequency in a reverberation chamber. There exists frequencies where the energy in the room is very high they are the resonances. These frequencies depend on the dimensions of the room, their number increases with frequency [66]. In Figure 2.8, there are two regions:

- Low frequency where modes are discrete, the cavity acts as a selective filter.

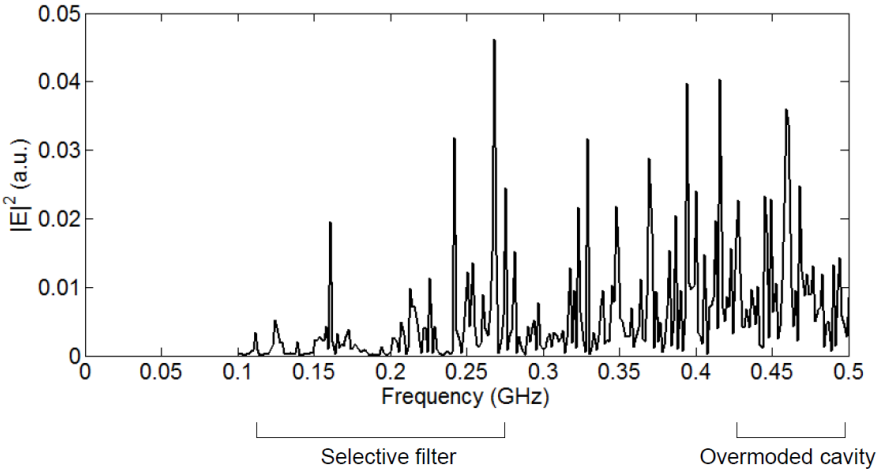

Figure 2.8 Frequency response of a cavity. To regions are observable: one in low frequencies where the modes are discreet and another in high frequencies where the modes are highly overlapped [62].

- From a certain frequency called Schroeder's frequency [67] , modal density becomes very high and it is impossible to differentiate them. From this frequency modal distribution apparently becomes constant and modes are statistically distributed. In this case the room is said to be overmoded.

The frequency distribution of modes or eigenfrequencies in a rectangular room with no source has been rigorously studied electromagnetism [66]. It is possible in this case to count the number of modes and the analytically mode density. The method is the same as the one used in acoustics in 1939 [68, 69]. For a rectangular cavity defined in previous sections, the eigenvalues (wave number) is given by:

$$k_{lmn}^2 = \omega^2 \mu\varepsilon = \left(\frac{l\pi}{L_x}\right)^2 + \left(\frac{m\pi}{L_y}\right)^2 + \left(\frac{n\pi}{L_z}\right)^2 \tag{2.3}$$

where, l, m and n are integers. Therefore, the number of modes $N_s(f)$ with frequencies less than or equal to f is given by [66]:

$$N_s(f) = \frac{8\pi V}{3c_0^3} f^3 - \frac{L_x + L_y + L_z}{c_0} f + \frac{1}{2} \tag{2.4}$$

The first term on the right side of (2.4) is Weyl's classical approximation of the number of modes N_W which is valid for large cavities [70]:

$$N_W(f) = \frac{8\pi V}{3c_0^3} f^3 \tag{2.5}$$

Modal Density is thus given by for the exact model:

$$D_S(f) = \frac{dN_s}{df} = \frac{8\pi V}{c_0^3} f^2 - \frac{L_x + L_y + L_z}{c_0} \tag{2.6}$$

And Weyl's approximation gives:

$$D_W(f) = \frac{dN_W}{df} = \frac{8\pi V}{c_0^3} f^2 \tag{2.7}$$

Weyl's expressions above are valid for rooms with non rigid walls and of arbitrary shape [71]. When thinking about the modal density, one intuitively associates it to a certain number of modes resonating around the working frequency. The modal density can therefore be defined as the average number M_B of modes found in a bandwidth B,

$$D_m(f) = \frac{M_b}{B} \tag{2.8}$$

This equation is particularly useful since it depends directly on B, we use it in what follows to determine the dimension of the prototype using the model proposed by Schroeder in [67, 72, 73]. In the case where the band is wide enough D_m becomes an average value and $D_m = D_W$. It is then possible to calculate the value from which a statistical approach of a cavity becomes valid. This frequency is an equivalent to Schroeder's frequency in acoustics, it corresponds to the frequency at which $M_B = 3$ modes are superimposed in their band at -3 dB (modal bandwidth). The average width between two peaks must be less than $\frac{B_m}{3}$.

$$M_B = B_m D_W(f) \tag{2.9}$$

Schroeder's frequency is thus equal to:

$$f_{sch} = c_0 \left(\frac{3}{8\pi} \frac{\langle Q \rangle}{V} \right)^{1/3} \tag{2.10}$$

where $\langle Q \rangle$ is the average quality factor that will be presented in the following subsection.

In the absence of any treatment, the frequency response of a parallelepipedic room presents a series of peak amplitudes which correspond to the natural frequencies of the room. Their density increases with frequency.

Another disadvantage of the presence of standing waves is to create unequal distribution of energy which favours a certain number of points at the expense of others. In any case, standing waves are avoided. The usual way to avoid this is to build irregularly shaped cavities avoiding simple geometric shapes. The number of excited modes also depends on the respective positions of the source and the measuring point.

2.2.3 Modal Representation of Large Chambers

In the context of linear systems studied under a harmonic steady state, the most general technique employed to deal with their spatio-temporal evolution is that of Green's functions $G(\boldsymbol{r}, \boldsymbol{r'})$ where $\boldsymbol{r}$ is the observation point coordinates and $\boldsymbol{r'}$ is the source points position within the bounded space Ω.

$$\boldsymbol{E}(\boldsymbol{r}, \omega) = j\omega\mu \int_{\Omega} \underline{\boldsymbol{G_{ee}}}(\boldsymbol{r}, \boldsymbol{r'}) \cdot \boldsymbol{J_e}(\boldsymbol{r}) d\boldsymbol{r'} \tag{2.11}$$

with $\cdot$ the inner vector product, ω the pulsation and Ω the bounded space. The dyadic Green's function $\underline{\boldsymbol{G_{ee}}}(\boldsymbol{r}, \boldsymbol{r'})$ used in this case is intended to link the electric field to electric currents, hence the subscript "ee". In practice, the problem of finding a solution $\boldsymbol{G}(\boldsymbol{r}, \boldsymbol{r'})$ is far from trivial, and only for very simple canonical geometries it is possible to express it in closed form [74]. It is therefore possible to find Green's function for a rectangular Cavity but not when the cavity is loaded with stirrers and/or EUTs [75].

The problem of modelling wave propagation through the use of Green's functions can be simplified by the use of spectral expansions. This standard procedure [74, 76, 77] consists of expressing the Green's functions as a linear combination of the eigenfunctions $\{\boldsymbol{e}_n(\boldsymbol{r})\}$ of Helmholtz equation, defined as

$$\nabla^2 \boldsymbol{e}_n(\boldsymbol{r}) + k_n^2 \boldsymbol{e}_n(\boldsymbol{r}) = 0, \tag{2.12}$$

The set of eigenfunctions $\{\boldsymbol{e}_n(\boldsymbol{r})\}$ form a complete basis of orthogonal functions that is to say capable of representing all fields distributions satisfying the boundary conditions set by the medium, this implies:

$$[\boldsymbol{e}_n | \boldsymbol{e}_m] = \int_{\Omega} \boldsymbol{e}_n^{\dagger}(\boldsymbol{r}) \boldsymbol{e}_m(\boldsymbol{r}) = \delta_{mn}, \tag{2.13}$$

where † stands for the Hermitian transpose and δ_{mn} is Kronecker's symbol. Since the family of eigenfunctions $\{\boldsymbol{e}_n(\boldsymbol{r})\}$ form a complete basis, it is thus possible to express the corresponding Green functions $G_k(\boldsymbol{r}, \boldsymbol{r'})$ as follows:

$$G_k(\boldsymbol{r}, \boldsymbol{r'}) = \sum_n A_n \boldsymbol{e}_n(\boldsymbol{r}) \tag{2.14}$$

with the green functions being solutions of the following equation:

$$\nabla^2 G_k + k^2 G_k = -4\pi\delta(\boldsymbol{r}, \boldsymbol{r'}) \tag{2.15}$$

Therefore,

$$\sum_n A_n (k^2 - k_n^2)\boldsymbol{e}_n(\boldsymbol{r}) = -4\pi\delta\left(\boldsymbol{r} - \boldsymbol{r'}\right) \tag{2.16}$$

and thus

$$A_n = \frac{4\pi \boldsymbol{e}_n^\dagger(\boldsymbol{r'})}{k_n^2 - k^2} \tag{2.17}$$

Therefore the Greens function expression becomes:

$$G_k(\boldsymbol{r}, \boldsymbol{r'}) = 4\pi \sum_n \frac{\boldsymbol{e}_n^\dagger(\boldsymbol{r'})\boldsymbol{e}_n(\boldsymbol{r})}{k_n^2 - k^2} \tag{2.18}$$

and the fields expression can thus be obtained:

$$\boldsymbol{E}\left(\boldsymbol{r}, \omega\right) = 4\pi \sum_n \frac{\gamma_n \boldsymbol{e}_n(\boldsymbol{r})}{k_n^2 - k^2} = 4\pi \sum_n \gamma_n \boldsymbol{e}_n(\boldsymbol{r})\psi_n(\omega) \tag{2.19}$$

with

$$\gamma_n = \int_\Omega \boldsymbol{J_e}(\boldsymbol{r'}, \omega)\boldsymbol{e}_n^\dagger(\boldsymbol{r'})dr'^3 \tag{2.20}$$

$$\psi_n(\omega) = \frac{1}{k_n^2 - k^2} \tag{2.21}$$

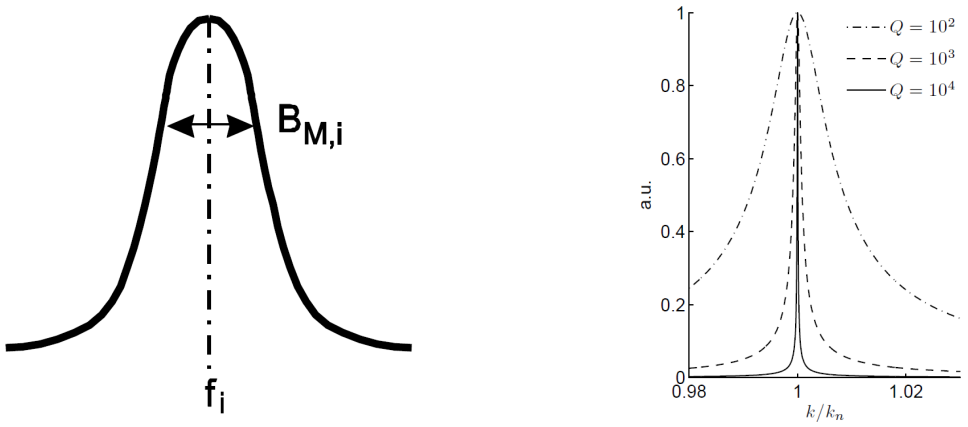

(a) (b)

Figure 2.9 (a) Definition of the half-power modal bandwidth (b) Some examples of peak normalized modal response $\psi_n(\omega)$, plotted against the normalized frequency $k = k_n$ for a varying quality factor Q.

γ_n are the modal coefficients and k_n are the square root of the eigenvalue associated to the eigenfunction $\boldsymbol{e}_n(\boldsymbol{r})$ and $k = k(\omega)$ the wave number. This expression allows physical insight of a reverberations room. The family $\{\psi_n\}$ have expressions of Lorentzian functions and are the representation of a mode in frequency. They correspond to the response of a damped harmonic resonator in time (damped sinus). In the ideal case of undamped resonances, the generic k_n is purely real and corresponds to a resonance frequency

$$f_n = \frac{k_n c_0}{2\pi} \tag{2.22}$$

In practice, dissipation mechanisms in the cavity lead to the appearance of an imaginary part in k_n, whose amplitude is much smaller than the real part for reverberation chambers where as we have seen in the previous section the walls act as mirror for EM waves. In this case, the dissipation mechanisms can be treated as weak perturbations by adding a small imaginary part to ψ_n

$$k_n \to k_n \left(1 - \frac{j}{2Q_n}\right) \tag{2.23}$$

where Q_n is the composite quality factor of the n-th resonance or normal mode. Q_n is called composite because as we will see in the following section it is composed of different factors corresponding to the different loss mechanisms within the medium. The quality factors involved in electromagnetic reverberation chambers are very easily higher that several thousand units, so that the frequency of resonance can be regarded as unaffected by the introduction of losses, which thus behave as a weak

perturbation. While for an increasing Q_n the peak-value of $\psi_n(\omega)$ increases, the function becomes more tightly concentrated around its resonance frequency see Figure 2.9a. The smaller the quality factor, the larger the frequency spread of the mode around its resonance frequency. It is then possible to excite a mode around its central frequency. This bandwidth is called the modal bandwidth. The modal bandwidth $B_{M,n}$ of a mode n the half-power modal bandwidth of a mode at -3dB see Figure 2.9b. It represents the frequency band on which it can be considered that the mode contributes to the response of the room. It is centred on the resonance frequency of a mode. Modal bandwidth expression is:

$$\frac{B_{M,n}}{f_n} \approx \frac{1}{Q_n} \tag{2.24}$$

The combinations of $\{\psi_n(\omega)\}$ therefore act as very efficient narrow-band filters. This modal bandwidth associated with an important number of modes at high frequencies is responsible of the important modal overlap presented in Figure 2.11.

The number of M modes excited in the room thus depends on the quality factor. In the case where the chamber is overmoded, modes are statistically distributed, the quality factor of each mode may be taken as being equal to the mean quality factor on the frequency band excited by the signal. Access to the actual number of excited modes in room M is impossible in practice.

For a given excitation only a limited number of modes around the working frequencies will contribute significantly to the cavity's response. A coherence band noted B_c is then defined corresponding to the frequency band over which the modes will contribute to the rooms response when the injected signal is a harmonic (Figure 2.10). A signal can excite several bands of coherence. Each coherence band can be regarded as independent from each other. This approach thus allows to grasp the degrees of freedom underlying the field distribution within the cavity. In this case, only the sum of the modes contributing within the coherence band is necessary. This coherence band has been shown to be equal to πB_M.

The modes contributing to the rooms response is thus defined by the set of M modes: $M = \{m : f_m - f < B_c/2\}$ for each each excited coherence band. This limitation in the number of terms in the modal decomposition simplifies equation (2.19) to finite sum. The number of modes excited by a signal is thus equal to the product of the number of coherence bands by the number of superimposed modes. The study of the field statistics in the room based on these two parameters ensures diffusiveness in the room.

The modal decomposition has a limited number of parameters. Nevertheless, it is impossible in practice to use it without further considerations. The main limitation of this model is the lack of information on the behaviour of modal topography $\{e_n\}$ as well as the modal weight coefficients $\{\gamma_n\}$ and the number inter-distance and position of the resonance frequencies $\{f_n\}$. Therefore statistical analysis is more often used when only macroscopic values such as the field are needed. In

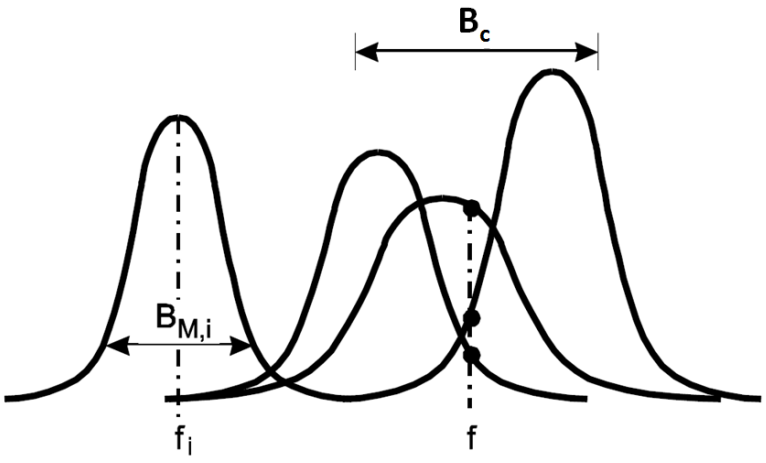

Figure 2.10 A schematic illustration of the local contributions provided to the electric energy by each resonant mode within a cavity. Only the modes with a frequency of resonance within a distance $B_c/2$ from the working frequency actively contribute [62].

the following, we describe the statistical approach of the room reverberation response at frequencies where the cavity can be considered overmoded or diffuse.

2.2.4 Diffuse Field and Statistical Approach of Modelling Reverberating Chambers

In theory, a reverberation chamber is a perfectly diffuse system defined by an isotropic and homogeneous field in the entire volume of the cavity. The field can then be considered as consisting of an infinite number of plane waves propagating in all directions in space with the same probability of directions. In case the room is overmoded, a large number of modes will be excited and their contributions will add themselves. In this case, the study of the field in a reverberation chamber can only be approached with simplified models based on geometrical optics or propagation laws [55]. A statistical approach is often most suitable to describe a reverberation chamber.

In the previous section we showed that the spectral representation models the field in the chamber. The analytical expressions of the modal weight and modal topography are not necessary, only the expression of the electric field at a given point is of interest. The idea of a statistical approach is to keep the global properties of the system (macroscopic) that are observable for many independent measurements while making statistical considerations on the parameters of the sum (microscopic) (2.19). In order to model the response of a room, the coefficients present in the modal representation are represented as random variables hence the idea of a random spectral model. These random variables such as modal weight, are often considered complex whose real and imaginary parts are governed by a Gaussian distribution. This assumption is valid if the number of independent stirring position (field distribution) is important.

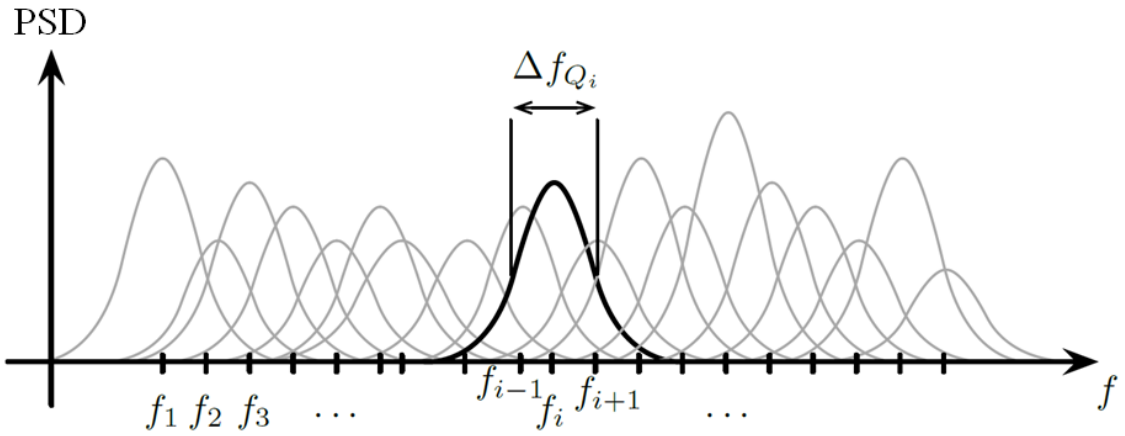

Figure 2.11 Illustration of modal overlap. In the frequency ban Δf_{Q_i} the associated modes at frequency f_i, f_{i-1} and f_{i+1} overlap and their Power Spectral Density (PSD) contribute by addition at frequency f_i [78].

Many definitions exist to ensure field diffusivity in a reverberation chamber. In [79] "A reasonable guideline for proper operation of the tuner is a minimum tuning ratio of 20 dB" . In other words, the ratio of the maximum power to the minimum power (at a selected test point and over all tuner positions) should be at least 20 dB. Apparently, implementation of this criteria (though not theoretically derived) assures acceptable levels of field uniformity, or spatial homogeneity, for a large number of applications.

In [80] two metrics are given by calculating threshold values for the Quality Factor when assessing Stirred vs Unstirred Energy or based on Probability Density Functions.

The first condition gives $Q \gg Q_{thr}$ with:

$$Q_{thr} = \left(\frac{4\pi}{3}\right)^{2/3} \frac{V^{1/3} f}{2c_0} \tag{2.25}$$

Q_{thr} being the calculated threshold quality factor. The second calculation method gives:

$$Q \gg \left(\frac{4\pi}{3}\right)^{2/3} \frac{3V^{1/3} f}{2c_0} \tag{2.26}$$

These two conditions are quite close. However, it was shown in [81] that a high modal density does not guarantee field diffusivity, conditions on the number of modes as well as on modal overlap are necessary. Therefore, another possibility is the Schroeder's frequency f_{sch} defines a lowest usable frequency and was derived in the previous section. This frequency corresponds to a modal overlap of

3. This definition seems to be too restraining however and statistical characteristics of a diffuse fields appear before this frequency.

In the standard EN 61000-4-21 [4] the condition is taken on the fields uniformity on 8 points over the 3 polarisations within the chamber. The Lowest Usable Frequency or (LUF) is defined as the lowest frequency that satisfies field uniformity. In the standard, a rule of thumb is given and the LUF is said to be found for frequencies just above three times the first resonance frequency. The condition for field uniformity is set by the lowest possible value of the standard deviation over the different measuring points and stirring position. However another condition sets the LUF at a frequency where the number of mode N is equal to 60 from equation (2.4). A minimum number of stirring position is also fixed. Tables presenting the minimum stirring position and standard-deviations are presented in Appendix C.

All the conditions above concern a classical use of where a frequency sweep is undertaken. In such a case it is the modal overlap that is of interest since the room will be excited one frequency after another the quality factor and modal overlap have to be such that for all frequencies there should be no sharp nulls especially after averaging over stirring positions. During a time-reversal process however, the signals used are usually wideband. A sufficient condition to obtain Gaussian-type fields is thus that the number of modes over the covered band at each point of the room be important enough. A typical value that is taken is that the number of modes is above 100 over the entire bandwidth of the signal with no sharp nulls of the transfer function.

In the end, many metrics can be used to define diffusiveness within a chamber showing the importance of this condition in RC testing models.

Statistics of diffuse fields

It is important to understand that the diffuse-field condition is not only invoked as a simple ideal approximation. The most important point is that when a field is diffuse, its statistical properties does not depend any longer on the fine details of the cavity, by definition. The direct consequence is that the results of a test can be expected to be independent from the cavity, i.e., they can be reproduced in other test facilities. It is this simplification that is important, since it ensures that reverberating cavities can be regarded as fit for metrology tasks.

For bounded medium applications, the statistical properties are preponderant. Two important statistical properties need first to be clarified when considering reverberation chambers in diffuse state:

- RCs will be considered as Ergodic: A medium has ergodic properties if the average value of a quantity (such as the electric field in space in this case) asymptotically converges towards the average of a large number of measurements taken in time. In an ergodic system it is possible to exchange energy in its various forms within the cavity, so that it diffuses uniformly in space over time. A medium is said to be stationary if its steady-state its statistical properties such as expected values are independent of time. All ergodic processes are stationary. This ergodic

property can be expressed as follows:

$$\lim_{n\to\infty}\sum_{k=1}^{n}\|\boldsymbol{E}(\boldsymbol{r_k})\| = \langle\|\boldsymbol{E}(\boldsymbol{r})\|^n\rangle \tag{2.27}$$

where n is the number of samples of the field in the space, and where $\langle\ \rangle$ correspond to an average over time. This first statistical property, considers only one trajectory: along almost any trajectory of an ergodic billiard, the mass spends equal time in the vicinity of each position and direction. As a consequence, (phase) space average is equal to time average along almost any trajectory. The ergodic property of the cavity ensures that a single sensor, collecting the echoes constituting the impulse response of a scenery, is enough to capture the necessary information for a Time Reversal experience. However, not all bounded mediums are ergodic: A rectangular 3D room is never ergodic (only four directions along each trajectory). This counter-example stresses the necessity of considering directions as well as positions, since in a ergodic billiard, the mass spends equal time in the vicinity of all positions.

- and reciprocity: A medium has reciprocity properties if when reversing the transmitters and receivers position the statistics of the medium is unchanged.

Another important statistical property is mixing, it involves two different observation times along a group of initially adjacent trajectories, and can therefore be considered as a correlation property: if sufficient time separates the two observations (strictly speaking an infinitely long time), a set of waves, following initially adjacent trajectories, separates completely and spreads over the whole room. The waves can thereafter be considered as statistically independent: no one knows any longer the position nor the direction of any of them. Mixing billiards constitute a subset of ergodic billiards. In the case of a mixing room with perfectly reflecting boundaries (no losses on the boundaries), this assumption can be proved by means of energy conservation. Mixing ensures that the energy is equidistributed in the room after sufficient time, i.e. after mixing time. Since adjacent trajectories in a mixing room diverge at an exponential rate, intensity reduces exponentially along any trajectory. Therefore, to conserve energy, the number of arrivals must compensate for the divergence. Hence, the number of arrivals is exponentially increasing with time in any mixing room.

The statistical properties of the electric field within a reverberation chamber were first developed using heuristic consideration [82], more thorough proof were presented using spectral decomposition [77] and a plane-wave decomposition method [3, 55]. Here, we shall present the statistical properties of the MSRC using the plane-wave integral method.

The electric field $\boldsymbol{E}$ at location $\boldsymbol{r}$ in a source-free , finite volume can be modelled using an angular spectrum of plane waves [83, 84]:

$$\boldsymbol{E}(\boldsymbol{r}) = \int_{\Omega}\boldsymbol{F}(\Omega)\exp(j\boldsymbol{k}\cdot\boldsymbol{r})d\Omega \tag{2.28}$$

If the room is well stirred the following properties are found [3, 55]:

- The mean value of the electric-field $\langle \boldsymbol{E}(\boldsymbol{r}) \rangle$ is uniform 0 since the angular spectrum is equal to zero. $\langle \boldsymbol{E}(\boldsymbol{r}) \rangle = \int_{\Omega} \langle \boldsymbol{F}(\Omega) \rangle \exp(j\boldsymbol{k} \cdot \boldsymbol{r})\, d\Omega = 0$
- The mean-square value of the electric-field $\left\langle \left| \boldsymbol{E}(\boldsymbol{r})^2 \right| \right\rangle$ is E_0^2 is constant and independent of position. This property corresponds to field uniformity of an ideal reverberation chamber.
- In a same way the mean-value of the magnetic field is equal to 0 and its mean-square value is equal to $\left\langle \left| \boldsymbol{H}(\boldsymbol{r})^2 \right| \right\rangle = \frac{E_0^2}{\eta^2}$ where η is the wave impedance of the medium.
- The Power density S is equal to 0
- The mean energy density $\langle W \rangle$ is equal to εE_0^2 where ε is the rooms permittivity.
- The probability density function of real and imaginary parts of the square components of the field follow a normal distribution:

$$f(E_{pl}) = \frac{1}{\sqrt{2\pi}\sigma} \exp\left[-\frac{E_{pl}^2}{2\sigma^2} \right] \tag{2.29}$$

  where p is a component of the square field $\{x, y, z\}$ and l denotes or the imaginary or real part of the square component
- The variance of the real and imaginary parts is equal to half the complex components $\left\langle E_{pl}^2 \right\rangle = \frac{E_0^2}{6} = \sigma^2$
- The magnitude of the electric field such as E_p components are chi-distributed with two degrees of freedom or Rayleigh distributed [85]:

$$f(|E_p|) = \frac{|E_p|}{\sigma^2} \exp\left[-\frac{|E_p|^2}{2\sigma^2} \right] \tag{2.30}$$

- The squared magnitude of the electric field components $|E_p|^2$ are chi-squared distributed with two degrees of freedom or exponential distribution:

$$f\left(|E_p|^2 \right) = \frac{1}{2\sigma^2} \exp\left[-\frac{|E_p|^2}{2\sigma^2} \right] \tag{2.31}$$

The total electric field magnitude $|\boldsymbol{E}|$ is chi distributed with 6 degrees of freedom and is equal to [85]

$$f\left(|\boldsymbol{E}|\right) = \frac{|\boldsymbol{E}|^5}{8\sigma^6} \exp\left[-\frac{|\boldsymbol{E}|^2}{2\sigma^2}\right] \tag{2.32}$$

- The squared magnitude of the total electric field is chi-squared distributed with six degrees of freedom

$$f\left(|\boldsymbol{E}|^2\right) = \frac{|\boldsymbol{E}|^4}{16\sigma^6} \exp\left[-\frac{|\boldsymbol{E}|^2}{2\sigma^2}\right] \tag{2.33}$$

In summary a diffuse field is characterised by the following properties [55, 77, 82]:

- The real and imaginary parts of each of the spatial components of the field can be considered independent and identically distributed.
- The fields distribution is Gaussian complex.
- The field is homogeneous and reciprocal.
- The phase of the field is evenly distributed over 2π radians.

If a field is not perfectly diffuse in a RC a bias is introduced in the statistical properties of the field [86, 87].

2.3 Quality Factor of Mode-Stirred Chambers

2.3.1 Definition

The quality factor (Q) [88] is probably one of the most important figures of merit for Mode-Stirred Chambers (M-S.C.) by its ability to quantify losses. However, few measurements have been undertaken to measure Q and its variation with frequency and even fewer comparison with theoretical model exist [89, 90]. In most cases, the net quality factor were considered at very high frequencies where the power is mostly dissipated by the walls. Even so, some differences have been observed between model and measurements. The set-up presented here aims to determine which parameters of the different quality factor models could explain such differences, we present an experimental set-up that enables us to differentiate the different components of the net quality factor for a very large frequency band. Results are produced in three separate reverberating chamber, parametric and statistical considerations are then undertaken on the various components of the quality factor model. One important experimental observation is that even at lower frequencies the power dissipated

through the walls is more important than the power dissipated in the load of the receiving antenna even if the model shows otherwise.

At the frequencies considered here, the chamber is highly overmoded, the the test facility is considered to be a perfectly diffuse system. The electromagnetic environment is then characterized as being isotropic, randomly polarized and uniform. The field arriving at any point in the volume can be described as an infinite sum of plane waves propagating in all directions of the volume with the same probability [3]. In such an environment a statical approach is more suitable given the environment complexity. A mode-stirred chamber usually consists of a rectangular test chamber with metal walls and a stirrer that allows smoothing out the sharp nulls of the field. These test facilities allow a large field to build up inside. The Element Under Test (E.U.T.) is thus exposed to high field levels consisting of several different polarizations. The most common figure of merit when considering a mode stirred chamber is the quality factor Q. This factor measures the ability of a chamber to store energy in the form of a high field strengths and is defined as:

$$Q = \frac{\omega U}{P_d}. \tag{2.34}$$

U is the energy stored in the cavity, P_d is the power dissipated and ω is the angular frequency of operation. Hence, it is desirable to have Q as high as possible in order for the strongest field to build up inside the chamber. This is usually done by using highly conductivity materials such as steel or aluminium for the test facility walls [79, 91].

There are several experimental protocols that allow the evaluation of the net quality factor referred to as (Q_{net}), the impulse response method and power-ratio method are the two most common. The impulse response method enables the determination of the quality factor by considering decay rate within the chamber [92–94]. The power ratio method is the most frequently used method for measuring the quality factor [46, 51, 55, 79, 90, 95, 96]. A traditional experimental set-up is shown in figure(2.12). In such a configuration, the net input power P_t and the received power are measured using a spectral or network analyser and the quality factor Q_{net} is determined as in (2.35). The average quality factor is then found by integrating the response for various position of the stirrer like during immunity tests.

$$\langle Q_{net} \rangle = \frac{2V}{\pi} \frac{\omega^3}{c^3} \frac{\langle P_r \rangle}{\langle P_t \rangle} \tag{2.35}$$

where $\langle\ \rangle$ is the ensemble average over the stirrer positions. Measurements up until now, provide the average net quality Q_{net} factor of the test facility under consideration and some significant differences with the theory developed in [55] have been shown. As we will see in the following section, the expression of the quality factor is intricately related to the different loss mechanisms taking place

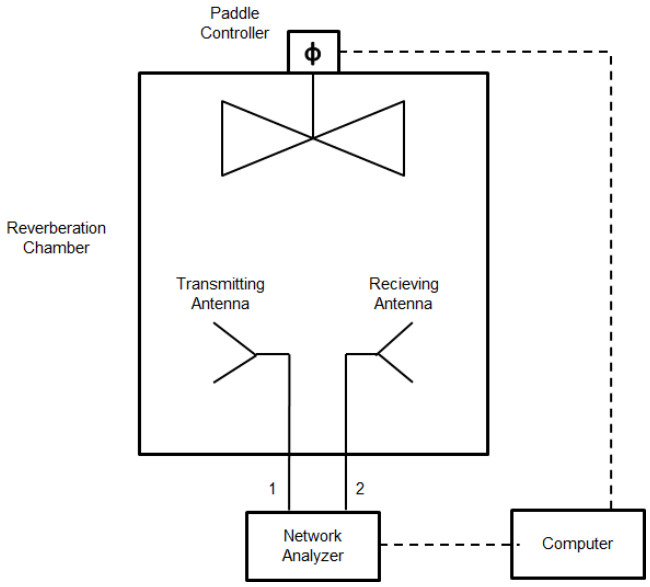

Figure 2.12 Traditional measurement configuration.

within the facility. Each loss mechanism can be associated to a different component of the net quality factor, Q_{net}. The net quality factor measured as in Figure 2.12 takes into account all the loss mechanisms inside the mode-stirred chamber. In order to understand differences between model and measurements we provide an experimental set-up that allows to separate the different components of the quality factor using the power ratio method and validate the results for two chambers, in the first part. It is then possible to compare theory and experimental results for the different components of Q_{net}.

2.3.2 Model of the quality factor

The model developed for the net quality factor is expressed as a sum of the various loss mechanisms taking place in the test facility. Each loss mechanism can be associated to a different contributor of the net quality factor. The net quality factor can be broken down into four terms [55] as follows:

$$1/Q_{net} = 1/Q_{walls} + N_A/Q_{ant} + 1/Q_{aper} + 1/Q_{abs}, \tag{2.36}$$

where Q_{walls} is the quality factor corresponding to losses in the walls, Q_{ant} corresponds to the power dissipated in the load antenna, N_A is the number of identical antennas in the chamber, Q_{aper} define aperture leakage and Q_{abs} are absorption losses when the chamber is loaded with absorbers. In the case where neither absorbers nor apertures are present within the enclosure, as it is the case for our protocol, the equation reduces to the two first terms in the right part of the equality. The net quality

factor thus becomes:

$$1/\langle Q_{net}\rangle = 1/\langle Q_{walls}\rangle + N_A/\langle Q_{ant}\rangle\,. \tag{2.37}$$

The theoretical expression of the quality factor due wall losses for a rectangular cavity is given in [66, 97].

$$\langle Q_{walls}\rangle = \frac{3V}{2\mu_r S\delta_s}\frac{1}{1+(3\pi/8k_0)\,(1/a+1/b+1/c)}, \tag{2.38}$$

where a, b and c are the lengths of the edges of the chamber.$V = abc$ is the volume. $S = 2ab{+}2ab{+}2bc$ is the total surface area of the walls assumed to be made of a good conducting metal. k_0 is the wave-number for the fields inside the chamber, $\mu_r = \mu_w/\mu_0$ is the relative permeability of the walls and $\delta_s = \sqrt{2/\omega\mu_w\sigma_w}$ is the skin depth of the field in the metal walls. When the walls are considered as highly conducting and the frequency is sufficiently high enough, Q_{walls} can be simplified to [91]:

$$\begin{aligned}\langle Q_{walls}\rangle =& \frac{3V}{2\mu_r S\delta_s}\\ =& \frac{3V}{2\mu_r S}\sqrt{\frac{\omega\mu\sigma}{2}}\end{aligned} \tag{2.39}$$

Expression (2.39) will be considered hereafter as the quality factor expressing the loss mechanism through walls [66, 91].For a reverberating chamber having high conductivity walls Q_{walls} is proportional to the square root of frequency and is the dominant contributor of Q_{net} in (2.37) for high frequencies. The power dissipated in the load of an antenna can be written as the product of the cavity power density $S_c = c\,U/V$and the averages effective area of the receiving antenna $\langle A_e\rangle = \eta_{ant}\;m\;\lambda^2/8\pi$ [98, 99]. The quality factor of antenna can be expressed as:

$$\langle Q_{ant}\rangle = \frac{2}{\eta_{ant} m}\frac{\omega^3}{c^3}\frac{V}{\pi}. \tag{2.40}$$

It is important to notice that the antenna quality factor in (2.40) does not depend on the type of antenna but only on the impedance mismatch m and the efficiency η_{ant} of the antenna. For an efficient antenna and match loaded Q_{ant} is proportional to frequency cube and is the dominant contributor of Q_{net} in 2.37 for low frequencies.

2.4 Experimental Measurements and Comparison to Theory

If the number of antennas augments between two measurements within the same chamber then in (2.37) the net quality factor should plummet in the frequency range where the power dissipated in the antennas predominates. Measurements for such configuration should therefore show the same tendency. For the configuration shown in Figure 2.12 we do not measure the power but the S-parameters. Relation (2.35) can then be restated as,

$$\langle Q_{net} \rangle = G_{ant} \langle Q_{ant} \rangle \tag{2.41}$$

with,

$$G_{ant} = \left\langle \frac{|S_{21}|^2}{\left(1 - |S_{11}|^2\right)} \right\rangle . \tag{2.42}$$

Improved models are presented in [100] but in this section the ratio from (2.42) is used. By changing the number of antennas, while keeping the experimental conditions exactly the same, it is possible to extract each component of the net quality factor defined in (2.37). Indeed, the problem then becomes a system of two equations with two unknowns. The more antennas added the more the separation between both net quality factors will be visible on a wide frequency band. It is then possible to evaluate the quality factor due to losses through the walls but also through the antenna loads. The number of antennas between both set-ups (N_{A_1} and N_{A_2}) should be sufficient enough to be able to differentiate net quality factors between measurements and the antennas small enough not to significantly change the volume of the test facility.The first measurements on the effects of antenna loading in a reverberating chamber were produced in [51] but no comparison with theory were undertaken. If we set N_{A_1} and N_{A_2} such that $N_{A_2} \geq N_{A_1}$ the equation system's solution is

$$\begin{cases} \langle Q_{ant} \rangle = & \dfrac{(N_{A_2} - N_{A_1}) \langle Q_{net_2} \rangle \langle Q_{net1} \rangle}{\langle Q_{net_2} \rangle - \langle Q_{net_1} \rangle} \\ \\ \langle Q_{walls} \rangle = & \dfrac{(N_{A_2} - N_{A_1}) \langle Q_{net_2} \rangle \langle Q_{net_1} \rangle}{N_{A_2} \langle Q_{net_2} \rangle - N_{A_1} \langle Q_{net_1} \rangle} \end{cases} \tag{2.43}$$

$\langle Q_{net_1} \rangle$ and $\langle Q_{net_2} \rangle$ are the average values of the quality factors for the first and the second (more antennas) measurements, respectively. It is important to notice in (2.43) that if the quality factor for both measurements are not separated on the frequency range it will not be possible to evaluate

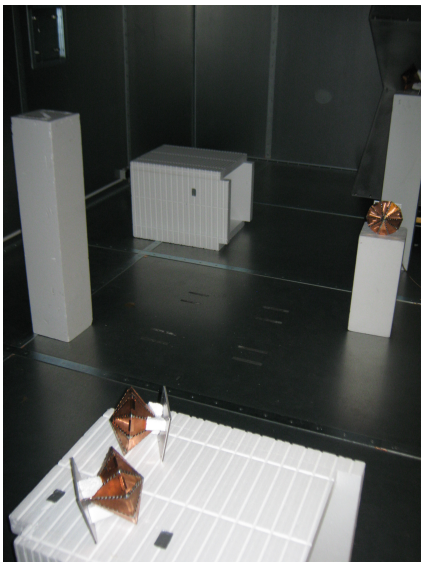

Figure 2.13 Measurement set-up.

correctly the average contributions of the different quality factors. Indeed, for such a case the denominator tend towards 0.

2.4.1 Experimental set-up

The measurements consisted of 10^4 frequency points from 400 MHz to 8 GHz for 20 stirrer position. The test volume under consideration for the first chamber has a length of 5.8m, a width of 3.2 m and a height of 2.4m and $L = 3.08$m , $W = 1.84$m and $H = 2.44$m for the smaller one. Measurements shall always be presented for both chambers in order to further validate our experimental results. The chamber can be considered as overmoded and perfectly diffuse for the frequency range considered. The antennas considered in our set-up are wide-band small monopole antenna that are well adapted for frequency ranges of 400 MHz to 8 GHz. In the frequency range under consideration μ_r can be considered equal to unity [101]. The antennas were placed on polyester columns as seen in Figure 2.13 and experimental measurements have shown that loading with those columns does not affect S-parameters.

In order to explain differences between model and theory it is thus desirable to obtain experimental data for the different quality factors. It is important to point out that only estimators of the quality factor are obtainable through such a process. In the following section, considerations on uncertainty levels are also undertaken to understand if differences between measurements and theory are not imputable to uncertainties due to experimental protocol. Measurements, of the different isolated quality factor showing the uncertainty levels for both chambers are then presented and compared to theory. It is then possible to find where significant differences between measurements and theory are observable.

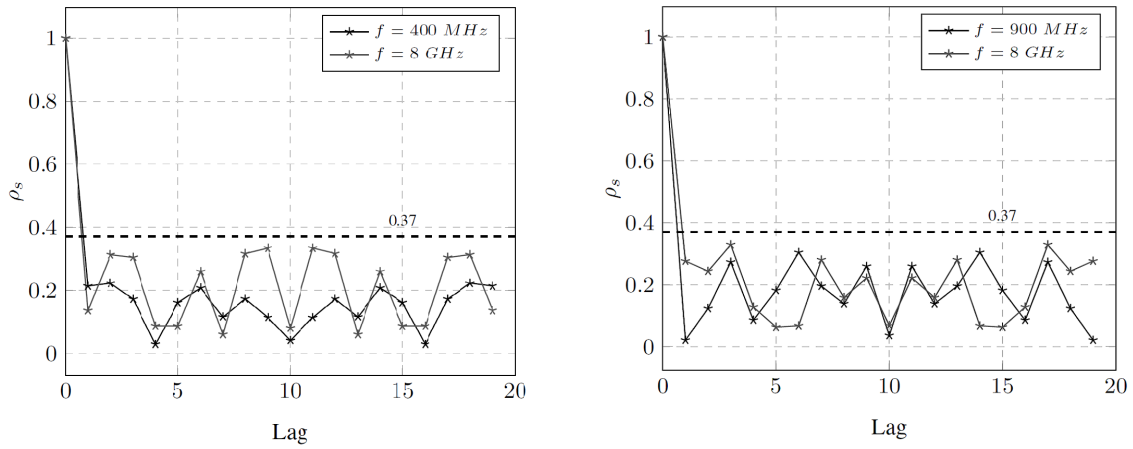

(a) large room (b) small room

Figure 2.14 Correlation coefficient for the 20 stirrer positions ρ_s. The black dashed line is equal to 0.37.

2.4.2 Measurement Uncertainty ans Estimators

As discussed previously, experimental results depend on the number of stirrer positions but also in our case on the frequency band on which averaging was made. Hence, only estimators of the mean net and isolated quality factors are obtainable. In order to validate our measurements, we first need to show they are independent enough when changing the stirrer position on all the frequency range considered. The values of the correlation coefficient presented in Figure 2.14 for the lowest and highest frequency are well below 0.3 from [4].

In the following section we discuss the uncertainty levels obtained during our measurements in order to explain if differences between measurements and theory are due to experimental protocol.

To determine the uncertainty levels of the estimated isolated Q-factor we need to compute the variance of the corresponding estimator referred to as $\sigma_{Q_{ant}}$ and $\sigma_{Q_{walls}}$ from the following expression:

$$\sigma_{Q_{ant}} = \sqrt{\left(\frac{\partial Q_{ant}}{\partial Q_{net_1}}\right)^2 \sigma^2_{Q_{net_1}} + \left(\frac{\partial Q_{ant}}{\partial Q_{net_2}}\right)^2 \sigma^2_{Q_{net_2}}}, \tag{2.44}$$

where $\sigma_{Q_{net_1}}$ and $\sigma_{Q_{net_2}}$ are the standard deviations for the quality factor estimators of both measurements. The equation is the same for $\sigma_{Q_{walls}}$ by replacing Q_{ant} by Q_{walls} in (2.44).

The partial derivative from equation (2.44) and for Q_{walls} are given by:

$$\frac{\partial Q_{ant}}{\partial Q_{net_1}} = \frac{N_{A_1} - N_{A_2}}{\langle Q_{net_1} \rangle^2 \left(\frac{1}{\langle Q_{net_2} \rangle} - \frac{1}{\langle Q_{net_1} \rangle} \right)^2} \tag{2.45a}$$

$$\frac{\partial Q_{ant}}{\partial Q_{net_2}} = \frac{N_{A_2} - N_{A_1}}{\langle Q_{net_2} \rangle^2 \left(\frac{1}{\langle Q_{net_2} \rangle} - \frac{1}{\langle Q_{net_1} \rangle} \right)^2} \tag{2.45b}$$

$$\frac{\partial Q_{walls}}{\partial Q_{net_1}} = \frac{(N_{A_2} - N_{A_1}) N_{A_2} Q_{net_2}^2}{(N_{A_2} Q_{net_2} - N_{A_1} Q_{net_1})^2} \tag{2.45c}$$

$$\frac{\partial Q_{walls}}{\partial Q_{net_2}} = \frac{-(N_{A_2} - N_{A_1}) N_{A_1} Q_{net_1}^2}{(N_{A_2} Q_{net_2} - N_{A_1} Q_{net_1})^2} \tag{2.45d}$$

Therefore, it is possible to estimate the uncertainty levels for the isolated Q-factors from our estimators. In the experimental result section, the uncertainty boundaries are drawn as dash dotted lines surrounding the mean curves showing the accuracy of our experimental estimators.

In the theoretical model, some parameters present in the equations (2.39) and (2.40) may change with frequency and have to be considered when evaluating the differences between theory and measurement of the isolated factor. The case of the wall permeability has already been discussed in introduction but some considerations on the ranges and influence of other parameters such as wall conductivity σ_w must also be analysed.

As discussed in introduction the relative permeability of walls can be considered as unity for the frequency range considered $\mu_w = 1$ [101]. However, some parameters intervening in antenna and wall quality factor may vary with frequency. That is especially the case for the wall conductivities where very little data is available for steel [102]. The values can span over two order of magnitudes on the frequency range. These variations have drastic implications when calculating the average quality factor of walls.

Another parameter on which no data is available is antenna efficiency η_{ant}, we consider that efficiency in he chamber can span from 0.6 to 1 on the frequency range.

Measurements, of the different quality factor for both chambers are presented and compared to theory in the following section. The different theoretical curves due to ranges from unknown parameters are considered and the uncertainty curves are also shown. It is then possible to find where significant differences between measurements and theory are observable.

In order to obtain a better separation of the curves, a frequency averaging is performed using $N_F = 20$ points. All the figures below are presented with frequency averaging. The theory explaining how N_F the number of frequency used for frequency averaging was obtained is given in Appendix

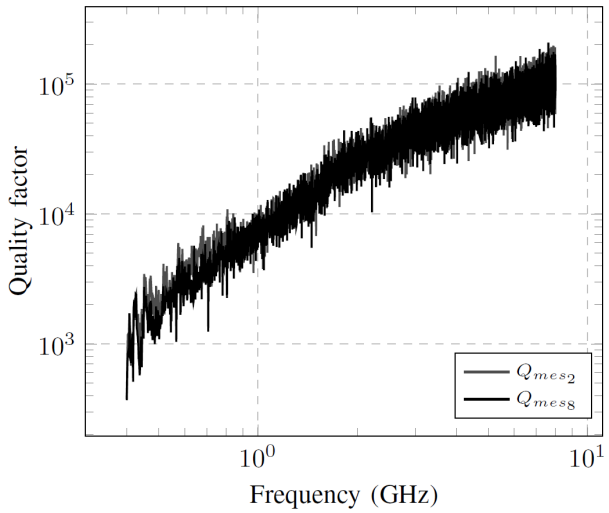

Figure 2.15 Net Quality factor for different numbers of antennas inside the mode-stirred chamber with no frequency averaging.

B. Figure 2.16 and 2.15 show the influence of frequency averaging for Q_{net_2} and Q_{net_8} in the large chamber. When no frequency averaging is undertaken no separation between curves is visible. Frequency averaging is thus necessary in order to obtain isolated Q-factors.

Figure 2.16 shows the average values for the net quality factor when the chamber is loaded with $N_{A_1} = 2$ and $N_{A_2} = 8$ antennas (Q_{mes_2}, Q_{mes_8}) and the net quality factor predicted by theory Q_{th_2} and Q_{th_8}. Figures are shown on loglog graphics in order to better observe the different trends on the frequency range. Since no values were available for σ_w and η, the theoretical curves were produced for a wall conductivity of $\sigma_w = 4.43\ 10^5$ S/m and an antenna efficiency of $\eta_{ant} = 1$ for the first chamber and $\sigma_w = 2.364\ 10^5$ S/m and $\eta_{ant} = 1$ for the smaller one in order to best fit experimental curves.

As past observations have shown the theoretical model seems to overestimate actual experimental results. Moreover, the different trends of the curves on the frequency range do not seem to follow theory. We can note, especially for the large RC case, that the evolutions (i.e., the slopes) of theoretical models with frequency are not identical to those observed experimentally. A close look at the slopes between 400 MHz and 800 MHz highlights slopes that go like $f^{2,3}$ and $f^{2,6}$ for the large and small chamber, respectively. If the antenna-load losses dominate the curves should have followed a f^3 law. This suggests that either Q_w is lower than predicted by theory or Q_a is higher than predicted.In order to have more insight on the evolution of the different contributions with frequency, these need to be isolated.

However, as predicted by theory, only at lower frequencies are the curves $\langle Q_{net_1} \rangle \geq \langle Q_{net_2} \rangle$ well separated. It will not be possible to differentiate the antenna quality factor at high frequencies where most of the losses are due to losses through the walls. However, even at low frequencies, the

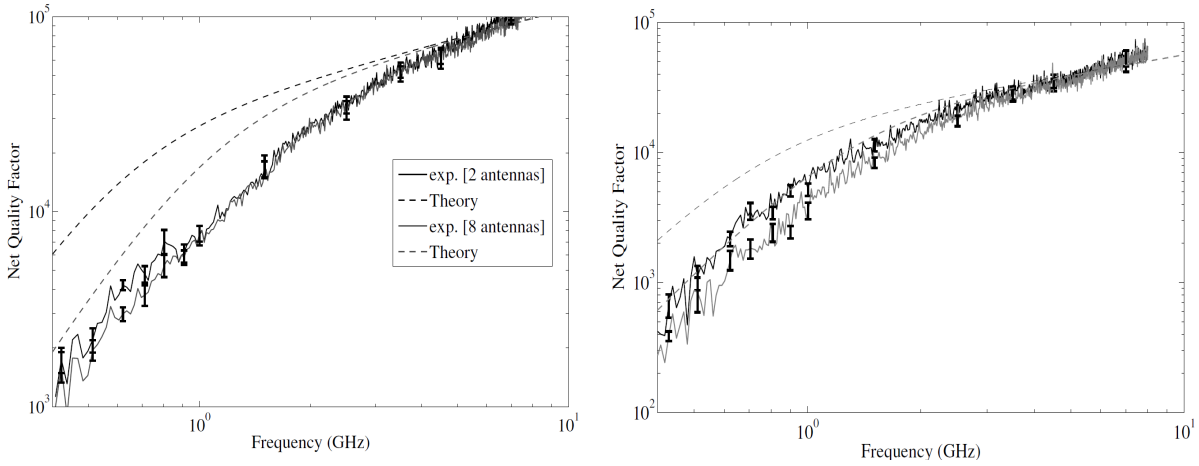

(a) large room (b) small room

Figure 2.16 Net quality factors obtained for the large chamber (upper plot) and the small chamber (lower plot). Values were obtained for two (black solid line) and eight (grey solid line) antennas and comparison to theoretical model for the case of two (black dashed line) and eight antennas (grey dashed line).

net quality factor does not fall by the coefficient predicted by theory (N_{A_1}/N_{A_2}). The separation between both curves is very small. Therefore, even at low frequencies the losses through the walls are significant compared to the losses through the load of the antennas. In order to obtain a better separation between curves a frequency averaging has been performed on all measurements.

2.4.3 Walls and antennas contributions

Figure 2.17 show the variations with frequency of the average antenna quality factor as determined in (2.43) for both chambers. After the black dashed line it is impossible to prove the validity of the antenna quality factor for higher frequencies. These frequency values correspond to the first appearance of negative data for uncertainty levels and should therefore not be considered.

Figure 2.18 compares theoretical model and measurement for the antenna quality factor for different antenna efficiency in the frequency domain where the differentiation is possible. In the frequency range considered we find a good agreement with theory.

Figure 2.19 presents the variations of measured and theoretical wall quality factor for the conductivity range considered in 2.4.2. First of all it is important to notice by looking at the scales of the quality factor in Figure 2.18 and Figure 2.19 that the quality factor of antenna is superior to the quality factor of the walls for all the frequency range. The losses through the walls are always dominant for our set-up which is not the result expected by theory. Indeed the measured quality factor corresponding to the losses through the walls in (2.43) drop significantly below the theoretical model even for the case where the conductivity of the walls is not very high. Moreover, even at higher frequencies the slope of the curve does not follow theory. Figure (2.19) also show two theoretical curves from

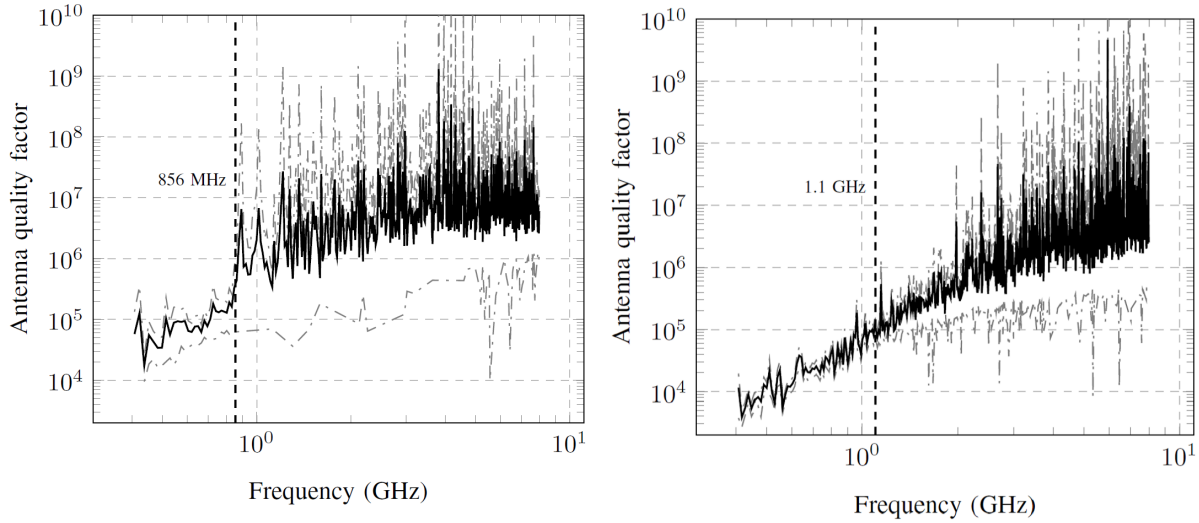

(a) large room (b) small room

Figure 2.17 Antenna quality factor variation with frequency.

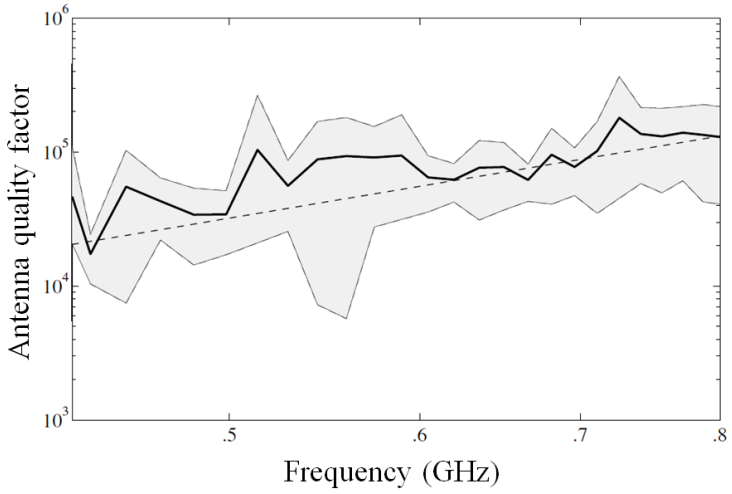

Figure 2.18 Mean antenna quality factor variation with frequency obtained experimentally (solid line) and theoretically in the large chamber. Theoretical curves were obtained by using (2.40) with antenna efficiencies of 100% (dashed line). The grey zone correspond to the uncertainty levels obtained for the experimental data.

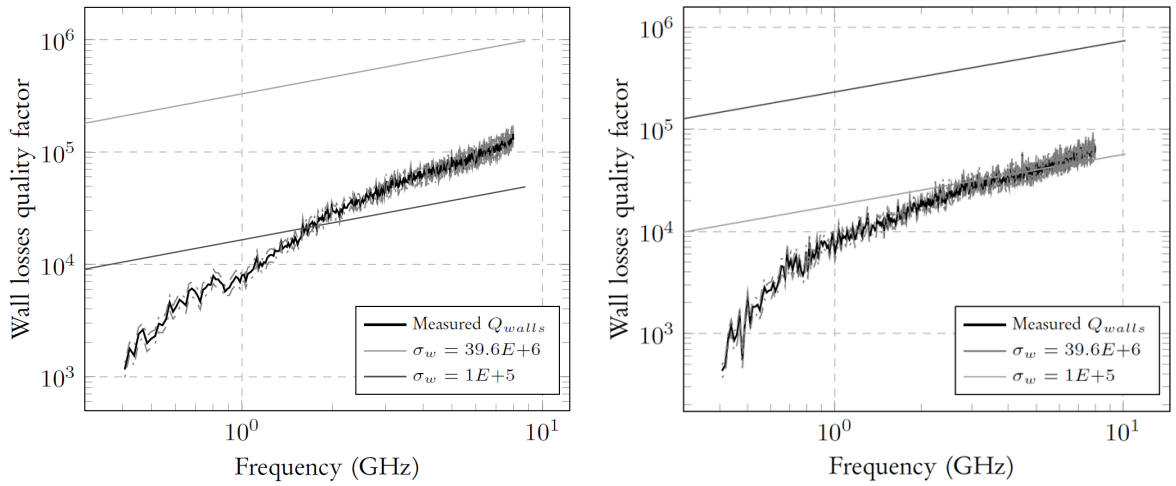

(a) large room (b) small room

Figure 2.19 Wall losses quality factor variation with frequency. For the 2.19a Large and 2.19b Small room

equation (2.39) for conductivities σ_w ranging from 10^5 to 39.6 10^6 which seem to be plausible values for steel on the frequency range [102]. The values of the wall quality factor are indeed in comprised between the range of conductivities considered but the slopes of the wall quality factor does not seem to correspond to the theoretical model even at high frequencies. No explanation can be given that could explain this difference to theory. The uncertainty levels for the wall quality factor are very low and could not explain a variation of trend.

In order to compare experimental results to theory, we have plotted in Fig. 2.18 the reliable part, i.e., the low-frequency range, of the antenna quality factor (solid line). The theoretical model given by (6) was superposed with an antenna efficiency of 100% (dashed line) which appears to be in good agreement. We can observe that the evolution in f^3 is indeed obtained.

By using 2.43 we isolate the contribution of the walls reported in Fig. 2.19: the upper and lower plots correspond to the large and small RC, respectively. Mean values (thin solid line) as well as confidence intervals (dotted lines) are reported. The theoretical model given by (2.39) is superimposed for two conductivity values of 39.6 10^6 (solid line) and 10^5 (dashed line); note that these values are plausible at microwave frequency [102].

For both chambers, we can note that we are not dealing with single-slope curves unlike theoretical model. Besides, curves slopes do not seem to coincide with a $\sqrt{f}$ law as predicted by theory. More specifically, for the large chamber, Q_w follows a $f^{1.8}$ law below 1.7 GHz and goes like f beyond. For the small chamber, Q_w follows a $f^{3.3}$ below 1 GHz and goes like f beyond. Interestingly, Q_w seems to share the same law for high frequencies, which highlights that the loss mechanism is likely to be the same. From the literature, the loss mechanism is expected to be due to wall losses described by (2.39). In spite of the law that differs from $\sqrt{f}$, if we compute the ratio involving quality factors Q_w

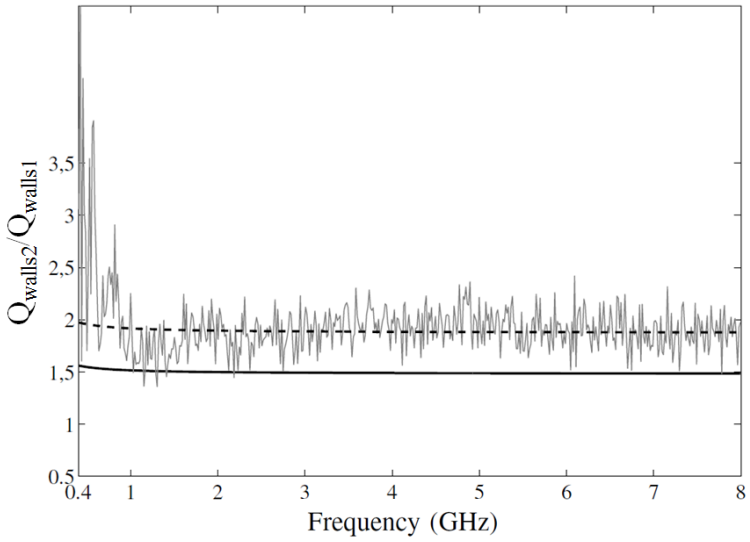

Figure 2.20 Ratio of the quality factors due to the walls. Theoretical results consider same conductivities (solid black curve) and non-identical conductivities that differ from 13%; experimental data are also presented (grey curve).

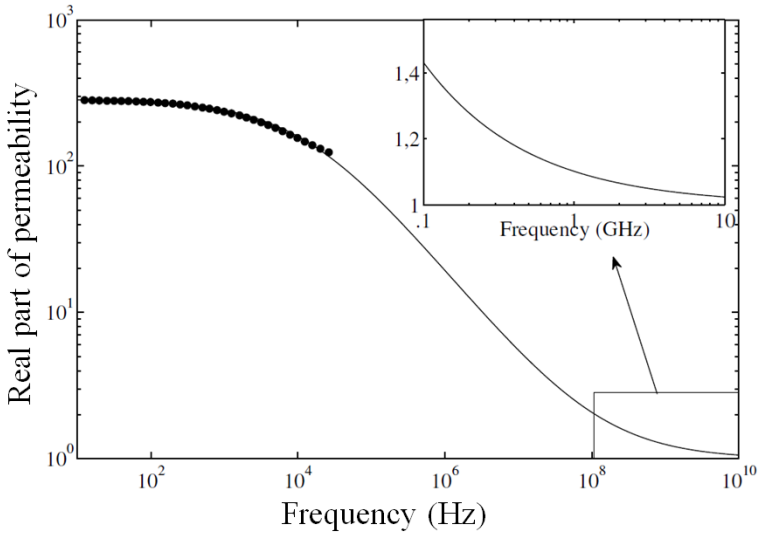

Figure 2.21 Example of data taken from Ref. [103] (symbols) measured at low frequency. An analytical model is superimposed (solid line) providing an insight of μ′ law in the microwave range (inset), i.e., between 100 MHz and 10 GHz.

related to each chamber, one would expect the following

$$R_Q = \frac{Q_{w,L}}{Q_{w,S}} = \frac{V_L S_S}{S_L V_S} R_{\alpha\sigma} \tag{2.46}$$

with $R_{\alpha\sigma} = \sqrt{\mu_{rS}\sigma_L/\mu_{rL}\sigma_S}$ and where subscripts 'L' and 'S' refer to the large and small chambers, respectively Fig. 2.20 shows the Q_w ratio (grey curve) obtained by using experimental data from Fig. 2.16. We superposed the theoretical prediction given by (11) where equal permeabilities and conductivities for both chambers were assumed (solid bold line), i.e., for $R_{\alpha\sigma} = 1$, and for $R_{\alpha\sigma} = 1.26$ (dashed line). For this last case, we can see that experimental results are in better agreement. Beyond 1 GHz, the invariance indicates that the walls play indeed a major role. Below 1 GHz the ratio follows likely a $1/f$ law given the slopes of $Q_{w,L}$ and $Q_{w,S}$.

Interestingly, we can note that the curve remains invariant in the frequency range where Q_w goes like f. When this law is met, the invariance of Q_w ratio highlights that the loss mechanism is linked to the walls surface. The permeability of steel that constitutes generally the metallic walls of RCs is often regarded as a constant equal to unity [55, 91] while some studies highlight the fact that μ_r in steel is a decreasing function of frequency [103]. The decrease rate does not necessarily imply that μ_r tends to 1 in the microwave frequency range. Accordingly, the classic law of Q_w varying as $\sqrt{f}$ must likely be revisited. Unfortunately, the constitution of the steel material of the two RCs used herein is not perfectly known. However, as specified in [103], frequency law followed by the complex permeability $\mu(\omega)$ reads,

$$\mu(\omega) = \frac{\mu'(0) - \mu'(\infty)}{1 + i\omega\tau(\omega)} + \mu'(\infty) \tag{2.47}$$

in which $\mu'(0)$ and $\mu'(\infty)$ are the low- and high-frequency permeability constants; τ represents a relaxation time assumed to be real, and a function of frequency. In order to have some insight about the order of magnitude of $\mu(\omega)$, we have taken from Fig. 3 of Ref. [103] some measured data of μ' reported in Fig. 10 (symbols); relation (2.47) is also reported with a relaxation time $\tau(f) = 8\,10^{-3}/f^{0.685}$, $\mu'(0) = 285$ and $\mu'(\infty) = 1$. In the inset we can observe the evolution of μ' in the frequency range of interest, i.e., from 100 MHz to 10 GHz. We can see that the parameter is not constant over the frequency range and that μ_r in (2.39) would deserve to be regarded as a decreasing function of frequency. The extrapolation performed here does not allow us to be sure that the curve has the right frequency law in the frequency range of interest. If the proper law happened to be a $1/f$ law, it could explain the evolution of the quality factor due to walls losses. These results lead us to analyse if the same Q-factor laws are observed if RC walls are made up of non-magnetic materials.

An aluminium RC

In order to study see the possible effect of non-magnetic materials on Q-factors law (the one due to walls losses), we considered a 1.4 m $\times$ 1.5 m $\times$ 0.8 m reverberation chamber made of aluminium. S-parameters measurements were performed from 500 MHz to 8.5 GHz. About 2600 points linearly spaced in the frequency domain were measured. From these S-parameters measurements, we processed

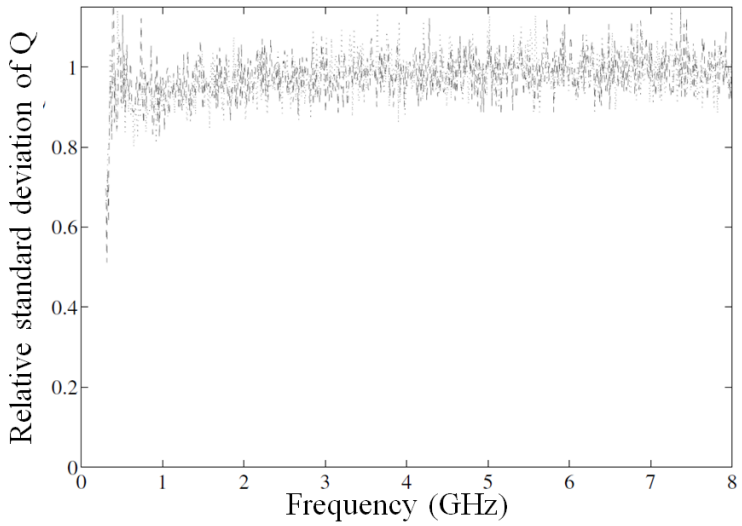

Figure 2.22 Sample relative standard deviation of Q.

the quality factor due to wall losses. Fig. 2.23 shows the values obtained for Q_w (grey curve) and the analytical model given by (2.39) is reported (solid line). The conductivity and the relative permeability values considered for the analytical model are 10^6 S/m and 1, respectively. Note that the aluminium conductivity considered herein is almost 40 times lower than the usual value. From Fig. 2.23, we cannot neither claim that Q_w follows a linear law nor that it does not follow such law. The case of aluminium should deserve more investigation to highlight the eventual law followed by Q_w and the role of walls material in Q_w law.

Conclusion

In this section we presented an experimental set-up allowing to isolate the different loss mechanisms taking place inside the chamber. The measurement is divided in two parts: we first, measure the net Quality factor with few antennas inside the chamber and by changing the number of antennas, while keeping the experimental conditions exactly the same, it is possible to extract each component of the net quality factor. A frequency averaging had to be used in order to separate the net quality factors for both set-ups. A comparison was then possible between theoretical model and experimental results for each component of the quality factor. One important experimental observation is that even at lower frequencies the power dissipated through the walls is more important than the power dissipated in the load of the receiving antenna when the model shows otherwise. It is not possible in such a case to extract on a very large frequency range the antenna quality factor without the uncertainty levels becoming very important. A comparison for different parameters in the theoretical model is also undertaken to show the variations of theory with these parameters. Another interesting experimental result is that the antenna quality factor seem to correspond to theoretical model in the frequency

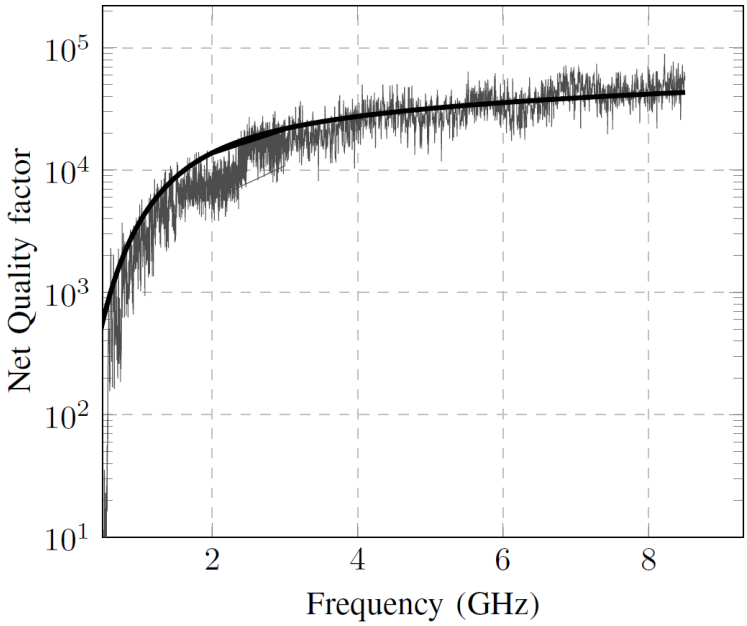

Figure 2.23 Estimated quality factor squared in an RC made up of aluminium (grey curve). The analytical model (black solid line) given by (2.37) is superimposed with a conductivity of 10^6 S/m.

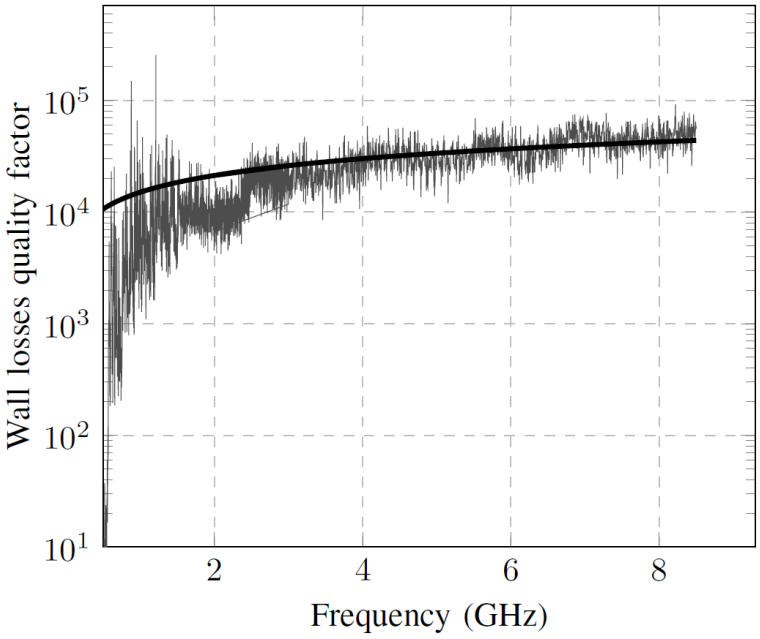

Figure 2.24 Wall losses quality factor variation with frequency. The analytical model (black solid line) given by (2.39) is superimposed with a conductivity of 10^6 S/m.

range where uncertainty levels are low enough. Moreover, the trend of the wall quality factor does no seem to follow the theoretical model even at high frequencies. No explanation can be given for now to explain such differences between model and experimental results.

2.5 Another Figure of Merit of M-SC : The Maximum Field

Another significant figure of merit of M-SCs and probably the most important when dealing with the classical use of reverberation chambers is the maximum field inside the test facility. These studies are of particular interest because they allow to apprehend the maximum field levels available to stress onto the Element Under Test and primarily onto its most critical component. Most studies when considering reverberating chamber deal with classical usage of the facility, as presented in the previous section, where the EUT is illuminated via a Vector Network Analyser (VNA) connected to the chamber allowing to analyse the EUT on a wide frequency band. One or more mechanical stirrer allows a certain number of independent measurements. The maximum field onto the EUT is the parameter used in the actual standard IEC 61000-4-21 [4]. It defines a number of stirrer positions needed in regards of the chamber volume in order to obtain a quasi-homogeneous repartition of the maximum-field inside the chamber over all the stirrer positions. This area of study is tightly related to Extreme-Value theory.

In this section we shall present the impulse response model used during this thesis. This model will be used in the following chapter to calculate conversion efficiencies and compare chambers in classic regime and when TR is used. This model allows in particular to evaluate the statistics of the maximum of an impulse response in a multipath environment like RCs. This quantity is important for this work since it corresponds to the limiting value for amplification module. The maximum field of an impulse response plays an important role when considering using time-reversal for amplification purposes since the maximum amplification is limited by this value.

2.5.1 Probabilistic Modelling of Impulse Responses Observed in Multipath Environments

In this section we study in a more detail manner some probabilistic properties of impulse responses in multipath propagation medium. In such mediums the impulse responses $h(t)$ have a random behaviour. One metric commonly used to describe their macroscopic features is the power-delay profiles (PDP) [104, 105]. Even if this kind of approach gives some information of the channel response, it does not provide deep insight in its statistical properties. In this section we thus derive some general results about the probability law followed by impulse responses $h(t)$ in the case of strongly diffusing multipath propagation. Special attention is paid to the prediction of how likely is $h(t)$ to locally fluctuate higher than its mean envelope, the PDP. The impact of the channel and signal characteristics on the fluctuations are also considered. Previous approach have used a shot noise

approach to model an impulse response within complex multipath medium [36, 106, 107]. Here, only the fact that the propagation is strongly diffuse is considered.

2.5.2 Modeling $h(t)$ as a random process

The impulse response of a cavity results from the superposition of second-order responses of the Helmholtz equation for each of its resonances as described in section 2.2.3. The time-domain response a mode resonating at the angular frequency $\omega_k = 2\pi f_k$ of a cavity when described by a Lorentzian can be written as

$$\psi_k(t) = e^{-t/\tau_k} \cos(\omega_k t + \varphi_k) \tag{2.48}$$

with $\tau_k = Q_k/\omega_k$ the time constant related to the quality factor Q_k of the resonance. In the rest of this paper it will be assumed that $\tau_k = \tau$ implying that τ operates as an average time constant. The overall impulse response is the sum of all the excited modes giving:

$$h(t) = e^{-t/\tau} \sum_{k=1}^{N} \alpha_k \cos(\omega_k t + \varphi_k), \tag{2.49}$$

with α_k the set of modal weights in time domain associated to the excitation of each resonance and φ_k their respective phase-shift angles. The sum is taken over the N resonance that are significantly contributing when the medium is excited over B_T frequency band.

First of all we derive the root-mean square (rms) envelope of the impulse responses, hereafter referred to as $h_0(t)$. This quantity can be written as:

$$h_0(t) = A_0 e^{-t/\tau}, \tag{2.50}$$

and can be derived by expressing conservation-of-power properties [94, 108, 109]. Here, $h_0(t)$ will be used as a scale function. Local fluctuations will be modelled as a random process $w(t)$, i.e.,

$$h(t) = h_0(t) w(t) \tag{2.51}$$

the rms envelope can be extracted from equation (2.49) as

$$h_0^2(t) = \langle h^2(t) \rangle = e^{-2t/\tau} \left[\left\langle \sum_{k=1}^{N} |\alpha_k|^2 \cos^2(\omega_k t + \varphi_k) \right\rangle + \left\langle \sum_{k \neq n} \alpha_k \alpha_n \cos(\omega_k t + \varphi_k) \cos(\omega_n t + \varphi_n) \right\rangle \right]. \tag{2.52}$$

The brackets correspond to an ensemble average of a random variable over its possible realizations. The modal weighs $\{\alpha_k\}$ are generally assumed to be independent and identically distributed, as discussed in [110]. As a result, the cross-products $\langle \alpha_k \, \alpha_n \rangle$ only differ from 0 when $k = n$. Therefore the summations over all $k \neq n$ are equal to zero. A further reason for this result is the product of cosine functions with random frequencies and phase-shift angles . This property also leads to an average equal to zero for $k \neq n$, as soon as the phase shifts can be considered as uniformly distributed over all possible angles $\varphi_k \sim \mathscr{U}(0, 2\pi)$ which is the typical distribution assumed for such variables in diffuse medium. This gives from equation (2.52)

$$A_0 = \sqrt{\left\langle \sum_{k=1}^{N} |\alpha_k|^2 \cos^2(\omega_k t + \varphi_k) \right\rangle} \tag{2.53}$$

the average of this product can then be approximated by the product of the averages giving:

$$A_0 = \sqrt{\left\langle \sum_{k=1}^{N} \cos^2(\omega_k t + \varphi_k) \right\rangle \left\langle \sum_{k=1}^{N} |\alpha_k|^2 \right\rangle} = \sqrt{\frac{1}{2} \left\langle \sum_{k=1}^{N} |\alpha_k|^2 \right\rangle} = \sigma_\alpha \sqrt{\frac{N}{2}} \tag{2.54}$$

where σ_α is the standard deviation of the random variable $\{\alpha_k\}$.

$h_0(t)$ describes the way energy evolves (on average) in the response of a reverberating medium when the driving excitation is stopped. This kind of model is useful in order to characterize the power-delay spread of a channel or macroscopic properties of chambers such as decay-times, however it does not provide further information about the differences between impulse responses sharing the same power-delay profile. More insight can be obtained by analysing the statistical properties of $w(t) = h(t)/h_0(t)$. From equations (2.49) and (2.54)one obtains:

$$w(t) = \sqrt{\frac{2}{N}} \sum_{k=1}^{N} \beta_k \cos(\omega_k t + \varphi_k) \tag{2.55}$$

where $\beta_k = \alpha_k / \sigma_\alpha$ are standardized random variables, with $\langle \beta_k^2 \rangle = 1$ and $\langle \beta_k \rangle = 0$. Noticing that the summation in (2.55) can be interpreted as a 2D random walk, the statistical properties of $w(t)$

can be obtained:

$$\sum_{k=1}^{N} \beta_k \cos\left(\omega_k t + \varphi_k\right) = \mathbb{R}e\left\{s(t)\right\} \tag{2.56}$$

with

$$s(t) = \sum_{k=1}^{N} \beta_k e^{j\xi_k} \tag{2.57}$$

where $\xi_k = \omega_k t + \varphi_k$. Since $\{\varphi_k\} \sim \mathscr{U}(0, 2\pi)$, then $\{\xi_k\}$ is also uniformly distributed: $\{\xi_k\} \sim \mathscr{U}(0, 2\pi)$, $\forall\ (t,\ \omega_k)$. The summation in (2.56) can now be interpreted as a random walk in the complex plane, with random steps along random directions $\{\xi_k\}$. This class of random processes is known to present a probability distribution with circular symmetry thus only depending on the norm of $s(t)$. The central-limit theorem states that $s(t)$ can then be approximated as a Gaussian process. For such distributions, $s(t)$ is fully characterized by its first two moments.

The isotropy of $s(t)$ leads to an average equal to zero. Therefore, only the variance σ_s^2 of $s(t)$ needs to be calculated. Since $s(t)$ is a stationary process $\sigma_s^2 = N$, $\forall t$, the isotropy of $s(t)$ results into

$$\left\langle \mathbb{R}e\left\{s(t)\right\}^2 \right\rangle = \frac{\left\langle |s(t)|^2 \right\rangle}{2} \tag{2.58}$$

Taking into account these properties $w(t)$ can be described as a stationary process, with a standard deviation equal to one $\sigma_w = 1$ and a zero average $\mu_w = 0$, i.e., following a standard normal probability law. Since these conclusions are based on the central-limit theorem, they can be expected to hold as long as $N \gg 1$, the individual contributions for each resonance needing to be weakly correlated.

2.5.3 Probability Law for the Peak-Value of $h(t)$

$h(t)$ was found to be an exponentially-modulated Gaussian random process. Using this model it is possible to compute the probability distribution of its peak values. This is of practical importance when evaluating the performance of time-reversal and of reverberation chambers [36, 94].

In order further study the impulse response, $h(t)$ is approximated as a discrete time-series, by sampling it at $t = kT_c,\ \in\ [0, +\infty[$, with T_c a time step discussed later in this section. We first assume that the samples $\{h_k = h(kT_c)\}$ are independent. Let $K = \max_t |h(t)|$ be the peak value of $h(t)$, the

probability law of M can be written as

$$F_K(x) = P(K < x) = P(|h_k| < x, \forall k), \tag{2.59}$$

which for independent $\{h_k\}$, translates into

$$P(K < x) = \prod_{k=0}^{\infty} P(|h_k| < x). \tag{2.60}$$

This kind of probability law is characteristic of an extreme-value law, where the maximum value is observed in a set of N independent identically distributed (iid) random variables. The difference here is that the samples are not identically distributed, since their standard deviation is exponentially decreasing with their order k.

Since $w(kT_c)$ follows a normal distribution law decreasing exponentially by $\exp(-kT_c/\tau)$ every time step, the standard deviation of $h(t)$ becomes $\sigma_k = \exp(-kT_c/\tau)\sigma_w$ with $\sigma_w = 1$. The set $\{|h_k|\}$ therefore follows by definition a half-normal distribution giving for its cumulative distribution function,

$$P(|h_k| < x) = \operatorname{erf}\left[\frac{x}{\sigma_k\sqrt{2}}\right] = \operatorname{erf}\left[x\frac{\exp(kT_c/\tau)}{\sqrt{2}}\right] \tag{2.61}$$

so that (2.59) results into

$$F_K(x) = \prod_{k=0}^{N} \operatorname{erf}\left[x\frac{\exp(kT_c/\tau)}{\sqrt{2}}\right] \tag{2.62}$$

As the standard deviation of late-time samples decreases exponentially, it is clear that their contribution to the peak value K can be expected to be negligible. It is therefore possible to truncate the sum in (2.62) to a number N of samples, where N can be chosen such that the probability of having $|h_N| > A_0$ is significantly different from zero, e.g., greater than 5%. This condition is equivalent to asking for a standard deviation of h_N/A_0 larger than $1/2$, i.e.,

$$\sigma_{h_N/A_0} = \exp\left(-NT_c/\tau\right) > \frac{1}{2} \tag{2.63}$$

which after simplifications gives the conditioning for N

$$N < \frac{\tau}{T_c} \ln 2 \tag{2.64}$$

In order to hold, (2.62) required the samples $\{h_k\}$ to be independent. This variable being normally distributed, it is sufficient to ensure that they are uncorrelated to insure sample independence. In order to guarantee independence it is necessary to assess the time step T_c enabling this property. This can be done by computing the auto-correlation function of $w(t)$:

$$R_w(\delta) = \langle w(t)w(t+\delta)\rangle \tag{2.65}$$

which following equation (2.55) can be shown to be

$$R_w(\delta) = \frac{2}{N}\sum_{k=1}^{N}\frac{\beta_k^2}{2}\cos(\omega_k\delta) = \langle\cos(\omega_k\delta)\rangle \tag{2.66}$$

The result of this average will definitely depend on the probability distribution function of the resonances of the medium. General asymptotic formulas, such as Weyl's [111], can be used, we will assume that $\{f_k\} \sim \mathscr{U}(f_1, f_2)$; this approximation holds as long as the fractional bandwidth B_T/f_c does not go beyond 10%. This yields with a similar type of demonstration than in [112],

$$R_w(\delta) = \cos(2\pi f_c\delta)\,\mathrm{sinc}(\pi B_T\delta) \tag{2.67}$$

The time-window T_c required in order to have uncorrelated samples $\{h_k\}$ can now be estimated as

$$T_c = \int_0^\infty R_w^2(\delta)d\delta = \frac{1}{4B_T}, \tag{2.68}$$

is chosen to provide an equivalent coherence time even though $R_w(\delta)$ does not have a compact support, i.e., $\nexists T_c$ such that $R_w(\delta) = 0, \forall\delta > T_c$.

Figure 2.25 shows the evolution of the probability density function of $x = M/A_0$ when T_c/τ takes different values. The skewness decreases and the modes value increases when T_c/τ decreases. These tendencies are also represented in Figure 2.26 where the spread of the quantiles diminishes and the value of the mode increases when T_c/τ increases. Comparison of the model with experimental

results will be presented in sec. 3.3.3. Figure 2.27 presents the $w(t)$ for an impulse response obtained in one of Supélecs RCs used for experimental validation in sec. 3.3.3.

Figures 2.25 and 2.26 are representations of the evolution of the probability density function of the maximum of an impulse response over T_c/τ. As it can be seen from those figures, the limiting factor for the maximum level occurs for small T_c/τ. In such cases, values of up to 4 times higher the rms values can be obtained for the 95% quantile. This parameter and the limiting quantile used will be of prime importance when considering amplification possibilities offered by a TRAS. This value defines a risk assessment of saturating the amplifiers 5% of the times when the time-reversed impulse response is amplified.

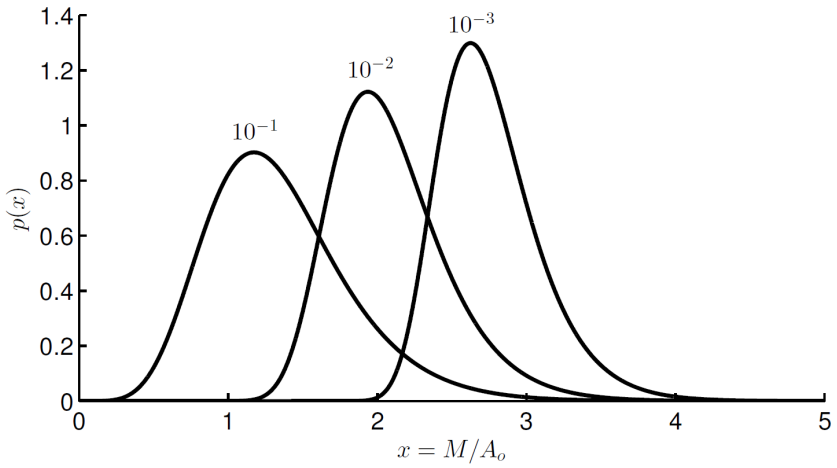

Figure 2.25 Probability density functions of $\max_t |h(t)/h_0|$ as predicted by (2.62) for three values of T_c/τ.

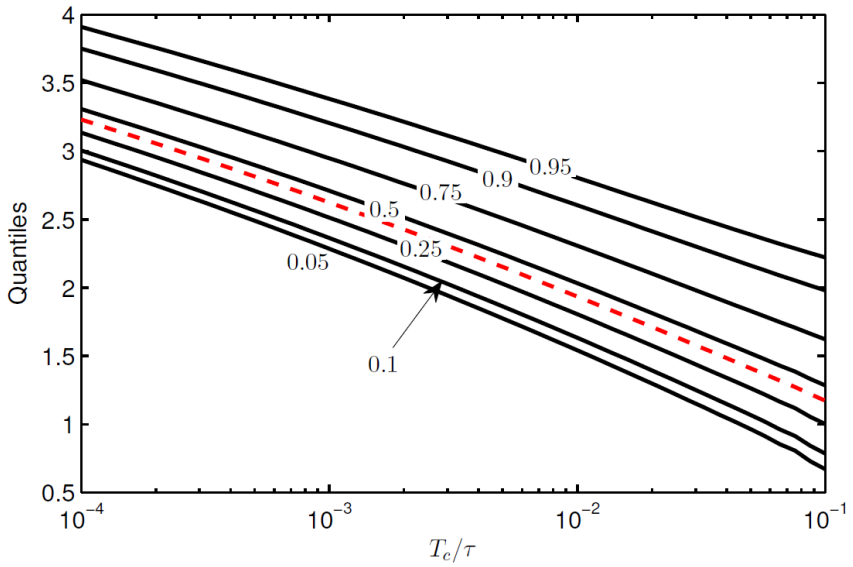

Figure 2.26 Evolution of quantile spread with T_c/τ.Red dashed curve:mode.

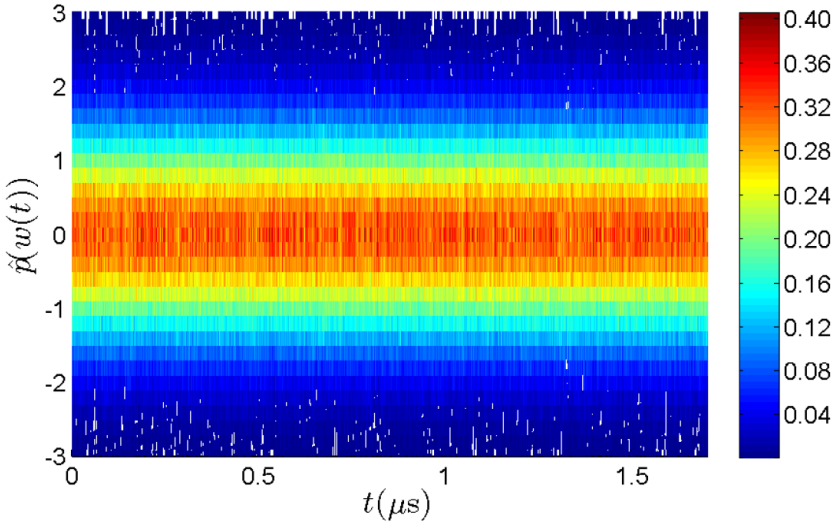

Figure 2.27 Empirical pdf of $w(t)$, derived for 50 bins over time.

Conclusion

In this chapter fundamental aspects of the physical processes taking place in a complex propagation medium were presented. The dual representation of image theory and modal representation of reverberation chambers were announced. Some important notions such as field diffusivity and mixing

were introduced. The physical processes that allow a chamber to diffuse, the importance of diffused reflections and intrinsic losses during propagation were also presented. Statistical properties of a diffused field were given. Diffusion is an important notion in the rest of this work since the models developed here will consider the field to be diffused in the chamber. Various definitions of threshold values guaranteeing field diffusivity were also offered.

In the third section of this chapter, we presented an experimental set-up that allows to isolate the different loss mechanisms occurring inside a reverberation chamber. The measurement is divided in two parts: we first, measure the net Quality factor with few antennas inside the chamber and by changing the number of antennas, while keeping the experimental conditions exactly the same, it is possible to extract each component of the net quality factor. A comparison was then possible between theoretical model and experimental results for each component of the quality factor. One important experimental observation is that even at lower frequencies the power dissipated through the walls is more important than the power dissipated in the load of the receiving antenna when the model shows otherwise. Another interesting experimental result is that the antenna quality factor seems to correspond to theoretical model in the frequency range where uncertainty levels are low enough. Moreover, the trend of the wall quality factor does not seem to follow theoretical model even at high frequencies. These results are quite important when designing a reverberation chamber. The refocusing properties and efficiency of a time-reversal process depend on the quality factor of the cavity. A theoretical derivation of the probability density function of the maximum level of an impulse response in a reverberation chamber was also given. The importance of the quality factor and of the bandwidth of the injected impulse was found. The experimental validation of this derivation will be shown in the following chapter. The fluctuations of the maximum levels of an impulse response in a reverberation chamber will be used in the rest of the work. The impulse response is the signal that will be amplified and its maximum level determines the fluctuations the maximum amplification allowed for the amplifying device.

Chapter 3

Time-Reversal in Reverberating Environments

3.1 Time-Reversal Characteristics

3.1.1 Introduction and Application Fields

To introduce time-reversal concepts, let us consider the simple example of a breaking glass falling to the ground from a table. Physically, it would be conceivable to replay this scene backwards, if the speed and direction of each of the glass fragments are measured. Indeed, if each fragment are sent back in the exact opposite direction where they came from and with the same velocity, the fragments would supposedly converge to their initial point. The principle of time reversal is thus quite simple. However, in this example the extreme sensitivity to initial conditions because of the non-linear effects occurring during the fall and breaking of the glass as well as the large number of particles hinders the success of this experience.

However, in wave physics time reversal is possible because the amount of information needed to describe a wave field scenery is reduced considerably than in the previous example of the broken glass. Indeed, the smallest amount of information needed for the experiment to work is of the order of magnitude of the smallest wave-length. Moreover, the systems linearity enables the non-propagation of a position or velocity error. For these reasons, time-reversal of waves is possible even in complex systems.

Time reversal (TR) is described as a spatio-temporal focusing initially developed in acoustics by Mathias Fink in 1989 [113]. The first time reversal experiments in microwaves were held in 2003 by G. Lerosey in Supélec opening the way to applications in this frequency range [114, 115].The time reversal technique can generate wave fronts converging towards the initial source point in weakly dissipative media [116]. The time-reversed wavefront converges in a non-ideal replica of the divergent wavefront associated to the source. It is an efficient method for focusing wave fronts in complex propagation environments. It has the ability to take advantage of the spectral diversity of the environment and allows to focus both in space and time [117]. Spatial and temporal focusing means that the spatial as well as temporal shape of the wavefront is reproduced, at the location of the source associated to the divergent wavefront [118].

In principle, to obtain time reversal one must impose boundary conditions allowing a reverse chronology evolution of the propagation. This configuration is only possible if the propagation environment verifies reciprocity properties as well as time symmetry of wave propagation equations [119]. As explained in 2.2.4 a medium follows reciprocity relations if the Green's function between two arbitrary points within the environment stay invariant by reversing the transmitter and receiver functions [120]. The time symmetry or T-symmetry condition on propagation equations when reversing the time variable ensures that the time inverted version of a wavefront is also solution of the propagation equations. These two conditions therefore ensure that a wavefront propagate "backward". These necessary conditions for time reversal are realised for scalar wave propagation [121] and wave vectors of electromagnetism in weakly dissipative media [122].

It is possible to identify sources associated with a wavefront time-reversed using the equivalence principle of Huygens surface [123, 124]. This combination of time-reversal and Huygens surface properties is what is commonly called a Time-Reversal Electromagnetic Chamber (TREC) [125].

The development of time reversal has lead to applications in acoustics and electromagnetism in various domains. Some application fields of time-reversal in acoustics and ultrasounds are sonar and radar [126, 127] medical imagery and treatments [128–131]. It is also possible with this technique to make any type of surface become tactile [132, 133]. It has also found applications in non-destructive flaw detections in materials [134]. Time reversal is also commonly used in modern imaging processes thanks to the DORT method [135]. Indeed, in 2003, Prada et al. showed that the DORT method (Decomposition of the Time Reversal Operator) combined with non-linear signal processing, Maximum Likelihood estimators and Multiple Signal Classification (MUSIC), enabled to observe two diffusers separated by sub-wavelength distances [136, 137]. The analytical formalism of DORT-MUSIC method was developed by Devaney and Lehman [138, 139].

Its use in the field of electromagnetism has lead to applications in imaging [60, 140], Wireless Telecommunications [141] or EMC testing [125]. In telecommunications focusing properties would improve communications between transmitters and receivers in multipath environments [142]. The ability to focus in space and time has enhanced the wireless transmission rate and reduce the correlation between received on separate receivers signals [141]. Time reversal for through-the-walls applications has also been studied both in simulation [143] and experimentally [144] and for detection purposes[145]. Non linear time-reversal techniques have been used for target detection [146, 147].

3.1.2 Time-Reversal Process for electromagnetic Waves

To illustrate the implementation of a time reversal process, let us consider the diagram in Figure 3.1, where a transmitting antenna S is surrounded by N receivers/transmitters called TRM (Time Reversal Mirror) [148, 149].

There are two stages in order to focus a wave using a time reversal process. The first, is a calibration phase. During this phase the transmitter S radiates a signal $s(t)$ and the corresponding responses are recorded at the output of the N TRMs. These signals are represented by $y_i(t)$ where $i \in [1..N]$ corresponds to the TRMs.

During the second phase the signals received by each antenna are time-reversed and re-injected in their respective TRM. The re-transmitted wavefront is a non-ideal converging image of the signal transmitted during the first stage by S. The signal propagates backwards and refocuses on the antenna and the signal obtained is a non ideal replica of $s(t)$.

A Time reversal process is a spatio-temporal adaptation of a matched filter [150]. Such a filter maximizes the amplitude of the field at a given time and location. In a non-dissipative media time reversal is equivalent to an inverse filter and thus also maximizes the SNR (Signal-to-Noise Ratio).

As mentioned in the introduction, there are three constituent principles for a time reversal process to work. The propagation medium is linear and has to follow reciprocity relations, the propagation

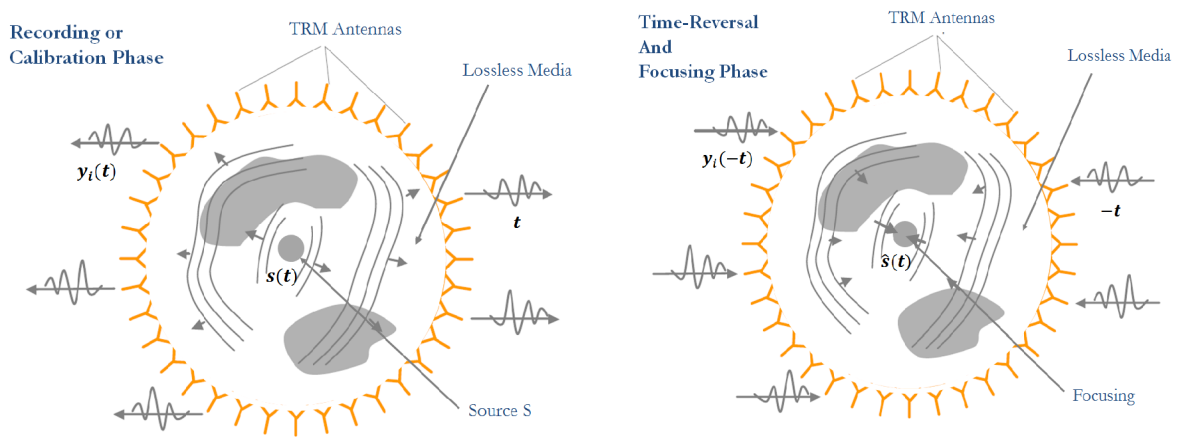

(a) (b)

Figure 3.1 Schematic illustration of the far-field time-reversal by dipolar sources. (a) A source S generates a wave. The electric components are recorded on a close surface. (b)This electric field is time-reversed and re-emitted by the TRM sources and the back-propagated wave is generated [115].

equation must be T-symmetric or invariant under a time shift of the wavefield propagator and follow the equivalent surface principle. The principle of reciprocity was introduced in the previous chapter. In what follows, a more thorough presentation of the time-symmetry of the propagation equations as well as the surface equivalence principle will be undertaken. Here, we will show that a necessary condition for a correct back-propagation of a wavefront is the symmetry of the Helmholtz equations. $\boldsymbol{\mathcal{E}}_{wf}(\boldsymbol{r},t)$ describes the spatio-temporal dependence of the desired wavefront to time-reverse. It is a solution of the Helmholtz equation written in free space:

$$\Delta\boldsymbol{\mathcal{E}}_{wf}(\boldsymbol{r},t)-\mu\varepsilon\frac{\partial^2\boldsymbol{\mathcal{E}}_{wf}(\boldsymbol{r},t)}{\partial t^2}=0 \tag{3.1}$$

The time-reversed version of the wave is $\boldsymbol{\mathcal{E}}_{wf}(\boldsymbol{r},-t)$. Since equation (3.1) contains only second order derivatives it is clear that the time-reversed expression of $\boldsymbol{\mathcal{E}}_{wf}(\boldsymbol{r},t)$ is also solution of the Helmholtz equation. Indeed $\partial(-t)^2$ is equal to $\partial(t)^2$.

A more detailed derivation of the time-reversed field are given in [151, 152]. The end result of the time-reversed field $\boldsymbol{E_{TR}}$ at position $\boldsymbol{r}$ in frequency domain comes from equation (2.11) and is given by:

$$\boldsymbol{E_{TR}}(\boldsymbol{r})=-2j\mu_0\omega^2\mathrm{Im}\left\{\underline{\boldsymbol{G}}(\boldsymbol{r},\boldsymbol{r'})\right\}\boldsymbol{p}^* \tag{3.2}$$

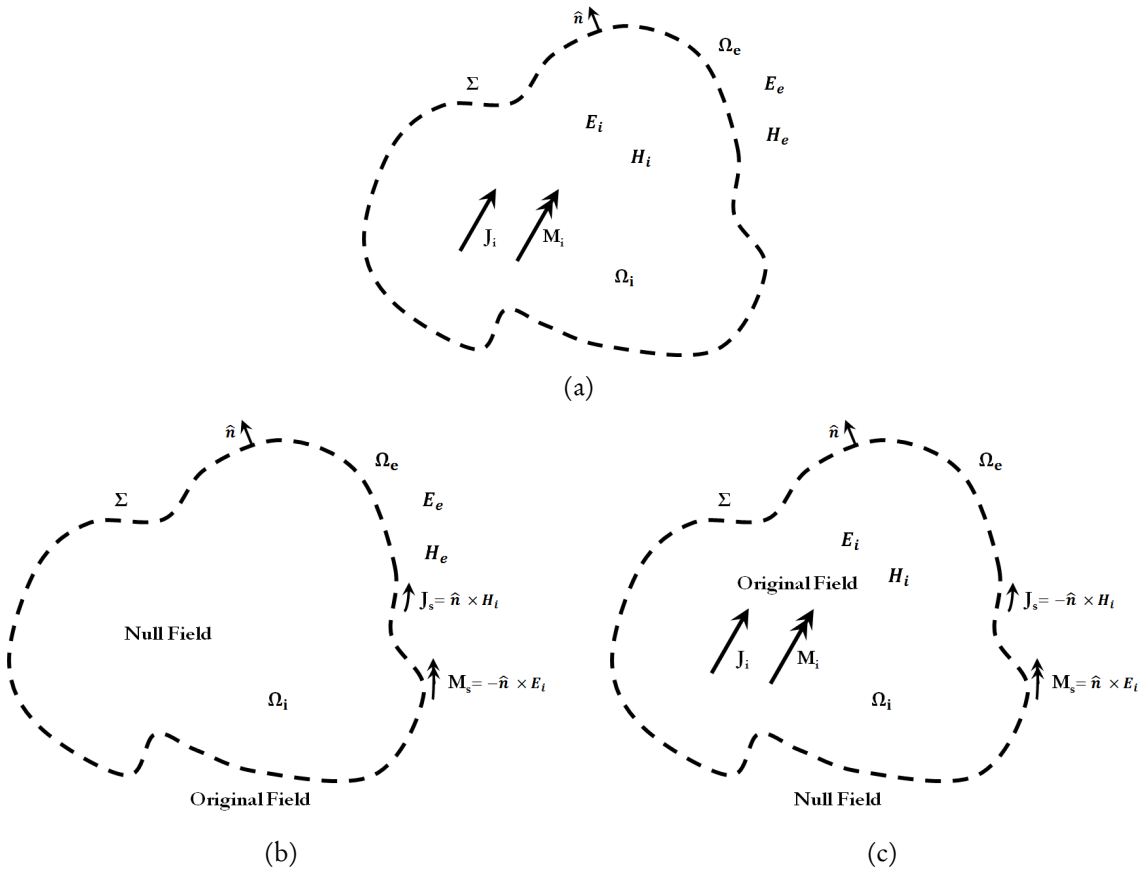

Figure 3.2 An illustration of the field Equivalence Principle. (a) The original problem containing sources in Ω_i and an arbitrary mathematical surface Σ dividing Ω_i and Ω_e. (b) Equivalence for the external problem. (c) Equivalence for the internal problem. Note the establishment of the null fields in these cases.

where $\underline{\boldsymbol{G}}(\boldsymbol{r}, \boldsymbol{r'})$ is the dyadic Greens function between observation point $\boldsymbol{r}$ and source point $\boldsymbol{r'}$, $\boldsymbol{p}^*$ is the conjugate of the source amplitude and $\boldsymbol{E_{TR}} = \mathscr{F}\{\boldsymbol{\mathcal{E}}_{TR}\}$. This result is important because it shows that only the propagative part of the radiated signal is effectively refocused. Therefore we can conclude that the time-reversed field can propagate thanks to the invariance of the Helmholtz equation by time reversal.

For the propagation to be effective in a time-reversal cavity, the current distributions (on the TRMs) associated to the time-reversed field must be determined. The equivalent surface principal was first stated by Love and Mc. Donald [153] and allows the determination of the currents distribution needed for an effective time reversal process. It shows that it is possible to find an equivalent surface Ω_e over which the distributed electric and magnetic currents express a radiation field taking place inside the surface. The conjugate of this distribution corresponds to the currents needed on the cavity to obtain refocusing after a time-reversal process.

When considering a magnetic $\boldsymbol{M_i}$ and electric current distribution $\boldsymbol{J_i}$ in volume Ω_i, the Love's equivalent principal state that there exists equivalent magnetic $\boldsymbol{M_s}$ electric $\boldsymbol{J_s}$ surface currents on the Σ surface surrounding Ω_i that generate the same electromagnetic field distribution in the outer region to Σ (Figure 3.2). At the same time the equivalent currents generate a null field distribution within Σ. Equivalence is obtained between the two configurations for electric currents $\boldsymbol{J_s}$ and agnetic $\boldsymbol{M_s}$ given by:

$$\begin{cases} \boldsymbol{J_s} = \hat{\boldsymbol{n}} \times \boldsymbol{H_i} \\ \\ \boldsymbol{M_s} = -\hat{\boldsymbol{n}} \times \boldsymbol{E_i} \end{cases} \tag{3.3}$$

where $\hat{\boldsymbol{n}}$ is a unit normal vector directed from Σ towards Ω_e. $\boldsymbol{H_i}$ and $\boldsymbol{E_i}$ are the magnetic and electric fields impacting the Huygens surface Σ. It is also possible to find equivalent magnetic and electric surface currents that generate a null field in Ω_e and the same electromagnetic field distribution within Ω_i. The equations then become (see Figure 3.2c):

$$\begin{cases} \boldsymbol{J_s} = -\hat{\boldsymbol{n}} \times \boldsymbol{H_i} \\ \\ \boldsymbol{M_s} = \hat{\boldsymbol{n}} \times \boldsymbol{E_i} \end{cases} \tag{3.4}$$

The Huygens principle differs when considering a time reversal process. The equivalent sources must generate the time-reversed version of the spatio-temporal field distribution generated by Σ in the region Ω_i and a null field in region Ω_e (see Figure 3.2). The time symmetry property of the Helmholtz equation enables to show that the equivalent current distributions $\boldsymbol{J_s}^*(\boldsymbol{r}, \omega)$ and $\boldsymbol{M_s}^*(\boldsymbol{r}, \omega)$ can generate the time-reversed version of the field in region Ω_i. The equivalence theorem on a surface is thus necessary for a time reversal process in order to define sources that allow the generation of the time-reversed field distribution.

In practice, a time-reversal cavity is impossible to realise since the space between TRMs must be of $\lambda/2$ or less in order to collect enough information to appropriately refocus the wave, meaning that an important number of antennas is needed. In the following section, we show the interest of complex propagation media for time-reversal purposes.

3.1.3 Time Reversal in Complex Propagation Mediums and Adaptation to Reverberation Chambers

Time-reversal in complex propagation media such as reverberation chambers or containing multiple scatterers cf. Figure 3.3 use the kaleidoscope effect presented in section 2.2.1 in order to reduce the

number of necessary TRMs for an effective time reversal process. In such a case one TRM will record not only the direct field but also all the reflected signals corresponding to image-sources and therefore collect more information needed for a good TR refocusing. In the most extreme case, only one antenna will be necessary for a good refocusing if the number of reflection is sufficient. In this section we shall present time reversal focusing properties when considering and a complex propagation media and its adaptation to a reverberation chamber. Time-reversal in complex propagation media such as reverberation chambers or containing multiple scatterers cf. Figure 3.3 use the kaleidoscope effect presented in section 2.2.1 in order to reduce the number of necessary TRMs. The kaleidoscopic effect acts as a virtual random phased array [154]. In this case one TRM will record not only the direct field but also all the reflected signals corresponding to image-sources and therefore collect more information needed for a good TR refocusing. In the most extreme case, only one antenna will be necessary for a good refocusing if the number of reflection is sufficient. In this section we shall present time reversal focusing properties when considering and a complex propagation media and its adaptation to a reverberation chamber.

The focal spot benefits from the presence of scatterers. Indeed, resolution is improved when using a time-reversal process in a multiple scattering media since the TRMs receive impulse responses containing information from the multiple reflections taking place in the scattering media allowing a virtual increase of the TRM antenna aperture [155]. The resolution is thus optimized for a similar configuration between free-space propagation when the scatterers are placed between TRMs and the source [156]. The multipath propagation taking place in the media allows super-resolution of the focusing wave[157, 158]. In such a case $\mathrm{Im}\{\underline{\boldsymbol{G}}(\boldsymbol{r},\boldsymbol{r'})\}$ can be sharper than in homogeneous medium. The main effect of the micro structured medium is to modify the effective wavelength (homogenization result) [159, 160].

At least two phenomena can enhance resolution:

- A locally strongly scattering medium can change the effective wavelength,
- an extended scattering medium can enhance the directional diversity.

In both cases statistical stability can be an issue (broadband sources and/or large mirrors can bring stability).

In the following two sections, the principles of RT in heterogeneous environments by studying the focus on the spatial and temporal focusing properties.

Spatial Focusing Properties

Figure 3.3 represents the propagation of waves in a high-order scattering media. The source position will be noted $\boldsymbol{r_1}$ and the position N TRMs will be noted by $[\boldsymbol{r_{p1}},\ldots,\boldsymbol{r_{pn}}]$. The electric field measured at the l-th TRM coming from the source will be noted $\boldsymbol{E}(\boldsymbol{r_{pl}},\boldsymbol{r_1},\omega)$. The source is considered to be a point-source having a current density distribution of $\boldsymbol{J_s}(\boldsymbol{r_1},\omega)$. The fields measured by the source antenna coming from the l-th TRM is noted $\boldsymbol{E}(\boldsymbol{r_1},\boldsymbol{r_l},\omega)$and the current density of the point source TRMs are $\boldsymbol{J_{pl}}(\boldsymbol{r_{pl}},\omega)$.

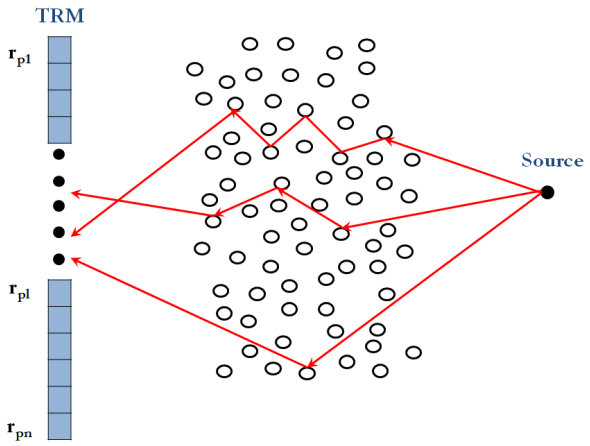

Figure 3.3 Time reversal Process (First Phase) of a emitted signal from a source using N TRMs in a complex propagation media.

The time-reversed signal injected in the l-th MRT allows the back-propagation of the wave in the complex media and a spatial refocusing of the wave. The current density is given by:

$$\boldsymbol{J_{RT\ pl}}\left(\boldsymbol{r_{pl}},\omega\right)=\boldsymbol{E}\left(\boldsymbol{r_{pl}},\boldsymbol{r_1},\omega\right)\delta\left(\boldsymbol{r}-\boldsymbol{r_{pl}}\right) \tag{3.5}$$

The expression of the time-reversed field emitted by one TRM and received on the other side of the scattering media at $\boldsymbol{r_2}$ is:

$$\boldsymbol{E_{RT_i}}\left(\boldsymbol{r_2},\omega\right)=\boldsymbol{E}^{*}\left(\boldsymbol{r_1},\boldsymbol{r_{pl}},\omega\right)\boldsymbol{E}\left(\boldsymbol{r_2},\boldsymbol{r_{pl}},\omega\right) \tag{3.6}$$

The field at $\boldsymbol{r_2}$ will thus be a summation of the fields produced by all the TRMs:

$$\boldsymbol{E_{RT}}\left(\boldsymbol{r_2},\omega\right)=\sum_{l=1}^{N}\boldsymbol{E_{RT_i}}\left(\boldsymbol{r_2},\omega\right)=\sum_{l=1}^{N}\boldsymbol{E}^{*}\left(\boldsymbol{r_1},\boldsymbol{r_{pl}},\omega\right)\boldsymbol{E}\left(\boldsymbol{r_2},\boldsymbol{r_{pl}},\omega\right) \tag{3.7}$$

Expression (3.7) is an estimator of the spatial-correlation given by:

$$W\left(\boldsymbol{r_2},\boldsymbol{r_1},\omega\right)=\left\langle\boldsymbol{E}^{*}\left(\boldsymbol{r_1},\boldsymbol{r_{pl}},\omega\right)\boldsymbol{E}\left(\boldsymbol{r_2},\boldsymbol{r_{pl}},\omega\right)\right\rangle \tag{3.8}$$

$\langle\ \rangle$being an ensemble average. The thinnest dimension of the focal spot will be constrained by correlation function of the complex media. As mentioned previously, super-resolution can thus be

sharper than in homogeneous media. This relationship between spatial focusing and correlation function also exists for diffuse fields. Spatial-correlation function are equal to $\frac{\sin(\boldsymbol{k}.(\boldsymbol{r_2}-\boldsymbol{r_1}))}{\boldsymbol{k}.(\boldsymbol{r_2}-\boldsymbol{r_1})}$ [161] the wave-number is invariant in reverberation chambers so that the focal spot is the same than in free-space for a time-reversal cavity [162]. There is no super-resolution phenomena when time-reversal is used in reverberation chambers. The focal spot is then limited by the diffraction limit and its half-width dimension is equal to $\lambda/2$ where λ is the wavelength corresponding to the central frequency. Still, using a reverberation chamber or a complex propagation media allows to considerably reduce the number of MRT necessary to obtain an efficient refocusing [163]. In the following, we shall present the time refocusing properties of a time-reversal process in complex propagation media.

Time Focusing Properties

Now lets consider the contribution of multi-paths environments in improving time-focusing. The notations used for the positioning of the source and TRMs in the previous section will be reused. However here, we consider the impulse response between the source S and the l-th TRM noted $h(\boldsymbol{r_1}, \boldsymbol{r_{pl}}, t)$. The source transmits a pulse $x(t)$in the first phase, its response is recorded by the TRM l. If we use the model presented in (2.1) for the impulse response between $\boldsymbol{r_{pl}}$ and $\boldsymbol{r_1}$, the impulse response recorded by the l-th TRM coming from the source can be written as follows:

$$h(\boldsymbol{r_{pl}}, \boldsymbol{r_1}, t) = \sum_{k=0}^{\infty} A_k \delta(t - t_k) \tag{3.9}$$

Where, as in section (2.1), the impulse response is modelled as a series of echoes coming from the multiple scattering and reflections in the media. Part of those reflections are recorded by the different TRMs. The signal recorded by the TRMs can thus be expressed as:

$$s(t) = x(t) \otimes h(\boldsymbol{r_{pl}}, \boldsymbol{r_1}, t) \tag{3.10}$$

During the second phase, a time-reversed wavefront is generated focusing on the punctual source. The signal $y(t)$ re-emitted by the TRMs is:

$$y(t) = x(-t) \otimes h(\boldsymbol{r_{pl}}, \boldsymbol{r_1}, -t) \tag{3.11}$$

The signal $z(t)$ arriving back on the source coming from TRM l is thus equal to:

$$z(t) = x(-t) \otimes h(\boldsymbol{r_{pl}}, \boldsymbol{r_1}, -t) \otimes h(\boldsymbol{r_1}, \boldsymbol{r_{pl}}, t) \tag{3.12}$$

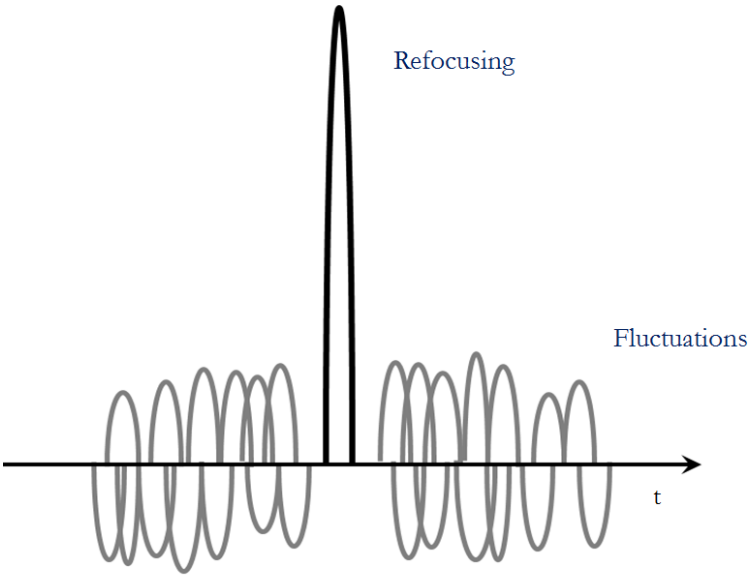

Figure 3.4 Temporal focusing and inherent fluctuations of time reversal

The media being reciprocal the impulse response $h\left(\boldsymbol{r_{pl}}, \boldsymbol{r_1}, t\right)$ is equal to $h\left(\boldsymbol{r_1}, \boldsymbol{r_{pl}}, t\right)$. Using this property and by replacing the impulse response by its model one can obtain:

$$z\left(t\right) = x\left(-t\right) \otimes \left(\sum_{k=0}^{\infty} A_k \delta\left(-t + t_k\right)\right) \otimes \left(\sum_{j=0}^{\infty} A_j \delta\left(t - t_j\right)\right) \tag{3.13}$$

In reality the number of reflections is not infinite even if very important otherwise the energy would be infinite, we note N_e this number. When expanding the two sums, we obtain:

$$z\left(t\right) = \underbrace{\sum_{k=0}^{N_e} A_k^2 x\left(-t\right)}_{\text{Focusing part}} + \underbrace{\sum_{k \neq j}^{N_e} A_k A_j x\left(t + t_k - t_j\right)}_{\text{Fluctuations}} \tag{3.14}$$

As we can see from the equation above the correlation product corresponding to the refocusing of the wave can be divided in two. The echoes interfere constructively at focusing time giving the first part of the equation $\sum_{k=0}^{N_e} A_k^2$. Figure 3.4 is a graphical representation of equation (3.14). Outside of the focusing time window the echoes sum incoherently and their fluctuations arise. Equation (3.14) also shows that summing in phase an important number of multipath echoes maximizes the amplitude of the coherent signal. Moreover, an increase of multipath propagation also increases the decorrelated summation allowing a decrease of the fluctuation level. This small derivation gives a

better understanding as to why complex propagations allow good performances when considering time-reversal experiments. Time Reversal works all the better (resolution enhancement) as the clutter is important. The main physical reason is that TR exploits multi-pathing which enhances the directional diversity. As shown in this section, not all the energy from the time-reversed signal is effectively refocused. Part of the energy is lost due to the intrinsic fluctuations taking place in a time reversal process. In the following section a further study of the energy effectively refocused as well as the energy lost in the fluctuations will be undertaken.

Starting back from equation (3.12) and by summing over all of the N TRMs when using the reciprocity theorem, it is possible to find that:

$$z(t) = \sum_{l=1}^{N} x(-t) \otimes h(\boldsymbol{r_{pl}}, \boldsymbol{r_1}, -t) \otimes h(\boldsymbol{r_{pl}}, \boldsymbol{r_1}, t) = x(-t) \sum_{i=1}^{N} R_{ii}(t) \tag{3.15}$$

where $R_{ii}(t) = \sum_{l=1}^{N} h(\boldsymbol{r_{pl}}, \boldsymbol{r_1}, -t) \otimes h(\boldsymbol{r_{pl}}, \boldsymbol{r_1}, t)$ is the autocorrelation of all the impulse responses. Signal $z(t)$ is thus a non-exact replica of signal $x(-t)$.

Spatial Correlation In MRSC

As we have seen in the previous subsection, spatial correlation functions are of great importance to assess time reversal focusing quality since the spatial focus spot is related to those functions. Spatial coherence also determines the number of independent measurements that can be made at different positions in the cavities. The spatial correlation function between two points $\boldsymbol{r_1}$ et $\boldsymbol{r_2}$ of the cavity can be expressed with this statistical approach. The correlation functions can be written as functions of the distance r as follows [112, 161, 164]:

$$\rho(r) = \frac{\langle \boldsymbol{E}(\boldsymbol{r_1}) \cdot \boldsymbol{E^*}(\boldsymbol{r_2}) \rangle}{\left[\left\langle |\boldsymbol{E}(\boldsymbol{r_1})|^2 \right\rangle \left\langle |\boldsymbol{E}(\boldsymbol{r_2})|^2 \right\rangle \right]^{1/2}} \tag{3.16}$$

where $\langle\ \rangle$ indicates a ensemble averaging. This expression is found to be [112]

$$\rho(r) = \frac{\sin(kr)}{kr} \tag{3.17}$$

where $r = \|\boldsymbol{r_2} - \boldsymbol{r_1}\|$ The correlation function can also be expressed for longitudinal components of the field:

$$\rho_l(r) = \frac{3}{(kr)^2}\left[\frac{\sin(kr)}{kr} - \cos kr\right] \tag{3.18}$$

and tangential components of the field:

$$\rho_t(r) = \frac{3}{2}\left\{\frac{\sin(kr)}{kr} - \frac{1}{(kr)^2}\left[\frac{\sin(kr)}{kr} - \cos(kr)\right]\right\} \tag{3.19}$$

It is then possible to find a direct relation between tangential and longitudinal correlation:

$$\rho(r) = \frac{1}{3}\left[2\rho_t(r) + \rho_l(r)\right] \tag{3.20}$$

To finish, there also exists a mixed correlation function between electric and magnetic field components:

$$\rho_m(r) = \frac{-3j}{2(kr)^2}\left[\sin(kr) - \cos(kr)\right] \tag{3.21}$$

3.2 Time-Reversal efficiency and performance

3.2.1 Efficiency of Reverberating Chambers

A parameter that provides a considerable amount of insight with regard to the overall operation of a chamber is the power gain, as a function of frequency, between a transmitting antenna inside the chamber and a receiving antenna/sensor inside the chamber. In this section, a first-order theoretical model for the chamber gain versus frequency is derived with the help of the Q_{net} models of the previous section. A calculation for the power transfer characteristic, or gain, of a chamber with a receiving antenna can be initiated from the definition of the gain in Equation 3.22 [95, 96].

$$G_{ant} = \frac{P_{out}}{P_{in}} \tag{3.22}$$

where G_{ant} is the gain of the chamber with receiving antenna, P_{in} is the power delivered to the chamber from the transmitting antenna and P_{out} is the power available to the receiving antenna from the chamber.

Next, Equation 3.22 can be manipulated as follows:

$$G_{ant} = \frac{\omega U/P_{in}}{\omega U/P_{out}} = \frac{Q_{net}}{Q_{ant}} \tag{3.23}$$

If all antennas are uncorrelated and have the same characteristics P_{out} can be re-written $N_r P_{ant}$ where N_r is the number of receiving antennas and P_{ant} is the power available on one antenna.

Equation 3.22 becomes:

$$G_{ant} = \frac{\omega U/P_{in}}{\omega U/\left(N_r P_{ant}\right)} = N_r \frac{Q_{net}}{Q_{ant}} \tag{3.24}$$

Q_net also varies when adding antennas inside the cavity. Formulation thus becomes:

$$G_{ant} = \frac{\left(\frac{N_{ant}}{Q_{ant}} + \frac{1}{Q_{walls}}\right)^{-1}}{Q_{ant}/N_r} = \frac{N_r}{N_{ant} + \frac{Q_{ant}}{Q_{walls}}} \tag{3.25}$$

where N_{ant} is the total number of antennas inside the chamber. The experimental case where two antennas one transmitting and one receiving are placed in the chamber is presented in 4.2.1. However some insight can be obtained when examining the theoretical formulation.

When $N_r = 1$ and $N_{ant} = 2$ the antenna gain becomes:

$$G_{ant} = \frac{\left(\frac{2}{Q_{ant}} + \frac{1}{Q_{walls}}\right)^{-1}}{Q_{ant}} = \frac{1}{2 + \frac{Q_{ant}}{Q_{walls}}} \tag{3.26}$$

which yields when replacing by their theoretical expressions:

$$G_{ant} = \frac{1}{2 + \frac{4}{3}\sqrt{\frac{2\mu_r}{\mu_0 \sigma}}\frac{S}{c^3 \pi}\omega^{2.5}} \tag{3.27}$$

in the case the impedance mismatch and antenna efficiency are taken to be equal to unity. For this configuration the $\omega^{2.5}$ dependence in the second term of the denominator of Equation (3.27) can be attributed to the loading of the receiving antenna decreasing with ω^3 combined with the chamber wall loss increasing with $\omega^{1/2}$.

The ratios of quality factors of (3.26) can be rewritten as the following power ratio:

$$\frac{Q_{ant}}{Q_{walls}} = \frac{P_{walls}}{P_{out}} \tag{3.28}$$

Here, $P_{out} \propto \omega^{-3}$ and $P_{walls} \propto \omega^{1/2}$. At low frequencies, however, the first term in the denominator of Equation (3.27) dominates. Thus there are two distinct frequency regions. The transition point between these two regions can be calculated by setting the second term in the denominator equal to unity and solving for the corresponding value of ω. There is thus a transition point where below $P_{out} > P_{walls}$ so that power extraction from the chamber by the receiving antenna dominates over power loss to the chamber walls. This is an important notion that is necessary for the conception of a prototype as will be shown in the last chapter of this work.

3.2.2 Contrast and self-averaging properties of time-reversal in complex media

Another property that was not mentioned previously is time-reversal self-averaging. Indeed up until now, only the focusing quality of a time-reversal process for impulse signals were considered. What happens when a continuous or a slowly varying signal is sent in a complex media? No spatio-temporal focusing is obtainable when considering complex propagation medias. If a monochromatic signal is sent backwards through a RC, it will propagate but it will never converge thus limiting the time-reversal process to signals having a sufficient bandwidth when considering complex media. In a time-reversal cavity such as the one presented in Figure 3.1 it would be possible however to focus such waves. Therefore, when using a limited number of TRMs in a complex media there is a loss of information that leads to a limitation of the technique for signals with a certain bandwidth. Bandwidth is thus an essential parameter when considering a time-reversal process. In what follows, a formal derivation will allow to model the importance of bandwidth on the focusing quality and the signal-to-noise ratio of time-reversal in complex media.

The first observation of the influence of bandwidth on the SNR in complex media were given in [165]. This paper also showed that spatial or temporal expression of the signal-to-noise ratio are the same. At the time Arnaud Derode and Mathias Fink explained the phenomenon in terms of "grains of information". In their model, the impulse response is seen as a succession of small grains of information lasting δt decorrelated from one another. δt being the time of the initial impulse. Arnaud Derode showed that the amplitude of the peak after refocusing is proportional to the summation of the N grains of information contained in the time-reversed impulse signal giving $N = T/\delta t$, where T is the time length of the time-reversed signal. On the other hand, the fluctuations come from an incoherent summation of these grains. The spatial or temporal SNR thus varies as $\sqrt{N}$. This model is only valid for diffuse regimes, when the information grains are uncorrelated otherwise if the grain of information is always the same, refocusing will not be possible.

It is also possible to make the same type of model in the frequency domain. The ratio then becomes $\sqrt{\frac{\delta\nu}{\delta\omega}}$ where $\delta\omega$ is the correlation or coherence bandwidth also noted B_c in Chapter 2.2.3 and $\delta\nu$ is the signal bandwidth.

To characterise self-averaging in time-reversal transmission let us consider the equivalent transfer function $G(\omega) = |H(\omega)|^2$ which is the Fourier transform of $R_{ii}(t)$ from equation (3.15). $G(\omega)$ is an equivalent transfer function. This equivalent transfer function is now real and positive, the main mechanism by which coherence was lost (the random phase-shifts) is now absent.

In order to simplify the model the focusing time will be taken at $t = 0$. The signal at focusing time is thus:

$$z(0) = \int_{B_t} G(\omega) X(\omega) d\omega. \tag{3.29}$$

As explained in 2.2.3 each coherence band can be considered independent. It is then possible to transform equation (3.30) in a discrete sum over the number of coherence bands noted N_c.

$$z(0) \simeq \sum_{i=1}^{N_c} \int_{B_c^i} G(\omega) X(\omega) d\omega. \tag{3.30}$$

Here the coherence bands B_c are considered identical which is a valid approximation the if the signal bandwidth considered are not very wide. Indeed, modal bandwidth varies very slowly with frequency. B_c^i is thus the i-th coherence band centred around frequency $\omega_i/2\pi$. The number of coherence bands is the signal bandwidth divided by the coherence bands $N_c = \left\lceil \frac{B_t}{B_c} \right\rceil$. The injected signal $X(\omega)$ is assumed to vary very slowly with frequency.

Using the notations

$$X_i = X(\omega_i) \tag{3.31}$$

$$G_i = 2\mathrm{Re}\left\{ \int_{B_c^i} G(\omega) d\omega \right\}, \tag{3.32}$$

Equation 3.30 can be approximated as:

$$z(0) = \sum_{i=1}^{N_c} X_i G_i \tag{3.33}$$

The value taken by $z(0)$ is a random function of the random transfer function $G(\omega)$. In order for $z(0)$ to be deterministic, it can be related to basic information about the cavity. This condition can

be expressed in statistical terms as

$$\sigma_z^2(0) = \left\langle \left[z\left(0\right) - \langle z(0) \rangle \right]^2 \right\rangle \tag{3.34}$$

The residual statistical dispersion of $z(0)$ can be used to measure the ability of time reversal in ensuring a proper transmission of a signal through a complex medium. We will consider the contrast [7]:

$$\Lambda_p = \frac{\langle z(0) \rangle^2}{\sigma_z^2(0)} \tag{3.35}$$

This metric is closely related to an SNR ratio in signal theory. The contrast in equation (3.35) is noted by a subscript p since it is measured at the refocusing time of the peak of the signal, for a pulse refocusing around $t = 0$. In such a case this measure is related at its instantaneous power. By replacing the expressions of (3.33) into (3.34) one obtains:

$$\sigma_z^2(0) = \sum_i X_i^2 \left\langle \left| G_i - \langle G_i \rangle \right|^2 \right\rangle + \sum_{i \neq j} X_i X_j \left\langle \left(G_i - \langle G_i \rangle \right) \left(G_j - \langle G_j \rangle \right)^* \right\rangle \tag{3.36}$$

The different terms of the summation can be considered weakly correlated since each term is function of its correlation bandwidth. The second term of (3.36) can thus be approximated by 0 simplifying into:

$$\sigma_z^2(0) = \sum_i X_i^2 \sigma_{G_i}^2 \tag{3.37}$$

where σ_{G_i} are the variances of the N_c iid random variables $\{G_i\}$. When dealing with large cavities, even for relatively large bandwidths with $B_T \gg B_c$, the statistical moments of the random function $G(\omega)$ can be expected to be independent of the frequency of observation, resulting in identical $\sigma_{G_i}^2$, $\forall i$. Therefore,

$$\langle z(0) \rangle = \overline{G}_i \sum_{i=1}^{N_c} X_i = N_c \overline{G}_i \overline{X} \tag{3.38}$$

and

$$\sigma_z^2(0) = \sigma_{G_i}^2 \sum_{i=1}^{N_c} X_i^2 = N_c \, \sigma_{G_i}^2 X_{rms}^2 \tag{3.39}$$

where $\overline{X}$ and X_{rms} are respectively the arithmetic and quadratic averages of $X(\omega)$ over B_T ; thus (3.35) gives [7]

$$\Lambda_p = \Lambda_{G_i} \frac{B_t}{B_c} \kappa^2 \tag{3.40}$$

where $\Lambda_{G_i} = \dfrac{\overline{G}_i^2}{\sigma_{G_i}^2}$ is the contrast of $G(\omega)$ sampled at frequency $\omega_i/2\pi$ and $\kappa = \dfrac{\overline{X}}{X_{rms}}$ is a shape factor giving $\kappa \leq 1$.

Equation (3.40) gives insight to some interesting properties of time-reversal transmissions. First of all, the received signal will be characterized by a decreasing uncertainty as the number of coherence bandwidths covered by the excitation signal increases. This is what is referred as the self-averaging property. During a time-reversal transmission the N_c degrees of freedom available are excited in a coherent way, i.e., in phase, since eventual random phase-shifts introduced by $H(\omega)$ are set to zero by phase-conjugated excitations. Second, (3.40) shows what is the role of the statistics of the propagation medium. For the case of a cavity in a diffuse-field configuration, $H(\omega)$ is well modelled by a complex Gaussian process with iid real and imaginary parts; hence, $G(\omega)$ can be modelled as an exponential random process, i.e., $\Lambda_{G_i} = 1$. The shape of the signal to be transmitted also plays a part, while for pulse-like signals $\kappa \simeq 1$, for more complex shapes with their energy not concentrated around the time $t = 0$ but spread over a larger time supports, the final contrast will be found to be lower than expected.

The reason for the absence of coherent transmission is not the fact that $x(t) \simeq 0$ at the time of sampling; even with a non-negligible coherent signal, it could not be observed at the receiving end, because of the random-walk process. The need for wideband signals presented in acoustics is actually not a criteria. As proven by this analysis, the actual criteria is to ensure $B_T/B_c \gg 1$. In the case of reverberating media, the final bandwidth B_T can be narrow enough to regard the signal $x(t)$ as quasi-harmonic; as an example, for a standard electromagnetic reverberation chamber, at 1 GHz, with $Q \simeq 10^4$, the coherence bandwidth would be of the order of 100 kHz, thus resulting in at least 100 degrees of freedom when applying a transmitting signal with $B_T/f_c \simeq 1\%$. The resulting peak contrast Λ_p would be around 20 dB, thus a fairly clear transmission.

3.2.3 Coherent-transmission efficiency through reverberating media with multiple antennas input or output

In this subsection we will analyse the peak-contrast in reverberation chambers and express the case where multiple transmission antennas are used as well as the case where the signal is refocused on multiple antennas.

Single-Source Refocusing

Here we present a more general approach of refocusing property of time reversal by assessing the ability of time-reversal transmissions to reproduce specific pulsed shapes at the receiver; the transmission of data is an example of an application where it is not sufficient to generate a maximum in the instantaneous power observed at the receiver. In this respect, an alternative analysis is presented for the case of a reverberating cavity [7, 81], where the received signal $z(t)$ was described as the superposition of a coherent term containing $x(t)$ and a residual noise $n(t)$

$$z(t) = \alpha x(t) + n(t) \tag{3.41}$$

For the sake of simplicity, it will be assumed that $x(t)$ reaches its peak intensity at $t = 0$. We can then introduce the following definition of the peak contrast valid for a classic time-reversal process when the refocusing noise presents an exponential decay [7],

$$\Lambda_p = \frac{\alpha^2 x(0)^2}{\max\limits_t \langle n^2(t) \rangle} \tag{3.42}$$

Optimal transmission through time reversal therefore requires that for a given input energy at the transmitter end, the fraction of energy at the receiver maintaining a coherence with $x(t)$ be maximized. Here we thus consider the ratio between the energy of the coherent part of the received signal and the total energy value of the residual part rather than just assessing the ratio between the signal at $t = 0$ over the rms value of the residual late-time fluctuations as done in (3.40):

$$\Lambda = \frac{\mathscr{E}_c}{\mathscr{E}_n} \tag{3.43}$$

The shape of the template has a non-negligible impact on the performance of time reversal and for its effect to be accounted, we introduce shape factors for the pulse [166]

$$\chi_x = \frac{|x(0)|^2}{\mathscr{E}_x} \tag{3.44}$$

and the shape factor for the fluctuations

$$\chi_n = \frac{\max_t \langle n^2(t) \rangle}{\mathscr{E}_n} \tag{3.45}$$

knowing that $\mathscr{E}_c = \alpha^2 \mathscr{E}_x$, a relationship between energy and peak contrast Λ_p can thus be obtained:

$$\Lambda_p = \Lambda \frac{\chi_x}{\chi_n} \tag{3.46}$$

the original definition of contrast (3.40) can be related to Λ by approximating the residual part with an exponential profile, with a time-constant $\overline{Q}/\omega_c$, where $\overline{Q}$ is the average composite quality factor of the cavity. This relation was shown to give [7, 81]:

$$\Lambda_p = \frac{\overline{Q}}{\pi} \frac{B_T}{f_c} \kappa^2 \Lambda \tag{3.47}$$

The value of Λ depends on the Greens functions of the media and are independent of signals shape and bandwidth. This contrast energy, can be shown to be close to one for a diffusive medium [81]. Hence, the best-case performance of a time-reversal transmission system will be limited to half the received energy following a time-evolution set by the original signal $x(t)$, while at least the same amount of energy will be wasted in fluctuations that have no use. The result is a coherent-transmission efficiency limited to $1/2$. The coherent energy is thus limited during a time-reversal process. Equation (3.46) can be approximated when neglegting the shape factor byby [7]:

$$\Lambda_p \simeq \Lambda \frac{T_n}{T_x} \simeq \Lambda \frac{B_T}{B_c} \tag{3.48}$$

where T_x is the half-power duration of $x(t)$ and T_n is the time-domain support of the incoherent part related to the relaxation time of the chamber. By comparing equations (3.47) with (3.48) it appears that $B_c = \pi B_m$ as stated in the second chapter.

Multiple-Source configurations

In the case there are multiple transmission antennas the energy contrast is multiplied by [166]:

$$D\left(N_{ant}, \overline{\mu}_r\right) = \frac{N_{ant}}{1 + \left(N_{ant} - 1\right) \overline{\mu}_r} \tag{3.49}$$

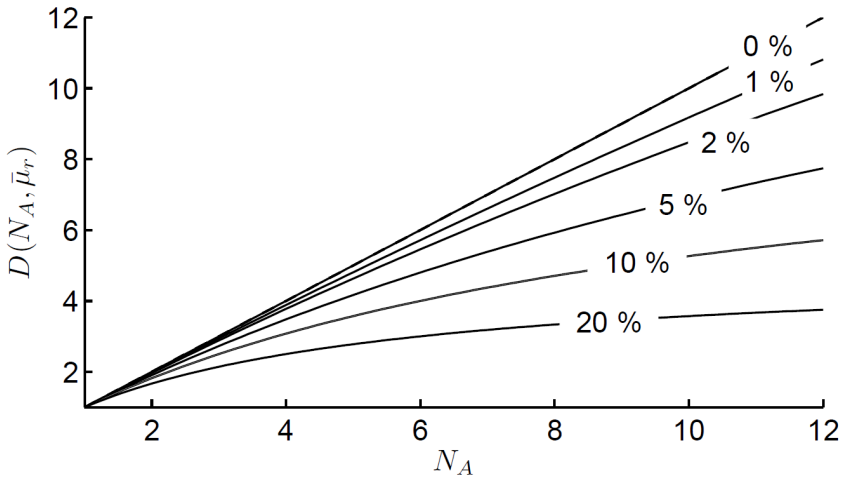

Figure 3.5 The diversity factor $D\left(N_{ant}, \overline{\mu}_r\right)$ as a function of the number of sources N_{ant} and the average spatial degree of coherence $\overline{\mu}_r$ (in percent units over each line) [166].

The function $D\left(N_{ant}, \overline{\mu}_r\right)$ can have a multiplicative effect on the energy contrast of a single-source configuration, since (3.49) implies that $D\left(N_{ant}, \overline{\mu}_r\right) \geq 1$. In the ideal case of $\overline{\mu}_r = 0$, we expect $D\left(N_{ant}, \overline{\mu}_r\right) = N_{ant}$, resulting in a potentially dramatic improvement of the energy contrast. However this case is in practice never achievable. In the more realistic case of $\overline{\mu}_r$, the trend of $D\left(N_{ant}, \overline{\mu}_r\right)$ as a function of N_{ant} and $\overline{\mu}_r$ is show in Figure 3.5. It can be observed that as the number of sources increases, the incremental improvement in the overall energy contrast decreases with N_{ant}. Moreover, as $N_{ant} \to \infty$, there exists a maximum attainable improvement given by

$$\lim_{N_{ant} \to \infty} D\left(N_{ant}, \overline{\mu}_r\right) = \frac{1}{\overline{\mu}_r} \tag{3.50}$$

Even a relatively weak average spatial coherence leads to an upper limit to the improvement: $\overline{\mu}_r = 0.1$, usually regarded as a negligible level of coherence, directly leads to a maximum improvement of a factor 10 which, though not negligible, implies that it is not possible to do better than the performance that would be obtained with 10 independent antennas in an idealised setup.

The maximum coherent energy is thus limited and depends on the statistical properties of the media. The peak-contrast is the product of the energy contrast by the shape factor of the impulse which is not limited by the statistics of the media. Large bandwidths thus allow to increase the peak-contrast. Howeve, in practice the bandwidth is limited by electronics and the number of TRMs is limited. The statistics of the media are thus quite important to characterize the peak-contrast.

Contrast when refocusing over multiple antennas

In the past few years, time-reversal has been used to address multiple output antennas with a single input [39, 40, 167]. As shown in the previous section, when the number of receiving antenna is increased the efficiency decreases. The more antennas are present in the chamber the less efficient the chamber. Taking back equation (3.25) her one can easily see that the higher the frequency the lower the efficiency also, meaning that to obtain a gain in refocusing the chamber must be at the limit of the overmoded regime. Also recalling equation (3.47) we have

$$\Lambda_p = \frac{\overline{Q}}{\pi}\frac{B_T}{f_c}\kappa^2\Lambda \tag{3.51}$$

When adding antennas the new quality factor will change and $\overline{Q}$ will diminish especially in low frequency where the antennas are supposed to be the dominating loss mechanism. However the contrast Λ_p does not decrease by a factor $1/N_{ant}$ so that the number of contributions of the antennas does not result in a proportionality factor.

As mentioned previously only half of the total energy will be coherent. Therefore, in the best case scenario when considering refocusing on multiple sources that energy will be equally divided between N_r the number of receiving antennas giving then $1/\left(2N_r\right)$. The other factors of Λ_p will not change except the composite quality factor. If the antennas are completely independent from each other, recalling equation (3.43) the expression becomes when adding antennas:

$$\Lambda = \frac{N_{ant}\,\mathscr{E}_c}{N_{rec}\,\mathscr{E}_n}, \tag{3.52}$$

where N_{ant} is the total number of antennas and N_{rec} is the number of receiving antennas. The peak-constrast thus becomes:

$$\Lambda_p = \frac{\overline{Q}}{\pi}\frac{B_T}{f_c}\kappa^2\frac{N_{ant}}{N_{rec}}\Lambda \tag{3.53}$$

where $\overline{Q}$ is the quality factor when adding antennas.

However, in practice there will be added fluctuations due to cross factors between antennas. Not all the coherent energy will be indeed refocused. A simple derivation allows to model this phenomenon. In such a case, the refocused signal $z_k(t)$ on the k-th antenna can be expressed as:

$$z_k(t) = \sum_{m=1}^{N_r} a_m h_m^*(-t) \otimes h_k(t) \tag{3.54}$$

$$z_k(t) = \underbrace{a_k R_{kk}(t)}_{\text{Useful Part}} + \underbrace{\sum_{m \neq k} a_m R_{m,k}(t)}_{\text{Added Fluctuations}} \tag{3.55}$$

However, as we have shown in the previous chapter, the effect of loading a reverberation chamber with antennas does not affect the quality factor so much even at low frequency, explaining the good focusing abilities of a time-reversal process having multiple refocusing antennas.

3.2.4 Works on High-Power using TR Techniques

The spatio-temporal focusing properties presented in this section validate time-reversal as a potential amplification system or TRAS (Time Reversal Amplification System).

Indeed, when a long signal is focused by time reversal, pulse compression can result in a gain in the amplitude of the focused signal. The first study on this topic was performed by Montaldo et al. in 2001 [168]. Their goal was to generate an acoustic shock wave at the output of a waveguide. At first, a 2 ms pulse, at 1 MHz with a very large bandwidth of 75%, is generated by a source point S to the outside of the waveguide (Figure 3.6). The signals are recorded at the other end of the guide using 7 piezoelectric transducers constituting the Time- Reversal Mirror (TRM). Due to reflections from the walls of the waveguide, the signals received on the TRM possess a significant delay spread, here in the order of 2000 ms, or 1000 times the duration of the initial pulse. After retransmitting the time-reversed signal, a remarkable time compression is achieved at the source point S. The duration of the pulse generated after TR is identical to the initial pulse with the same shape and time of 2 ms. The key point to obtain large amplitudes is to retransmit the signal returned temporally with maximum power. The effects of spatial and temporal compressions then provide a pulse of high-amplitude. By comparing the signal after TR with that which would have been achieved without the guide (in free-water), remarkable gains (about fifteen dB) were measured.

Further improvements on this technique were engaged by Matthieu Davy [38] and Hong [37] in electromagnetics by using opened cages in order to obtain refocusing on a particular position outside of the chamber. However, this is not the most efficient use of the cage since the quality factor of the cage will be degraded and thus the room efficiency. Moreover, the opening acts as an antenna and has to be parametrised in order to obtain the best refocusing. In the second chapter, we saw that the reverberation chambers dimensioning is of prime importance when considering a TRAS since a trade-off between the power received by the output antennas and the power injected must also be considered not only the quality factor that in the case of reverberation chambers increases with frequency.

However, no studies exists as to the performance of a TRAS and their variation with the properties of the cage, the type of signal to refocus nor the gain that can be obtained by simple time-reversal

or with signal-processed time reversal such as 1-bit. In the studies that follows we will present the efficiency of time-reversal compared to a classic use of a reverberation chamber. In what follows, we shall first present the power-efficiency improvement when considering a time-reversal process compared to the classical use of time-reversal.

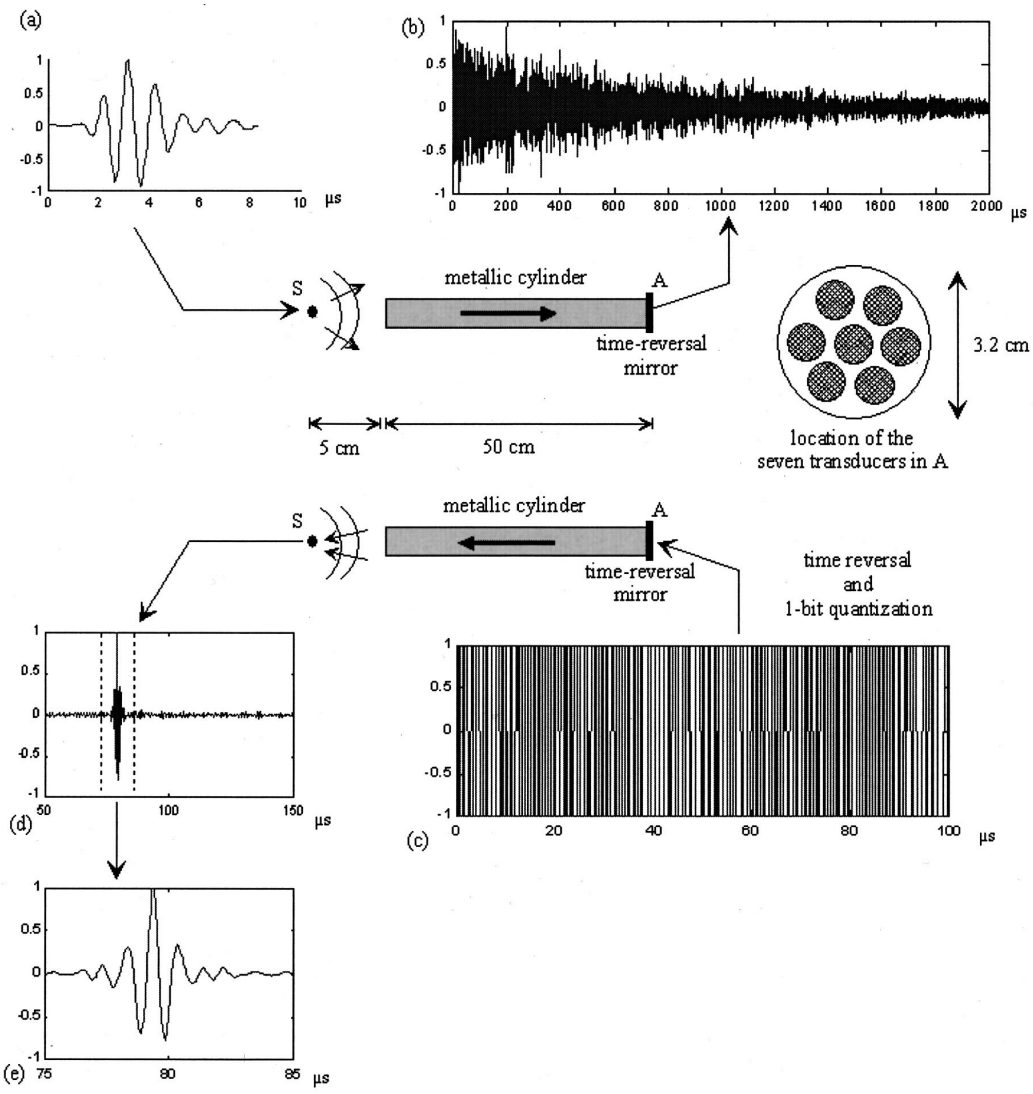

Figure 3.6 Experimental demonstration of 1-bit time reversal in a metallic waveguide. (a) The acoustic source transmits a pulsed signal in water. (b) Normalized signal received on one of the seven transducers in A at the end of the 50-cm-long, 3.2-cm-diam metallic waveguide; the signal spreads over more than 2 ms. (c) The signal is time reversed, 1-bit quantized and retransmitted from the same transducer in A. For presentation reason, only the first 100 ms are plotted. (d) Normalized signal obtained in S after 1-bit time reversal from the seven transducers in A and back propagation through the guide. (e) Zoom of the time reversed signal between the dashed lines: the time-reversed signal (e) is similar to the source signal (a) [168].

3.3 Improving Mode-Stirred Chambers Efficiencies and Reliability with Time-Reversal

One of Reverberation chambers (RCs) most recognised properties is their capability of converting harmonic signals into high-intensity fields, by creating a pool of stored electromagnetic energy, thanks to their relatively long time constants. The stored energy can reasonably be expected to be uniformly spread over the entire volume of the RC, thus allowing for an ideally global excitation of an equipment under test (EUT). Yet, this property also implies that, at each instant, only a portion of the energy injected into the RC interacts with the EUT. This observation is the starting point of our proposal for using time reversal (TR) as an alternative to harmonic or continuous-wave (CW) excitations.

In this section we study the ability of reverberation chambers in generating high-intensity field levels from relatively low-power input signals for the case of time-reversed signals. The statistical spread typical of time-harmonic excitations is shown to be dramatically reduced when considering a time-reversal process. The reliability of radiative tests is improved while limiting the need for a large number of independent realizations. Both methods are compared by forcing the two excitations input signals to display the same peak instantaneous power. Experimental results are provided, supporting the conclusions of our theoretical analysis. Studies of applications of TR to RCs are not new [81, 114, 169, 170], but they have been mainly concerned with demonstrating the possibility of producing focusing signals while propagating through non-anechoic media. We are rather interested in assessing how much TR can increase the peak intensity of the power used to stress an EUT. This section addresses this topic by analysing the conversion efficiency of an RC when using TR signals rather than standard harmonic ones. The problem is tackled from a theoretical point of view, in order to provide predictive tools for the design of TR excitations. The obtained results are then proven experimentally.

As mentioned previously, a fourth advantage exists when using time-reversal, namely the possibility of controlling the polarization of the resulting field, as proven in [171]. In practise, experiments are often limited by the peak-power that can be injected in the signal amplification module. The comparisons are therefore carried out by taking into account this fundamental limitation of power amplifiers, the maximum peak instantaneous power (PIP) they can handle. This constraint calls for an analysis different from that presented in [172] that was concerned with energy efficiency levels therefore requiring to model the highly fluctuating behaviour of RC-generated impulse signals. Only point-like focusing are considered herein.

3.3.1 Conversion Efficiencies

In this section an RC will be modelled as a linear system that converts an input signal $x(t)$, say a voltage, applied at the input port of an excitation antenna, into a vector electric field $\boldsymbol{e}(\boldsymbol{r}, t)$ measured within the RC at the position $\boldsymbol{r}$. The variable $\boldsymbol{r}$, will be dropped for the sake of brevity. The results derived here are valid for any $\boldsymbol{r}$ within the test volume, where a diffuse-field approximation holds. The

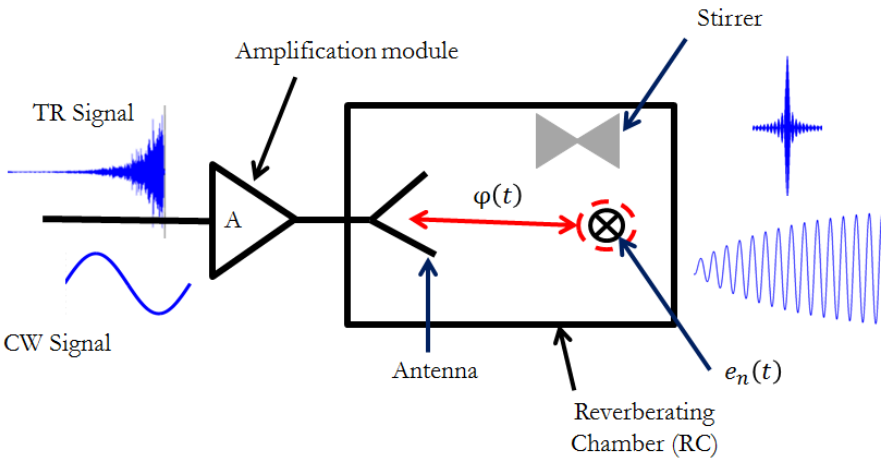

Figure 3.7 Diagram of the system used for the model, $\varphi(t)$ is an impulse response of the RC $e_n(t)$ is the field measured over direction n in the chamber

average composite quality factor Q of the RC will be considered to be a good estimate of the composite quality factors experienced over the bandwidth used, around a working frequency f_c. The average time constant of the RC will thus be defined as $\tau = Q/\pi f_c$. The field thus generated is expected to stress a portion of circuit in an EUT, which will "receive" the power $p_r(t)$ as a linearly-polarized antenna, i.e.,

$$p_r(t) = C_r \left[\boldsymbol{e}(t).\hat{\boldsymbol{q}}\right]^2 = C_r f^2(t) \tag{3.56}$$

where C_r represents the sensitivity of the receiver, assumed to be non-dispersive, while $\hat{\boldsymbol{q}}$ is the polarization-vector of the receiver. Similarly, we consider the input available power $p_i(t) = C_i x^2(t)$ applied at the antenna input port, with C_i a constant of units equal to a conductance. In order to generate the maximum radiated stress, the conversion efficiency should be maximized

$$\eta_S = \eta\left[x_S(t)\right] = \frac{\|p_r(t)\|_\infty}{\|p_i(t)\|_\infty} = \frac{C_r}{C_i}\frac{\left\|f_S^2(t)\right\|_\infty}{\left\|x_S^2(t)\right\|_\infty} \tag{3.57}$$

where the subscript S is used in order to distinguish different excitation signals. This conversion efficiency represents the power that is effectively refocused on the EUT after being injected in the antenna. There are two reasons for choosing the L_∞ norm. First, the output PIP stressing the EUT should be as high as possible. Second, this maximum should at the same time be generated by an input signal with the lowest PIP, in order to avoid any strain on power amplifiers and subsequent non-linear distortions or potential thermal stress. The $\hat{\boldsymbol{q}}$-aligned component of the electric field,

$f(t)$, is linearly related to the excitation signal through a transfer function $\Phi(\nu)$, such that $f(t) = \mathscr{F}^{-1}\{\Phi(\nu)X(\nu)\}(t)$, where $\mathscr{F}^{-1}\{\ \}$ is the inverse Fourier transform between the frequency variable ν and the time variable t. The function $X(\nu)$ is the Fourier spectrum of the excitation signal. The following derivations will assume excitation signals with spectra centred at the frequency f_c, covering the bandwidth $B_T = f_2 - f_1$.

Conversion efficiency for harmonic signals

In the case of a harmonic excitation of the room $x_{CW}(t) = A\ cos(2\pi f_c t)$ and thus the conversion efficiency is

$$\eta_{CW} = \frac{C_r}{C_i}\left|\Phi(f_c)\right|^2 = \frac{C_r}{C_i}W(\nu) \tag{3.58}$$

where $W(\nu) = |\Phi|^2$. In practice, the response of RCs is randomized by means of stirring techniques; as a result several realizations of $\Phi(\nu)$ can be generated and the resulting efficiency can take very different values. This point will be discussed further on.

Conversion efficiency for time-reversed signals

In the case of time-reversed excitations, the input signal is chosen to be

$$x_{TR} = g(t) \otimes \varphi(-t) = \mathscr{F}^{-1}\{\Phi^*(\nu)G(\nu)\}(t) \tag{3.59}$$

where $G(\nu)$ is the Fourier spectrum of the signal $g(t)$ chosen to stress the receiver; $\otimes$ stands for the convolution operator applied to the time variable. Any kind of signal can be chosen for $g(t)$, but time reversal has been demonstrated mainly with short pulses. The derivations computed here also show that better efficiencies are indeed obtained by choosing a $g(t)$ with the most compact support. Therefore, EUTs with a relaxation time longer than that of the cavity, typically in the microsecond range, are not suited to this technique, as their bandwidths would not cover enough degrees of freedom, as explained in the rest of the paper. This limitation can be overcome by using trains of short pulses; this kind of signals does not appear to have been considered so far in the literature and deserve investigations on their own as a practical solution.

Since the electric field $f(t)$ at the receiver position will have a spectrum $|\Phi(\nu)|^2 G(\nu)$, if $g(t)$ presents a maximum intensity at $t = 0$, the same will occur for $f(t)$, given that $|\Phi(\nu)|^2$ is real-positive and corresponds to the spectrum of the auto-correlation function of $\varphi(t)$, i.e., with its maximum at

$t = 0$ giving,

$$\|p_r(t)\|_\infty = p_r(0) = C_r \left[\int_{B_T} G(\nu) W(\nu) d\nu \right]^2 = C_r \mathscr{I}^2. \tag{3.60}$$

Solving the integral $\mathscr{I} = \int_{B_T} G(\nu) W(\nu) d\nu$ by parts yields

$$\mathscr{I} = [G(\nu) C_w(\nu)]_{B_T} - \int_{B_T} G'(\nu) C_W(\nu) d\nu = G(f_2) C_W(f_2) - \int_{B_T} G^{'}(\nu) C_W(\nu) d\nu, \tag{3.61}$$

with $G^{'}(\nu)$ the first derivative of $G(\nu)$ with respect to ν and

$$C_W(\nu) = \int_{f_1}^{\nu} W(s) ds \simeq (\nu - f_1) \bar{W} \tag{3.62}$$

a primitive of $W(\nu)$. The linear approximation in (3.62) assumes an average value $\bar{W}$ of W constant over B_T ; indeed, typical RCs present slowly-varying statistical moments for the scalar components of the electric field, as shown in sec. 3.3.3. This approximation holds for $\nu - f_1 \gg B_c$, where the $B_c = 1/\tau$ is the coherence bandwidth of $\Phi(\nu)$: in other words, as soon as the integration is carried out over enough significantly different portions of $W(\nu)$. Making use of this approximation in (3.61) and solving by parts the integral therein yields

$$\mathscr{I} = \bar{W} \int_{B_T} G(\nu) d\nu = \bar{W} \bar{G} B_T \tag{3.63}$$

and finally substituting it into 3.60 gives

$$\|p_r(t)\|_\infty = C_r \left(\bar{W} \bar{G} B_T \right)^2. \tag{3.64}$$

This result holds for receivers modelled as in (3.56), i.e., presenting a flat frequency response over B_T. An eventual constant group delay could be included, but is not explicit in (3.56) as it would not affect the PIP. When dealing with dispersive responses, (3.64) should be modified by weighting $W(\nu)$ by the transfer function of the receiver, before computing its average value over B_T . Depending on its degree of frequency dispersion, this latter could reduce the frequency average and thus the peak received power. As thus, the case of a flat response must be regarded as a best case for TR excitations.

Calculation of $\|p_i(t)\|_\infty$ for a time-reversal process

Before computing $\|p_i(t)\|_\infty$, we need to recall that TR makes sense only for impulse-like signals $g(t)$ covering a bandwidth $B_T \gg B_C$, i.e., for $B_T/f_c \gg \pi/Q$; under these conditions, $g(t)$ has a time support $T_g \ll \tau$, implying that the macroscopic features of $\varphi(-t) \otimes g(t)$ are dominated by those of $\varphi(t)$.

Impulse responses in an RC can be modelled as random processes, with a root-mean-square (rms) envelope following $\langle|\varphi(t)|\rangle = A_0^2 \exp(-2t/\tau)$ [94] and sec.2.5 The local deviations of the peak power of these kind of signals with respect to their rms envelope can be expressed as an overshoot factor sec.2.5

$$K = \frac{\sqrt{\|p_i(t)\|_\infty}}{A_0}, \tag{3.65}$$

whose cumulative distribution function is

$$F_K(x) = \prod_{k=0}^{n} \operatorname{erf}\left[\frac{x}{\sqrt{2}} \exp\left(\frac{k}{B_T \tau}\right)\right], \tag{3.66}$$

with $N \geq 4B_T\tau \ln(2)$ as demonstrated in section 2.5. It is now sufficient to express A_0 as a function of $W(\nu)$; since $A_0^2 = \langle x_{TR}^2(0)\rangle$,

$$\langle x_{TR}^2(0)\rangle = \int_{B_T}\int_{B_T} G(\nu_1)G^*(\nu_2)\,\langle\Phi(\nu_1)\Phi^*(\nu_2)\rangle\, d\nu_1 d\nu_2, \tag{3.67}$$

where

$$\langle\Phi(\nu_1)\Phi^*(\nu_2)\rangle = \left\langle|\Phi(f_c)|^2\right\rangle \mu(\nu_2-\nu_1) \tag{3.68}$$

is the frequency covariance function, which can be factorized into a slowly-varying power spectral density $\left\langle|\Phi(f_c)|^2\right\rangle = \langle W(\nu)\rangle$, here assumed to be constant over B_T, such that $\langle W(\nu)\rangle \simeq \bar{W}$, and a frequency-coherence $\mu(\nu_2-\nu_1)$ with a much narrower support, of the order of the modal bandwidth B_m of the RC as discussed in [166].

For any signal $g(t)$ such that its spectrum varies over scales much larger than B_C, the coherence function has sifting properties over B_C:

$$\int_{B_T} G^*(\nu_2)\mu(\nu_2-\nu_1)d\nu_2 \simeq G^*(\nu_1)B_C, \tag{3.69}$$

yielding

$$A_0^2 = \left\langle x_{TR}^2(0) \right\rangle = \bar{W} B_C \int_{B_T} |G(\nu)|^2 , \tag{3.70}$$

where the last integral represents the energy of $g(t)$, in the mathematical sense. Using (3.64) and (3.70), the conversion efficiency of time-reversed excitations is

$$\eta_{TR} = \frac{C_r}{C_i} \frac{B_T}{B_C} \frac{\bar{W} \kappa^2}{K^2} \tag{3.71}$$

with

$$\kappa^2 = B_T \bar{G}^2 \left(\int_{B_T} |G(\nu)|^2 \right)^{-1} \leq 1 \tag{3.72}$$

a shape factor attaining its maximum value for flat Fourier spectra.

3.3.2 Power Gain

Average Gain

How do η_{CW} and η_{TR} compare? In order to answer this question, two points should be considered: the random nature of $W(\nu)$ and the fact that, in case of harmonic excitations, an RC is typically operated jointly with a stirring technique.

We first interest ourselves in finding an asymptotic model giving the average peak-power gain G_{av}^P which corresponds to the mean ratio between conversion efficiencies. This value gives a good idea of the average increased efficiency when using time-reversal.

When driven by continuous wave the field inside the RC is non-polarized and its maximum value is given by:

$$||e_n|\,|_{\infty,CW}^t = A^2 \left\| \Phi\left(f_c\right) \right\|^2 \tag{3.73}$$

Assuming an ideal reverberation chamber [3], the average quadratic field amplitude is evenly distributed along the three field components.

$$\left\langle \left| \Phi_p\left(f_c\right) \right|^2 \right\rangle = \Phi_{av}^2\left(f_c\right) \quad \forall p \tag{3.74}$$

Where $\langle\ \rangle$ is an ensemble average. The average peak-power efficiency of a RC when driven by a CW wave is thus equal to:

$$\langle \eta_{CW} \rangle = 3\Phi_{av}^2 (f_c) \tag{3.75}$$

In [172], the ratio between peak-field inside the chamber and energy of the TR signal was found to observe the following inequality:

$$\left\langle \frac{||e_n||_{\infty,TR}^t}{\varepsilon_{TR}} \right\rangle \leq 2B_T\Phi_{av}^2 (f_c) \tag{3.76}$$

In the case the RC is excited with a time-reversed signal, if the signals are normalised, the mean peak power $\left\langle \sqrt{P_{TR}} \right\rangle$ is equal to the mean maximum power of the impulse responses $H_m = \underset{t}{max} |h(t)|^2$ of the RC. The impulse response follows an exponential decay with time and the energy injected within the RC is equal to:

$$\langle \varepsilon_{TR} \rangle = \langle P_{TR} \rangle \int_0^{+\infty} e^{-2t/\tau} \tag{3.77}$$

where $\tau = Q/(\pi f_c)$ the relaxation time of the RC. We obtain:

$$\frac{\langle \varepsilon_{TR} \rangle}{\langle P_{TR} \rangle} = \frac{\tau}{2} \tag{3.78}$$

From 3.75, 3.78 and 3.76 we find that the average peak-power field efficiency follows:

$$G_{av}^P \leq \frac{B_T Q}{3\pi f_c} \tag{3.79}$$

Equation 3.79 that a simple asymptotic model is obtainable when considering peak-power efficiency gain. We can see that TR techniques are of particular interest when considering wide-bands and for high quality factor RC's. However this asymptotic model is insufficient when considering peak-power since these values vary between measurements and are thus local maximums as we can see in Figure 3.8. We will therefore derive in what follows a method to calculate the gain dispersion around its average value.

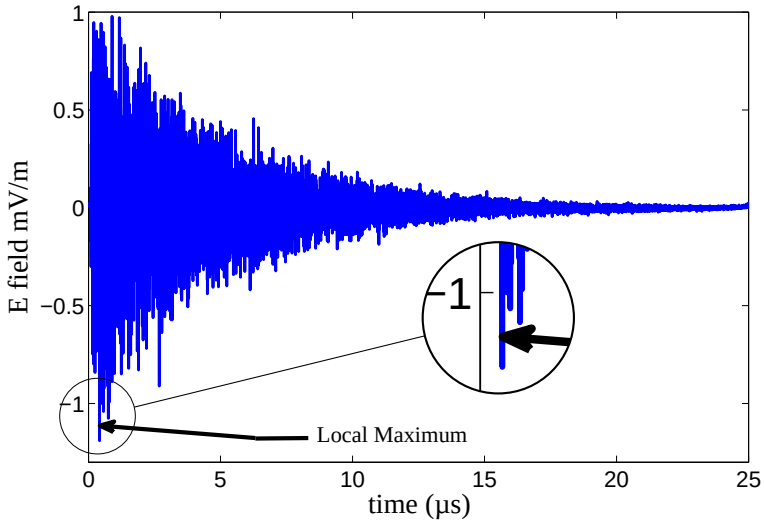

Figure 3.8 Impulse response example

Statistical Considerations

The assumption of an overmoded RC, as defined in [173], implies that $W(\nu)$ is bound to follow an exponential probability law [77, 174]. As a result, η_{CW}, when computed for a single realization, is widely dispersed around its average value: e.g., $\eta_{CW}/\langle\eta_{CW}\rangle \in (0.05, 3.00)$ with 90% probability. The poor predictability of the actual stress generated by an RC is improved by having N realizations, introducing stirring techniques [5]. This pragmatic approach is acknowledged by introducing

$$\eta_{CW}^{N} = \max_{i\in[1,N]} \eta_{CW}^{(i)} \tag{3.80}$$

i.e., the performance of the harmonic excitation will be evaluated as the highest one out of N realizations. As a result, $x = \eta_{CW}^{N}/\langle\eta_{CW}\rangle$ will follow the probability law [45, 175, 176]

$$p_N(x) = N(1-e^{-x})^{N-1}e^{-x} \tag{3.81}$$

The strong skewness of this family of probability laws (see Figure 3.9) implies that the statistical mode should be regarded as a more accurate estimator of typical values taken by η_{CW}^{N}, instead of its average. Therefore, the two conversion efficiencies will be compared by taking the ratio of their

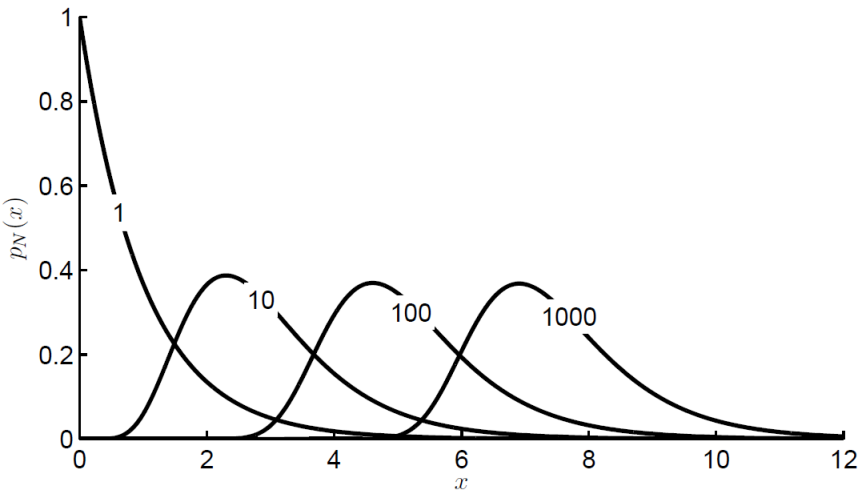

Figure 3.9 Probability distributions of $\eta_{CW}^N / \langle \eta_{CW} \rangle$ for a varying number N of realizations.

modes, a quantity hereafter referred to as the power gain

$$G_P^N = \frac{\mathrm{Mo}\left[\eta_{TR}\right]}{\mathrm{Mo}\left[\eta_{CW}^N\right]} \tag{3.82}$$

with Mo[.] the mode of a population of samples. The rationale for naming this quantity power gain is to be found in the possibility of obtaining the same order of magnitude of stress onto the EUT, while using a lower PIP at the input of the RC, i.e., at the output of the power amplifier. This observation is a direct consequence of having defined the conversion efficiency (3.57) as quantity normalized to a fixed peak instantaneous input power.

As opposed to the case of harmonic excitation, time-reversal excitation is characterized by a self-averaging property [165], as long as $B_T \gg B_C$. This property is apparent in the definition of $C_W(\nu)$ in (3.62), where the integral is taken over a stationary random process $W(\nu)$ which takes only positive real values. The low coherence of $W(\nu)$ outside sub-bandwidths of the order of B_C implies that the integral can be recast as a discrete sum

$$C_W(\nu) \simeq B_C \sum_{i=1}^{N_\nu} W(s_i) \tag{3.83}$$

with $s_i - s_{i-1} = B_C$, $\nu - f_1 = N_\nu B_C$ and N_ν is the number of coherence bands which correspond to the number of degrees of freedom. The stationary of $W(\nu)$ over B_T here translates into i.i.d. $W(s_i)$; hence the central-limit theorem allows stating that C_W, and ultimately $\|f_{TR}(t)\|_\infty$, follow a normal

distribution with relative standard deviation approximated by $\sqrt{B_C/B_T}$. This property is confirmed by experimental results presented in the following section. This means that the wider B_T becomes the less dispersed the distribution will become as mentioned in section 2.5.

Use of a sufficiently large bandwidth can therefore be expected to reduce the uncertainty in the TR-generated field. Convergence to a weakly fluctuating $\|F_{TR}(t)\|_\infty$ invites the following approximation: to consider that the randomness of η_{TR} is only due to $\left\|x_{TR}^2(t)\right\|_\infty$. Under this assumption, the pdf of η_{TR} can be expressed as a function of the pdf of the random variable $1/K^2$, as apparent from (3.71)

$$p_{K^{-2}}(x) = \frac{x/\alpha^{-3/2}}{2\alpha} p_K\left(\sqrt{\alpha/K}\right) \tag{3.84}$$

where $p_K(x)$ is the first derivative of $F_K(x)$ that was computed numerically and $\alpha = C_r B_T \bar{W}_\kappa / C_i B_C$. This pdf serves as a reference in the following section.

The mode, and also the average, of η_{TR} are well approximated as

$$\mathrm{Mo}\left[\eta_{TR}\right] \simeq \langle \eta_{TR} \rangle \simeq \frac{C_r}{C_i}\frac{B_T}{B_C}\langle W(f_c)\rangle \left(\frac{\kappa}{\mathrm{Mo}\left[K\right]}\right)^2 \tag{3.85}$$

where

$$\mathrm{Mo}\left[K\right] \simeq a \ln^b\left(\frac{4B_T}{B_C}\right) \tag{3.86}$$

was shown to be accurate to better than 1% in, when $a = 0.749$ and $b = 0.678$

For an harmonic excitation, the mode is

$$\mathrm{Mo}\left[\eta_{CW}^N\right] = \langle \eta_{CW} \rangle \ln N = \frac{C_r}{C_i}\frac{B_T}{B_C}\langle W(f_c)\rangle \ln N \tag{3.87}$$

Therefore from expressions (3.85) (3.87) the power gain in 3.82

$$G_p^N = \frac{B_T}{B_C}\frac{\kappa^2}{\ln N}\left[a \ln^b\left(\frac{4B_T}{B_C}\right)\right]^{-2} \tag{3.88}$$

It could be surprising, at first sight, to see that for $N = 1$, G_p is expected to be infinite. This is a direct consequence of the high probability of observing a weak field intensity for a single realization.

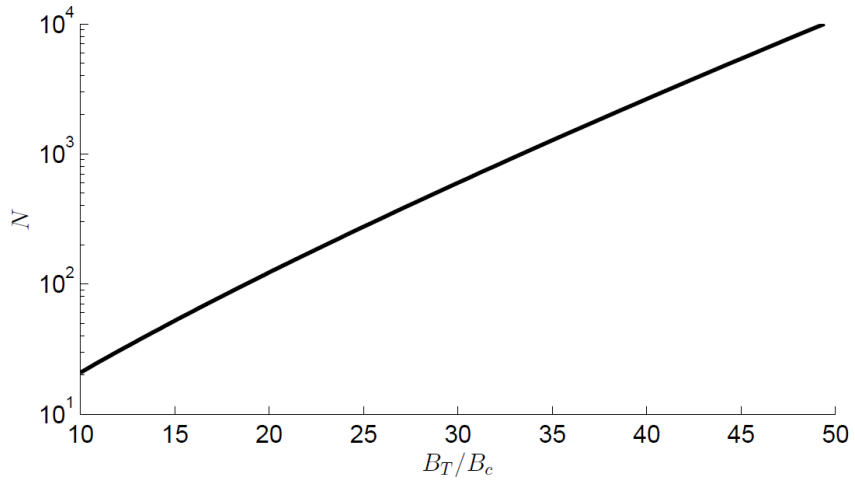

Figure 3.10 Equivalent number of independent realizations required in a CW driven RC in order to ensure the same typical efficiency than a TR-driven one, as given by (3.89).

Equation (3.88) provides a direct estimate of how many realizations should be carried out in case of an harmonic excitation, in order to obtain a performance similar to that obtained with TR excitations. Enforcing $G_p^N = 1$, it would be needed

$$N = \exp\left\{\frac{B_T}{B_C}\left[a\ln^b\left(\frac{4B_T}{B_C}\right)\right]^{-2}\right\} \tag{3.89}$$

independent realizations. A graphical representation of (3.89) in Figure 3.10 shows that keeping up can quickly become unaffordable. Equation (3.89) can also be interpreted as the ratio, between the bandwidth that should be spanned for CW frequency stirring, with respect to that needed by a TR signal in order to obtain the same efficiency. The underlying reason for this potentially huge difference in the performance is to be found in the collaborative nature of TR, where the N degrees of freedom are used coherently at the same time, as opposed to the CW case, where they are used separately in a non-coherent manner.

3.3.3 Experimental Validation

One of Supelec's RCs was used for the validation; its dimensions are $6.6 \times 3.0 \times 2.5$ m^3 with an expected lowest usable frequency around 400 MHz. We did not study η_{CW}^N experimentally, since two decades of research on RCs have thoroughly validated the good accuracy of (3.81) when using harmonic excitations [5, 175]. It is sufficient to estimate $\langle W(\nu)\rangle$, as discussed in sec. 3.3.2. The validation therefore focused on the performance of TR excitation and the power gain, so that we did not apply any stirring technique, as TR is based on self-averaging. A monocone antenna, mounted

between a corner of the RC and the stirrer, was used for the excitation of the RC. Transfer functions between this antenna and a phase-sensitive electro-optical probe (Enprobe EFS-105) were measured by means of a vector network analyzer, collecting data over 5000 frequency samples in the bandwidth $[1.8, 2.2]$ GHz. The probe was made to scan a hemispherical surface with a radius of 1 m, thanks to the low-perturbation robot depicted in Figure 3.11, together with the probe. 3431 positions were thus considered, uniformly distributed with an average distance of 3.75 cm, i.e., $\lambda/4$ at 2 GHz.

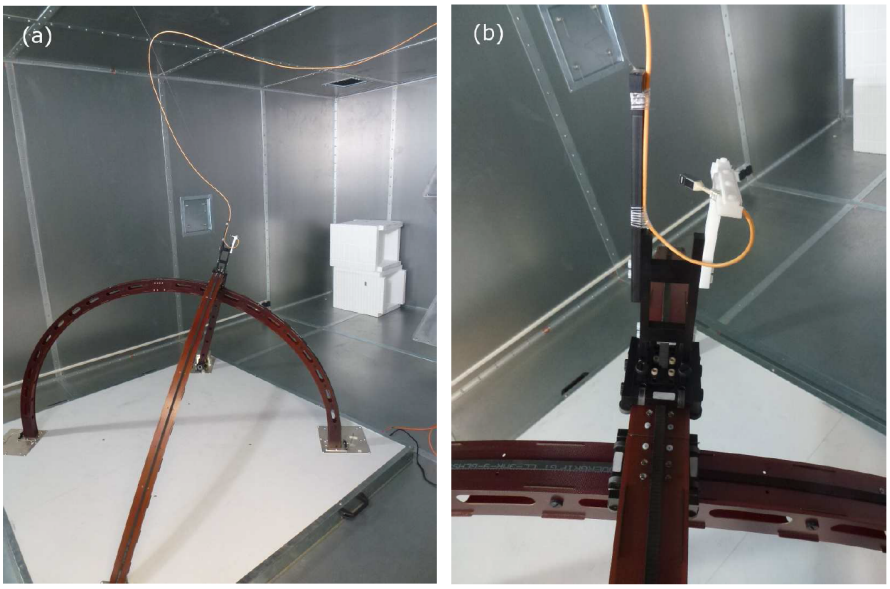

Figure 3.11 The hemispherical positioner (a) and the electro-optical probe (b) used during the experimental validation.

From this set of data we first computed η_{CW}, shown in Figure 3.12 to be indeed slowly varying. Field-related results were not corrected for the antenna factor of the probe, since our models refer to ratios of efficiencies affected by the same constants. Therefore efficiencies are all reported in arbitrary units (a.u.).

Time-domain responses $\Phi(t)$ of the RC were computed at each position, for several bandwidths B_T , up to 256 MHz. It was thus possible to estimate a time constant $\tau = 2.14$ μs by means of a least-square fitting of $\langle \varphi(t)^2 \rangle$; τ is needed in order to compute the coherence bandwidth $B_C = 467$ kHz required by our models.

Having direct access to the impulse responses, TR excitations can be defined as in (3.59), and their actual peak values recorded; all the results about TR excitations involve $G(\nu) = 1$ over B_T, i.e., a sine cardinal pulse in the time domain. The histogram of the peak values, normalized to $A_0 = \bar{W} B_C B_T$ (see (3.70)), is shown in Figure 3.13, together with the theoretical pdf of the overshoot factor K, obtained by numerically differentiating in (3.66). These results refer to two bandwidths, $BT = 32$ and 256 MHz, corresponding to fractional bandwidths 1.6 % and 12.8 %. Both distributions present

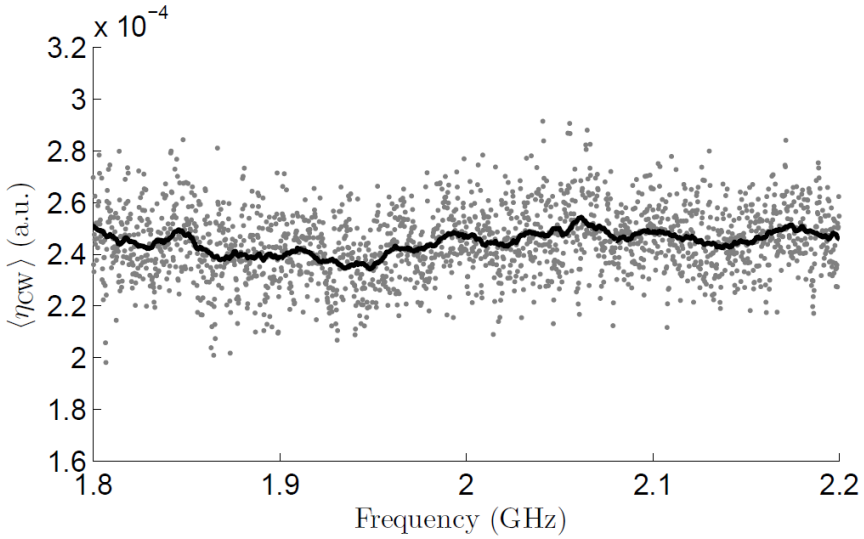

Figure 3.12 Estimate of η_{CW} (grey dots) and its smoothed version (black line) obtained with a moving average over a 20 MHz bandwidth.

a good agreement, while their mode passes from 2.25 to 2.85, i.e., slightly more than a 25 % change for an eightfold increase in the excitation bandwidth.

Conversely, the output field generated by these excitations is expected to be proportional to the bandwidth, as stated by (3.60). Figure 3.14 confirms this prediction for the average value of TR output fields. In order to assess whether their average value is a good representative of TR-generated fields, Figure 3.15 presents the histograms obtained by computing $(\|F_{TR}\|_\infty - u)/\sqrt{u}$ with $u = (B_T/B_C)\bar{W}$. If TR-generated fields were normally distributed according to the central-limit theorem, the previous operation should lead to a random variable well described by a standard normal distribution. The results in Figure 3.15 confirms that this assumptions are clearly confirmed for $B_T = 32$ MHz, while for $B_T = 2$ MHz the approximation, while not perfect, is still reasonable. This last observation is surprising, since for $BT = 2$ MHz, the input signal just covers slightly more than 4 coherence bandwidths, i.e., a very low number of degrees of freedom. These results have a strong effect on the confidence margin of TR-generated fields, as discussed in the next section.

The TR efficiency was then assessed, first for its average value shown in Figure 3.16. The sub-linear dependence in B_T is a direct consequence of how the maxima of an RC impulse response increase, although slowly, with B_T as shown in sec. 2.5.2. The slight discrepancy (about 6 %) between theory and experiments could seem surprising, since previous results were in very good agreement for both the numerator and the denominator of η_{TR}. In fact, predicting the pdf of the ratio of random variables is not a simple matter, in particular in the case of interest, since the numerator and denominator are not independent, having a common origin in the impulse responses of the RC. Having chosen to approximate the field generated by TR as a deterministic quantity is the reason for this residual error,

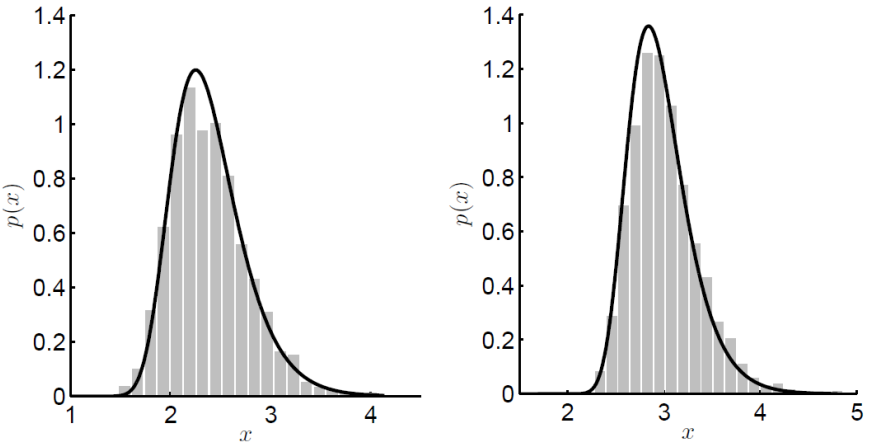

Figure 3.13 Empirical and theoretical pdfs of $\|x_{TR}(t)\|_\infty / A_0$, for $B_T = 32$ MHz (left) and 256 MHz (right).

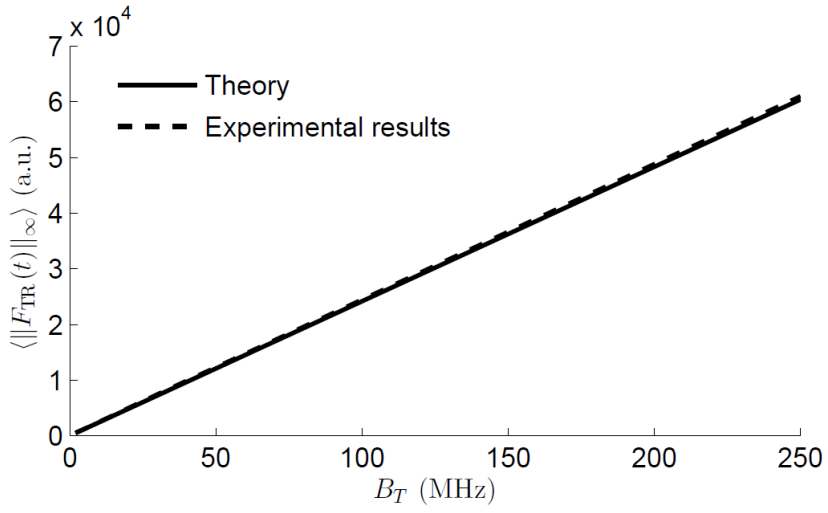

Figure 3.14 Estimate of $\langle \|F_{TR}\|_\infty \rangle$ as a function of B_T.

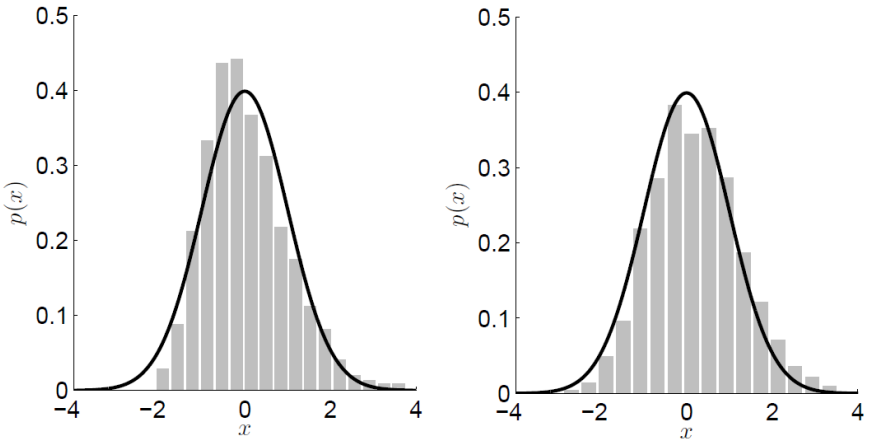

Figure 3.15 Empirical and theoretical pdfs of $(\|F_{TR}\|_\infty - u)/\sqrt{u}$ with $u = (B_T/B_C)\bar{W}$, for $B_T = 2$ MHz and 22 MHz

which is confirmed in the comparison of the empirical and theoretical probability distributions (3.84) in Figure 3.17.

We finally, present data confirming the validity of (3.88), shown in Figure 3.18. Attention should be brought to the meaning of $G_P^N \ln N$: it does not represent the final power gain, but a normalized version independent of N. The slight disagreement is a direct consequence of the one in the modelling of η_{TR}.

Confidence Intervals

The good agreement of experimentally estimated TR-generated peak fields with a standard Gaussian distribution implies that indeed output fields do converge as dictated by the central-limit theorem, i.e., they span a confidence interval C_{TR} corresponding, e.g., to a 95% probability,

$$\frac{C_{TR}}{\langle \eta_{TR} \rangle} = 2\sqrt{\frac{B_C}{B_T}} \tag{3.90}$$

to be compared with the one obtained for η_{CW}^N

$$\frac{C_{CW}}{\langle \eta_{CW} \rangle} = 2 \ln \left[\frac{1 - \sqrt[N]{0.025}}{1 - \sqrt[N]{0.975}} \right] \times \frac{1}{\ln N} \tag{3.91}$$

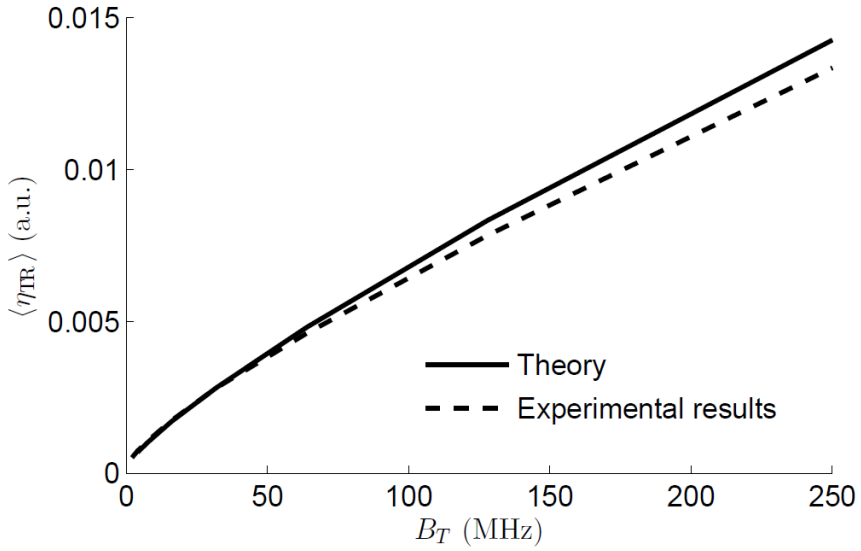

Figure 3.16 Estimate of $\langle \eta_{TR} \rangle$ as a function of B_T.

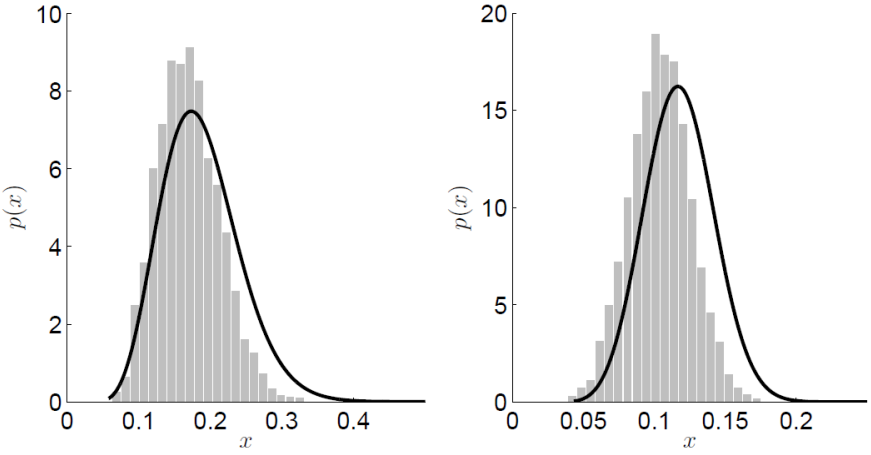

Figure 3.17 Empirical pdfs of $\eta_{TR}/(B_T\bar{W}/B_C)$ and approximate pdf obtained by assuming a deterministic output as defined in (3.84) for $B_T = 32$ MHz (left) and $B_T = 256$ MHz

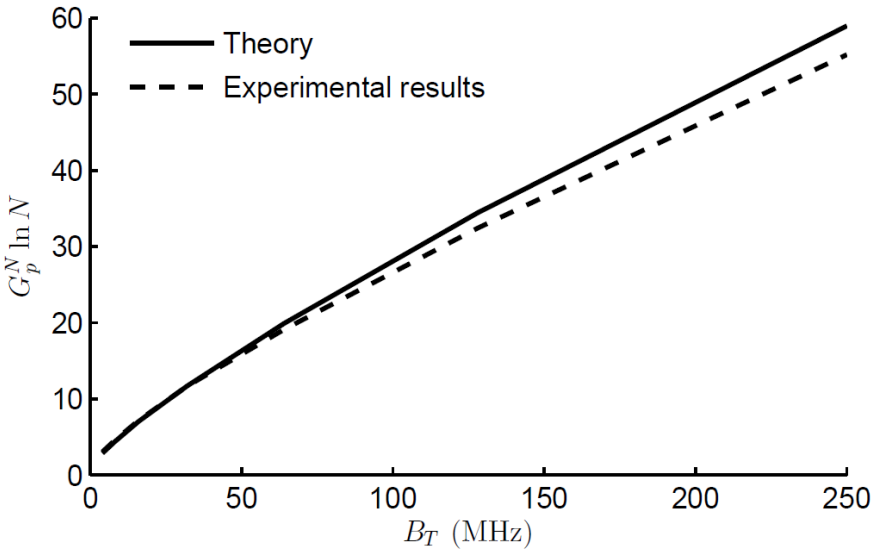

Figure 3.18 Normalised gain $G_p^N \ln N$ as a function of B_T.

These confidence intervals, represented as functions of the available number of degrees of freedom, are shown in Figure 3.19. The self-averaging property of TR excitations is the inherent cause for its faster convergence.

It could therefore be disappointing to have η_{TR} still featuring a pdf that does not appear to converge to a deterministic value. In fact, the reasons for the statistical dispersion of η_{TR} are utterly different from those that are behind η_{CW}. In the case of TR, the output field does converge to a deterministic value, as demonstrated in the previous section in Figure 3.15; but when normalized to the input peak power, it is the stronger dispersion of this last quantity that increases the spread of η_{TR}.

Conversely, in the case of CW excitations, the statistical dispersion only depends on the output fields, meaning that its actual value is hardly predictable. Therefore, in the case of TR excitations, a non deterministic η_{TR} has a simple meaning: while the output field is predictable with a high degree of accuracy, the actual amount of peak input power is not. As such, it could require more, or less, peak power than expected on average, but this uncertainty will hardly have any major effect on the field intensity.

The benefits of driving an RC with TR signals has been confirmed on three levels:

- a higher conversion efficiency,
- a reduced uncertainty in the actual field level
- without the need for multiple realizations (stirring).

The increase in the efficiency can well be translated into a conditioning on the peak-instantaneous power specifications for power amplifiers. Our work has also proven that TR does not necessarily

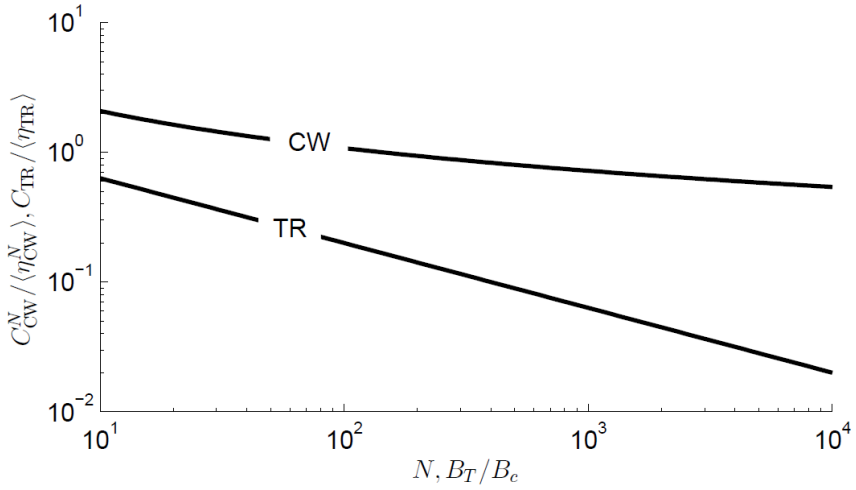

Figure 3.19 Relative confidence intervals of the conversion efficiencies for a 95 % probability, as a function of the number of degrees of freedom.

rhyme with wide-band signals, as acoustical TR has got us used to. Narrow bands can be interpreted as TR excitation signals, since the only constraint is $B_T/B_C \gg \pi/Q$, with RCs easily displaying $Q \geq 1000$, it should be possible to keep using standard power amplifiers while taking advantage of TR benefits.

The price to pay is the need to think in terms of spatially-resolved stresses. A TR-driven RC works by focusing part of the injected energy over a reduced region of space during a short time interval. As a result, tests would need to be repeated when switching from one position to the next one, not unlike an anechoic chamber, where directions are tested one after the other.

Conclusion

In this chapter a general presentation of electromagnetic time-reversal and its properties was undertaken. First a general overview of a time-reversal process in free-space or "Time-Reversal Cavity" was presented showing the theoretical validity of time-reversal as well as its experimental limitations. It was then explained that time-reversal is best suited for complex propagation environments which allow to considerably reduce the number of time-reversal mirrors. A state-of-the-art of the different fields of applications of time-reversal devices was also presented. Simple models were presented to measure time and space refocusing properties of a time-reversal process in complex propagation media. Moreover, the importance of spatial-correlation was introduced. Other important properties were also announced allowing a better understanding of time-reversal efficiency and performance when considering reverberation chamber or diffuse fields. The self-averaging properties and the metric used to measure contrast levels were also introduced. Derivations quantifying the coherent transmission

efficiency with multiple antennas injecting or receiving the refocused signals were introduced. The coherent energy was found to be almost constant during a time-reversal process. The limitations of adding antennas injecting the time-reversed signal were also discussed. The model obtained when considering multiple antennas on which the signal is refocused is limited to the case where all the antennas are considered statistically independent. In the last section, a comparison between classic use of reverberation chambers and time-reversal is exposed. Time-reversal was found to ensure higher field intensities, reduce the uncertainty levels of the actual measured field and reduce the need of multiple realizations. Important metrics such as conversion efficiencies comparing the maximum received peak-power to the maximum input peak-power for both time-reversal and harmonic excitation of the reverberation chamber were derived. The experimental validation of the statistical model derived in the previous chapter of the maximum-field of the impulse response was also offered. A model of the average power gain was introduced. The confidence intervals of the statistics of the power gain were presented. Time-reversal conversion efficiency is most important when considering using it for amplification purposes.

Chapter 4

Time-Reversal Techniques as a Potential HPEM source

4.1 Introduction

The properties presented up until now have shown the interest of time-reversal properties as a potential solution for an amplification system or TRAS (Time Reversal Amplification System). When pulsed signals have to be amplified, the maximum peak input instantaneous power (MPP) the amplifier can handle is one of the most critical figures of merits. For solid-state technologies, this level corresponds to the saturation of the amplifier. If the entry signal has a higher amplitude than the accepted level, the signal will be distorted and amplification will be saturated to the maximum level of the amplifier. Another problem encountered with solid-state devices is that their performances are degraded for pulsed signals.

In this chapter theoretical aspects of an indirect amplification scheme allows to provide an amplification margin, boosting the MPP of a wide-band amplifier. The two-step procedure relies on the statistical properties of diffusive media, where low frequency coherence involves widely spreading impulse responses. By first spreading the pulse intended for amplification, its MPP can be reduced by several orders of magnitude, and subsequent compressed by the same medium excited by a time-reversed version of the signal. Theoretical bounds and working regimes are derived and proved accurate by means of experimental tests carried out in a reverberation chamber adapted to the frequencies of the amplifier.

The objective here is to show the possibilities introduced by time-reversal focusing properties in order to obtain signals above saturation limit of an amplification module. One of the most common limits for signal amplification is the saturation levels of amplification. Above this level, the signal is only distorted compared to its reference level. The equations developed here are not necessarily for HPM considerations, but for any amplifier expected to be at the limit of its capabilities. However, this technique appears well suited for High-Power considerations when adding gain is limited by state-of-the-art or because of system complexity. Sometimes the entire system has to be changed or even discarded for a more recent one in order to get better performances. We will also present the importance of coupling mechanisms measured by Quality factors when using reverberation chambers. Two important loading effects are considered then antenna and wall dissipation.

The indirect amplification chain is presented in parallel to a direct amplification system in Figure 4.1. During the first stage, the multiple reflections in the diffuse medium allow a time-spread of an original pulse emitted within the chamber. The advantages of this time-spread are twofold:

- the solid-state amplifier is not in a inefficient pulse regime anymore
- the maximum-level of the signal to amplify is reduced compared to the previous saturated one

The signal is recorded and a time-reversed version is generated with an Arbitrary Waveform Generator (AWG) or using a Vector Signal Generator (VSG). The signal can thus be further amplified since the maximum signal-level is lower than the saturation level of the amplification module. The

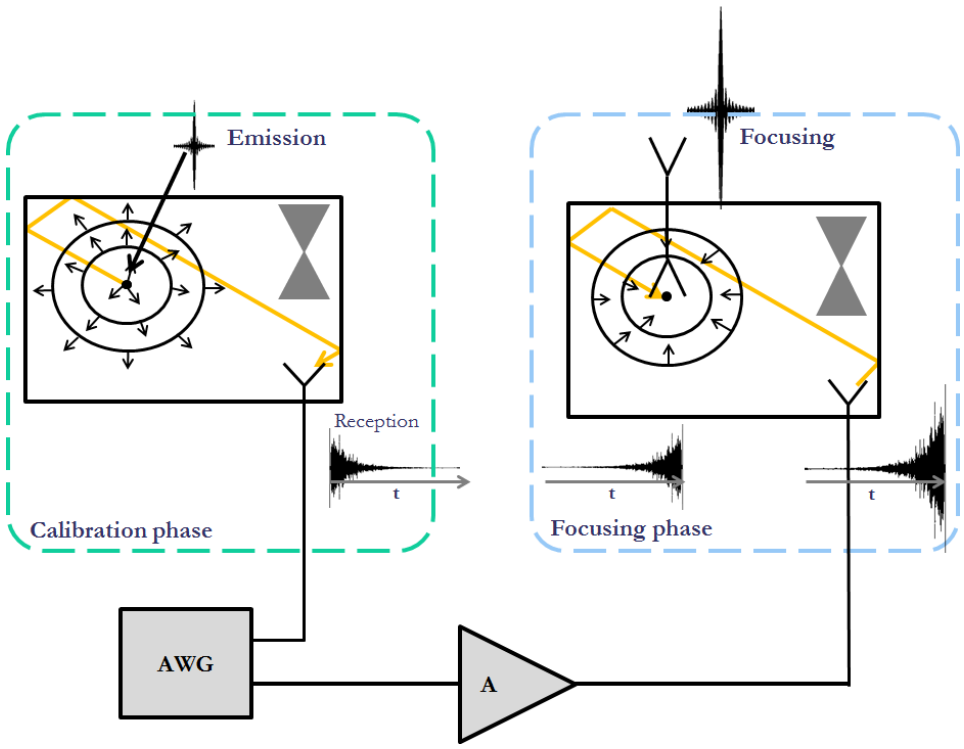

Figure 4.1 Schematic representation of the proposed procedure, showing the spreading and TR-compressive phases.

signal is then refocused at the same area where the pulse was first emitted. The added amplification allows an increase in the refocused peak.

Previous works using time-reversal for amplification purposes were presented in sec. 3.2.4 but no theoretical models were developed considering the diffuse medium nor assessing the importance of the reverberation chamber size as well as its efficiency. The theoretical developments presented here are verified by experimental results using a small cage adapted to the technical specifications defined for the scope of this work.

In the first part of this chapter the theoretical models are developed. Two main metrics are studied:

- the amplification margin corresponding to the ratio between the first statistics of the emitted pulse and the maximum peak-power of the impulse response. This work is based on previous work presented in sec. 2.5.2 on the impulse response $h(t)$
- the effective amplification after second passage through the medium

The studies presented here consider diffusive media, not only reverberation chamber such as multi-scattering media (forests of cylinders), long complex-shaped waveguides, etc. The medium is coupled to the outside world by means of two antennas, and allows radiating the amplified pulse signal outside. The second part of this chapter focuses on the validation of the models developed

using a small aluminium cavity whose dimensions and quality factor measurements were presented in sec. 2.4.3. These measurements were undertaken with Vector Network Analyser. The last part of the chapter presents the complete setup as well the different components developed and used in order to obtain amplified signals in time domain during this PhD.

4.2 Theoretical modeling

The scheme illustrated in Figure 4.1 is analysed in this section, when considering a pulse $p(t)$ with a Fourier spectrum $P(\nu)$, centered at the frequency f_c, covering the bandwidth B_T. The frequency variable is ν with an angular frequency $\omega = 2\pi\nu$. The equivalent time support of $p(t)$, T_p is defined as

$$T_p = \mathscr{E}_p / [p(0)]^2 \tag{4.1}$$

having introduced the signal-energy of $p(t)$

$$\mathscr{E}_p = \int_{B_T} d\nu \, |P(\nu)|^2. \tag{4.2}$$

The media under consideration are supposed to be well-approximated by a diffusive regime, in which propagation undergo a large number of weakly-dissipating, or elastic, scattering events, with an overall relaxation time much larger than the mean free path [177]. This kind of conditions are found in reverberant media, such as metallic cavities with geometrical dimensions much larger than the wavelength at the working frequency. In particular, in order to enable high efficiencies, the media of interest will have to be confined, i.e., with finite volume and reflective boundaries. Their inner volume may contain scatterers. Under these conditions, propagation is analogous to percolation [76], with a very low incidence of line-of-sight propagation.

The transfer function between the input and output antennas in Figure 4.1 will be referred to as $\Phi(\nu)$. For diffusive media, $\Phi(\nu)$ is typically modeled as a random process, characterized by a power spectral density $\langle |\Phi(\nu)|^2 \rangle = \langle W(\nu) \rangle$, where the brackets stand for the ensemble average, i.e., over all possible random realizations. Signals applied to an antenna are defined as incident waves, thus related to available power.

We first define the efficiency of signal transmission through the medium, defined for harmonic signals; the reduction in the MPP of a pulse signal is then considered, in order to shed some light on the actual margin on amplification gain that can be obtained from this procedure. Finally, time-reversal compression is discussed and the realized gain of the procedure obtained.

4.2.1 Transmission efficiency

Transmission of signals through a reverberating medium is here discussed. Coupling with the external world is assumed to be ensured by means of two antennas, respectively used as input and output ports. Before looking into the case of pulsed signals, we discuss the case of harmonic, or continuous wave (CW) signals. When injecting an input signal into the spreading medium, during its propagation over an ideally long period of time, part of it will eventually trickle out through the two antennas, while the rest will be dissipated inside the medium.

Following the diffusive assumption made in sec. 4.2, energy stored within the medium will couple on average in the same way onto the two antennas, independently from their specific features, if well-matched and with unitary radiation efficiencies. Hence, naming the average output power $\langle P_{\text{out}} \rangle$, we have

$$P_{\text{in}}(\nu) = 2 \langle P_{\text{out}}(\nu) \rangle + \langle P_d(\nu) \rangle , \tag{4.3}$$

with $P_d(\nu)$ the power dissipated in the medium. Defining $U(\nu)$ the electromagnetic energy stored within the medium and $P_{\text{loss}}(\nu)$ the power "lost", as given by the right-hand side of (4.3), the definition of the average composite quality factor is $Q(\nu) = \omega \langle U(\nu) \rangle / \langle P_{\text{loss}}(\nu) \rangle$ [55].

The transmission efficiency can now be defined as

$$\eta(\nu) = \frac{\langle P_{\text{out}}(\nu) \rangle}{P_{\text{in}}(\nu)} = \frac{\langle P_{\text{out}}(\nu) \rangle}{\omega \langle U(\nu) \rangle} \frac{\omega \langle U(\nu) \rangle}{P_{\text{in}}(\nu)} = \frac{Q(\nu)}{Q_{ant}(\nu)}, \tag{4.4}$$

The injected Power P_{in} is deterministic contrarily to the received signal, $Q_{ant}(\nu)$ the contribution of the antenna coupling to the over quality factor, related as $1/Q(\nu) = 2/Q_{ant}(\nu) + 1/Q_{walls}(\nu)$. (4.4) takes into account the observation that at steady state the input power must exactly compensate the lost one. (4.4) can also be recast as

$$\eta(\nu) = \frac{Q_{walls}(\nu)}{2Q_{walls}(\nu) + Q_{ant}(\nu)} \tag{4.5}$$

which gives a better understanding of the relative importance of the two power-loss mechanisms in the medium.

4.2.2 Relaxation-induced peak reduction: Margin

Time spreading of an input signal $p(t)$ and the subsequent reduction of the peak power of the output signal $y(t)$ can be measured as

$$M = \frac{\|p^2(t)\|_\infty}{\|y^2(t)\|_\infty}, \tag{4.6}$$

a quantity assessing the reduction in the ratio of the peak powers of the two signals. M will be referred to as the amplification margin represented in Figure 4.2. For $p(t)$ attaining its peak at $t = 0$,

$$\|p^2(t)\|_\infty = \left[\int_{B_T} d\nu \; P(\nu)\right]^2 = \bar{P}^2 B_T^2 \tag{4.7}$$

with $\bar{P}$ the average of the spectrum of $p(t)$, taken over its bandwidths B_T. As opposed to the deterministic input pulse, the output signal $y(t)$ is not predictable and can be modelled as a random process. Under the approximation of a diffusive regime for wave propagation through the medium, its response to a pulse $p(t)$ was found in sec. 2.5.2 to be given by

$$\|y^2(t)\|_\infty = \left\langle |y(0)|^2 \right\rangle K^2 \tag{4.8}$$

where K is an overshoot factor that assesses how much $y(t)$ can differ from its root-mean-square (rms) peak value. K is a random variable with a cumulative probability function first derived in sec. 2.5.2 and measured in sec. 3.3.3 is here recalled for clarity

$$F_K(x) = \prod_{k=0}^{N} \operatorname{erf}\left(x \mathrm{e}^{k/B_T\tau}/\sqrt{2}\right), \tag{4.9}$$

with $N \geq 4B_T\tau \ln 2$. The main assumption behind (4.8) is that $p(t)$ has time-domain support $T_p \ll \tau$. The rms $\left\langle |y(0)|^2 \right\rangle = h_{rms}$ was also derived in equation (3.70) in sec. 3.3.1

$$\left\langle |y(0)|^2 \right\rangle = \langle W(\nu) \rangle \, B_c \mathscr{E}_p. \tag{4.10}$$

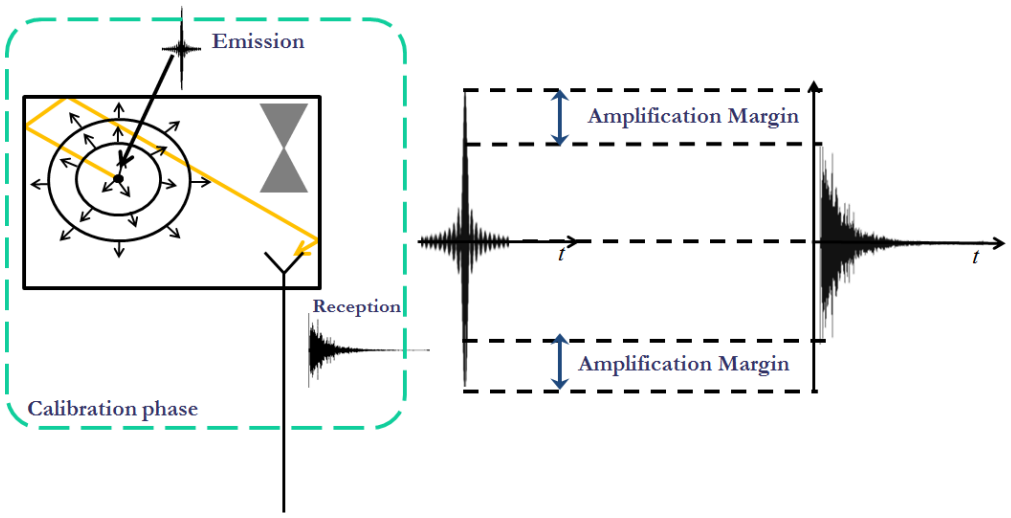

Figure 4.2 Schematic representation of the amplification margin M.

The observation that $\langle W(\nu)\rangle = \langle P_{\text{out}}/P_{\text{in}}\rangle$ implies that it can be approximated as $\langle W(\nu)\rangle \simeq \eta$. Hence, stitching together the previous equations

$$M = \left(K^2 \eta T_p B_c\right)^{-1}. \tag{4.11}$$

Recalling (4.4) and that $B_c = 1/\tau$, (4.11) can be expressed as

$$M = \frac{Q_{ant}}{K^2 T_p \pi f_c} = K^{-2}\frac{\tau_a}{T_p}, \tag{4.12}$$

where $\tau_a = Q_{ant}/\pi f_c$ is the relaxation time of the medium explained by antenna-driven leakage from the medium to the outside world. One result given by equation (4.12) is that the amplification margin on the rms values only depend on the antenna losses and not the losses on the walls. Furthermore the margin is proportional to the bandwidth of the impulse signal $p(t)$. T_p also takes into account the shape factor of the impulse κ as presented in section 3.2.2. M can be restated when replacing Q_{ant} by its expression in 2.40 as:

$$\boxed{M = \frac{Q_{ant} B_T \kappa^2}{K^2 \pi f_c} = \kappa^2 K^{-2}\,\frac{B_T V \omega^2}{m \pi c^3}} \tag{4.13}$$

with m the impedance mismatch, c the velocity of the waves in the media and ω the angular frequency. Showing the importance of the volume on the margin.

Another factor that will be mentioned here will consider the ratio between the margin and the peak-contrast. This factor is a good indicator of the spreading and refocusing of the signal. Recalling equation (3.47) of Λ_p

$$\Lambda_p = \frac{\overline{Q}}{\pi}\frac{B_T}{f_c}\kappa^2\Lambda \tag{4.14}$$

The ratio between the margin and the peak contrast is given by:

$$\frac{M}{\Lambda_p} = \frac{Q_{ant}}{\overline{Q}}\frac{1}{\Lambda} \tag{4.15}$$

and is equal to the inverse of the room efficiency when the field is diffuse in the chamber. This equation can be seen as a generalisation of the room efficiency and it seems quite logical that this ratio is equal to the inverse of the efficiency since it measures the refocusing quality in the chamber. It is also possible to re-obtain the efficiency with multiple antennas when considering this equation.

4.2.3 Time-reversal compression : realized gain

For the second phase, consider signal $Ay(-t)$. with $A \sim M$, knowing that M is a random variable. The spread signal $y(t)$ now needs to be time-reversed, e.g., using a sampling and an AWG or a VSG using frequency modulation.

M behaves as a random variable, its exact value cannot be predicted beforehand, it fluctuates around its rms value. In short, this means that if the time-spread signal $y(t)$ were amplified by a factor G higher than the specific realization of M, there would be a risk of having the amplifier saturating. It is therefore more sensible to bet on an amplification G corresponding to a probability $\mathrm{P}(M < G) < \alpha$, with α acceptably low, e.g., 5%. Another possibility is to decrease this factor allowing some saturation thus further increasing the peak-value after refocusing but adding some fluctuations. Knowledge of the probability law of K (see (4.9)) gives access to that of M. In particular, $\mathrm{P}(M < G) = \mathrm{P}(K > \sqrt{\tau_a/T_p})$.

Within the scope of this section, we will first derive the realized gain after compression, considering a generic choice G, then focus on typical values in order to understand what is the performance that can be expected by this method. The statistical average of the outptut signal will be studied, as time-reversal transmissions are characterized by a self-averaging property that has them to converge to their own average, which is therefore a good representative of their actual value. The accuracy of this approximation is discussed in sec. 4.2.4, by introducing the notion of contrast, shown to go hand in hand with the realized gain.

Injecting a signal $\sqrt{G}y(-t)$ through the output port of the system in Fig. 4.1, the average of the random signal $\hat{p}(t)$ appearing at the input port is

$$\langle \hat{p}(t) \rangle = \eta \sqrt{G} p(t), \tag{4.16}$$

so that the realized gain is

$$G_r = \frac{\|\hat{p}^2(t)\|_\infty}{\|p^2(t)\|_\infty} = \eta^2 G \tag{4.17}$$

Recalling that $G \sim M$, i.e., G has the same order of magnitude than M, and that M is given in (4.12), we can estimate the order of magnitude of the realized gain as

$$\boxed{G_r \sim K^{-2} \frac{\tau_a/T_p}{(2+\tau_a/\tau_d)^2} \sim \frac{M}{(2+\tau_a/\tau_d)^2}}. \tag{4.18}$$

4.2.4 Some practical considerations

The fact that the peak reduction does not depend on the overall relaxation time of the medium, but only on the relaxation time due to energy leakage should not come as a surprise. Indeed, τ_a assesses how energy injected into the medium spreads over its volume, thus resulting into a reduction of the average energy density.

The peak reduction M represents a potential room created for further amplification. In practice, (4.17) is to be read as a correction of this potential, since signals twice transmitted through the medium will partially be dissipated in it, as testified by the term η^2. The potential and realized gain do not necessarily follow the same trend: this is the topic of this section, where their respective limitations are discussed.

The potential margin M can be linked to some physical features of the medium by recalling that

$$Q_{ant} = 16\pi^2 V/\lambda^3, \tag{4.19}$$

as predicted in [55] for the case of a reverberation chamber. In practice, Hill's derivation holds for any diffusive medium, as its only assumption is that of a random isotropic plane-wave spectrum, independently from any particular geometrical configuration. Finally

$$\tau_a = 16\pi f_c^2/f_o^3, \tag{4.20}$$

where $f_o = c/\sqrt[3]{V}$ is a characteristic frequency of the medium. Since K evolves rather slowly with the frequency 2.5.2, (4.12) is expected to increase as the square of the central frequency. At the same time, increasing the volume of the medium would be another mean of increasing the amplification margin.

Conversely, the realized gain, which takes into account dissipation within the medium, presents two different regimes, depending on the ratio τ_a/τ_d. For the case $\tau_a \ll \tau_d$, i.e., for negligible internal dissipation compared to energy leakage, (4.17) goes like

$$G_r \sim \frac{\tau_a/T_p}{2K^2}, \tag{4.21}$$

whereas for $\tau_a \gg \tau_d$ we obtain

$$G_r \sim K^{-2}\frac{\tau_a}{T_p}\frac{\tau_d}{\tau_a}, \tag{4.22}$$

These two regimes are expected to appear, respectively, in lower and higher frequency ranges. However, with the chamber used for experimental results the first region was not found since for the frequencies under consideration for the regime to hold the field in the chamber can not be considered as diffuse. As a matter of fact, dissipation, unless justified by absorbing materials, can be caused by finite conductivity in metallic reverberating media, leading to skin effect. The frequency separating these two regimes strongly depends on its physical features. For a given τ_a, if τ_d decreases, then the overall energy of $y(t)$, and thus of $\hat{p}(t)$ will decrease. So while the margin depends only on τ_a, trying to increase it is not a good policy, since the necessary condition to avoid wasting the amplification is $\tau_a \ll \tau_d$. A trade-off must thus be found to maximise the margin without loosing the refocusing properties.

In the lower frequency range the realized gain easily exceeds one as long as pulses much shorter than the antenna-leakage relaxation time are fed to the system. As opposed to this in the high-frequency regime, in order to ensure that the proposed procedure is still appealing, the condition $G_r \gg 1$ translates into

$$\frac{\tau_a}{\tau_d}K^{-2} \ll \frac{\tau_d}{T_p} \tag{4.23}$$

which implies a ratio τ_a/T_p larger than one by several orders of magnitude, thus interesting only with wide bandwidths. Typically several order of magnitudes of the coherence band are necessary in order to obtain a realised gain higher than one.

In the case of the aluminium chamber where the surface conductivity was found to be close to 10^6 S/m and with having a volume of 1.68 m when replacing τ_a and T_p by their expressions and for a

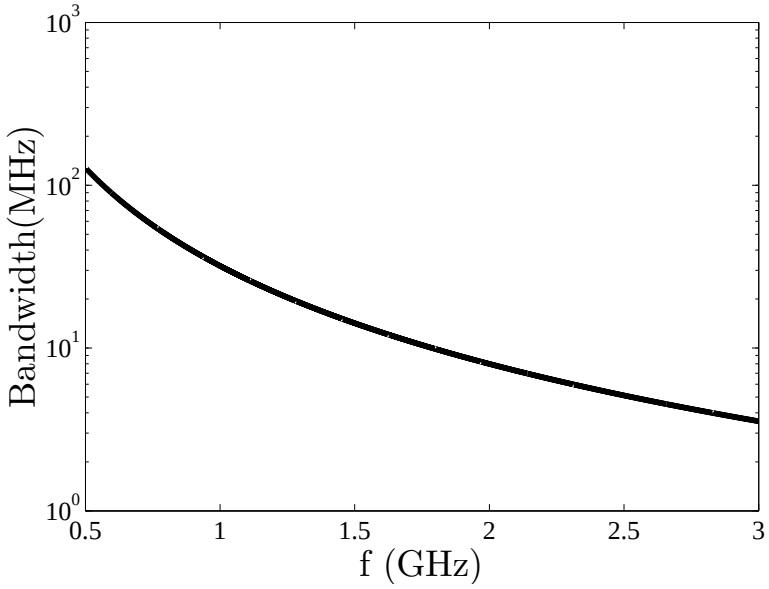

Figure 4.3 Evolution of necessary bandwidth for $\tau_a/T_p \ll 1$ to hold.

criteria of 100 one obtains:

$$\frac{\tau_a}{T_p} = \frac{16\pi V f^2}{c^3} B_T \kappa^2 \sim 100 \tag{4.24}$$

which in terms gives another condition on the couple central frequency and bandwidth variables :

$$f^2 \; B_T \; \kappa^2 \sim \frac{100 c^3}{16\pi V} \tag{4.25}$$

the right side of the inequality in the case of the aluminium chamber gives for a frequency of 1 GHz a bandwidth of 32 MHz. A graphical representation of the theoretical evolution of the necessary bandwidth in order to obtain significant amplification.

However it is possible to greatly reduce this bandwidth when using a 1-bit or when using a signal equalisation as it will be presented in the second part of this chapter.

4.3 Experimental results

In order to validate several predictions from the theoretical presented in the section above, experimental measurements were undertaken. The experimental results presented here were obtained using both the aluminium chamber presented in section 2.4.3 or the chamber in Supélec's laboratory. The experimental setup is the same than in section 2.4 and follows the classic measurement configuration

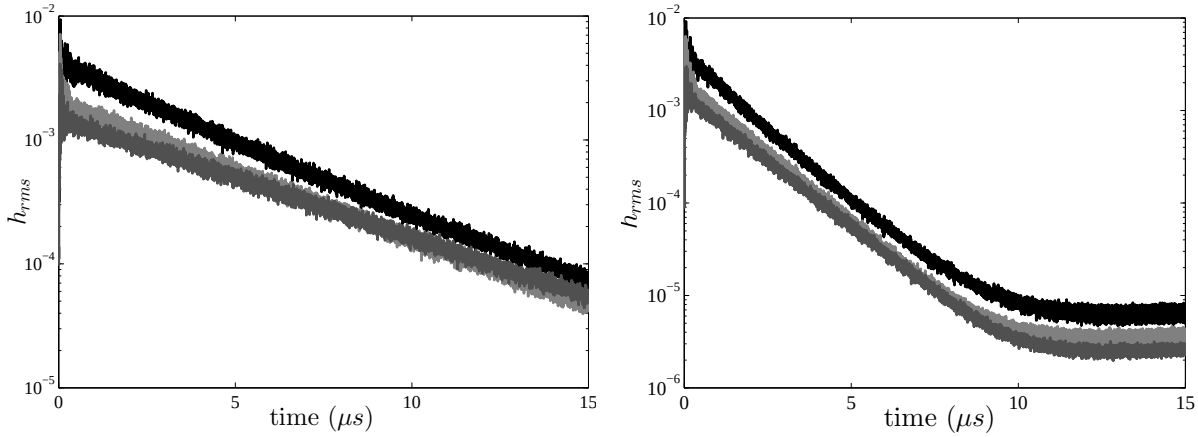

Figure 4.4 RMS value of the impulse response for 3 central frequencies : 1.15 GHz black-line, 2.15 GHz light-gray line and 3.15 GHz dark-gray line with no absorbent (a) and 1 absorbent in the middle of the room (b). with The spectrum of the injected signal is constant over $B_T = 300$ MHz.

from Figure 2.12. A Vector Network Analyser and the antennas used in both set-ups are the same ones used in section 2.4.

4.3.1 Supélec's steel room

The first measurements allowed to evaluate the assessments given by the margin formulation. The objective here is to show that the root-mean-square value of the impulse response in a chamber only depends on the antenna loading and that the margin increases with frequency. These measurements were carried in Supélec's reverberation chamber. Three sets of measurements for 1, 2 and 3 GHz were carried-out. For each frequency 7000 points over 300 MHz were taken and 100 stirring positions were assessed. The room was loaded with two antennas and a radiation absorbent material (RAM) was placed inside in the middle of the chamber or on the walls to observe which had more impact. The effect on the shape of the impulse is also considered here.

The evolution of the RMS value of the impulse response for different central frequency is shown in Figure 4.4. The impulse considered here is a frequency door over the complete bandwidth. As predicted by the model of the margin in equation (4.13) the margin increases with frequency. Moreover the ratios between curves seem to correspond to the predicted model when taking average values a $t \simeq 0$, however the noise at the beginning of the curve prevents from any proper conclusion.

Figure 4.5 represents the evolution of the RMS value of the impulse response when adding an absorbent in the chamber. The impulse considered here is the same as in the previous graphic. The predictions from the model still hold and the value at $t \simeq 0$ does not vary when adding absorbers. This result was also found in [94, 105] but no formal explanation was given. The slope changes because the overall quality factor changes but the value for small times does not depend on the overall

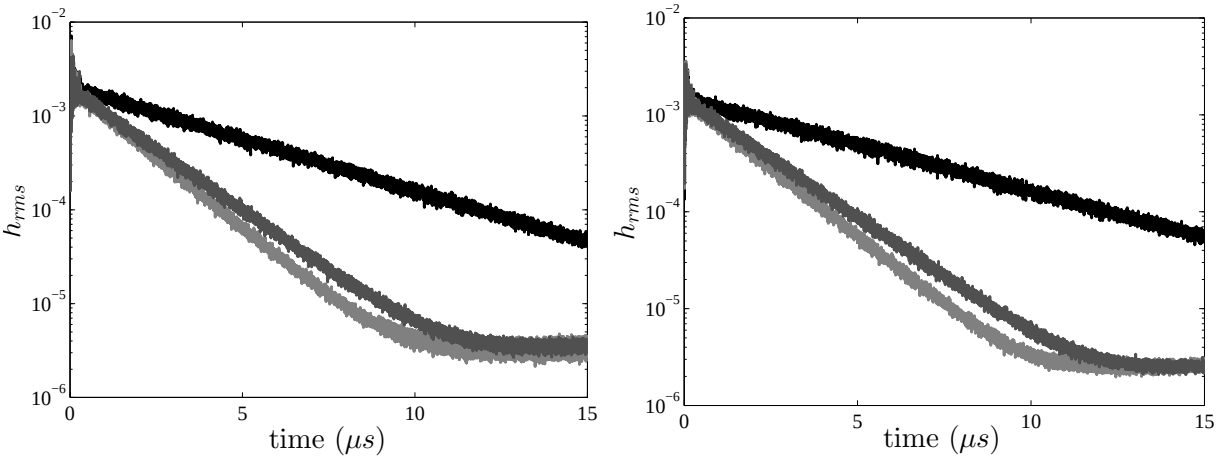

Figure 4.5 RMS value of the impulse response between for $f_c = 2.15$ GHz and $B_T = 300$ MHz (a) and $f_c = 3.15$ GHz and $B_T = 300$ MHz (b). No absorbent (black line), absorbent material on the walls (dark-gray line) and the absorbent placed in the middle of the chamber (light-gray line)

quality factor showing that only the antenna quality factor intervenes in the amplification margin. The absorbent seems to have more effect when it is placed in the middle of the chamber meaning that more modes are affected in such a set-up.

It is also important to show the evolution of the RMS curve when considering different pulse shapes. In this case the pulse shape factor κ changes. As mentioned in the previous chapter, $\kappa \leq 1$ meaning that depending on the pulse type the amplification margin M will increase for certain type of impulses. Figure 4.7 represents the variation of the RMS values when considering different impulses. Three impulses were modelled a door and two truncated gaussians with two different standard deviations σ. The slope of the curve does not change however the starting values do. However, even for the most extreme case the increase of the margin does not appear to be so different from one another meaning that κ is a slowly varying constant and good approximation of the margin can be obtained when considering $\kappa^2 \simeq 1$.

The last parameter that was measured with Supélec's cavity was the efficiency of the room. The efficiency is a measure of the amount of power the receiving antennas capture when the chamber is emitted. In the case where there are two antennas in the chamber the maximum efficiency available on the antennas is equally divided and $\eta_{max} = 1/2$.

Since we are dealing in a time-reversal experiment with a fixed stirrer, the mean value of η is not the only value that is of interest but the values of η for each stirrer position is important. Figure 4.7 represents the mean efficiency or $\langle |S_{21}|^2 \rangle$ and the efficiency $|S_{21}|^2$ for a single stirrer position. Theory states that the efficiency of a room increases at lower frequencies, that is why Figure 4.7 represents the efficiency at lower frequencies.

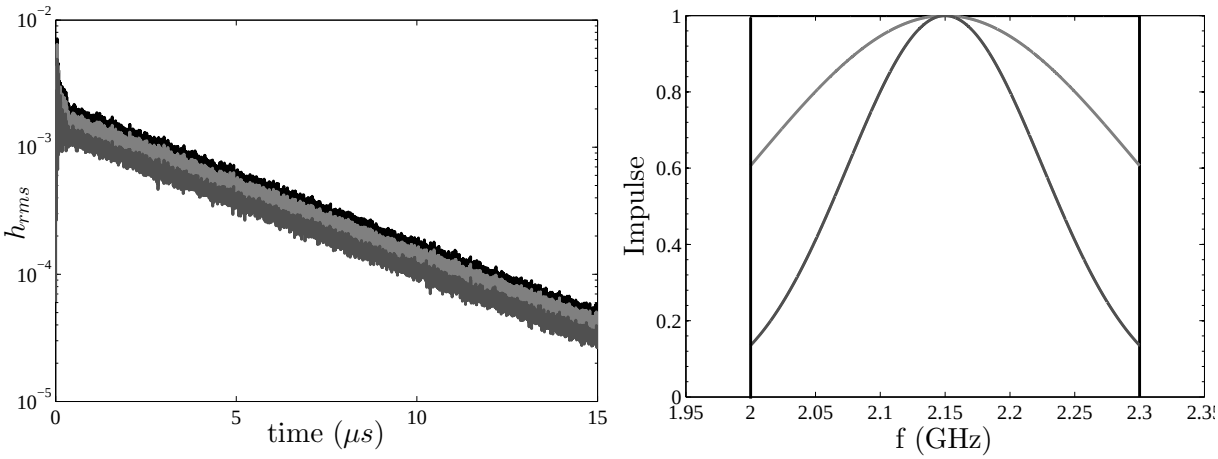

(a) (b)

Figure 4.6 RMS value of the impulse response for 3 different impulse signals (left) and their corresponding spectrum on the right.

Experimental data are confronted with the theoretical values of η from Hill's theory. Even with σ taken very low, the model does not seem to follow experimental data even for higher frequencies where the chamber is overmoded for $\mu_r = 1$. Only for permeability's of the order of 100 does the theory seem to concord to measurement. Moreover the efficiency levels of the room are very low even for a single stirrer position where all the fluctuations appear. The amount of power received on the antenna is very low. The efficiency levels are below 0.05 even at the lowest frequencies.

The experimental studies on Supélec's small room have allowed to confront data to the theoretical assessment made in section 4.2. The evolution of the margin corresponds to the theoretical model. However the efficiency of the room is so low that it is not well adapted for amplification using time-reversal. Moreover, there remained uncertainties on fundamental values such as wall conductivity and permeability in order to confront the theoretical values of the Margin and of the Real Gain with measurements. In order to do so, a smaller chamber using more conductive walls was used. The results of which are presented below.

4.3.2 THALES Aluminium room

For the aluminium chamber measurements were carried for 22001 frequency points between 300 MHz and 3 GHz over 20 stirring positions. In this case the room was loaded with only the stirrers and the two antennas. These measurements allow to verify the performances of an adapted chamber. A smaller chamber having higher wall conductivity was built in order to maximize efficiency. A picture of the aluminium chamber is presented in Figure 4.8. The efficiency of the the chamber is presented in Figure 4.9. The levels attained by η are several times higher than the ones obtained at Supélec and for one stirrer position the efficiency variations can go up to 0.45 whereas

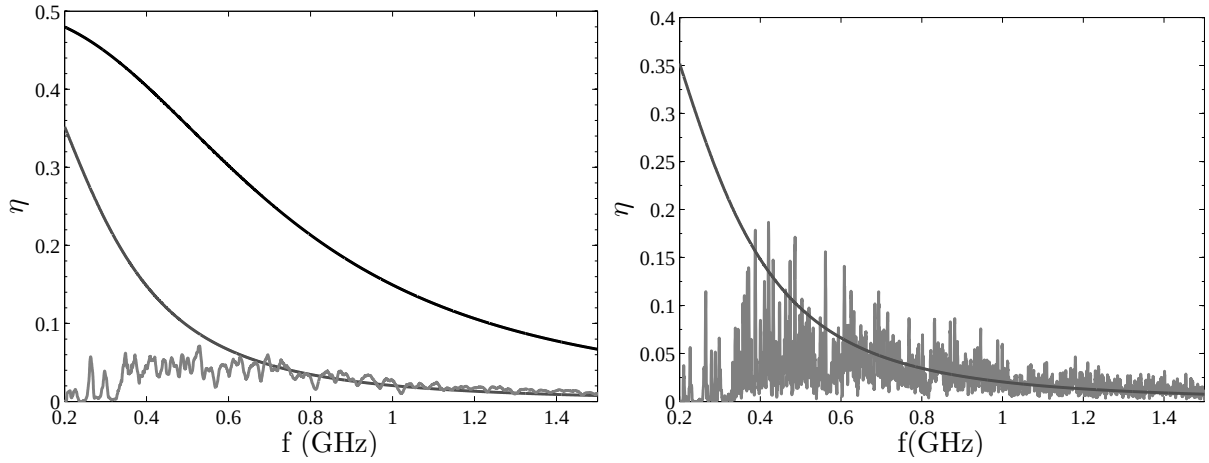

Figure 4.7 Room efficiency η of Supélec's small room. (a) Experimental measurement of the mean efficiency (light-gray) , model prediction with $\sigma_w = 2.364\ 10^5$ S/m as in 2.4 and $\mu_r = 1$ (dark line) and $\mu_r = 100$ (dark-gray line). (b) Experimental measurement of the efficiency (light-gray) for 1 stirrer position, model prediction with $\sigma_w = 2.364\ 10^5$ S/m and $\mu_r = 100$ (dark-gray line).

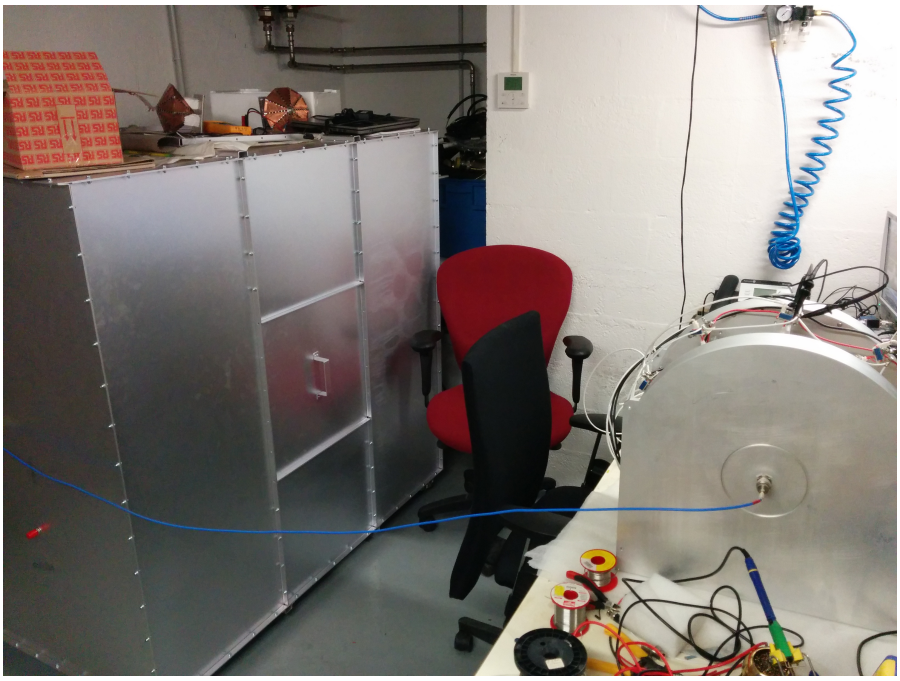

Figure 4.8 Reverberation chamber used for the validation of the theoretical work and the prototype.

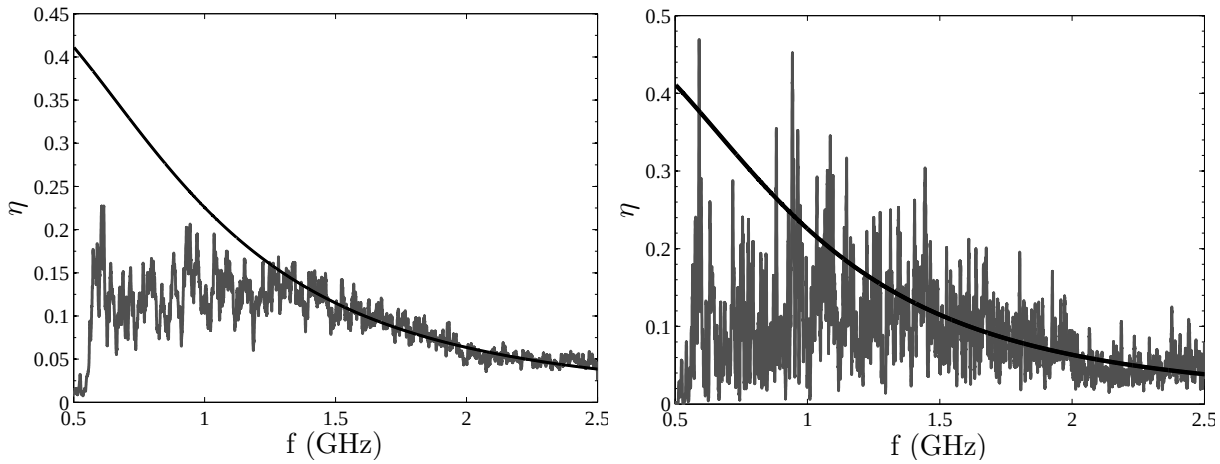

Figure 4.9 Room efficiency η of the aluminium small room. (a) Experimental measurement of the mean efficiency (dark-gray), model prediction with $\sigma_w = 10^6$ S/m as in 2.4and $\mu_r = 1$ (dark line) and (b) is the same graphic but for 1 stirrer position.

before the maximum was about 0.18. This allows a much better refocusing and therefore peak-value of the field.

For all the graphics below, the margin $\frac{\|p^2(t)\|_\infty}{\|y^2(t)\|_\infty}$ and the real gain $\frac{\|\hat{p}^2(t)\|_\infty}{\|p^2(t)\|_\infty}$ will be presented for impulses of 300 MHz with constant spectrum. For the theoretical model the shape factor is then equal to unity $\kappa^2 = 1$.

Margin

From equation (4.13) it is clear that the Margin increases as f^2. An estimate of the curves coefficient is obtained using a mean-square algorithm from the mean margin for frequencies between 500 MHz and 2.3 GHz. The f^2 curve with the estimated coefficient is confronted to experimental data in Figure 4.10 and we can see that the slope of the theoretical data can be well approached by a squared frequency curve.

In Figure 4.11 the theoretical model obtained in equation (4.12) is confronted to theoretical values of the mean margin $\langle M \rangle$ in dB. The evolution of the theoretical margin with the mean value of the margin concord except for frequencies below 0.8 GHz. For frequencies below that value the margin doesn't follow the theoretical curve but doesn't fall too far from theory. The same graphic representation is shown in Figure 4.12 but the incertitude levels (2 standard deviations) are also shown. As predicted by theory, the incertitude over the margin can be quite important more or less 4 dB, however the real gain is much more stable due to the self-averaging effects of time-reversal.

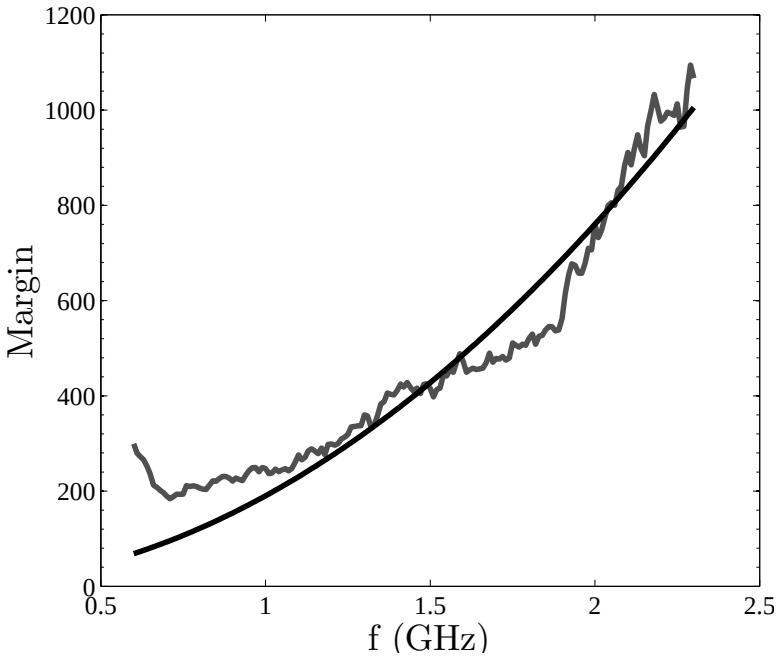

Figure 4.10 Margin in function of frequency and a curve in f^2. The black curve corresponds to a f^2 curve obtained with a mean-square algorithm and the grey curve is a measurement within the aluminium cavity used for the prototype.

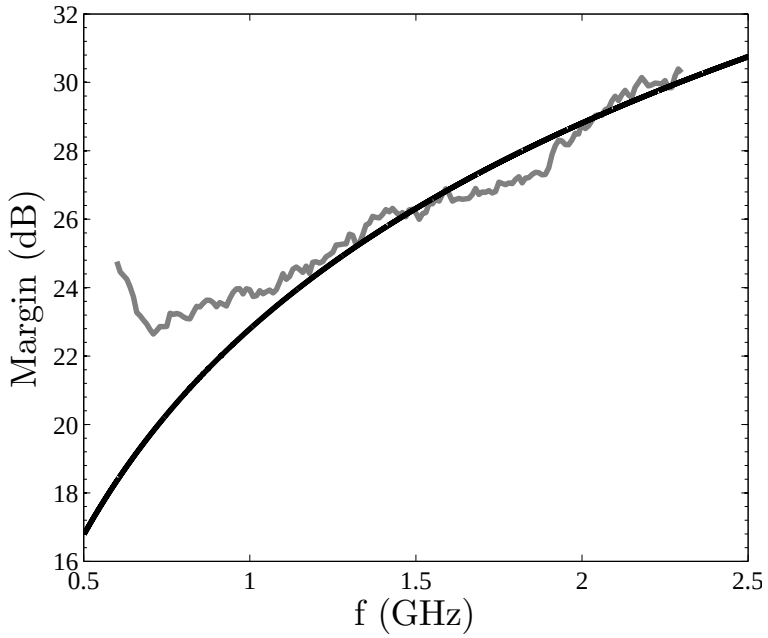

Figure 4.11 Margin in dB in function of frequency. The Black curve is the model coming from equation 4.12.

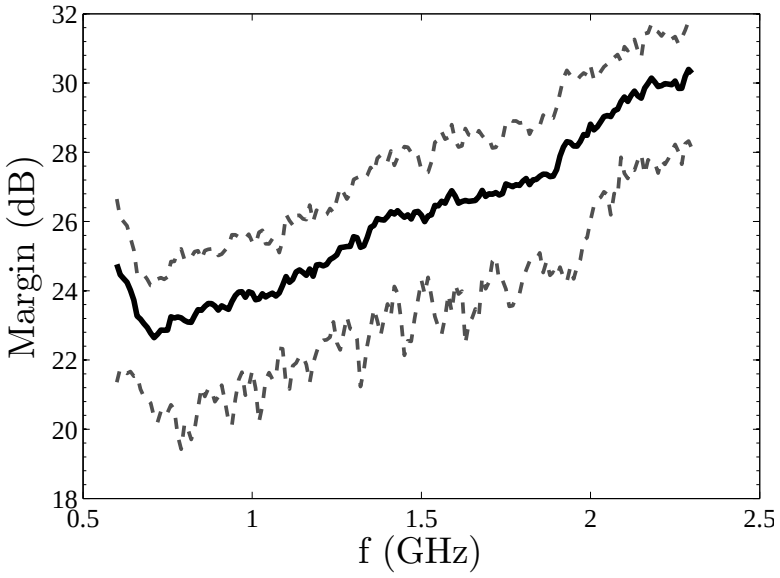

Figure 4.12 Margin in dB in function of frequency with std levels for incertitude. The Black curve is the experimental mean margin.

In the following the experimental values of the real gain $\frac{\|\hat{p}^2(t)\|_\infty}{\|p^2(t)\|_\infty}$ will be shown and confronted to theory.

Real Gain

Now the gain that can be added by using a classic time-reversal is presented. The signal in this case is not processed and only amplified to the the saturation level in the first stage. The real-gain G_r measures the focusing properties of a time-reversal process with in this case only two antennas places within the chamber. Since the chamber is not overmoded up until 800 MHz the field will not be diffuse up to that frequency and the theoretical models are not expected to follow experimental data.

Figure 4.13 shows the variation of the mean real gain with frequency for impulses of 300 MHz bandwidth. The experimental values are compared to theory from equation (4.18) where the values in the various components are replaced by the one in Hill's theory. The wall conductivity is taken to be $\sigma_w = 1e + 6$ S/m and its permeability equal to one. Even if some discussion were made over the validity of these formulas, theory and experiment of the real gain seem to concord at higher frequency where the field is diffuse. The real gain varies between 3 and 8 dB meaning that the dimensioning of the chamber is of prime importance.

The fact that there is a peak in the real gain shows that this chamber is well adapted for the frequencies considered here, with maximum efficiency at frequencies between 1.2 and 1.5 GHz depending on the signal bandwidth.

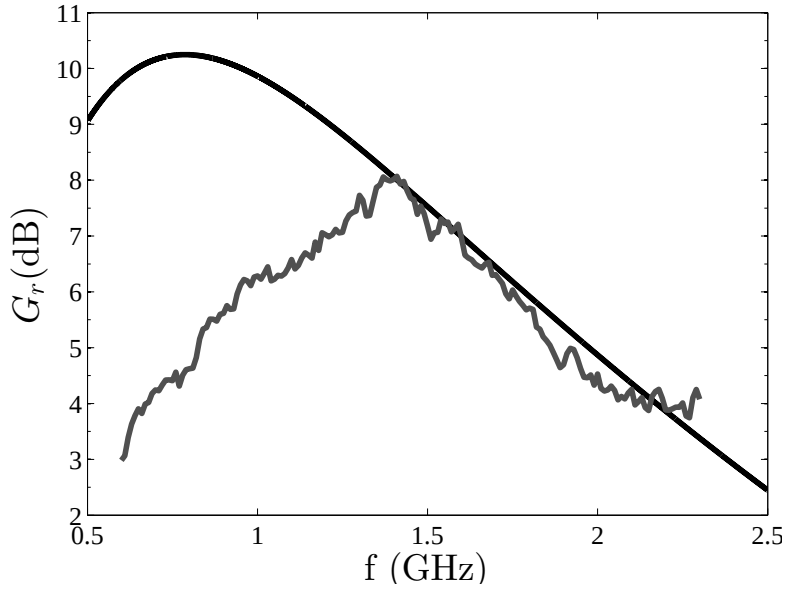

Figure 4.13 Real Gain with adjusted Hill model for Quality Factors.
$\sigma_w = 1e + 6$ S/m and $\mu_r = 1$. The gray curve corresponds to the measured mean real gain and the dark curve is the is the theoretical model of real gain taken from equation 4.18 and using Hill's theory for the Quality factors.

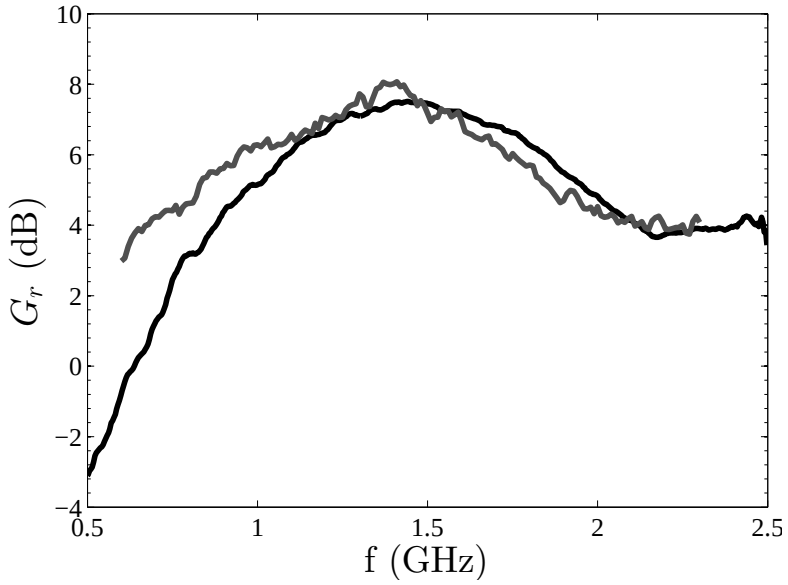

Figure 4.14 Real Gain with extracted Quality Factor.

In order to further evaluate the comparison between theory and experiments Figure 4.14 represents the mean real gain evaluated from $\frac{\|\hat{p}^2(t)\|_\infty}{\|p^2(t)\|_\infty}$ in light-gray and the experimental model now

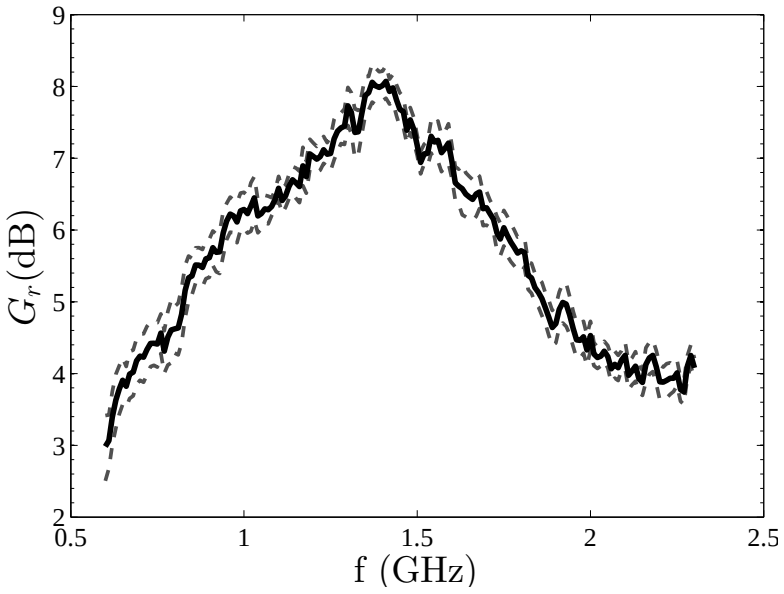

Figure 4.15 Real Gain with standard deviations for incertitude levels.

using the wall quality factor extracted from the overall quality factor in a similar method than in section 2.4. In this case, theoretical model is partially using experimental data since the model of the walls quality factor does not seems to hold. The two curve correspond even at lower frequency. However, in this case Hill's model does seem to give good values at higher frequencies.

As expressed before the uncertainty levels of the real gain are greatly diminished compared to the margin and this is due to the self focusing properties of time reversal. A representation of the uncertainty levels over which more than 95% of the real gain values are found is represented in Figure 4.15. The variation of the gain is less than 1 dB so that the theoretical model is a good approximation of the refocused gain.

The real gain varies quite drastically with frequency so that a classical time-reversal process might not be the best solution when considering an amplification system. Even on a small frequency range presented here the real gain varies over 5 dB. In order to increase the gain to interesting values it is possible or to increase the signal bandwidth but this can be limited by the apparatus or use a chamber with higher conductivity but that can be quite costly. Another solution is to use signal processing in order to amplify the impulse response the most adequately as possible and use the primary amplification module as appropriately as possible. In the next section, experimental results considering signal amplification will be discussed.

4.4 Signal Processing to Increase Efficiency

In this section, we consider signal processing that allow further improvement of a classical time-reversal technique without having to change experimental conditions. The aim here is to present two

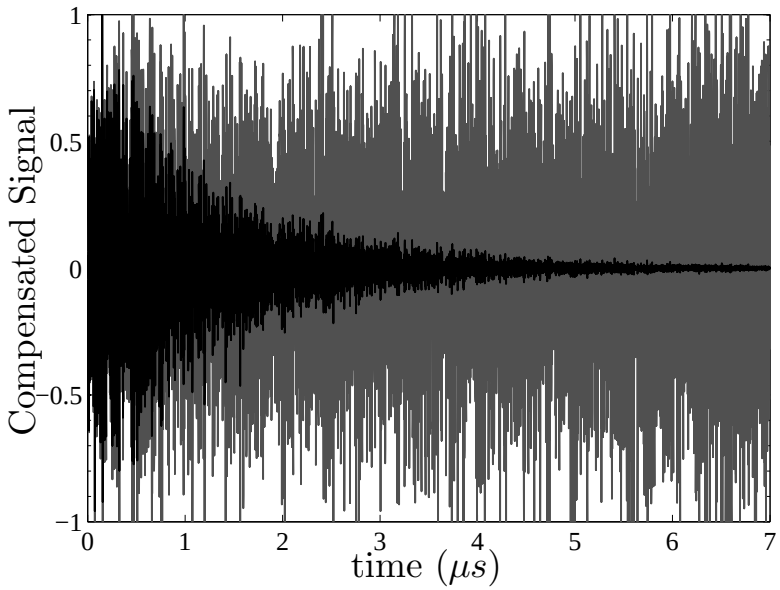

Figure 4.16 Compensated Signal and original impulse response.

types of signal processing in order to increase the refocused peak and to evaluate their effects on the contrast.

The first signal processing will considered a signal equalisation where the exponential envelope is compensated and the second one is the 1-bit signal that has already been used in previous works [38]. The signals used here are not normalised in energy since in practice the solid-state amplifiers that are not limited in energy but in the maximum power at the input.

4.4.1 Signal using envelope compensation

The first signal processing used allows to compensate exponential decay of the impulse responses thus allowing a better amplification of the refocused signal as shown in Figure 4.16. The idea is to increase the refocusing peak without having a significant impact on the contrast. The compensated signal and impulse response are shown in Figure 4.16. The signal is amplified two the saturation level of the amplifier during the whole refocusing phase allowing an increase in the focusing peak.

The added gain varies with the impulse time considered for the refocusing phase. The longer the signal, the better the amplification. Figures 4.17 and 4.18 for the small room at Supélec and the aluminium chamber. These figures represent the evaluated added gain by signal equalisation for different central frequencies when the impulse signal has a bandwidth of 300 MHz. The maximum added gain does not surpass 6 dB and saturates for times over 3 relaxation times of the room.

Another issue with this technique is that the exponential envelop must be well parametrised and the equalisation must stop before no information is contained in the impulse response. In this case the

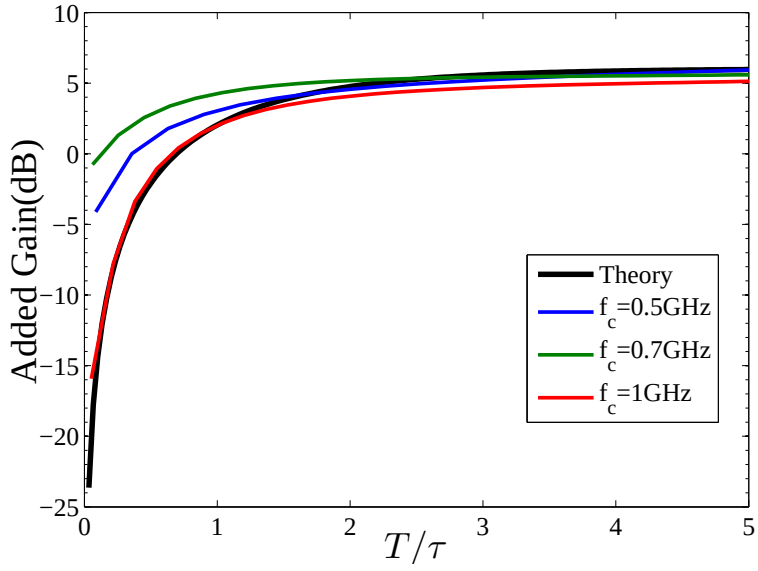

Figure 4.17 Added gain using exponential equalisation of the impulse response and variation over sampling time T/τ for Supélec's room.

equalisation amplifies the tail of the signal which contains mostly noise and the refocusing properties are completely lost.

A small theoretical model allows to verify the saturation level presented in Figures 4.17 and 4.18. This model only takes into consideration the refocusing peak and not the added noise or fluctuations.

During a classic time-reversal process the refocused signal z_{TR_c} can be expressed as:

$$z_{TR_c}(t) = h(t) \otimes h(-t), \tag{4.26}$$

where $h(t)$ is the impulse response of interest the reverberation chamber. If the focusing time is considered to be obtained at $t = 0$ the maximum peak power can thus be expressed as

$$z_{TR_c}(0) = \int_0^{+\infty} h^2(t)\, dt. \tag{4.27}$$

When the signal is equalised the expression of z_{comp} becomes:

$$z_{comp}(t) = h(t) \otimes [h(t)\, e(t)](-t), \tag{4.28}$$

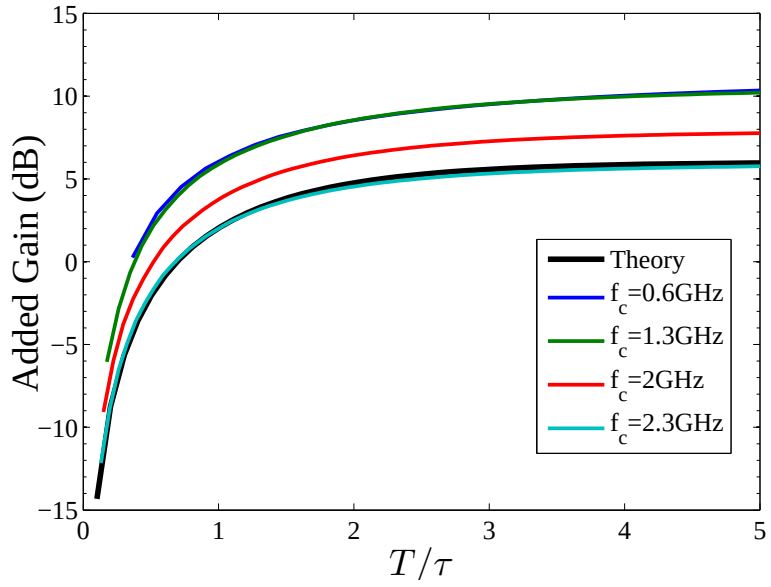

Figure 4.18 Added gain using exponential equalisation of the impulse response and variation over sampling time T/τ for the aluminium room.

in the case $e(t) \simeq \exp(+t/\tau)$ the peak-power at refocusing time becomes:

$$z_{comp}(0) = \int_0^T h^2(t) \exp(+t/\tau)\, dt, \tag{4.29}$$

where T is the time at which the re-emitted equalised signal is stopped. The expression of $h(t)$ follows an exponential decay so that recalling the expression used in sec.2.5 we have:

$$h(t) = h_0(t)\, w(t), \tag{4.30}$$

where $h_0(t) = A_0 e^{-t/\tau}$ corresponds to the RMS envelop of the impulse response as in (2.50) and $w(t)$ can be modelled as a random variable following a Gaussian distribution centred at 0 or $\mathcal{N}(0, \sigma_w)$. So that equation (4.29) can be restated as:

$$z_{comp}(0) = \int_0^T A_0^2 w^2(t) \exp(-2t/\tau) \exp(+t/\tau)\, dt = \int_0^T A_0^2 w^2(t) \exp(-t/\tau)\, dt \tag{4.31}$$

the variations of $w(t)$ depend on the bandwidth and fluctuate as $1/B_T$ which is much faster than the relaxation constant τ. Therefore, when considering $w^2(t)$ over long integration times the fluctuations

are already averaged over time thereby:

$$z_{comp}\left(0\right)=\int_{0}^{T}A_{0}^{2}w^{2}(t)\exp\left(-t/\tau\right)dt\simeq\int_{0}^{T}A_{0}^{2}\left\langle w^{2}(t)\right\rangle \exp\left(-t/\tau\right)dt=A_{0}^{2}\,\sigma_{w}^{2}\left(1-\exp\left(-T/\tau\right)\right)\tau. \tag{4.32}$$

On the other hand the peak-power attained after a classical time-reversal scheme is given by

$$z_{TR_{c}}\left(0\right)=\int_{0}^{T}A_{0}^{2}w^{2}(t)\exp\left(-2t/\tau\right)dt\simeq A_{0}^{2}\,\sigma_{w}^{2}\frac{\tau}{2} \tag{4.33}$$

The compensated gain therefore follows:

$$G_{comp}(T)=\frac{z_{comp}\left(0\right)}{z_{TR_{c}}\left(0\right)}=\frac{\left(1-\exp\left(-T/\tau\right)\right)\tau}{\tau/2}\simeq2\left(\left(1-\exp\left(-T/\tau\right)\right)\right)\leq2 \tag{4.34}$$

which in dB is equal to 6. It can be noticed that for the aluminium chamber for frequencies below 1.5 GHz the added gain can be a bit higher than the 6 dB expected with theory. However, in most cases for both chamber the theory seems to hold quite well.

It was shown in 2.5 that the standard deviation of $w(t)$ is equal to one $\sigma_w = 1$ and its average μ_w is equal to 0. As we will see in 4.4.3 the correlation factor ρ between the impulse response and the modified signal is an important element when comparing the added gain of classic and modified time-reversal. In order to better understand the evolution of the loss of correlation of the equalised signal with time when compared to the original impulse response, presented in Figure 4.20, the model of the impulse response in (4.30) $h(t)$ and the equalised signal $x(t)$ need to be normalised with their energy. The expression of the equalised signal $x(t)$ in the case of perfect equalisation is:

$$x(t)=h(t)e^{+t/\tau}=A_{0}w(t), \tag{4.35}$$

by perfect we mean that the equalised signal is not truncated because of rapid variations of the impulse response. Defining the normalised signals by $x'(t)=x(t)/\sqrt{\mathcal{E}_{comp}}$ and $h'(t)=h(t)/\sqrt{\mathcal{E}_{h}}$ we first calculate their corresponding energies:

$$\mathcal{E}_{h}=\int h^{2}(t)dt=A_{0}^{2}\int w(t)^{2}\exp\left(-2t/\tau\right)dt\simeq A_{0}^{2}\,\sigma_{w}^{2}\,\frac{\tau}{2}=A_{0}^{2}\,\frac{\tau}{2} \tag{4.36}$$

and for the equalised signal we have,

$$\mathcal{E}_{comp} = \int_0^T A_0^2\, w^2(t)dt \simeq A_0^2\, \sigma_w^2\, T \simeq A_0^2\, T \tag{4.37}$$

The correlation factor between both signals can now be expressed as:

$$\rho = \int x'(t)y'(t)dt = \int \frac{A_0\, w(t)}{\sqrt{\mathcal{E}_x}} \frac{h_0(t)\, w(t)}{\sqrt{\mathcal{E}_y}} dt \tag{4.38}$$

which gives by replacing with all their expressions:

$$\rho(T) = \int_0^T \frac{A_0^2\, w^2(t) e^{-t/\tau}}{\sqrt{\mathcal{E}_x \mathcal{E}_y}} dt = \int_0^T \frac{e^{-t/\tau}}{\sqrt{T\, \tau/2}} dt = \sqrt{\frac{2\tau}{T}} \left(1 - e^{-T/\tau}\right) \tag{4.39}$$

When $T/\tau \geq 3$ then ρ varies as $\sqrt{2\tau/T}$. The loss of correlation is slow with time T. Equation (4.32) gives the expression of the refocused signal corresponding to the correlation factor presented here. After $T/\tau \geq 3$, the injected energy by the equalised time-reversed signal compensates the loss of correlation between signals. Figure 4.20 shows the evolution of the correlation factor with time for different frequencies for impulses of 300 MHz bandwidths and their comparison to theory. The theoretical model holds for all frequencies. As predicted by the model ρ evolves very slowly with time.

Figure 4.19 represents the theoretical estimation of the added gain when using equalised signals compared to classic time-reversal. The case presented here is the same as before where the impulse is considered to have a constant spectrum over 300 MHz bandwidth. The trends of classic time-reversal still exist when using this type of signal. However, far better gains are obtained especially at low frequencies where the added gain can attain 8 dB.

In this section, predictive models were developed giving the added gain and the correlation loss when comparing equalised and classic time-reversal.

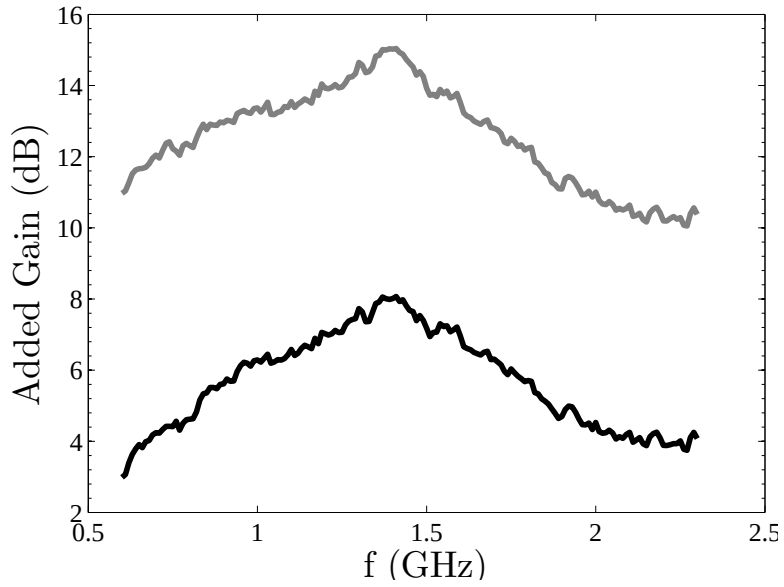

Figure 4.19 Comparison between classic time-reversal (black curve) and when using equalised signal (grey curve).

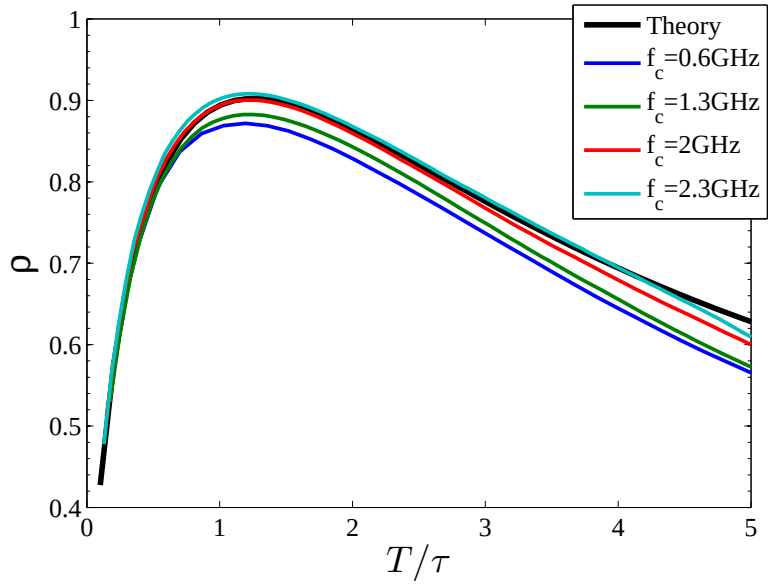

Figure 4.20 Evolution of the Correlation Factor ρ with time and comparison to theory.

4.4.2 1-bit signals

Another common signal amplification technique for time-reversal is by using 1-bit signals. Time-reversal is then said to be a 1-bit time-reversal process. The first 1-bit refocusing experiments were held by Derode in 1999 [36]. A theoretical model of the improvement of time-reversal method using

this technique is also presented in this paper. In this case only the sign of the signal is sent:

$$b(t) = \begin{cases} -1, & \text{if } s(t) \geq 0 \\ 1, & \text{if } s(t) < 0 \end{cases}$$

Using 1-bit time-reversal was proved to improve focusing gains in [36]. The expected added gain was found to be:

$$G_{1bit} = \sqrt{\frac{2}{\pi}} M_1 \frac{\int \sigma_x(t) dt}{\int \sigma_x^2(t) dt} \tag{4.40}$$

where M_1 is the maximum value of impulse response and $\sigma_x^2(t)$ the variance of the impulse response. If σ is taken to be constant, this ratio simplifies into $\sqrt{\frac{2}{\pi}} \frac{M_1}{\sigma_x}$ meaning that an amplification saturation must occur when the bandwidth is large enough.

A representation of the added gain using a 1-bit time-reversal signal is presented in Figure 4.21. Here again the added gains quite important. The real gain still follows the same trends than the classical time-reversal, however this time the gains obtained vary between 16 and 21 dB.

However, experimental data shows a saturation of the added gain of roughly $G_{1bit}^{dB} \simeq 13.4$ dB when comparing classical and 1-bit time-reversal when the bandwidth of the signal is over 50 MHz (eg. Figure 4.22).

The set-up presented here has the advantage of only using one receiving antenna compared to previous works and still allows some high peak-power refocusing levels. The variation of the contrast levels for the different signal compensation and for a classical time-reversal process are presented in Figure 4.23. The contrast levels are calculated from equation (3.35). As expected by theory the contrast levels increase with the bandwidth of the signal [114, 165]. Surprisingly, signal equalisation does not allows better contrast than the 1-bit signal processing even if the noise levels are much smaller in the first case as shown in Figure 4.24. The energy in the noise of the refocused signal using the equalised signals was found to be less than one fifth of those using a 1-bit time-reversal process. There seems to be a certain limitation to this. Indeed, the contrasts reach the same levels for higher frequencies. In both cases the contrast levels increase with frequency.

A trade-off over which signal processing is to be used can be made when considering the application. If for the application or test measurement only the peak value is of interest, then a 1-bit signal processing should be considered. However if a lower level of noise level is more important than the gain then equalisation can be used. Would it be possible to obtain to obtain added gains close to those achieved using a 1-bit time-reversal process while obtaining contrast levels close or even better than

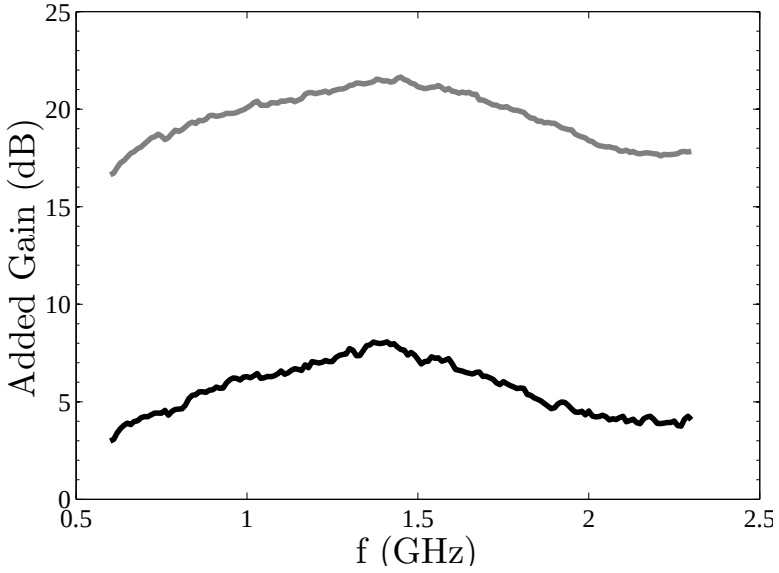

Figure 4.21 Comparison between classical time-reversal and when using 1-bit time-reversed signals.

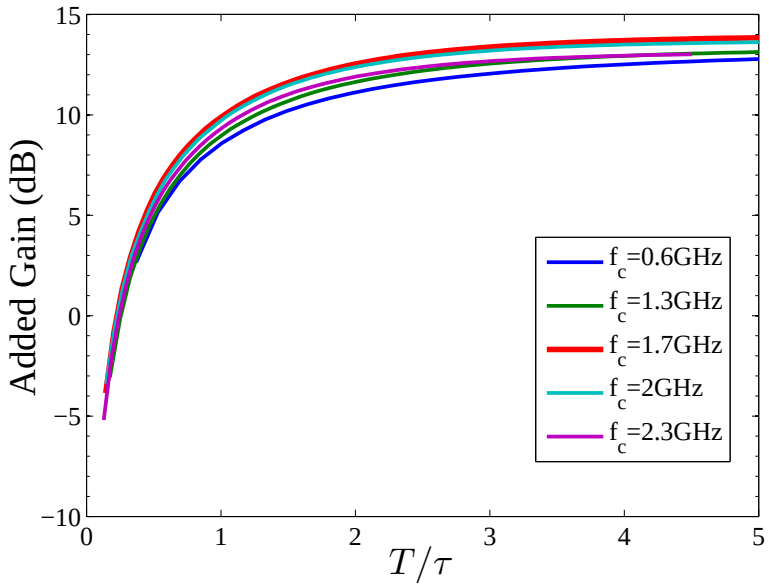

Figure 4.22 Added gain using 1-bit time-reversal of the impulse response and variation over sampling time T/τ for the aluminium chamber for signals of 300 MHz bandwidths.

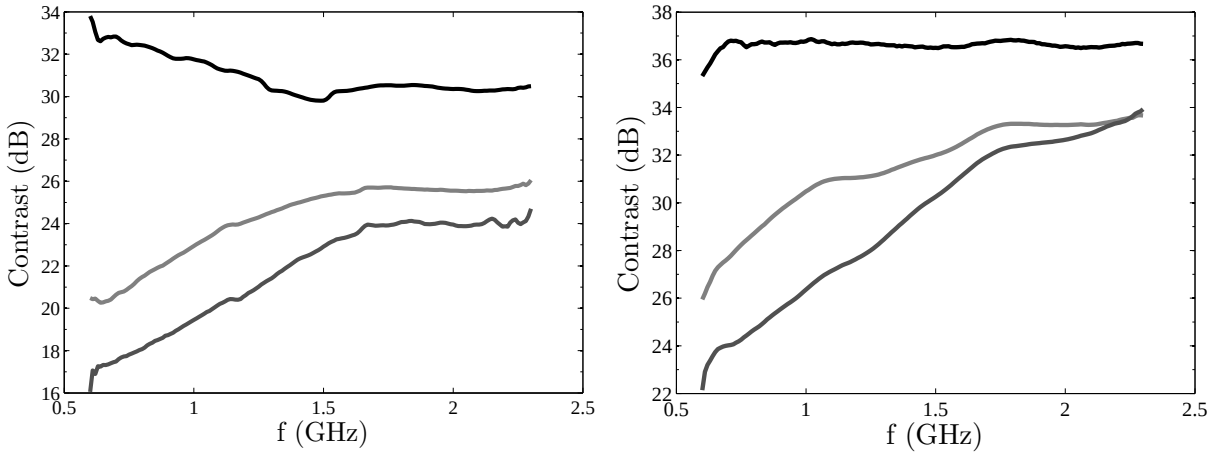

Figure 4.23 Contrast variations over frequency for classic time-reversal (black curve), signal equalisation (dark-gray curve) and 1-bit signal processing (light-gray line). The results are presented for signal of bandwidth: (a) 50 MHz and (b) 300 MHz

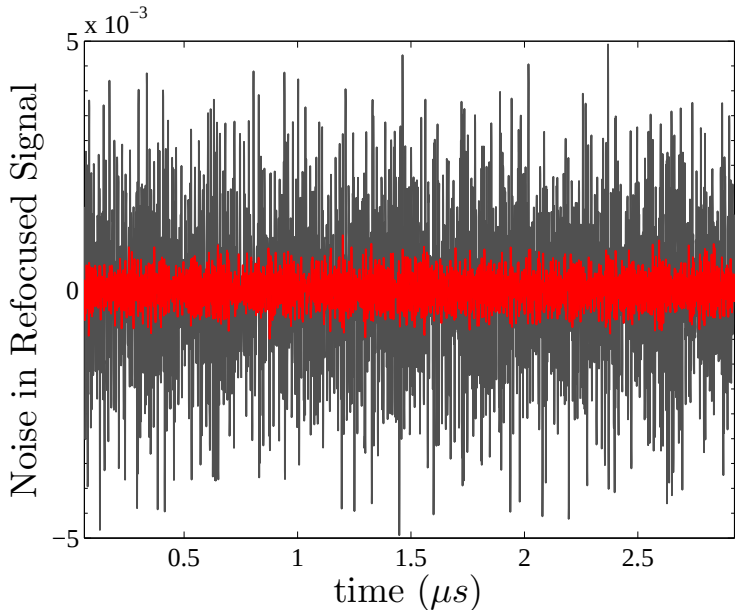

Figure 4.24 Noise in refocused signal for signal equalisation (red-curve) and 1-bit (grey-curve).

those obtained using a classic time-reversal process using variations of the signal processing mentioned in the last two sections? The studies presented below give elements of response to that question.

4.4.3 From envelope compensation to 1-bit signal

In order to give further explanations on the variations of contrast and gain between the signal processing presented above, the analysis presented here shows the contrast and gain trends when multiplying the equalised or the original impulse response signal by an amplification coefficient without changing the maximum level of the compensated signal. The maximum level of the injected signal is thus bounded by the maximum of the impulse response. The time-reversed signal will tend to a 1-bit case as the amplification coefficient increases. Recalling the model used for the refocused signal in equation (3.41) we have:

$$z(t) = \alpha x(t) + n(t). \tag{4.41}$$

Where $\alpha x(t)$ is coherent with the original signal $x(t)$ and $n(t)$ is the residual noise due to the distortion of the pulse introduced by the variations of the transfer function $H(f)$ of the medium. α can be seen as a sum of all the echoes adding coherently. The aim here is to show the evolution of the coherence coefficient when the impulse-response signal is distorted in order to try and shed some light on the additional gain added when using a 1-bit time-reversal signal process.

In [7, 81], it was shown that at best only half of the total injected energy will be efficiently refocused. Any distortion from an ideal time-reversal process will decrease its energy efficiency. This in turns leads to an increase amount of the total energy in the noise. This corresponds to the case where perfect time-reversal process is used. The more distorted the signal, the more the coherent factor that will be efficiently refocused α will be small and the energy in the noise will increase. However, as it was shown in the previous section, the added gain can still be significantly increased and contrast levels can be further improved when considering highly distorted signals instead of for example simple equalisation.

An explanation for this, is that the support over which the fluctuations maintain an almost constant average intensity after refocusing is for short pulses, much larger than that of the coherent part of the signal. The noise is proportional to the relaxation time of the cavity, i.e., $\bar{Q}/\omega_c$, in the case of a classic time-reversal process and the pulse $x(t)$ is proportional to $1/B_T$. Therefore, the application of classic or modified time-reversal to reverberating cavities though allowing the reception of clear reproductions of a template signal $x(t)$ is done at the expense of a reduced energy efficiency, since at least the same amount of energy is wasted into residual random fluctuations running over a long span of time.

In order to study in a more detailed manner the evolution of the contrast and the added gain, the equalised signal is multiplied by an amplification coefficient without changing the maximum level.

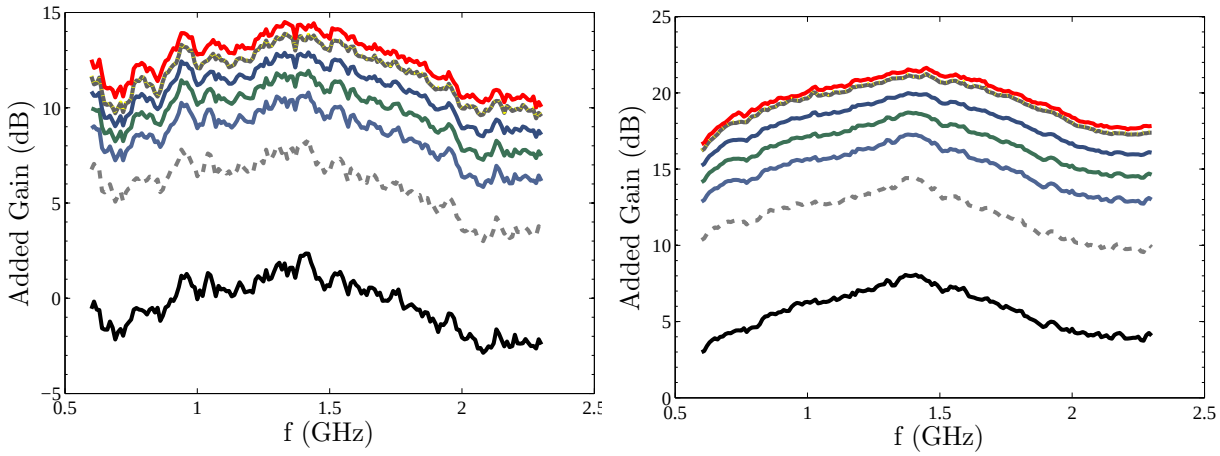

(a) (b)

Figure 4.25 Added Gain variations over frequency for classic time-reversal (black curve), signal equalisation (dashed light-grey curve), with a multiplication factor of 1.5 (light-blue), 2 (light-green), 3 (dark-blue), 15 (yellow) and 10000 (dashed dark-grey). The red curve corresponds to the 1-bit signal processing. The results are presented for signal of bandwidth: (a) 50 MHz and (b) 300 MHz

The 1-bit case becomes a limiting case of this process. Figure 4.25 and 4.26 represent the added gain and contrast levels when the signal is multiplied by different coefficients for bandwidths of 300 MHz and 50 MHz.

As expected, the added gain and contrast increase when the multiplying factor augments and the signal tends to the 1-bit case. For the contrast this is due to the fact that the time-constants of the noise are much larger than for the refocusing time. Therefore, even if the energy in the noise is more important when multiplying by the amplification factor, that energy is spread over time whereas the peak refocuses at much higher levels. However, this trend does not seem to hold for the contrast in Figure 4.26. When the equalised signal is multiplied by factors between 3 and 5 the contrast levels become higher than for 1-bit signals especially at lower frequencies and the added gains are close to those obtained with the 1-bit case. This is due to the fact that the equalised signal is shorter in time than the 1-bit case. The signal at long times has very little to no information grains especially at low frequencies and almost all the energy will not be refocused in the peak but will be found in the noise. This explains this discrepancy between 1-bit and multiplied cases of the equalised signal for the added gain and contrast.

Figures 4.27 and 4.28 show the evolution of the added gain for different fixed frequencies for impulse signals of 50 and 300 MHz bandwidths. The added gain and contrast levels saturate even for small amplification factors. For factors above 5 there seems to be a saturation of both contrast and added gain trends. This means that the physical process explaining the additional gain of the 1-bit time-reversal process is in close link to this amplification factor and varies sharply with it. The contrast seems to improve compared to the equalisation signal when the amplification factor is increased but,

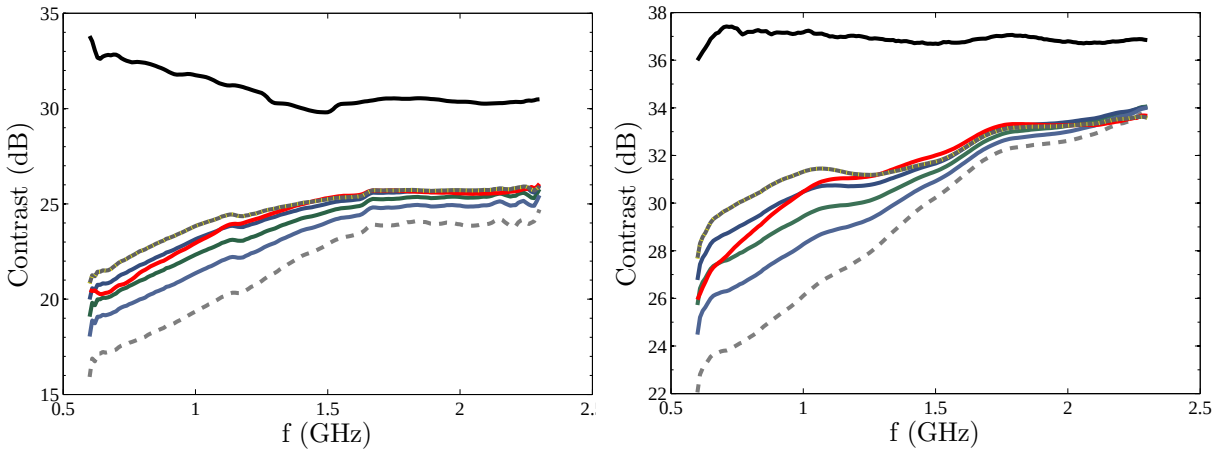

(a) (b)

Figure 4.26 Contrast variations over frequency for classic time-reversal (black curve), signal equalisation (dashed light-grey curve), with a multiplication factor of 1.5 (light-blue), 2 (light-green), 3 (dark-blue), 15 (yellow) and 10000 (dashed dark-grey). The red curve corresponds to the 1-bit signal processing. The results are presented for signal of bandwidth: (a) 50 MHz and (b) 300 MHz

as mentioned previously, this does not mean that the time-reversal process is more efficient just that the peak-power coming from the rapid impulse detaches itself more from the long-lasting noise even if the energy in the refocused noise is more important.

Figure 4.29 shows the evolution of the correlation factor between the original impulse response and the equalised impulse response when multiplied with the amplification factor. Surprisingly, the correlation factor varies very slowly when the signal is abruptly modified compared to the equalised case. The values vary between 0.7 when the signal is simply equalised to 0.56 when the signal resembles the 1-bit case. The loss of information in the signal thus varies very slowly with signal modification. These results prove that the maximum value of the impulse response is probably not the most adequate when considering signal amplification using time-reversal. The derivation below proves this assertion and shows that the value that should be considered when trying to obtain the maximum refocused peak-power is the root mean square (RMS) of the time-reversed signal. Lets consider that the refocused signal is obtained at $t = 0$ then we obtain:

$$z(0) = \int P^{*}(\omega)\, H(\omega)\, d\omega. \tag{4.42}$$

Where $z(t)$ is the refocused signal, $P^{*}(\omega)$ is the Fourier transform of the time-reversed signal and $H(\omega)$ is the corresponding transfer function between receiving and transmitting antenna of the

considered time-reversal process. When normalising by the energy of the different factors we obtain:

$$z(0) = \int \sqrt{\mathcal{E}_p}\sqrt{\mathcal{E}_h}\, p^*(\omega)\, h(\omega)\, d\omega = \sqrt{\mathcal{E}_p}\sqrt{\mathcal{E}_h}\, \rho \tag{4.43}$$

where ρ is a frequency coherence factor, $\mathcal{E}_h$ and $\mathcal{E}_p$ are the energies of the impulse response and the injected signal during the time-reversal process. The energy in the equalised time-reversed signal can be approximated by:

$$\mathcal{E}_p = (A * A_0)^2\, T = p_{rms}^2\, T \tag{4.44}$$

where A is the amplification coefficient, T is the duration of the signal with constant envelop and p_{rms} is the root mean square value of the equalised signal. This expression is only valid as long as the random process $w(t)$ described previously is still valid when considering the amplified compensated signal. The energy in the impulse response is equal to:

$$\mathcal{E}_h = \int h^2(t)dt = A_0^2 \int \exp(-2t/\tau)dt = A_0^2\, \frac{\tau}{2} \tag{4.45}$$

where A_0 is the root mean square value of the impulse response at $t = 0$. The refocused peak expression becomes:

$$z(0) = \rho(T)\; A_0\, p_{rms} \sqrt{T\, \frac{\tau}{2}} \tag{4.46}$$

The best case scenario that allows the highest refocused peak corresponds to the case where the root mean square value of the time-reversed signal is equal to the highest value possible while keeping the highest coherence ρ possible. As was shown in Figure 4.29 the correlation factor varies very slowly with the amplification factor and is always above 0.55 so that refocusing peak depends more on p_{rms}.

The signal must be chosen so that its root mean square value is closest to the maximum power allowed in the power amplifiers. The signal corresponding to maximum refocused peak-power is then the 1-bit time-reversed impulse response. For such a signal the rms value is equal to the maximum power that can be injected in the chamber. Contrary to what was studied previously the maximum value of the impulse response should therefore not be taken as the limiting factor for the margin but the its root mean square value when considering maximum power refocusing.

Special attention must be taken when interpreting equation (4.46). The peak value does not increase indefinitely when T goes to infinity since the correlation factor decreases after 3τ as proven in the previous section.

Figure 4.30 shows the evolution of the ratio between the maximum value of the impulse response and the rms value of the amplified signal for different frequencies. The higher the amplification factor the closer the ratio tends to unity. The ratio between root mean square of the time-reversed signal and the maximum of the impulse response varies from 0.3 for the equalised signal to 0.95 when multiplied by 20 or more. This difference between RMS and maximum values explains the 8.5 dB difference between the 1-bit refocusing and equalised refocusing. The correlation factor between a 1-bit signal and an amplified equalised signal by a factor 20 was found to be 0.97 showing that those signals are very close. The 1-bit time-reversal process correspond to a ratio of the rms to the maximum equal to 1.

Conclusion

The study undertaken in this section gives a new understanding of the physics underlying peak refocusing and presents the limiting factors when considering signal amplification using time-reversal. It also brings an innovative explanation as to why 1-bit time-reversal allows to obtain such important gains. 1-bit signal processing was found to be a limiting case of a signal equalisation multiplied by an amplification factor. The peak-refocused signal was found to depend on the correlation between the impulse-response and the time-reversed injected and the root mean square of the injected signal. The correlation factor was found to vary very slowly with the amplification factor even for cases close to a 1-bit signal processing. Consequently, the loss of information is much less important when transitioning from a classic time-reversal to a highly distorted signals than expected. For such signals, their RMS values are almost equal to the maximum of the impulse response which for a classic time-reversal was found to be close to a third of the maximum value in section 3.3. Therefore, the increase in energy compensates the loss of correlation between signals.

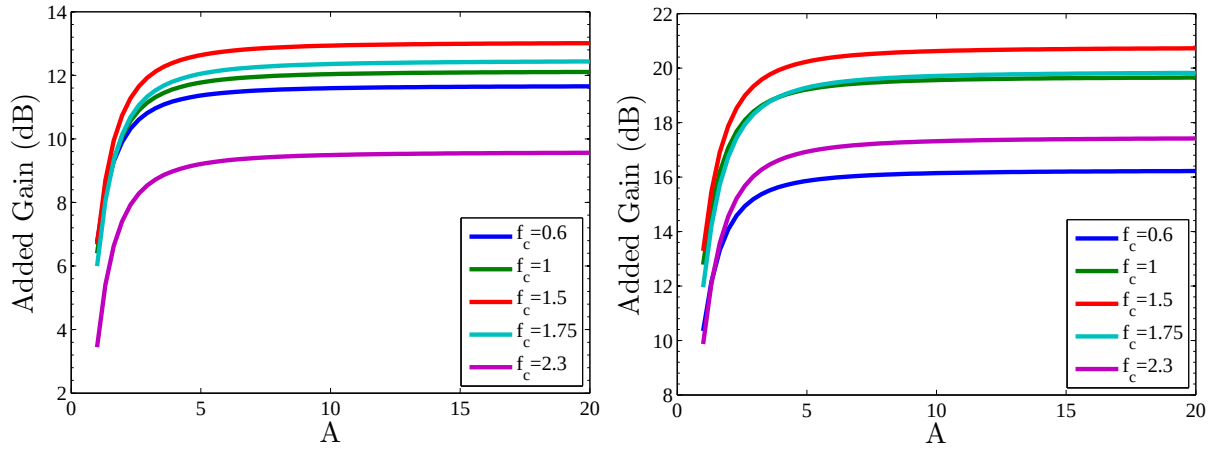

Figure 4.27 Added Gain variations while the Amplification Factor A is varied for different central frequencies: 600 MHz (blue curve), 1 GHz (green curve),1.5 GHz (red curve), 1.75 GHz (light-blue curve), 2.3 GHz (purple curve). $A = 1$ corresponds to signal equalisation case. The results are presented for signal of bandwidth: (a) 50 MHz and (b) 300 MHz

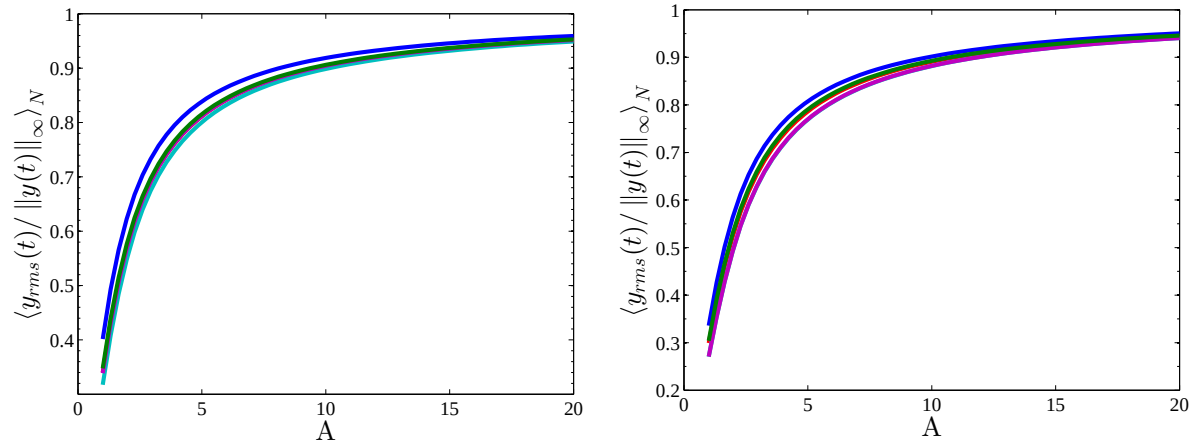

Figure 4.30 Ratio $\langle y_{rms}(t)/\|y(t)\|_\infty\rangle_N$ with the Amplification Factor A varied for different central frequencies: 600 MHz (blue curve), 1 GHz (green curve),1.5 GHz (red curve), 1.75 GHz (light-blue curve), 2.3 GHz (purple curve). $A = 1$ corresponds to signal equalisation case. The results are presented for signal of bandwidth: (a) 50 MHz and (b) 300 MHz

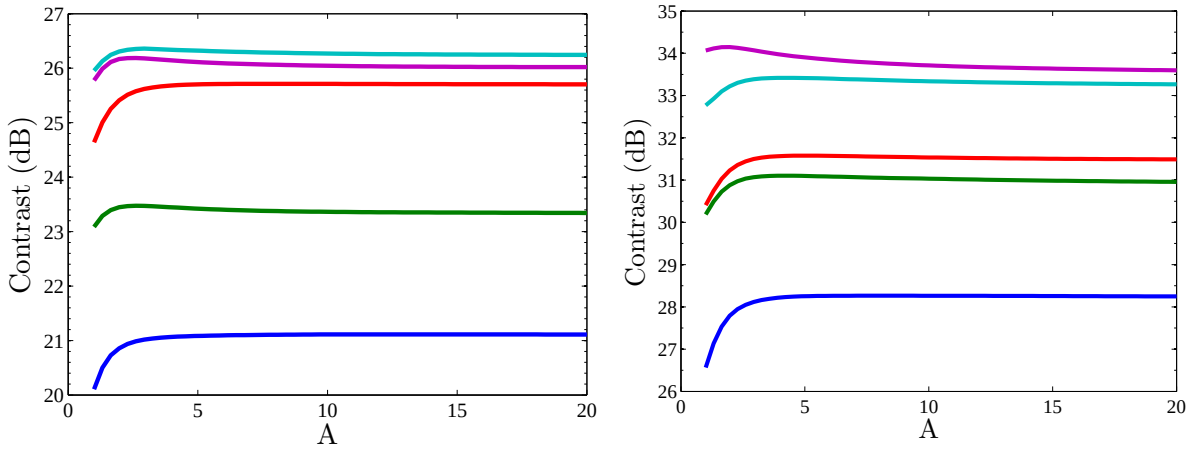

(a) (b)

Figure 4.28 Contrast variations while the Amplification Factor A is varied for different central frequencies: 600 MHz (blue curve), 1 GHz (green curve),1.5 GHz (red curve), 1.75 GHz (light-blue curve), 2.3 GHz (purple curve). $A = 1$ corresponds to signal equalisation case. The results are presented for signal of bandwidth: (a) 50 MHz and (b) 300 MHz

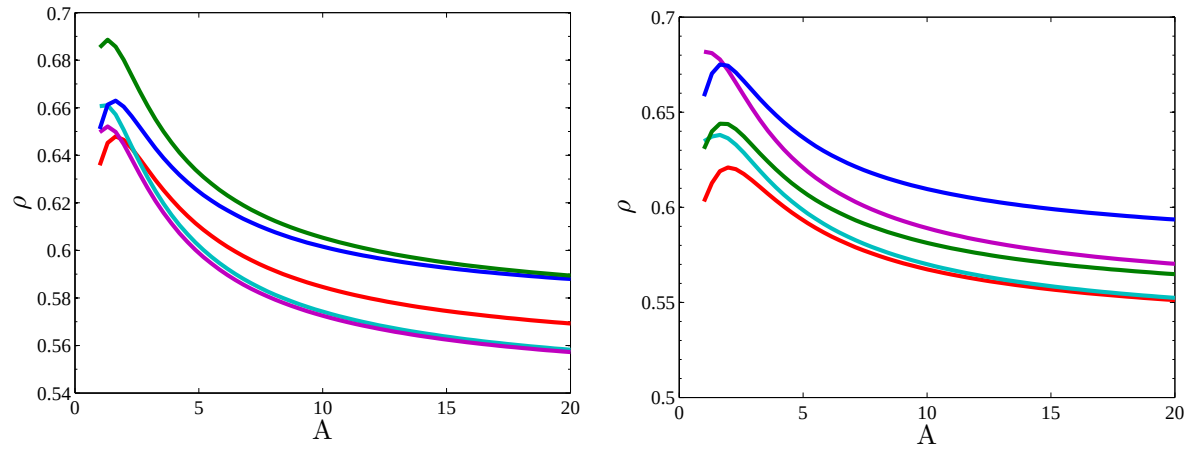

(a) (b)

Figure 4.29 Correlation Factor between the original impulse response and the equalised signal with the Amplification Factor A varied for different central frequencies: 600 MHz (blue curve), 1 GHz (green curve),1.5 GHz (red curve), 1.75 GHz (light-blue curve), 2.3 GHz (purple curve). $A = 1$ corresponds to signal equalisation case. The results are presented for signal of bandwidth: (a) 50 MHz and (b) 300 MHz

4.4.4 Models for the 1-bit time-reversal

Another approach is possible in order to improve the theoretical model presented previously in equation (4.46). Indeed in practise, access to some of the values presented might not be so direct. When considering a real 1-bit signal the statistical variations differ from the classic and envelop compensation case. An additional loss of correlation is then introduced as can be seen when comparing Figures 4.20 and 4.31. This loss can be modelled by additional factor in (4.39). In [36, 107] the impulse response is modelled as a "shot noise" process and the expected value of this statistical variation was found to be equal to $\sqrt{2/\pi}$ of the correlation factor. The model for the correlation factor of equation (4.39) thus becomes:

$$\rho(T) = \sqrt{\frac{2}{\pi}}\sqrt{\frac{2\tau}{T}}\left(1 - e^{-T/\tau}\right) \tag{4.47}$$

The result of equation (4.46) is then:

$$z_{1-bit}(0) = \rho_{1-bit}\sqrt{\mathcal{E}_{1-bit}}\sqrt{\mathcal{E}_h} = A_0\, p_{rms}\tau\sqrt{\frac{2}{\pi}}\left(1 - e^{-T/\tau}\right) \tag{4.48}$$

which is close to the result obtained in (4.32). The model for the added gain can be now be obtained in a similar fashion than in (4.34):

$$G_{1-bit}(T) = \frac{z_{1-bit}(0)}{z_{TRc}(0)} = \sqrt{\frac{2}{\pi}}\,\frac{A_0\, p_{rms}\tau\left(1 - e^{-T/\tau}\right)}{A_0^2\,\frac{\tau}{2}} = 2\,\frac{p_{rms}}{A_0}\sqrt{\frac{2}{\pi}}\left(1 - e^{-T/\tau}\right) \tag{4.49}$$

This solution can be further simplified by noticing that p_{rms}/A_0 is nothing else than the factor K presented in 2.5 since the rms value of the 1-bit signal is equal to the maximum value of the impulse response when considering normalised signals. The added gain for a 1-bit time-reversal process simplifies to:

$$\boxed{G_{1-bit}(T) = 2\,K\,\sqrt{\frac{2}{\pi}}\left(1 - e^{-T/\tau}\right)} \tag{4.50}$$

The added gain when comparing to a signal compensation is equal to $K \times \sqrt{2/\pi}$. The ratio K between the maximum value and its rms was found to have a mode close to 2.8 from equation (2.62) for the aluminium chamber under consideration. The maximum added gain compared to a classic time-reversal is thus equal to $Ad = 2\,K\,\sqrt{2/\pi}$ which in decibels becomes $20 \times \log_{10}\left(2 \times 2.8 \times \sqrt{2/\pi}\right) \simeq 13$ dB.

This coefficient Ad corresponds to the one found in [36]. Figures 4.31 and 4.32 below show the evolution of the correlation factor ρ and the added gain with time normalised to the decay-rate and their comparison to theory. Both models fit very well to theory, the small variation are due to the variations of the the mode of K for the different frequencies considered here.

Conclusion

In this section, we were able to develop a model that allows us to quantify the added gain and the correlation loss of a 1-bit time-reversal process compared to a classic time-reversal. The total gain of a 1-bit time-reversal process is simply the product between the realised gain presented in equation (4.18) and Ad.

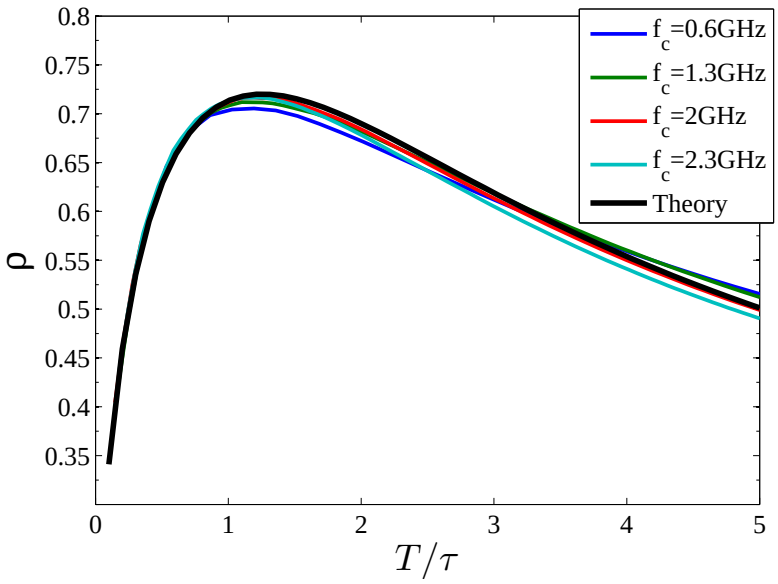

Figure 4.31 Evolution of the Correlation Factor ρ with sampling time T/τ for the aluminium room and comparison to theory.

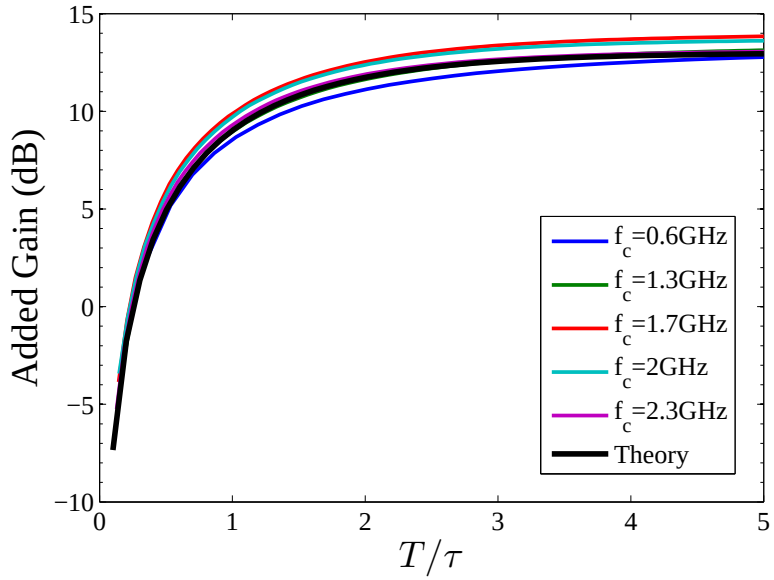

Figure 4.32 Added gain using 1-bit time-reversal of the impulse response and variation over sampling time T/τ for the aluminium chamber for signals of 300 MHz bandwidths and comparison to theory.

Truncated Impulse Response

One of the results illustrated in the previous section and that we didn't insist upon is that the slight difference in added gain between the 1-bit case and the amplified equalised signal is due to the fact that the equalised signal is shorter in time than the 1-bit case. There is still some information grains left in the far end side of the impulse response, however this added gain adds more noise before and after refocusing lowering contrast levels at low frequencies where the impulse response is shorter.

This result lead to another analysis in order to determine if it possible to increase the added gain without having too much effect on the noise levels. Figures 4.34 to 4.38 correspond to this other study. In this case, the impulse response is simply multiplied by different factors and truncated at the maximum of the original impulse response before being time-reversed as shown in Figure 4.33. The beginning of the signal thus tends rapidly to 1-bit case without cutting the rest of the signal out loosing the information.

The following graphics allow a comparison between equalisation and this truncated signal treatment. As previously 1-bit time-reversal is found to be a limiting case of this treatment, when multiplied by very high factors the truncated signal becomes similar to 1-bit on the entire time-range as can been seen in Figures 4.34 and 4.35 the contrast and added gains levels tend to a 1-bit time-reversal process when the original impulse response is simply multiplied. Surprisingly, when using this signal processing there seems to be some factors for which the added gain is close to the 1-bit case while obtaining higher contrast levels than classic time-reversal.

In order to shed some light on these results, the evolution of the added gains, contrast and correlation factor with the amplification factor are presented respectively in Figures 4.36, 4.37 and 4.38. The multiplying factor is swept from 1 to 1000. For factors above 30 the added gain saturates at levels close to the 1-bit case. Interestingly, for factors below 30 the contrast levels are higher than a classic time-reversal while the added gains are close to a 1-bit case. The correlation factor decreases very slowly with the amplification factor before saturating for values above 200. The correlation factors are close to 0.7 for factors around 50. Therefore, there exist a range of amplification factors between which the added gain is quite close to a 1-bit case and the contrast close or even better than classic time-reversal. A trade-off is then necessary in order to choose between contrast or added gain. Typically, an amplification factor of 25 allows both a good contrast and enhanced gains over the frequency span of interest.

There thus seems to be a way to amplify the refocusing peak while still obtaining good results for the contrast.

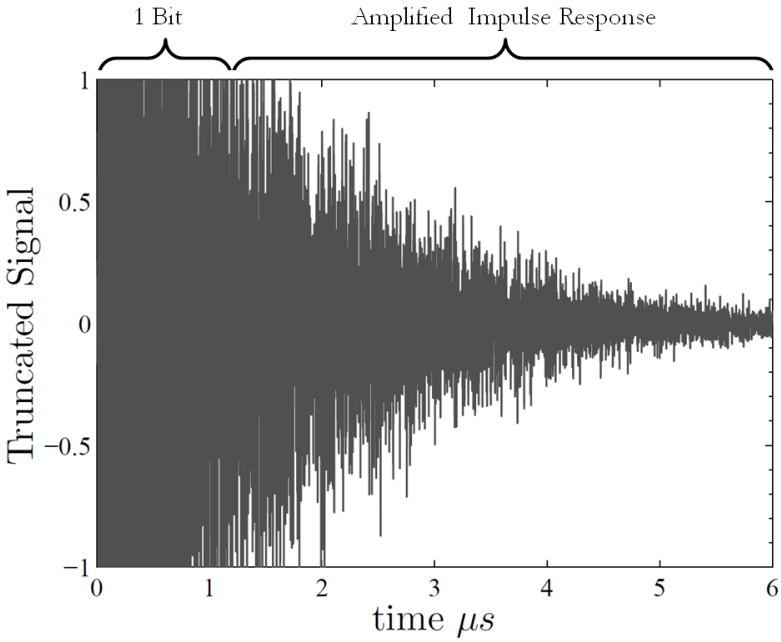

Figure 4.33 Normalised truncated signal, impulse-response multiplied by 4.

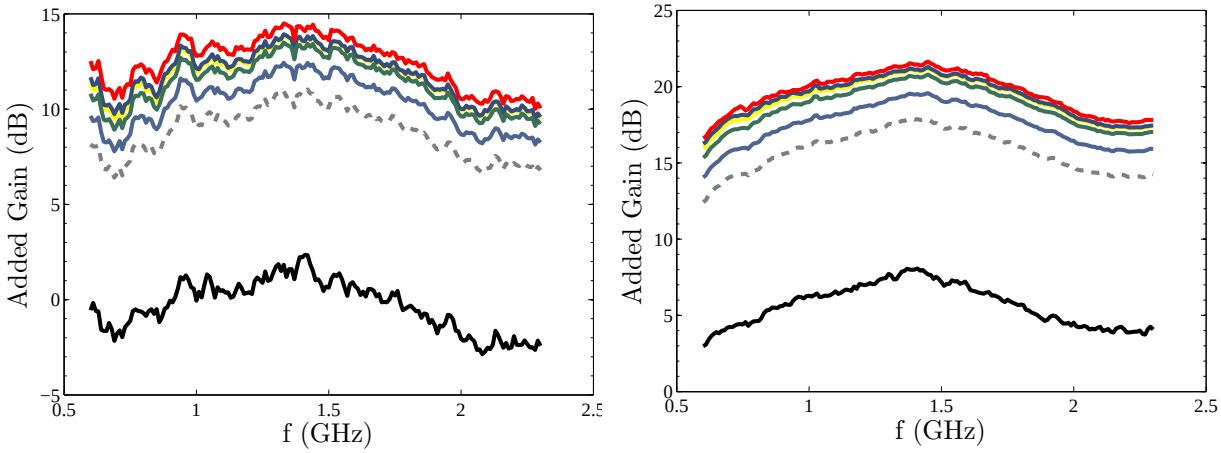

Figure 4.34 Added Gain variations over frequency for classic time-reversal (black curve) and truncated signals with multiplication factors of 5 (dashed light-grey), 10 (light-blue), 30 (light-green), 100 (yellow) and 10000 (dark-blue). The red curve corresponds to the 1-bit signal processing. The results are presented for signal of bandwidth: (a) 50 MHz and (b) 300 MHz

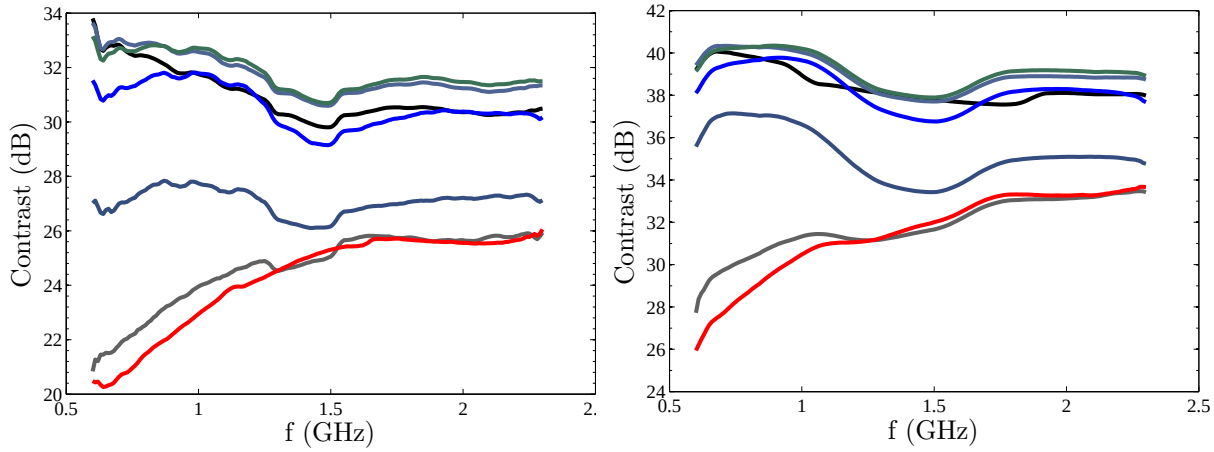

(a) (b)

Figure 4.35 Contrast variations over frequency for classic time-reversal (black curve) and truncated signals with multiplication factors of 5 (light-blue), 10 (light-green), 30 (blue), 100 (dark-blue) and 10000 (dark-gray). The red curve corresponds to the 1-bit signal processing. The results are presented for signal of bandwidth: (a) 50 MHz and (b) 300 MHz

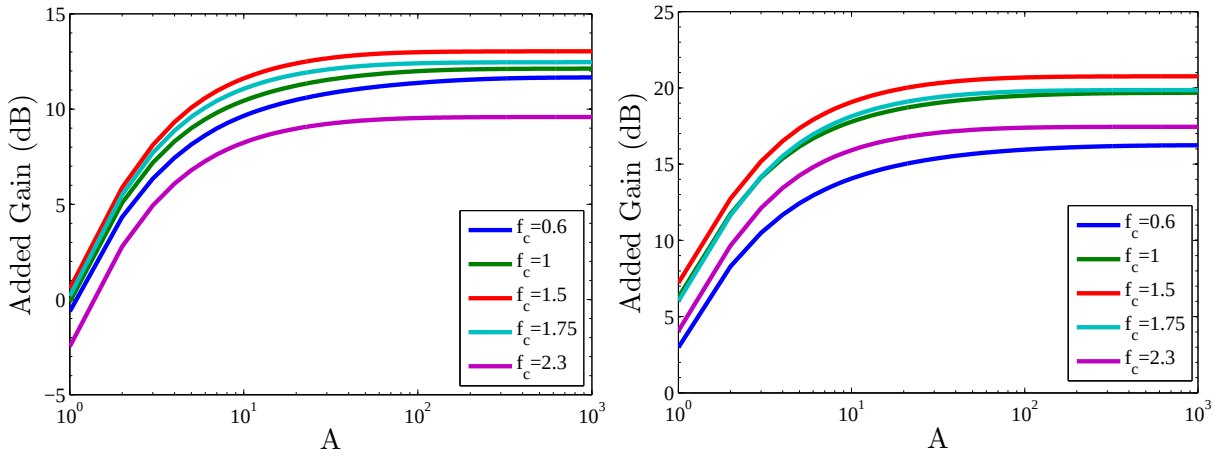

(a) (b)

Figure 4.36 Added Gain variations while the Amplification Factor A is varied for different central frequencies: 600 MHz (blue curve), 1 GHz (green curve),1.5 GHz (red curve), 1.75 GHz (light-blue curve), 2.3 GHz (purple curve). $A = 1$ corresponds to the original impulse response. The results are presented for signal of bandwidth: (a) 50 MHz and (b) 300 MHz

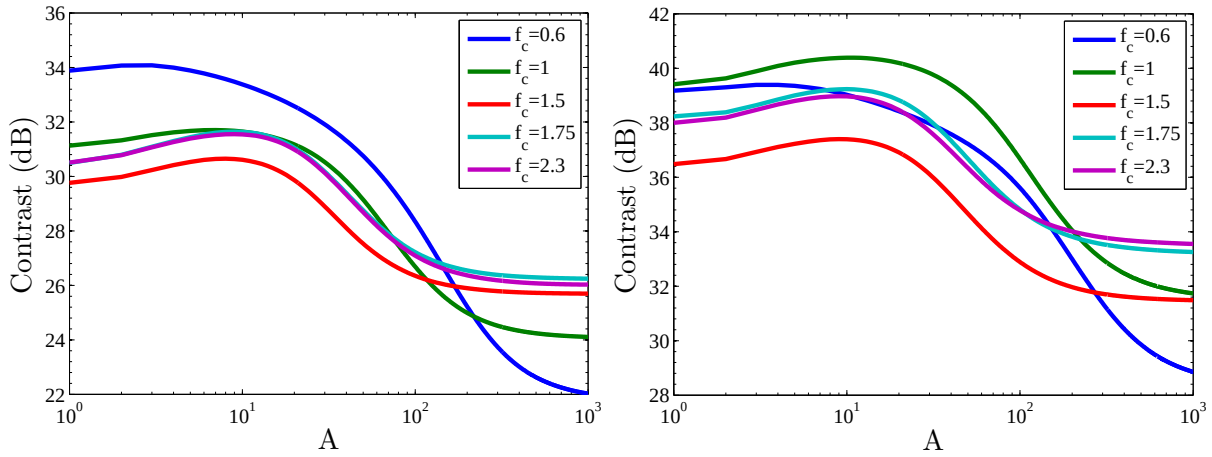

Figure 4.37 Contrast variations while the Amplification Factor A is varied for different central frequencies: 600 MHz (blue curve), 1 GHz (green curve),1.5 GHz (red curve), 1.75 GHz (light-blue curve), 2.3 GHz (purple curve). $A = 1$ corresponds to the original impulse response. The results are presented for signal of bandwidth: (a) 50 MHz and (b) 300 MHz

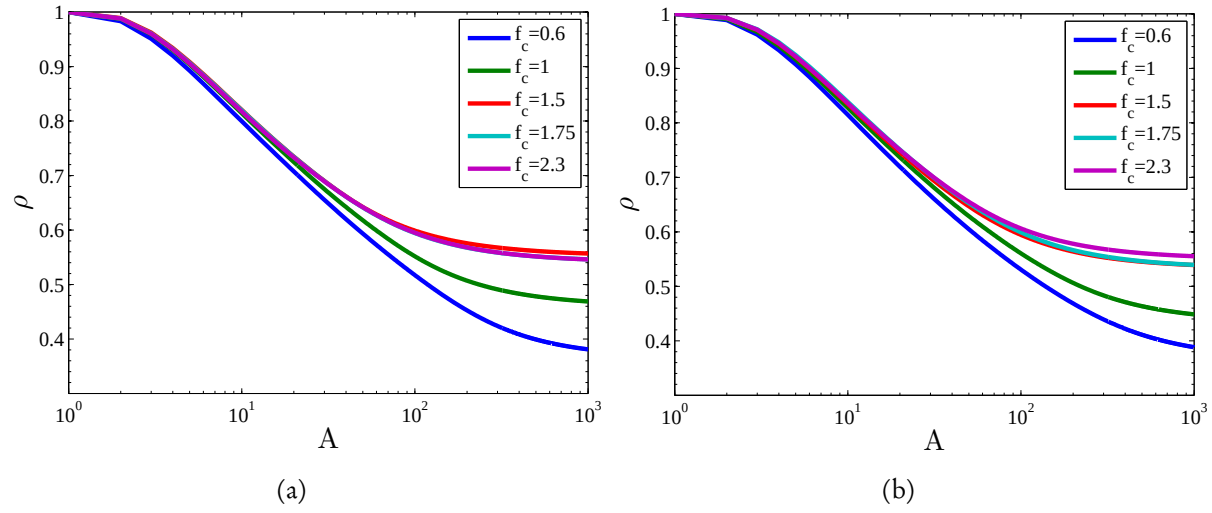

Figure 4.38 Correlation Factor of the original impulse response $A = 1$ with the Amplification Factor A varied for different central frequencies: 600 MHz (blue curve), 1 GHz (green curve),1.5 GHz (red curve), 1.75 GHz (light-blue curve), 2.3 GHz (purple curve). $A = 1$ corresponds to the original impulse response. The results are presented for signal of bandwidth: (a) 50 MHz and (b) 300 MHz

In order to further prove the models and the experimental data shown in this section, a prototype that allows to measure time-reversal properties in time was also developed during the course of this PhD. The results of which are presented in the next section.

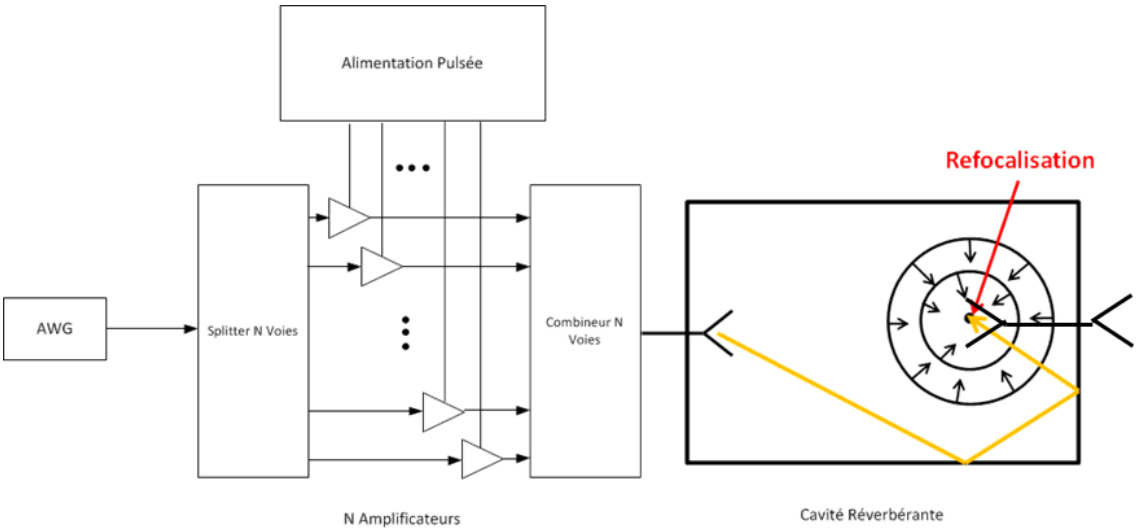

Figure 4.39 Architecture of the prototype with the amplification module.

4.5 TRAS Prototype Development and Experimental Verifications

Here the TRAS prototype used for experimental validation of a time-reversal amplification system is presented. The elaboration and conception of the different parts of the prototype have been part of a joint effort with THALES Communication & Security and myself during the three years of my PhD. A brief summary of the characteristics of the principal constituents of the proposed system is presented in this section

The technical specifications for the TRAS prototype were as followed:

- The TRAS should work between 0.5 and 2.5 GHz
- The output power should be of the order of several kWs
- The TRAS should be transportable
- The system should allow to refocus different impulse shape, bandwidth and central frequency
- The TRAS should allow control over the polarised refocused signal

The architecture proposed for the prototype is presented in Figure 4.39. An Arbitrary Waveform Generator or a Vector Signal Generator is connected to multiple amplification modules are put in parallel and controlled by a pulsed-power source via a wideband high-power splitter. The output signals from the N amplification modules are then recombined and the signal is sent via a emitting antenna inside the chamber. The signal is refocused on an output antenna placed somewhere else in the chamber and the signal is re-emitted to the outside via another antenna or sent towards measuring equipment.

4.5.1 Amplifiers

The amplifiers modules used for the prototype are solid-state power amplifiers using GaN technologies. The specifications of the TRAS system imply that the SSPA must:

- have the most linear phase over the frequency range
- have a good dynamic
- be the most linear as possible
- have good modularity in case one of the transistors stops working

An important part of systems that used vacuum technologies are being slowly replaced by solid-state technologies. However Power-Amplification has not yet seen such a shift in technology. The main reason for this is that up until recently, solid-state technologies were not capable of working at high temperature > 250 °C or at frequencies above 100 GHz. The development of new technologies have allowed to push this frontier especially with GaN. Gallium Nitrate is a material with high energy gap enabling the amplification of high-powers. The saturation speed of the electrons which is related to the amount of current allowed is high making GaN a good candidate for microwaves applications. Moreover its breakdown field is important allowing high output powers to be obtained and its' high thermal conductivity allows it to rapidly dissipate heat. The table of GaN characteristics is presented in annex. GaN allows the realization of transistors for generating power such as MESFETs (Metal - Semiconductor Field Effect Transistor) or HEMTs (High- Electron -Mobility Transistor) , used primarily for their good performance in transceiver systems and microwave signal processing.

The SSPA transistor that were used for the prototype are model CHK015A built by UMS (United Monolithic Semiconductors). These transistors are of HEMT type. The compression point at 1 dB of these transistors is attained at $P_{1dB} = 15$ W and are very large band (Specified to work between DC and 3 GHz).

The amplifiers were especially developed for this prototype. The polarisation circuit and input and output adaptation of the amplification card are quite complicated and are not of interest for what follows, however a picture of the complete circuit is presented in Figure 4.40 and the measured and simulated performances are shown in Figure 4.41. The obtained gain is quite linear and is equal to 12 dB and the $S11$ is belows -10 dB over all the frequency range meaning that most of the input power is transited to the transistor. Moreover, the measured and simulation values of the curves are very close showing that the simulations are valid.

A pulsed power source was also developed for the purpose of this work. The sequenced pulsed power is represented in Figure 4.42. A trigger signal coming from the generator commands the power sequence allowing the amplifiers to be powered only when needed. In such a case the transistors can be pushed above specifications allowing a gain in performances. A small delay is added to make sure that the signal will be transmitted to the amplifier when it is powered and to allow transients to

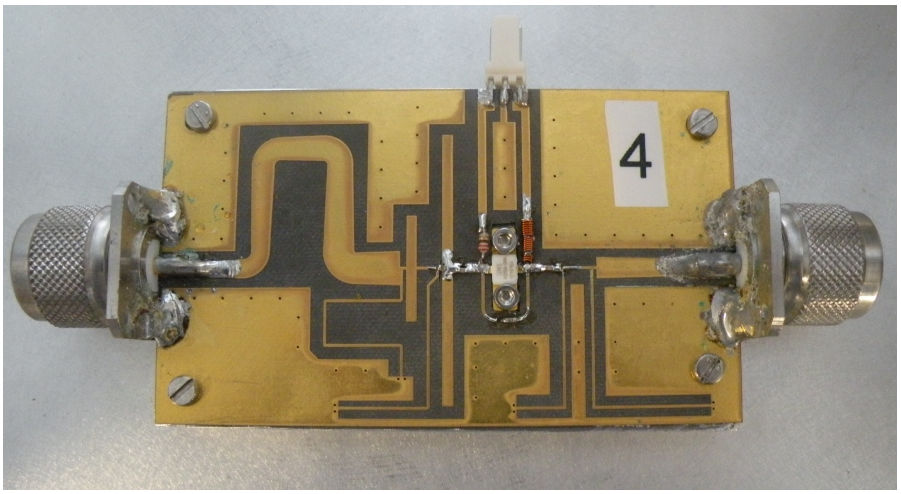

Figure 4.40 Photography of the Amplification cards used for the prototype.

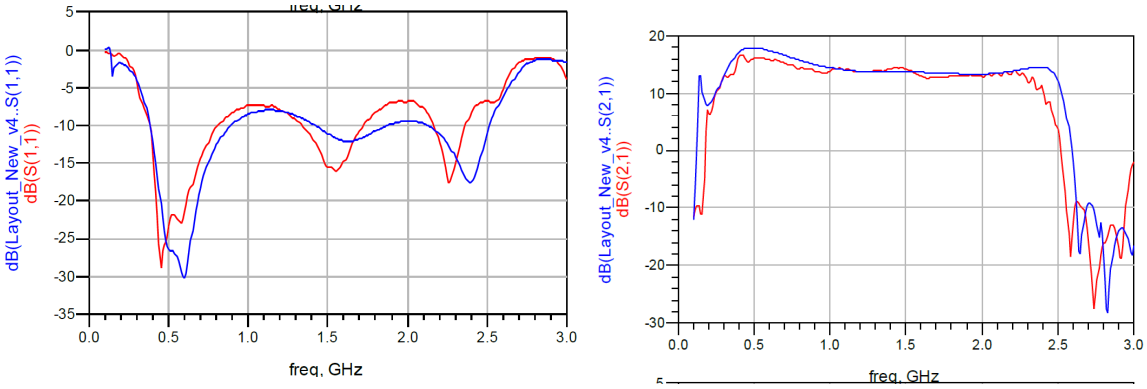

(a) (b)

Figure 4.41 Performances obtained with the solid-state amplifiers measurements vs simulation. (a) S11 and (b) S21

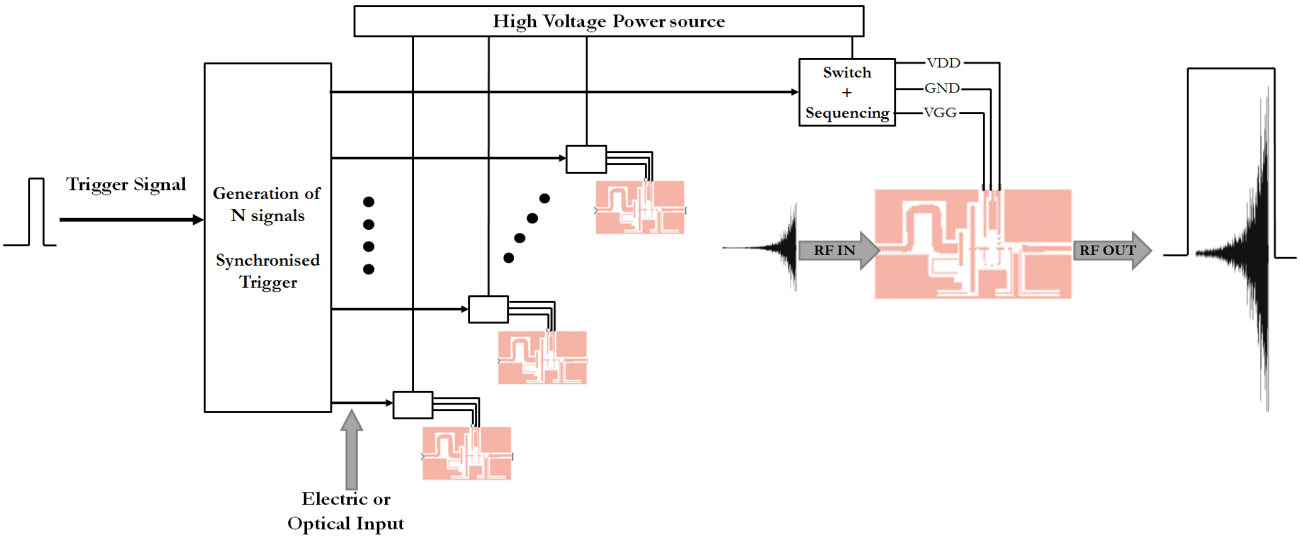

Figure 4.42 Schematic of the pulsed-power source.

vanish. However this type of power source needs to be very well calibrated in order to power the N amplifiers at the correct time.

4.5.2 Broadband Radial Waveguide Combining Technique and Vivaldi Antennas

In order connect the amplifiers in parallel a special type of Splitter/Combiner needed to be developed. This combiner needed to be able to withstand high power levels without distorting the input signal but also be wideband and function between 500 MHz and 2.5 GHz. The chosen solution was a passive microwave radial waveguide such as the ones in [178] represented in Figure 4.43. The advantages of such a solution are:

- Possibility of coupling an important number of amplifiers $N \leq 8$
- Large bandwidth
- Low losses: inferior to 1 dB
- The architecture must be compact compared to Wilkinson splitter
- Radial distribution of power in a passive waveguide
- High heat dissipation
- Possibility to use the device or as a combiner or as a splitter
- No parasite electromagnetic field within the cavity

This structure seems to be well adapted for frequencies above 10 GHz [179].

For our purposes the radial waveguide needed to be adapted for $N = 10$ amplifiers.

The architecture of such a device is quite simple a central probe transmits or receives the signals to or from the periphery. The first parameter that is needed for the design of such a waveguide is its

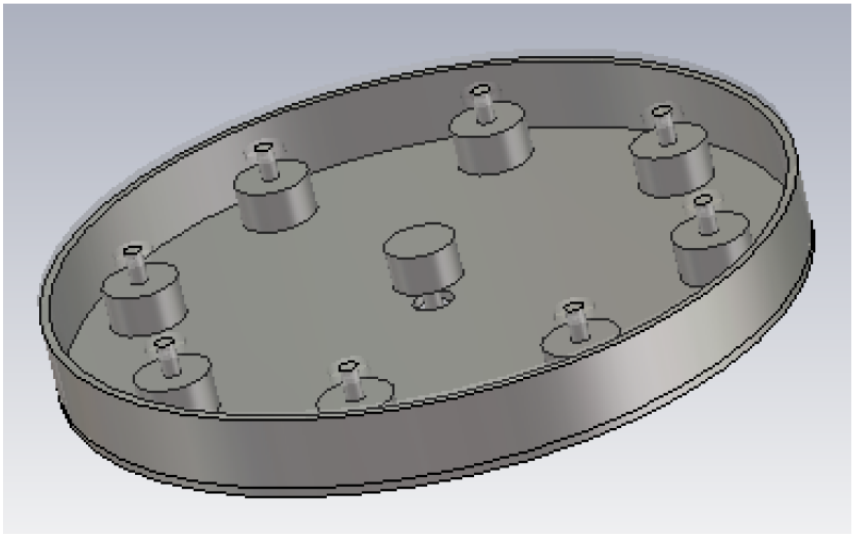

Figure 4.43 Plane cut of the splitter design from CST.

radius a simple formulation coming from [178] gives:

$$R = \frac{NW}{2\pi}, \tag{4.51}$$

where $N = 10$ is the number of outputs and $W = 150$ mm is the width of the waveguide at central frequency 1.5 GHz. The radius of the waveguide is thus equal to $R = 190$ mm. For the height of the cavity only the TEM mode must propagate. The distance between the plates must be small compared to the wavelength of the central frequency taking $H = 0.2 \times \lambda$ gives $H = 40$mm.

However some superior order modes will appear near the probes. The probes are placed at $\lambda/4$ of the edge of the radial cavity giving 50 mm.

The design of the radial line was made using CST. It is possible to subdivide the problem and therefore limit calculation time by decomposing the problem in equivalent zones such as the ones presented in Figure 4.44. The design optimisation from CST was used in order to minimize return losses S11 and to assure that S21 is stable on the desired bandwidth.

The probes position needed to be optimised in order to minimise reflections coming from the edge of the radial waveguide otherwise undesired coupling to the probes might appear and distortion in the signal introduced. Even if the probes are placed at $\lambda/4$ of the central frequency no model exist explaining why such a design is so broadband.

The distance between probes must also be adequate otherwise as it is shown on Figure 4.45 some nulls will appear.

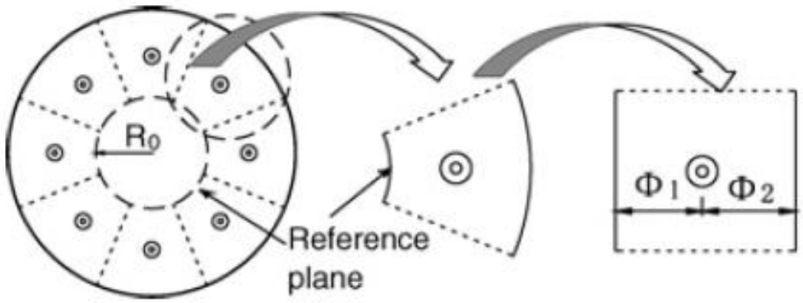

Figure 4.44 Decomposition of the splitters structure.

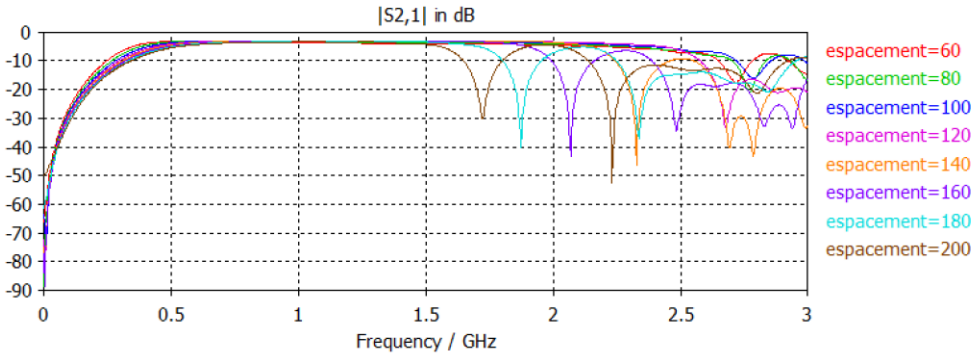

Figure 4.45 Parametrical simulations of the spacing between probes.

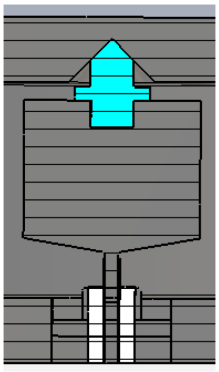

(a)

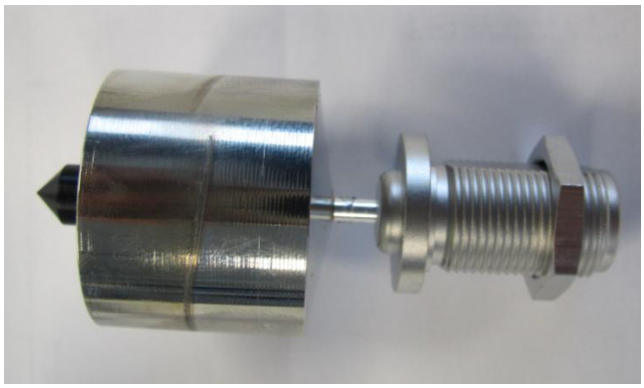

(b)

Figure 4.46 (a) End design of the probe and its output connection and (b) Photography of a probe with its connector welded.

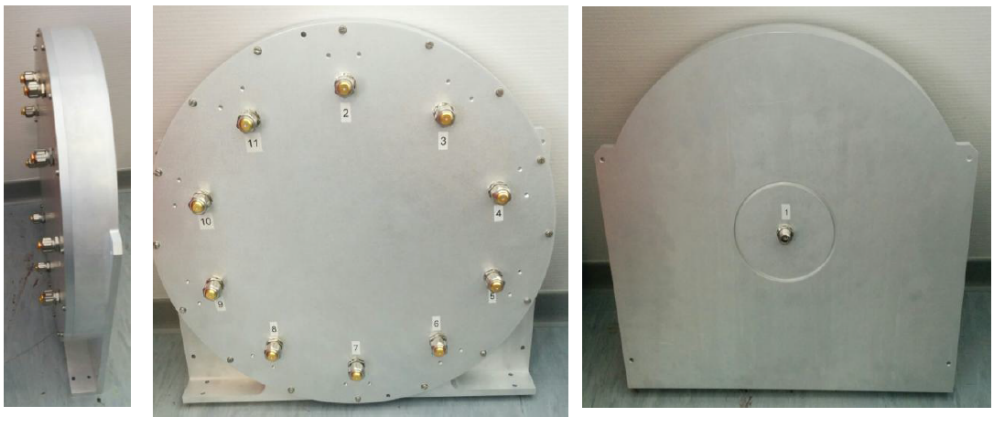

Figure 4.47 Photographies of the assembled splitter.

The output connection used are of type N. However as shown in the end design in Figure 4.49 in order to have a good mechanical stability a small derlin dice had to be added to the original design. These dices have no effect on the overall performances of the radial waveguide.

Finally, the performances of the assembled splitter are confronted to simulations in Figure 4.48 and 4.49. Since there are 10 ouputs the ideal level on each of the ouputs is equal to $10\log(1/10) = -10$ dB. The Figures below show good agreement between the CST simulations and experimental data. $|S21|$ varies very little with frequency over the complete desired bandwidth and $|S11|$ is below -10 dB on all the frequency range meaning that the power is well transmitted by the central probe to the ouput probes.

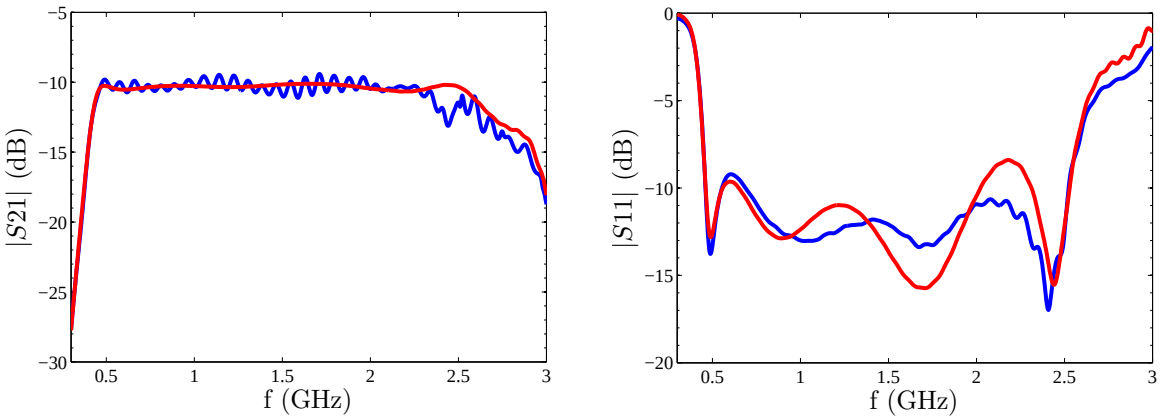

(a) (b)

Figure 4.48 Transmission $S21$ and $S11$ of the splitter measurements vs simulation.

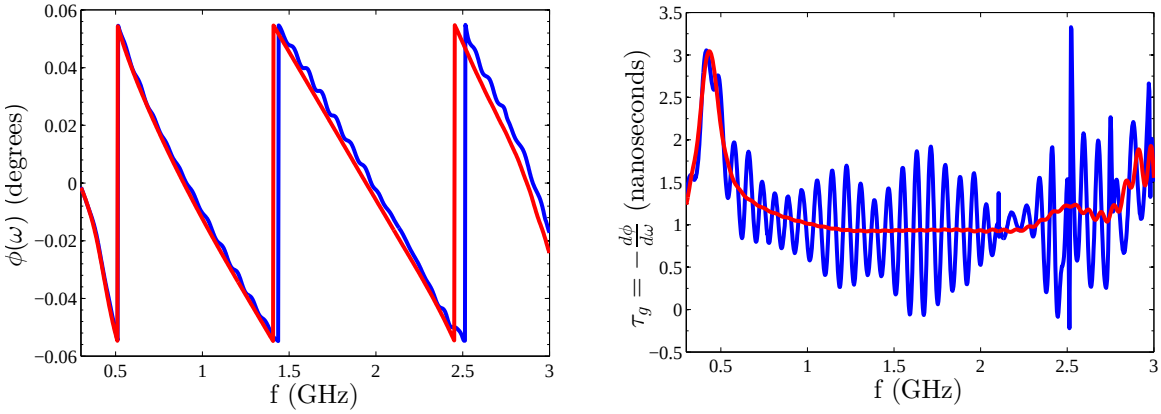

(a) (b)

Figure 4.49 Phase and group delay of the splitter measurements vs simulation.

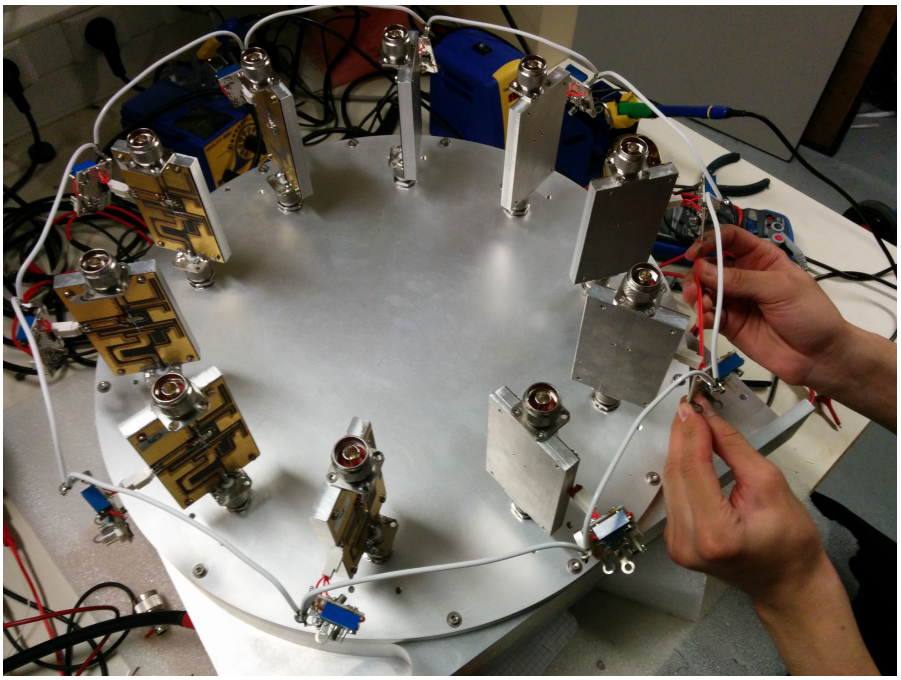

Figure 4.50 Assembled amplfiers on a splitter.

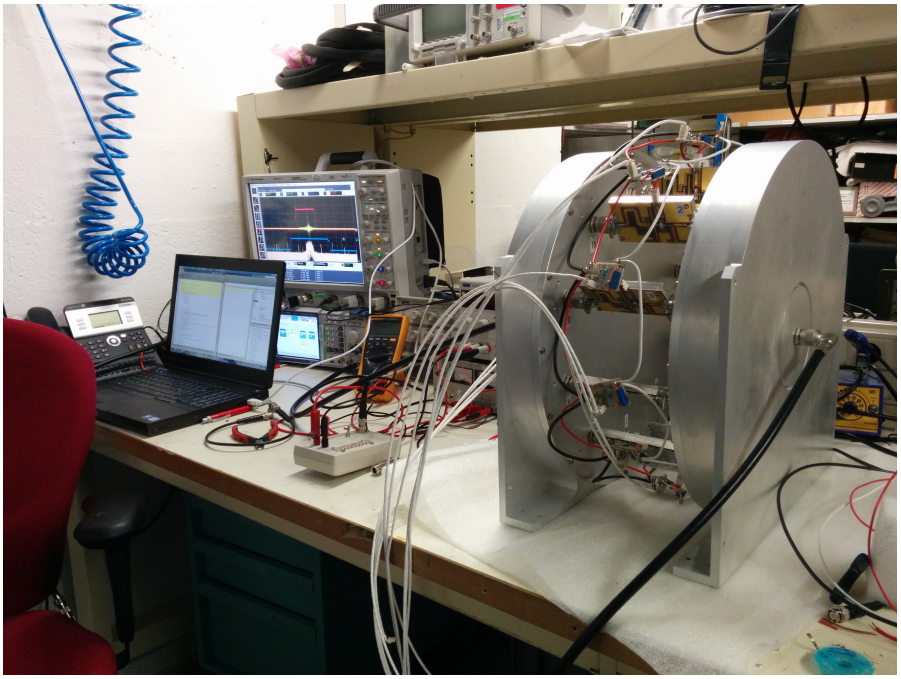

Figure 4.51 Complete amplfication module as presented in Figure 4.39.

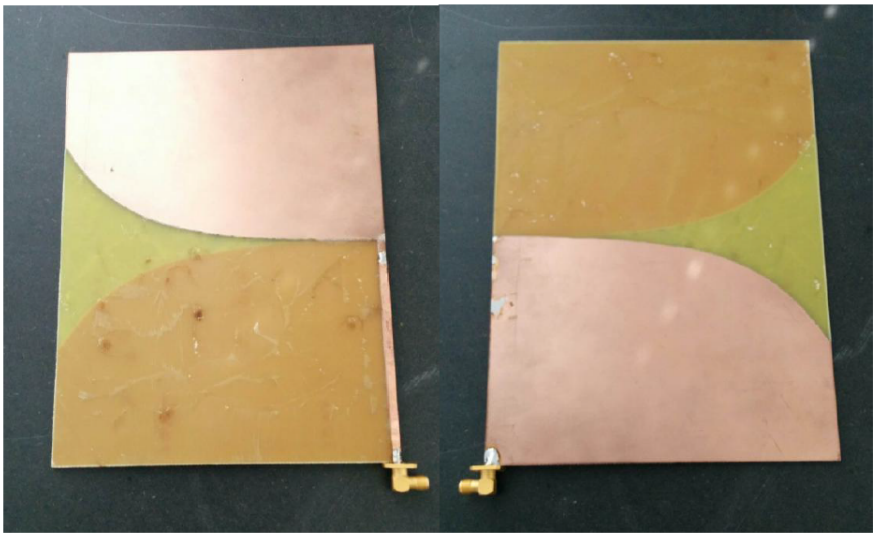

Figure 4.52 Vivaldi antennas used during high-power experiments.

Figures 4.50 and 4.51 show the completed amplification module suited to the purposes of this work.

The last object designed for the purpose of this work, were antennas that can operate for high power pulse. The antennas chosen for this work are Vivaldi because their design is well adapted to impulses. These antennas were also designed and optimised using CST. However, further improvements need to be made on the feed. The feed is on the border of the dielectric as in [180]. The antenna design parameters and coefficients are:

$$\begin{cases} y = & C_1 \exp R_x + C_2 \\ C_1 = & \dfrac{y_2 - y_1}{\exp R_{x_1} - \exp R_{x_2}} \\ C_2 = & \dfrac{y_1 \exp R_{x_2} - y_2 \exp R_{x_1}}{\exp R_{x_2} - \exp R_{x_1}} \end{cases} \tag{4.52}$$

For the antennas used here $R = 0.33$, $x_1 = 0$, $x_2 = 15$, $y_1 = 0$ and $y_2 = 15$ in cm. From Figure 4.53 it is possible to observe that simulation and measurements grossly agree on the frequency range considered. The differences are probably due to the fact that these antennas were hand made using a metallised FR4 thin plate. $S11$ falls belows -10 dB except between 600 MHz and 1 GHz where a maximum of -6 dB is attained.

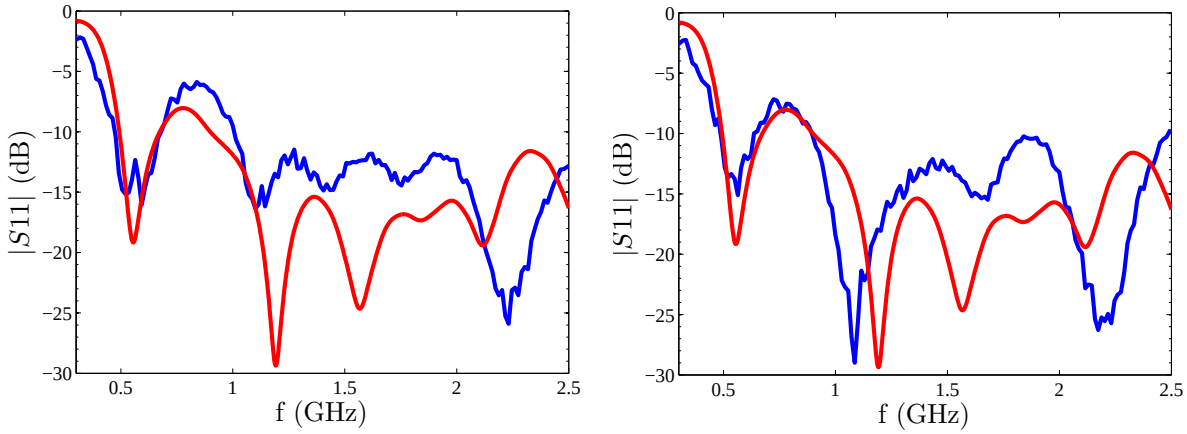

Figure 4.53 $|S11|$ in dB of the two antennas developped.measurements vs simulation.

All the components that have been developed during the course of this PhD have allowed to obtain the type of results in the next section.

4.5.3 Experimental Validations and Results

The amplification scheme used for these measurements follow the representation from Figure 4.1. For the sake of clarity the Figure is repeated below with numbers assigned to the signals that will be presented. For the cases presented here, a pulse having an almost flat spectrum with a 300 MHz bandwidth with a central frequency of 1.3 GHz will be considered.

The generator used here was a AWG7122C from Tektronix. This generator has two outputs with 8 GS/s sampling rate which is enough for frequencies below 2 GHz and the signals were recorded on an Agilent DSO6104A oscilloscope having 4 outputs and a maximum sampling rate of 20 GS/s. Various attenuators were connected at the input of the oscilloscope in order to protect it from the voltage levels.

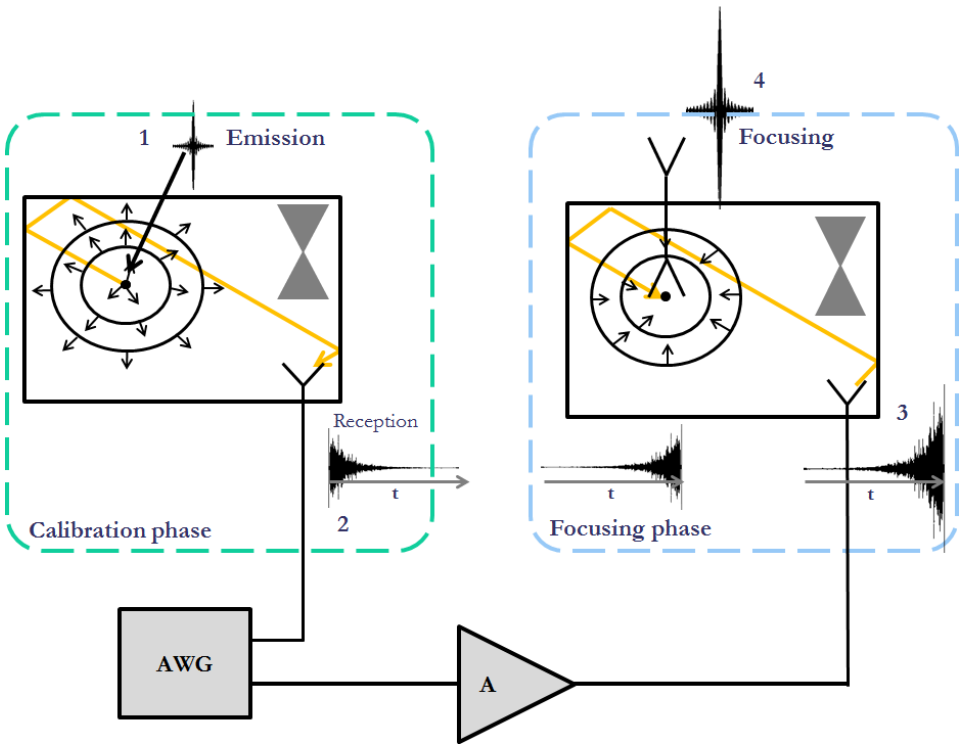

Figure 4.54 Schematic representation of the proposed procedure, showing the spreading and TR-compressive phases.

First, the input signal (1) is recorded in Figure 4.55. The distortion on the signal are likely due to saturation by the amplifier. The emitted signal is already amplified in order to obtain a good impulse response at the receiving antenna.

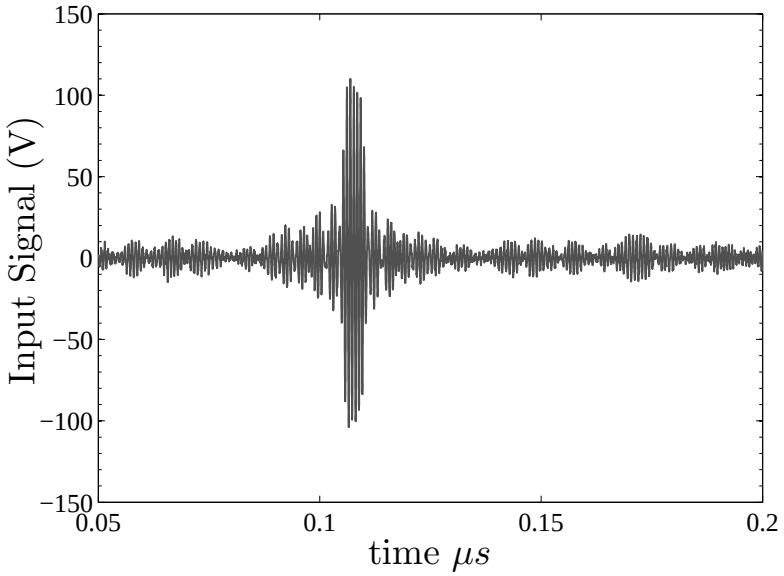

Figure 4.55 Input signal in the chamber.

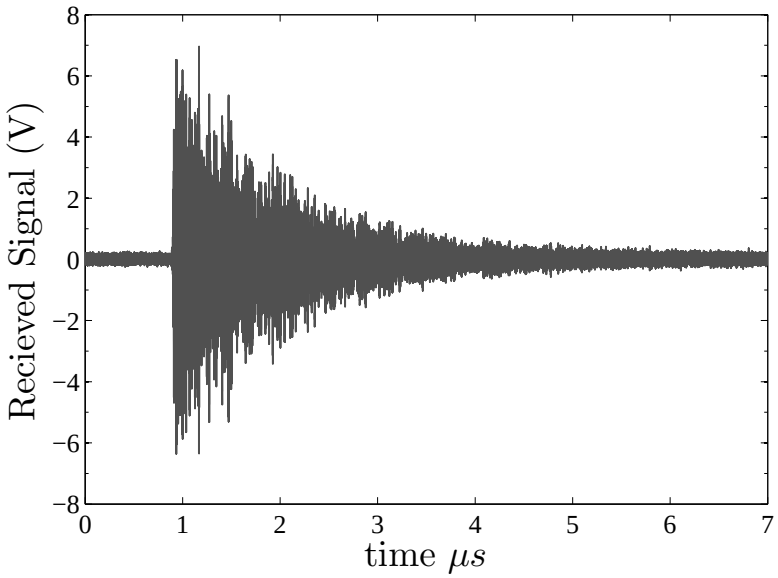

Figure 4.56 Input signal in the chamber.

The received signal corresponding to stage 2 in Figure 4.54 is plotted in Figure 4.56. The ratio between the maximum values of the impulse over the impulse response is found to be equal to $20\log(110/6.9) = 24.05$ dB which is close to experimental values obtained in Figure 4.12 which were equal to 24.3 dB and theoretical values from 4.11 which is equal to 23.5 dB.

The signal is then time-reversed and amplified (signal number 3 on Figure 4.54) as it is possible to see from this graphic, the maximum level of this signal is equal to the maximum level of the first emitted pulse meaning that the real gain also corresponds to the refocusing gain in the second part of the graphic.

The refocused signal signal number 4 on Figure 4.54 is presented in Figure 4.58. The Focusing gain is equal to 7.2 dB which is close to the 7.5 dB obtained with theory and presented in Figure 4.13. A 1-bit time-reversal process was also obtained in Figure 4.59. The obtained gain was equal to 19.8 dB also falling quite close the values obtained previously and the power obtained at the output of the chamber was equal to 6 kWs.

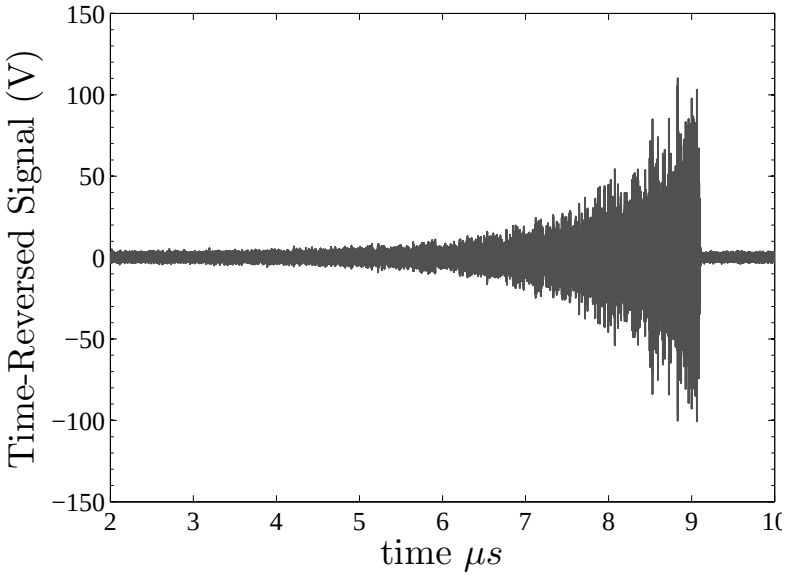

Figure 4.57 Amplified time-reversed signal.

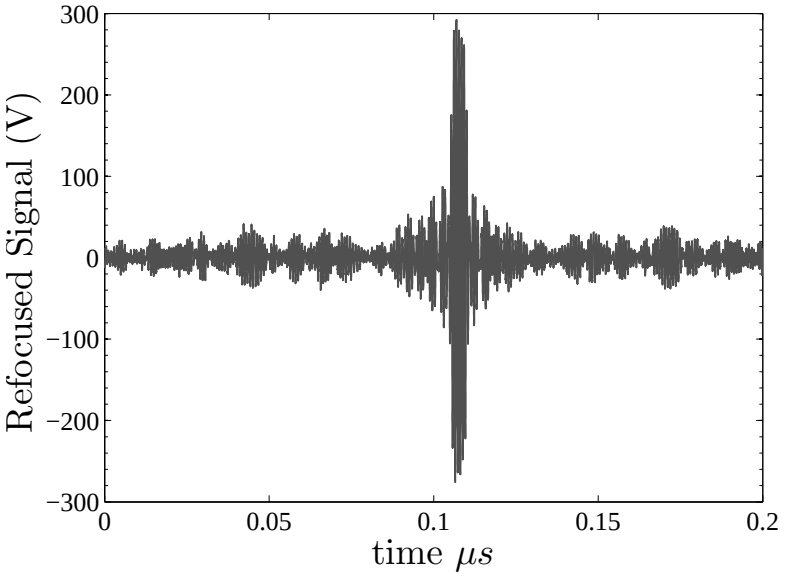

Figure 4.58 Refocused signal using classical time-reversal process.

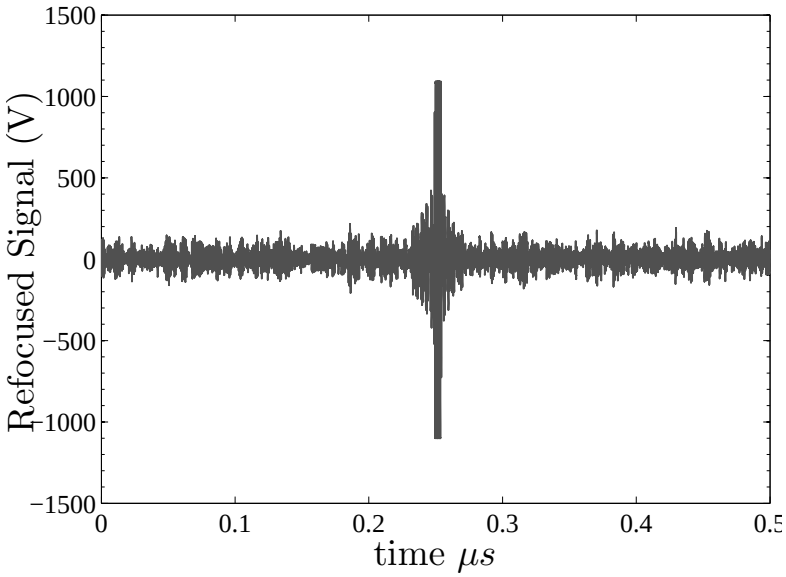

Figure 4.59 Refocused signal using a 1-bit time-reversal process.

In order to measure the refocused field a third vivaldi antenna was fixed on the outside of the chamber instead of connecting the output of the chamber to the oscilloscope. The field level outside the chamber was measured using an adapted E-3602 D-dot sensor attached to a T2001 transmitter from the Melopée sensors by THALES placed outside of the chamber at various distances from the cavity. The measured field level was found to be 3 kV/m at 1 m from the antenna but this level can be improved by using antennas with higher directivity.

Conclusion

In this chapter, two important parameters when considering time-reversal for amplification purposes were derived: the margin and the amplification gain. The first parameter corresponds to the ratio between the maximum power of the emitted and received power during the calibration phase and the real gain corresponds to the ratio between the first emitted signal and the refocused signal. The margin is closely related to the time-spread of the impulse response and corresponds to the maximum amplification available during the time-reversal stage. The margin was found to only depend on the losses due to the antennas placed within the chamber and follow a f^2 curvature. The real gain and the amplifications levels obtained during a full time-reversal process were presented. If the impulse during the calibration phase and the signal injected during the time-reversal phase have maximum levels that are equal to the saturation level of the amplification module the real-gain is equal to the refocusing property of the time-reversal phase. This was the case during our set-up and will most often be the case since part of the amplification can be obtained by simple data processing.

In both cases, the models and their respective properties were validated by experimental measurements using first a vector network analyzer in the reverberation chamber in CentraleSupélec. The efficiency of the available room was found to be insufficient on the frequency range considered for the purpose of this work and no values for the permittivity and permeability seemed to match experimental data leading to the building of a smaller more efficient room made out of aluminum. The experimental and theoretical curves of the margin using the antenna quality factor developed by Hill match very well confirming even more the results obtained in the second chapter. The slope of the margin curve was found to follow an f^2 tendency as predicted by the model. Theoretical curves of the real-gain were plotted showing that for higher frequencies the model developed by Hill with adjusted conductivity for the overall quality factor of the chamber seems to hold. For lower frequencies, the overall quality factor was plotted via the smoothed data obtained during the frequency measurement on the VNA. In that case the model of the real gain holds over the complete frequency range.

The second part of this chapter describes the complete set-up used during experimental validation in time-domain. Innovative solutions were developed to parallel 10 amplifiers using a cylindrical passive waveguide. The antennas and waveguide were developed using CST and the amplifiers were developed using ADS and Momentum. The measured and modelled curves of the performances of each of the components correlate quite well. The models and experimental data of the complete set-up again correspond on the frequency range considered. A dedicated triggered power for the amplifiers was also developed. The stage by stage signals are plotted for one set of values and confirm the theoretical models developed and the fact that the real-gain is also the refocusing gain when the maximum levels of the emitted signal during the calibration phase and the signal injected during the time-reversal phase are equal.

The importance of signal processing on the refocused peak-power was also shown. The 1–bit and signal equalization both show limitations when long lasting signals above 3τ are re-injected in the reverberation chamber, the impulse-response does not contain more information. This means that for times above 3τ, the refocusing properties of a time reversal process attains saturation. No improvement can be obtained by injecting higher power during the calibration phase. Since the noise levels evolve as $\sqrt{N}$ for a very long time and the maximum peak evolves as N, where N is the number of independent information "grains" as presented by DeRosny. Even if there is a loss of coherence when using 1-bit signals, the contrast level remain quite high and the difference between signal equalization and 1-bit on the contrast is not so important. The experimental set-ups using the VNA and AWG both prove the potentiality a TRAS as a future medium to high-power microwave source.

Conclusions and Perspectives

Conclusions

This work is at the confluence of multiple topics: electromagnetism, mode-stirred chambers, fundamental and room acoustics, solid-state amplifiers, high-power microwaves, statistics, diffusion and mixing theory, statistical and wave physics and signal processing. Evidently, this work does not attempt to be exhaustive on all of those topics but gives the tools to study the important parameters needed for the purpose of this research. Special attention was given to try and give physical meaning to the equations found and to validate them experimentally in frequency at first and then in time using a more complex set-up. Although heuristic, this approach allows a better understanding of general physics.

The refocusing properties of time-reversal and its amplification possibilities had already been observed but no thorough physical explanations nor mathematical equations had been derived. It is now possible to determine the performances' statistical fluctuations as well as their mean. At the core of this work was the description of a complete physical and engineering design for a Time-Reversal system optimized for Medium to High-Power applications. This system offers significant advantages over current technologies. One of the most significant advantages of a Time-Reversal Amplification System is the operation limitation of the solid-state amplifiers is pushed back allowing a compression gain in diffuse-field media. The field levels attained using such a process opens the way to otherwise unachievable applications for solid-state technologies. The association of solid-state technology and time-reversal could become in the future an affordable, reliable and compact vulnerability test system or jammer allowing control over the impulse generated.

The first part of this work introduced the context of the problem and the existing solutions producing high-power and medium power microwaves. In the aforementioned chapter the basic principle of the new solution studied during the course of this work was presented. The idea is to use the multiple reflections occurring in a reverberation chamber or in a randomly scattering diffusive media in order to obtain signals that last much longer than the emitted impulse. The maximum field-level received at the output of the chamber is lower than the emitted impulse due to losses

within the cavity. However the signal lasts longer, which allows better performance of the solid-state devices and further amplification. A time-reversal technique is then used to refocus a quasi-exact copy of the emitted impulse modulo fluctuations due to the refocusing mechanism. The properties of time-reversal and of solid-state devices are combined to design sources having the following properties:

- The Time-Reversal Amplification System can refocus wideband impulses. The bandwidth of the signal is limited by the solid-state devices functioning bandwidth, the efficiency of the room and the antennas. For the prototype the maximum efficiency of the chamber was above 0.46 but the average over stirrer position was around 0.15. The room efficiency diminishes with frequency and particular interest must be placed on the size of the chamber depending on the desired frequency range for the application. The antennas used were compact antipodals Vivaldis with a frequency ranging from 600 MHz to more than 4 GHz. The amplification module consisted in associating ten 15 W GaN HEMTs using a broadband radial waveguide combiner
- The output power of the device is of the order of 6 kWs or above when using state-of-the-art solid-state power amplifiers
- Amplifications of over 20 dBs are obtained with only one antenna
- The Time-Reversal Amplification System can be transportable. The total volume of the prototype is approximately equal to the volume of the chamber or 2 m^3 for the frequency range of interest
- The system allows to refocus different impulse shape, bandwidth and central frequency. The frequency range of the prototype is limited by the frequency range of the amplifiers but also by the efficiency of the chamber. If efficiency is too low the refocusing gains will decrease. The characteristics of the refocused signal depend on the sampling frequency of the generator. For the prototype, the AWG had a sampling frequency of 8 GS/s well above the maximum frequency of the solid-state amplifiers. Moreover, it was shown that the more compact in time the impulse the better the refocusing. The shape of the impulse thus plays an important role on the efficiency of the complete system. TRAS is well-suited for sinc type impulses but should be discarded when considering chirps or long lasting signals.
- The Time-Reversal Amplification System allows control over the polarization of the refocused signal. It was possible to simultaneously refocus on two antennas and two different signals

One of the main components of a time-reversal process is the reverberation chamber or a complex propagation media. Extensive experimentations enabled us to quantify the effects of loading a reverberation chamber with antennas. The set-up allowed to extract the different components of the quality factor of a chamber. The quality factor was found to play an important role in the compression gain of a time-reversal process. Some important conclusions were drawn bringing a better understanding of mode-stirred chambers' behaviors. The evolution in frequency of the antenna quality factor follows the theoretical model developed by Hill. However, the measured quality

factor assessing the losses on the walls and its theoretical model do not coincide except at very high frequencies. Furthermore, the conductivity and permeability found during the experiments do not correspond to the traditional values encountered when using steel. These results have already been partially published in conference [181]. The losses on the walls were found to be considerably more important than expected by theory even at a lower frequency. The effects of loading a chamber with antennas can almost be neglected. This means that a TRAS is well adapted to single output multiple output configuration. The fundamental parameters to consider to dimension a cavity for an efficient time-reversal have also been described. An important part of this work has thus been to study more precisely the mode-stirred chambers' behaviors. Significant regard was given to the maximum level of an impulse response since it is the limiting factor of the amplification margin allowed by the propagation of a wave in a diffused media. Its statistical probability density function was derived.

The third chapter dealt with time-reversal in a reverberating environment. The focus was put on the efficiency of a time-reversal process and its refocusing properties from a power and energy perspective. The conversion efficiencies were compared to a classical use of reverberating chamber and were accepted for publication in IEEE and in conferences [182–184]. The benefits of driving an RC with TR signals have been confirmed on three levels:

- a higher conversion efficiency,
- a reduced uncertainty in the actual field level
- without the need for multiple realizations (stirring).

The increase in the efficiency can well be translated into a condition on the peak-instantaneous power specifications for power amplifiers. This work has also proven that TR does not necessarily rhyme with wide-band signals, as acoustical TR has got us used to. Narrow bands can be interpreted as TR excitation signals. The only constraint is $B_T/B_C \gg \pi/Q$, with RCs easily displaying $Q \geq 1000$. It should be possible to keep using standard power amplifiers while taking advantage of TR benefits.

The fourth chapter introduced the last parameters describing the spreading and refocusing properties of a time-reversal process. This approach is quite new and the metrics studied correspond to the maximum power gain possible using a solid-state or microwave vacuum electronic device. The importance of the bandwidth, signal shape and chamber size were confirmed during the process. The efficiency levels obtained in the chambers of the laboratory have led to the construction of a dedicated low-cost chamber made of aluminium rather than steel. The aluminium chamber resulted in efficiencies that were twice as high to the ones obtained with steel cavities. This allowed much better performances of the system with just one single antenna. An experimental set-up confirmed the results obtained using a VNA in time-domain. Another important result is that time-reversal amplification will work best at the limit of overmodness and diffusivity of the field showing the limitation of our models. Some measurements were also undertaken using a VSG (Vector Signal Generator) instead of an AWG giving similar results that allowed to cut costs of the TRAS. Reflections on TRAS have led to two international patents.

Perspectives

The perspectives of this work are multiple. Although some derivations were completed in order to model the evolution of the different parameters when adding antennas, experimental validation of these models are necessary. Even if the efficiency of the aluminium room represented an improvement to the cavity made of steel the conductivity used is not the one given in bibliography and no conclusion can be given on whether the trends of the quality factor follow a linear law or not. Considering the importance of the reverberation media and its size further inquiry should be undertaken in the chamber. Eventually a derivation of a model describing the evolution of the quality factor corresponding to the losses on the walls should be attained. Special interest should be given to the evolution of the permittivity and permeability of the different materials used to build the chambers at the frequencies of interest, in order to obtain experimental proof of the difference between measures and experimental models. These results would also be of prime importance when considering the efficiency of the room. Another aspect that could be interesting would be a more detailed study of a mode-stirred chamber at the limit of overmodness. This process would achieve a valid model of the gain obtainable with a TRAS at lower frequencies. It would also be interesting to consider reducing the size of the chamber and using 2-D cavities with several openings as Hong and Fromenteze have done it. Models of the contrast and gain adapted to the 2-D case would be especially useful for future applications such as SIMO radar systems.

Another perspective would be to find out the maximum efficiency of the solid-state devices. Indeed although used in pulse-mode the amplification modules were mostly used in class-A or their most inefficient settings. In class-A the signal sent is well reproduced at the output, however in that regime the solid-state devices heat-up quite rapidly if not used in pulse mode. For 1-bit signals it is not necessary to put the solid-state devices in such an inefficient class and further improvement could be obtained. Lastly, during the course of this work 15 W amplifiers were used. Since then, 100 W solid-state power amplifiers have become available on the market allowing to obtain power levels of 100 kW pulses and giving further opportunities to TRAS as a solution for electronic warfare applications.

References

[1] J. Benford, J.A. Swegle, and E. Schamiloglu. *High Power Microwaves, Second Edition*. Series in Plasma Physics. Taylor & Francis, 2007.

[2] D.C. Wunsch and R.R. Bell. "Determination of Threshold Failure Levels of Semiconductor Diodes and Transistors Due to Pulse Voltages". In: *Nuclear Science, IEEE Transactions on* 15.6 (1968), pp. 244–259.

[3] D.A. Hill. "Plane wave integral representation for fields in reverberation chambers". In: *IEEE Transactions on Electromagnetic Compatibility* 40.3 (1998), pp. 209–217.

[4] IEC. *Standard 61000-4-21: Electromagnetic Compatibility (EMC) Part 4: Testing and Measurement Techniques, Sec. 21: Reverberation Chambers*. 2011.

[5] T. H. Lehman and G. J. Freyer. "Characterization of the maximum test level in a reverberation chamber". In: *Electromagnetic Compatibility, 1997. IEEE 1997 International Symposium on*. 1997, pp. 44–47.

[6] B. Démoulin and P. Besnier. *Les Chambres réverbérantes en électromagnétisme*. Collection Télécom. Hermes Science Publications, 2010.

[7] A. Cozza. *Stochastic modelling of large cavities - Random and coherent field applications*. Université Paris-Sud, Habilitation à Diriger la Recherche, 2012.

[8] P. Degauque and J. Hamelin. *Electromagnetic compatibility*. Oxford science publications. Oxford University Press, 1993.

[9] D.V. Giri and F.M. Tesche. "Classification of intentional electromagnetic environments (IEME)". In: *Electromagnetic Compatibility, IEEE Transactions on* 46.3 (2004), pp. 322–328.

[10] IEC. *Standard 61000-2-13: Electromagnetic compatibility (EMC) Part 2-13: Environment - High-power electromagnetic (HPEM) environments-Radiated and conducted*. 2005.

[11] D. Månsson, R. Thottappillil, and M. Bäckström. "Methodology for Classifying Facilities With Respect to Intentional EMI". In: *Electromagnetic Compatibility, IEEE Transactions on* 51.1 (2009), pp. 46–52.

[12] D. Månsson. "IEMI and EMC Considerations for Large Systems | Smart Grid Aspects". In: *Progress In Electromagnetics Research Symposium Proceedings, Stockholm* (2013), pp. 1366–1370.

[13] DG Pierce and DL Durgin. "An overview of electrical overstress effects on semiconductor devices". In: *Proceedings of the EOS/ESD Symposium*. 1981, p. 120.

[14] JH Yee, WJ Orvis, and Leroy C Martin. *Theoretical Modeling of EMP Effects in Semiconductor Junction Devices*. Tech. rep. DTIC Document, 1983.

[15] R.L. Davies and F.E. Gentry. "Control of electric field at the surface of P-N junctions". In: *Electron Devices, IEEE Transactions on* 11.7 (1964), pp. 313–323.

[16] R.J. Barker and E. Schamiloglu. *High-power microwave sources and technologies*. IEEE Press series on RF and microwave technology. IEEE Press, 2001.

[17] R. Hoad et al. "Trends in EM susceptibility of IT equipment". In: *Electromagnetic Compatibility, IEEE Transactions on* 46.3 (2004), pp. 390–395.

[18] DV Giri, FM Tesche, Carl E Baum, et al. "An overview of high-power electromagnetic (HPEM) radiating and conducting systems". In: *Circuit and Electromagnetic System Design Notes* 50 (2006).

[19] D.V. Giri. *High-power Electromagnetic Radiators: Nonlethal Weapons and Other Applications*. Electromagnetics library. Harvard University Press, 2004.

[20] Steven H Gold and Gregory S Nusinovich. "Review of high-power microwave source research". In: *Review of Scientific instruments* 68.11 (1997), pp. 3945–3974.

[21] C.D. Taylor and D.V. Giri. *High Power Microwave Systems And Effects*. Electromagnetics Library. Taylor & Francis, 1994.

[22] B.E. Kruger. "Efficient wideband high power generation for X- and Ku-band radars". In: *Radar Conference, 1995., Record of the IEEE 1995 International*. 1995, pp. 227–232.

[23] M. Kumar et al. "22-kW next generation low cost S-band solid state transmitter for surveillance and air traffic control radars". In: *Microwave Symposium Digest, 1995., IEEE MTT-S International*. 1995, 1601–1604 vol.3.

[24] T. Murae, K. Fujii, and T. Matsuno. "High power S-band solid-state amplifiers for surveillance and traffic control radars". In: *Microwave Symposium Digest, 2001 IEEE MTT-S International*. Vol. 2. 2001, 653–656 vol.2.

[25] M. Cicolani. "High power modular S-band solid state transmitter family for ATC and naval radar applications". In: *Microwave Symposium Digest. 2000 IEEE MTT-S International*. Vol. 3. 2000, 1723–1726 vol.3.

[26] V.L. Granatstein et al. "High Power Microwave Technology and Effects". In: *University of Maryland Short Course* (2005).

[27] V.L. Granatstein and I. Alexeff. *High-power Microwave Sources*. Microwave Library. Artech House, 1987.

[28] IEEE Nuclear and Plasma Sciences Society. *Modern microwave and millimeter-wave power electronics*. Ed. by R. J. Barker et al. Wiley-Interscience, IEEE PRESS, 2005.

[29] J. H. Booske. "Plasma physics and related challenges of millimeter-wave-to-terahertz and high power microwave generationa)". In: *Physics of Plasmas* 15.5 (2008), pp. –.

[30] R.S. Symons. "Tubes: still vital after all these years". In: *Spectrum, IEEE* 35.4 (1998), pp. 52–63.

[31] R.J. Trew, J.-B. Yan, and P.M. Mock. "The potential of diamond and SiC electronic devices for microwave and millimeter-wave power applications". In: *Proceedings of the IEEE* 79.5 (1991), pp. 598–620.

[32] R.J. Trew. "SiC and GaN transistors - is there one winner for microwave power applications?" In: *Proceedings of the IEEE* 90.6 (2002), pp. 1032–1047.

[33] R. Poisel. *Modern Communications Jamming: Principles and Techniques*. Artech House, 2011.

[34] M. Abrams. "Dawn of the E-Bomb". In: *Spectrum, IEEE* 40.11 (2003), pp. 24–30.

[35] M. Davy et al. "Focusing and amplification of electromagnetic waves by time reversal in an leaky reverberation chamber". In: *Comptes Rendus Physique* 11.1 (2010). Propagation and remote sensing Propagation and Teledection, pp. 37 –43.

[36] A. Derode, A. Tourin, and M. Fink. "Ultrasonic pulse compression with one-bit time reversal through multiple scattering". In: *Journal of applied physics* 85.9 (1999), pp. 6343–6352.

[37] S. K. Hong et al. “Focusing an arbitrary RF pulse at a distance using time-reversal techniques”. In: *Journal of Electromagnetic Waves and Applications* 27.10 (2013), pp. 1262–1275.

[38] M. Davy. “Application du retournement temporel en micro-ondes à l’amplification d’impulsons et l’imagerie”. PhD thesis. Université Paris 7 - Denis Diderot, 2010.

[39] D. Carsenat and C. Decroze. “UWB Antennas Beamforming Using Passive Time-Reversal Device”. In: *Antennas and Wireless Propagation Letters, IEEE* 11 (2012), pp. 779–782.

[40] S. K. Hong et al. “Single-Feed Beam-Steering of Short Pulses via Time Reversal”. In: *Antennas and Wireless Propagation Letters, IEEE* 13 (2014), pp. 794–797.

[41] T. Fromenteze, C. Decroze, and D. Carsenat. “Miniaturized device for passive microwave UWB beamforming”. In: *Antennas and Propagation (EuCAP), 2014 8th European Conference on*. 2014, pp. 354–358.

[42] T. Fromenteze, C. Decroze, and D. Carsenat. “Waveform Coding for Passive Multiplexing: Application to Microwave Imaging”. In: *Antennas and Propagation, IEEE Transactions on* 63.2 (2015), pp. 593–600.

[43] T. Fromenteze et al. “Computational imaging using a mode-mixing cavity at microwave frequencies”. In: *Applied Physics Letters* 106.19 (2015), pp. –.

[44] W.S. Wall and S.K. Hong. “Improved Time-Reversal-Based Beamforming Using a Self-Biasing Switch”. In: *Antennas and Wireless Propagation Letters, IEEE* 13 (2014), pp. 1337–1340.

[45] M. Hoijer. “Maximum power available to stress onto the critical component in the equipment under test when performing a radiated susceptibility test in the reverberation chamber”. In: *Electromagnetic Compatibility, IEEE Transactions on* 48.2 (2006), pp. 372–384.

[46] P. Corona et al. “Use of a Reverberating Enclosure for Measurements of Radiated Power in the Microwave Range”. In: *Electromagnetic Compatibility, IEEE Transactions on* EMC-18.2 (1976), pp. 54–59.

[47] H.-G. Krauthauser. “On the Measurement of Total Radiated Power in Uncalibrated Reverberation Chambers”. In: *Electromagnetic Compatibility, IEEE Transactions on* 49.2 (2007), pp. 270–279.

[48] K. Rosengren et al. “Characterization of antennas for mobile and wireless terminals by using reverberation chambers: improved accuracy by platform stirring”. In: *Antennas and Propagation Society International Symposium, 2001. IEEE*. Vol. 3. 2001, 350–353 vol.3.

[49] H. Mendez H. A. “A new approach to electromagnetic field-strength measurements in shielded enclosures”. In: *Wescon Technical Papers, Western Electronic Show and Convention*. 1968.

[50] H. A. Mendez. “Meaningful EMC Measurements in Shielded Enclosures”. In: *Electromagnetic Compatibility Symposium Record, 1969 IEEE*. 1969, pp. 137–137.

[51] Thomas A. Loughry. “Frequency Stirring: An Alternate Approach to Mechanical Mode-Stirring for the Conduct of Electromagnetic Susceptibility Testing”. In: *Phillips Lab. Kirtland A.F.B. N.M.* (1991).

[52] D.A. Hill. “Electronic mode stirring for reverberation chambers”. In: *Electromagnetic Compatibility, IEEE Transactions on* 36.4 (1994), pp. 294–299.

[53] C.L. Holloway et al. “Reverberation Chamber Techniques for Determining the Radiation and Total Efficiency of Antennas”. In: *Antennas and Propagation, IEEE Transactions on* 60.4 (2012), pp. 1758–1770.

[54] Stephen J. Boyes. “Reverberation Chambers and the Measurement of Antenna Characteristics”. PhD thesis. University of Liverpool, 2013.

[55] David A. Hill. “Electromagnetic Theory of Reverberation Chambers”. In: *NIST, NBS TN - 1506* 1506 (1998), p. 60.

[56] Heinrich Kuttruff. *Room acoustics*. CRC Press, 2009.

[57] D. I. Wu and David C. Chang. *An investigation of a ray-mode representation of the Green's function in a rectangular cavity*. Vol. 1312. NBS technical note. U.S. Government Printing Office, 1987.

[58] Do-Hoon Kwon, R.J. Burkholder, and P.H. Pathak. "Ray analysis of electromagnetic field build-up and quality factor of electrically large shielded enclosures". In: *Electromagnetic Compatibility, IEEE Transactions on* 40.1 (1998), pp. 19–26.

[59] E. N. Gilbert. "Ray statistics in reverberation". In: *The Journal of the Acoustical Society of America* 83.5 (1988), pp. 1804–1808.

[60] G. Montaldo et al. "The time reversal kaleidoscope: a new concept of smart transducers for 3D imaging". In: *Ultrasonics, 2003 IEEE Symposium on*. Vol. 1. 2003, pp. 42–45.

[61] J. Jouhaneau. "Acoustique des salles". In: *Techniques de l'ingénieur* c3360 (1995).

[62] Cozza. "Introduction to Reverberation Chambers - Their physics and practical applications".

[63] R. H. Bolt, P. E. Doak, and P. J. Westervelt. "Pulse Statistics Analysis of Room Acoustics". In: *The Journal of the Acoustical Society of America* 22.3 (1950), pp. 328–340.

[64] W. B. Joyce. "Exact effect of surface roughness on the reverberation time of a uniformly absorbing spherical enclosure". In: *The Journal of the Acoustical Society of America* 64.5 (1978), pp. 1429–1436.

[65] Trevor J Cox and Peter D'antonio. *Acoustic absorbers and diffusers: theory, design and application*. CRC Press, 2009.

[66] B.H. Liu, D.C. Chang, and M.T. Ma. *Eigenmodes and the Composite Quality Factor of a Reverberating Chamber*. NBS Technical Note 1066. National Bureau of Standards, Aug. 1983.

[67] M.R. Schroeder. "Statistical Parameters of the Frequency Response Curves of Large Rooms". In: *J. Audio Eng. Soc* 35.5 (1987), pp. 299–306.

[68] D-Y. Maa. "Distribution of Eigentoness in a Rectangular Chamber at Low Frequency Range". In: *The Journal of the Acoustical Society of America* 10.3 (1939), pp. 235–238.

[69] R. H. Bolt. "Frequency Distribution of Eigentones in a Thrre-Dimensional Continuum". In: *The Journal of the Acoustic Society of America* 10.3 (1939), pp. 228–234.

[70] H. Weyl. "Über die asymptotische Verteilung der Eigenwerte". In: *Nachrichten der Königlichen Gesellschaft der Wissenschaften zu Göttingen* (1911), pp. 110–117.

[71] R Balian and C Bloch. "Distribution of eigenfrequencies for the wave equation in a finite domain: I. Three-dimensional problem with smooth boundary surface". In: *Annals of Physics* 60.2 (1970), pp. 401 –447.

[72] M. R. Schroeder. "Frequency-Correlation Functions of Frequency Responses in Rooms". In: *The Journal of the Acoustical Society of America* 34.12 (1962), pp. 1819–1823.

[73] M. R. Schroeder and K. H. Kuttruff. "On Frequency Response Curves in Rooms. Comparison of Experimental, Theoretical, and Monte Carlo Results for the Average Frequency Spacing between Maxima". In: *The Journal of the Acoustical Society of America* 34.1 (1962), pp. 76–80.

[74] J. G. Van Bladel. *Electromagnetic fields*. Vol. 19. John Wiley & Sons, 2007.

[75] C-T. Tai and P. Rozenfeld. "Different Representations of Dyadic Green's functions for a Rectangular Cavity". In: *Microwave Theory and Techniques, IEEE Transactions on* 25 (1976). (Also see a report HDL-TR-1724 by the same authors with the same title, prepared for the U.S. Army Material Command, Harry Diamond Labs, Adelphi, Maryland, December 1975), pp. 597–601.

[76] Philip McCord Morse and Hermann Feshbach. *Methods of theoretical physics*. Vol. 1. McGraw-Hill, 1953.

[77] T. H. Lehman. "A statistical theory of electromagnetic fields in complex cavities". In: *Interaction Notes, Note* 494 (1993).

[78] E. Amador. "Modèles de compréhension par la théorie des images des phénomènes transitoires et du régime permanent en chambre réverbérante électromagnétique". PhD thesis. IETR - INSA de Rennes, 2011.

[79] M. L. Crawford and G. H. Koepke. *Design, Evaluation, and Use of a Reverberation Chamber For Performing Electromagnetic Susceptibility/Vulnerability Measurements.* NBS Technical Note 1092. National Bureau of Standards, 1986.

[80] C.L. Holloway et al. "Requirements for an effective reverberation chamber: unloaded or loaded". In: *Electromagnetic Compatibility, IEEE Transactions on* 48.1 (2006), pp. 187–194.

[81] A. Cozza. "Statistics of the performance of time reversal in a lossy reverberating medium". In: *Physical Review E* 80.5 (2009), p. 056604.

[82] J.G. Kostas and B. Boverie. "Statistical model for a mode-stirred chamber". In: *Electromagnetic Compatibility, IEEE Transactions on* 33.4 (1991), pp. 366–370.

[83] H. G. Booker and P. C. Clemmow. "The concept of an angular spectrum of plane waves, and its relation to that of polar diagram and aperture distribution". In: *Proceedings of the IEE - Part III: Radio and Communication Engineering* 97.45 (1950), pp. 11–17.

[84] P. C. Clemmow. *The plane wave spectrum representation of electromagnetic fields*. IEEE/OUP Series on Electromagnetic Wave Theory, 1966, vii, 185 p.

[85] A. Papoulis and S.U. Pillai. *Probability, Random Variables, and Stochastic Processes*. McGraw-Hill series in electrical engineering: Communications and signal processing. Tata McGraw-Hill, 2002.

[86] C.L. Holloway et al. "On the Use of Reverberation Chambers to Simulate a Rician Radio Environment for the Testing of Wireless Devices". In: *Antennas and Propagation, IEEE Transactions on* 54.11 (2006), pp. 3167–3177.

[87] J. M. Ladbury. "Monte Carlo simulation of reverberation chambers". In: *Digital Avionics Systems Conference, 1999. Proceedings. 18th*. Vol. 2. 1999, 10.C.1–1–10.C.1–8 vol.2.

[88] B. Esen. "Quality Factor of Microwave Chambers". MA thesis. Texas Tech. University, 1996.

[89] D.A. Hill. *Aperture Excitation of Electrically Large, Lossy Cavities*. NIST Technical Note 1361, 1993.

[90] Thomas F. Frost and Atindra K. Mitra. *Electromagnetic Compatibility Testing Studies*. NASA-CR-200839, 1996.

[91] J.M. Dunn. "Local, high-frequency analysis of the fields in a mode-stirred chamber". In: *Electromagnetic Compatibility, IEEE Transactions on* 32.1 (1990), pp. 53–58.

[92] M.R. Schroeder. "New method of measuring reverberation time". In: *The Journal of the Acoustical Society of America* 37 (1965), p. 409.

[93] J. M. Ladbury et al. *Rapid Evaluation of Mode-stirred Chambers Using Impulsive Waveforms*. NIST technical note. U.S. Government Printing Office, 1996.

[94] Robert E. Richardson. *Reverberant Microwave Propagation*. Technical Report 2000-2008. Naval Surface Warfare Center Dahlgreen Div VA, 2008.

[95] A.K. Mitra and T.F. Trost. "Power transfer characteristics of a microwave reverberation chamber". In: *Electromagnetic Compatibility, IEEE Transactions on* 38.2 (1996), pp. 197–200.

[96] A. K. Mitra. “Some Critical Parameters for the Statistical Characterization of Power Density witinh a Microwave Reverberation Chamber”. PhD thesis. Texas Tech. University, 1996.

[97] D.A. Hill. “A reflection coefficient derivation for the Q of a reverberation chamber”. In: *Electromagnetic Compatibility, IEEE Transactions on* 38.4 (1996), pp. 591–592.

[98] P. Corona, G. Latmiral, and Enrico Paolini. “Performance and Analysis of a Reverberating Enclosure with Variable Geometry”. In: *Electromagnetic Compatibility, IEEE Transactions on* 22.1 (1980), pp. 2–5.

[99] D.A. Hill. “Linear dipole response in a reverberation chamber”. In: *Electromagnetic Compatibility, IEEE Transactions on* 41.4 (1999), pp. 365–368.

[100] J. M. Ladbury and D. A. Hill. “An improved model for antennas in reverberation chambers”. In: *Electromagnetic Compatibility (EMC), 2010 IEEE International Symposium on*. 2010, pp. 663–667.

[101] D.R.J. White and M. Mardiguan. *A handbook series on electromagnetic interference and compatibility*. Vol. 3, pp. 2.10. Don White Consultants, 1988.

[102] T. Y. Otoshi and M.M.. Franco. “The electrical conductivities of steel and other candidate materials for shrouds in a beam-waveguide antenna system”. In: *IEEE Transactions on Instrumentation and Measurement* 45.1 (1996), pp. 77–83.

[103] N. Bowler. “Frequency-Dependence of Relative Permeability in Steel”. In: *AIP Conference Proceedings* 820.1 (2006), pp. 1269–1276.

[104] C.L. Holloway et al. “Early Time Behavior in Reverberation Chambers and Its Effect on the Relationships Between Coherence Bandwidth, Chamber Decay Time, RMS Delay Spread, and the Chamber Buildup Time”. In: *Electromagnetic Compatibility, IEEE Transactions on* 54.4 (2012), pp. 714–725.

[105] E. Genender et al. “Use of reverberation chamber to simulate the power delay profile of a wireless environment”. In: *Electromagnetic Compatibility - EMC Europe, 2008 International Symposium on*. 2008, pp. 1–6.

[106] A. Derode, A. Tourin, and M. Fink. “Limits of time-reversal focusing through multiple scattering: Long-range correlation”. In: *The Journal of the Acoustical Society of America* 107.6 (2000), pp. 2987–2998.

[107] K. J. Haworth et al. “Generalized shot noise model for time-reversal in multiple-scattering media allowing for arbitrary inputs and windowing”. In: *The Journal of the Acoustical Society of America* 125.5 (2009), pp. 3129–3140.

[108] J-D Polack. “La transmission de l’énergie sonore dans les salles”. PhD thesis. Univeristé du Maine, 1998.

[109] P. Penna. “Some Statistical properties of reverberation process in diffuse sound fields”. MA thesis. The Acoustics Laboratory, Danmark tekniske højskole, 1993.

[110] A. Cozza. “Source Correlation in Randomly Excited Complex Media”. In: *Antennas and Wireless Propagation Letters, IEEE* 11 (2012), pp. 105–108.

[111] H.J. Stöckmann. *Quantum Chaos: An introduciton*. Cambridge University Press, 2007.

[112] D.A. Hill. “Spatial correlation function for fields in a reverberation chamber”. In: *Electromagnetic Compatibility, IEEE Transactions on* 37.1 (1995), pp. 138–.

[113] M. Fink et al. “Self focusing in inhomogeneous media with time reversal acoustic mirrors”. In: *Ultrasonics Symposium, 1989. Proceedings., IEEE 1989*. 1989, 681–686 vol.2.

[114] G. Lerosey et al. “Time Reversal of Electromagnetic Waves”. In: *Phys. Rev. Lett.* 92 (19 2004).

[115] G. Lerosey. “Retournement temporel d’ondes électromagnétiques et application à la télécommunication en milieux complexes”. Theses. ESPCI ParisTECH, 2006.

[116] M. Fink. “Time-reversal of ultrasonic fields. Part I: Basic principles”. In: *Ultrasonics, Ferroelectrics, and Frequency Control, IEEE Transactions on* 39.5 (1992), pp. 555–566.

[117] F. Wu, J-L. Thomas, and M. Fink. “Time-reversal of ultrasonic fields. Part II: Experimental results”. In: *Ultrasonics, Ferroelectrics, and Frequency Control, IEEE Transactions on* 39.5 (1992), pp. 567–578.

[118] M. Fink et al. “Time-reversed acoustics”. In: *Reports on Progress in Physics* 63.12 (2000), p. 1933.

[119] J. de Rosny. “Milieux Réverbérant et réversibilité”. PhD thesis. Université Paris VI-Pierre et Marie Cuire, 2000.

[120] Rémi Carminati, Manuel Nieto-Vesperinas, and Jean-Jacques Greffet. “Reciprocity of evanescent electromagnetic waves”. In: *J. Opt. Soc. Am. A* 15.3 (1998), pp. 706–712.

[121] C. Draeger and M. Fink. “One-channel time reversal of elastic waves in a chaotic 2D-silicon cavity”. In: *Physical Review Letters* 79 (1997), p. 407.

[122] G Lerosey et al. “Time reversal of wideband microwaves”. In: *Applied Physics Letters* 88.15 (2006), pp. 154101–154101.

[123] R. F. Harrington. *Time-Harmonic Electromagnetic Fields*. Wiley-IEEE Press, 2001.

[124] A. Cozza. “Emulating an Anechoic Environment in a Wave-Diffusive Medium Through an Extended Time-Reversal Approach”. In: *Antennas and Propagation, IEEE Transactions on* 60.8 (2012), pp. 3838–3852.

[125] H. Moussa, A. Cozza, and M. Cauterman. “Directive wavefronts inside a time reversal electromagnetic chamber”. In: *Electromagnetic Compatibility, 2009. EMC 2009. IEEE International Symposium on*. 2009, pp. 159–164.

[126] WA Kuperman et al. “Phase conjugation in the ocean: Experimental demonstration of an acoustic time-reversal mirror”. In: *The Journal of the Acoustical Society of America* 103.1 (1998), pp. 25–40.

[127] R. Dubroca et al. “Time reversal-based processing for human targets detection in realistic through-the-wall scenarios”. In: *Radar Conference (EuRAD), 2011 European*. 2011, pp. 1–4.

[128] Jean-Louis Thomas, F. Wu, and M. Fink. “Self focusing on extended objects with time reversal mirror, applications to lithotripsy”. In: *Ultrasonics Symposium, 1994. Proceedings., 1994 IEEE*. Vol. 3. 1994, 1809–1814 vol.3.

[129] Jean-Louis Thomas and Mathias A Fink. “Ultrasonic beam focusing through tissue inhomogeneities with a time reversal mirror: application to transskull therapy”. In: *Ultrasonics, Ferroelectrics, and Frequency Control, IEEE Transactions on* 43.6 (1996), pp. 1122–1129.

[130] M. Fink. “Time reversal and phase conjugation with acoustic waves: industrial and medical applications”. In: *Lasers and Electro-Optics, 2005. (CLEO). Conference on*. Vol. 3. 2005, 2334–2335 Vol. 3.

[131] P. Kosmas and C.M. Rappaport. “Time reversal with the FDTD method for microwave breast cancer detection”. In: *Microwave Theory and Techniques, IEEE Transactions on* 53.7 (2005), pp. 2317–2323.

[132] Ros Kiri Ing et al. “In solid localization of finger impacts using acoustic time-reversal process”. In: *Applied Physics Letters* 87.20, 204104 (2005), pp. –.

[133] C. Hudin, J. Lozada, and V. Hayward. “Localized tactile stimulation by time-reversal of flexural waves: Case study with a thin sheet of glass”. In: *World Haptics Conference (WHC), 2013*. 2013, pp. 67–72.

[134] R.K. Ing and M. Fink. "Time recompression of dispersive Lamb waves using a time reversal mirror-application to flaw detection in thin plates". In: *Ultrasonics Symposium, 1996. Proceedings., 1996 IEEE*. Vol. 1. 1996, 659–663 vol.1.

[135] C. Prada et al. "Decomposition of the time reversal operator: Detection and selective focusing on two scatterers". In: *The Journal of the Acoustical Society of America* 99.4 (1996), pp. 2067–2076.

[136] C. Prada and J-L Thomas. "Experimental subwavelength localization of scatterers by decomposition of the time reversal operator interpreted as a covariance matrix". In: *The Journal of the Acoustic Society of America* 114.1 (2003), pp. 235–243.

[137] A. Baussard and T. Boutin. "Time-Reversal RAP-MUSIC Approach". In: *Electromagnetics in Advanced Applications, 2007. ICEAA 2007. International Conference on*. 2007, pp. 141–144.

[138] A. J. Devaney. "Super-resolution Processing of Multi-static Data Using Time Reversal and MUSIC". URL: http://www.ece.neu.edu/faculty/devaney/preprints/paper02n_00.pdf.

[139] S. K. Lehman and A. J. Devaney. "Transmission mode time-reversal super-resolution imaging". In: *The Journal of the Acoustic Society of America* 113.5 (2003), pp. 2742–2753.

[140] Chun H Wang, James T Rose, and Fu-Kuo Chang. "A synthetic time-reversal imaging method for structural health monitoring". In: *Smart Materials and Structures* 13.2 (2004), p. 415.

[141] P. Kyritsi et al. "Time reversal techniques for wireless communications". In: *Vehicular Technology Conference, 2004. VTC2004-Fall. 2004 IEEE 60th*. Vol. 1. 2004, 47–51 Vol. 1.

[142] G Lerosey et al. "Time reversal of electromagnetic waves and telecommunication". In: *Radio Science* 40.6 (2005).

[143] W. Zheng, Z Zhao, and Z.-P Nie. "Application of TRM in the UWB through wall radar". In: *Progress In Electromagnetics Research* 87 (2008), pp. 279–296.

[144] N. Maaref et al. "Electromagnetic imaging method based on time reversal processing applied to through-the-wall target localization". In: *Progress In Electromagnetics Research M* 1 (2008), pp. 59–67.

[145] J.M.F. Moura and Yuanwei Jin. "Detection by Time Reversal: Single Antenna". In: *Signal Processing, IEEE Transactions on* 55.1 (2007), pp. 187–201.

[146] Alexander Sutin et al. "Nonlinear detection of land mines using wide bandwidth time-reversal techniques". In: *Proc. SPIE 6217, Detection and Remediation Technologies for Mines and Minelike Targets XI*. Vol. 6217. 2006, 62171B–62171B–12.

[147] S. K. Hong et al. "Nonlinear Electromagnetic Time Reversal in an Open Semireverberant System". In: *Phys. Rev. Applied* 2 (4 2014), p. 044013.

[148] Didier Cassereau and Mathias Fink. "Focusing with plane time-reversal mirrors: An efficient alternative to closed cavities". In: *The Journal of the Acoustical Society of America* 94.4 (1993), pp. 2373–2386.

[149] M. Fink and C. Prada. "Acoustic time-reversal mirrors". In: *Inverse problems* 17.1 (2001), R1.

[150] Mickaël Tanter, Jean-Louis Thomas, and Mathias Fink. "Time reversal and the inverse filter". In: *The Journal of the Acoustical Society of America* 108.1 (2000), pp. 223–234.

[151] R Carminati et al. "Theory of the time reversal cavity for electromagnetic fields". In: *Optics letters* 32.21 (2007), pp. 3107–3109.

[152] J. de Rosny, G. Lerosey, and M. Fink. "Theory of Electromagnetic Time-Reversal Mirrors". In: *Antennas and Propagation, IEEE Transactions on* 58.10 (2010), pp. 3139–3149.

[153] A. E. H. Love. "The Integration of the Equations of Propagation of Electric Waves". In: *Philosophical Transactions of the Royal Society of London A: Mathematical, Physical and Engineering Sciences* 197.287-299 (1901), pp. 1–45.

[154] A. Sarvazyan, L. Fillinger, and L.R. Gavrilov. "Time-reversal acoustic focusing system as a virtual random phased array". In: *Ultrasonics, Ferroelectrics, and Frequency Control, IEEE Transactions on* 57.4 (2010), pp. 812–817.

[155] Philippe Roux, Benoit Roman, and Mathias Fink. "Time-reversal in an ultrasonic waveguide". In: *Applied Physics Letters* 70.14 (1997), pp. 1811–1813.

[156] A. Derode, P. Roux, and M. Fink. "Robust Acoustic Time Reversal with High-Order Multiple Scattering". In: *Phys. Rev. Lett.* 75 (23 1995), pp. 4206–4209.

[157] P. Blomgren, G. Papanicolaou, and H. Zhao. "Super-resolution in time-reversal acoustics". In: *The Journal of the Acoustical Society of America* 111.1 (2002), pp. 230–248.

[158] Geoffroy Lerosey et al. "Focusing beyond the diffraction limit with far-field time reversal". In: *Science* 315.5815 (2007), pp. 1120–1122.

[159] Christophe Gomez. "Time-reversal superresolution in random waveguides". In: *Multiscale Modeling & Simulation* 7.3 (2009), pp. 1348–1386.

[160] H. Ammari, É Bonnetier, and Y. Capdeboscq. "Enhanced Resolution in Structured Media". In: *SIAM J. Appl. Math.* 70.5 (2009), pp. 1428–1452.

[161] D.A. Hill and J.M. Ladbury. "Spatial-correlation functions of fields and energy density in a reverberation chamber". In: *Electromagnetic Compatibility, IEEE Transactions on* 44.1 (2002), pp. 95–101.

[162] D. Cassereau, F. Wu, and M. Fink. "Limits of self-focusing using closed time-reversal cavities and mirrors-theory and experiment". In: *Ultrasonics Symposium, 1990. Proceedings., IEEE 1990.* 1990, 1613–1618 vol.3.

[163] C. Draeger and M. Fink. "One-Channel Time Reversal of Elastic Waves in a Chaotic 2D-Silicon Cavity". In: *Phys. Rev. Lett.* 79 (3 1997), pp. 407–410.

[164] Liu Huikan. "Spatial correlation functions of fields in a reverberation chamber based on expansion of spherical Bessel functions". In: *Electromagnetic Compatibility, IEEE Transactions on* 48.2 (2006), pp. 427–428.

[165] A. Derode, A. Tourin, and M. Fink. "Random multiple scattering of ultrasound. II. Is time reversal a self-averaging process?" In: *Phys. Rev. E* 64 (3 2001), p. 036606.

[166] A. Cozza and F. Monsef. "Multiple-Source Time-Reversal Transmissions in Random Media". In: *Antennas and Propagation, IEEE Transactions on* 62.8 (2014), pp. 4269–4281.

[167] T. Fromenteze, D. Carsenat, and C. Decroze. "A Precorrection Method for Passive UWB Time-Reversal Beamformer". In: *Antennas and Wireless Propagation Letters, IEEE* 12 (2013), pp. 836–840.

[168] Gabriel Montaldo et al. "Generation of very high pressure pulses with 1-bit time reversal in a solid waveguide". In: *The Journal of the Acoustical Society of America* 110.6 (2001), pp. 2849–2857.

[169] C. Draeger and M. Fink. "One-channel time-reversal in chaotic cavities: theoretical limits". In: *The Journal of the Acoustical Society of America* 105 (1999), p. 611.

[170] C. Draeger, J-C. Aime, and M. Fink. "One-channel time-reversal in chaotic cavities: Experimental results". In: *The Journal of the Acoustical Society of America* 105.2 (1999), pp. 618–625.

[171] A. Cozza and H. Moussa. "Enforcing deterministic polarisation in a reverberating environment". In: *Electronics Letters* 45.25 (2009), pp. 1299–1301.

[172] A. Cozza. "Increasing peak-field generation efficiency of reverberation chamber". In: *Electronics Letters* 46.1 (2010), pp. 38–39.

[173] A. Cozza. “The Role of Losses in the Definition of the Overmoded Condition for Reverberation Chambers and Their Statistics”. In: *Electromagnetic Compatibility, IEEE Transactions on* 53.2 (2011), pp. 296–307.

[174] F. Monsef and A. Cozza. “Variability and Confidence Intervals of the Power Measured in a Reverberation Chamber”. In: *Electromagnetic Compatibility, IEEE Transactions on* 56.5 (2014), pp. 1238–1241.

[175] J.M. Ladbury et al. *Evaluation of the NASA Langley Research Center mode-stirred chamber facility*. Vol. 1508. NIST technical note. U.S. Government Printing Office, 1999.

[176] M. Hoijer, H.G. Krauthauser, and J. Ladbury. “On Maximum Power Available to Stress Onto the Critical Component in the Equipment Under Test When Performing a Radiated Susceptibility Test in the Reverberation Chamber”. In: *Electromagnetic Compatibility, IEEE Transactions on* 50.4 (2008), pp. 1020–1020.

[177] C. W. Kosten. “The mean free path in room acoustics”. In: *Acta Acustica united with Acustica* 10.4 (1960), pp. 245–250.

[178] K. Song, Y. Fan, and X. Zhou. “Broadband radial waveguide power amplifier using a spatial power combining technique”. In: *IET microwaves, antennas & propagation* 3.8 (2009), pp. 1179–1185.

[179] D.I.L. de Villiers. “Analysis and Design of Conical Transmission Line Power Combiners”. PhD thesis. University of Stellenbosch, 2007.

[180] H. Tang and X. Shui. “Design of A Side-feeding Resistance-loaded Antipodal Vivaldi Antenna”. In: *Proceedings of the 2nd International Conference on Computer Science and Electronics Engineering*. Atlantis Press. 2013.

[181] H. Vallon et al. “Effect of loading a mode-stirred chamber with antennas on Q-factor and comparison to theory”. In: *General Assembly and Scientific Symposium (URSI GASS), 2014 XXXIth URSI*. 2014, pp. 1–4.

[182] H. Vallon et al. “Étude du gain en puissance du retournement temporel en milieu réverbérant”. In: *Journée Nationale Microondes*. 2013.

[183] H. Vallon et al. “Increasing Peak-Power Field Generation Efficiency in Reverberation Chambers”. In: *AMEREM*. 73. 2014.

[184] H. Vallon et al. “Time-Reversed Excitation of Reveberation Chambers : Improving Efficiency and Reliability in the Generation of Radiated Stress”. In: *Electromagnetic Compatibility, IEEE Transactions on* to be published (2015).

[185] H. Vallon et al. “Améliorer la génération de champs forts grâce au retournement temporel”. In: *EMGE*. 2013.

[186] H. Vallon et al. “Etude probabiliste du gain en puissance du retournement temporel en milieu réverbérant”. In: *Assemblée Générale GdR Ondes*. 2013.

[187] H. Vallon et al. “Time Reversal Billard”. English and French. Pat. V.Réf. TCSINV14 003 N.Réf. BFF 14P0354. 2014.

[188] H. Vallon et al. “Time-Reversal Omnidirectionnal Device”. English and French. Pat. V.Réf. TCSINV14003 N.Réf. BFF 14P0784. 2014.

[189] T. Lemoine. “Tubés électroniques hyperfréquences- Technologies, tubes à grilles et klystrons”. In: *Techniques de l’ingénieur* e1620 (2009).

[190] T. Lemoine. “Tubes électroniques hyperfréquences -Tubes à ondes progressives et à champs croisés”. In: *Techniques de l’ingénieur* e1621 (2009).

[191] R.J. Barker, IEEE Nuclear, and Plasma Sciences Society. *Modern microwave and millimeter-wave power electronics*. IEEE Press, 2005.

[192] M. Frater and M. Ryan. *Electronic Warfare for the Digitized Battlefield*. Norwood, MA, USA: Artech House, Inc., 2001.

[193] R. Poisel. *Foundations of Communications Electronic Warfare*. Artech House Electronic Warfare Library. Artech House, 2008.

[194] K.B. Alexander. *Electronic Warfare in Operations: U. S. Army Field Manual FM 3-36*. DIANE Publishing Company, 2012.

References Sorted by Topic

Electromagnetics and Electromagnetic Compatibility

[8] P. Degauque and J. Hamelin. *Electromagnetic compatibility*. Oxford science publications. Oxford University Press, 1993.

[13] DG Pierce and DL Durgin. "An overview of electrical overstress effects on semiconductor devices". In: *Proceedings of the EOS/ESD Symposium*. 1981, p. 120.

[14] JH Yee, WJ Orvis, and Leroy C Martin. *Theoretical Modeling of EMP Effects in Semiconductor Junction Devices*. Tech. rep. DTIC Document, 1983.

[15] R.L. Davies and F.E. Gentry. "Control of electric field at the surface of P-N junctions". In: *Electron Devices, IEEE Transactions on* 11.7 (1964), pp. 313–323.

[17] R. Hoad et al. "Trends in EM susceptibility of IT equipment". In: *Electromagnetic Compatibility, IEEE Transactions on* 46.3 (2004), pp. 390–395.

[71] R Balian and C Bloch. "Distribution of eigenfrequencies for the wave equation in a finite domain: I. Three-dimensional problem with smooth boundary surface". In: *Annals of Physics* 60.2 (1970), pp. 401 –447.

[76] Philip McCord Morse and Hermann Feshbach. *Methods of theoretical physics*. Vol. 1. McGraw-Hill, 1953.

[83] H. G. Booker and P. C. Clemmow. "The concept of an angular spectrum of plane waves, and its relation to that of polar diagram and aperture distribution". In: *Proceedings of the IEE - Part III: Radio and Communication Engineering* 97.45 (1950), pp. 11–17.

[84] P. C. Clemmow. *The plane wave spectrum representation of electromagnetic fields*. IEEE/OUP Series on Electromagnetic Wave Theory, 1966, vii, 185 p.

[90] Thomas F. Frost and Atindra K. Mitra. *Electromagnetic Compatibility Testing Studies*. NASA-CR-200839, 1996.

[110] A. Cozza. "Source Correlation in Randomly Excited Complex Media". In: *Antennas and Wireless Propagation Letters, IEEE* 11 (2012), pp. 105–108.

[153] A. E. H. Love. "The Integration of the Equations of Propagation of Electric Waves". In: *Philosophical Transactions of the Royal Society of London A: Mathematical, Physical and Engineering Sciences* 197.287-299 (1901), pp. 1–45.

[180] H. Tang and X. Shui. "Design of A Side-feeding Resistance-loaded Antipodal Vivaldi Antenna". In: *Proceedings of the 2nd International Conference on Computer Science and Electronics Engineering*. Atlantis Press. 2013.

High-Power ElectroMagnetics

[1] J. Benford, J.A. Swegle, and E. Schamiloglu. *High Power Microwaves, Second Edition*. Series in Plasma Physics. Taylor & Francis, 2007.

[2] D.C. Wunsch and R.R. Bell. "Determination of Threshold Failure Levels of Semiconductor Diodes and Transistors Due to Pulse Voltages". In: *Nuclear Science, IEEE Transactions on* 15.6 (1968), pp. 244–259.

[9] D.V. Giri and F.M. Tesche. "Classification of intentional electromagnetic environments (IEME)". In: *Electromagnetic Compatibility, IEEE Transactions on* 46.3 (2004), pp. 322–328.

[10] IEC. *Standard 61000-2-13: Electromagnetic compatibility (EMC) Part 2-13: Environment - High-power electromagnetic (HPEM) environments-Radiated and conducted*. 2005.

[11] D. Månsson, R. Thottappillil, and M. Bäckström. "Methodology for Classifying Facilities With Respect to Intentional EMI". In: *Electromagnetic Compatibility, IEEE Transactions on* 51.1 (2009), pp. 46–52.

[16] R.J. Barker and E. Schamiloglu. *High-power microwave sources and technologies*. IEEE Press series on RF and microwave technology. IEEE Press, 2001.

[18] DV Giri, FM Tesche, Carl E Baum, et al. "An overview of high-power electromagnetic (HPEM) radiating and conducting systems". In: *Circuit and Electromagnetic System Design Notes* 50 (2006).

[19] D.V. Giri. *High-power Electromagnetic Radiators: Nonlethal Weapons and Other Applications*. Electromagnetics library. Harvard University Press, 2004.

[20] Steven H Gold and Gregory S Nusinovich. "Review of high-power microwave source research". In: *Review of Scientific instruments* 68.11 (1997), pp. 3945–3974.

[21] C.D. Taylor and D.V. Giri. *High Power Microwave Systems And Effects*. Electromagnetics Library. Taylor & Francis, 1994.

[22] B.E. Kruger. "Efficient wideband high power generation for X- and Ku-band radars". In: *Radar Conference, 1995., Record of the IEEE 1995 International*. 1995, pp. 227–232.

[23] M. Kumar et al. "22-kW next generation low cost S-band solid state transmitter for surveillance and air traffic control radars". In: *Microwave Symposium Digest, 1995., IEEE MTT-S International*. 1995, 1601–1604 vol.3.

[24] T. Murae, K. Fujii, and T. Matsuno. "High power S-band solid-state amplifiers for surveillance and traffic control radars". In: *Microwave Symposium Digest, 2001 IEEE MTT-S International*. Vol. 2. 2001, 653–656 vol.2.

[25] M. Cicolani. "High power modular S-band solid state transmitter family for ATC and naval radar applications". In: *Microwave Symposium Digest. 2000 IEEE MTT-S International*. Vol. 3. 2000, 1723–1726 vol.3.

[26] V.L. Granatstein et al. "High Power Microwave Technology and Effects". In: *University of Maryland Short Course* (2005).

[27] V.L. Granatstein and I. Alexeff. *High-power Microwave Sources*. Microwave Library. Artech House, 1987.

[28] IEEE Nuclear and Plasma Sciences Society. *Modern microwave and millimeter-wave power electronics*. Ed. by R. J. Barker et al. Wiley-Interscience, IEEE PRESS, 2005.

[30] R.S. Symons. "Tubes: still vital after all these years". In: *Spectrum, IEEE* 35.4 (1998), pp. 52–63.

[34] M. Abrams. "Dawn of the E-Bomb". In: *Spectrum, IEEE* 40.11 (2003), pp. 24–30.

[189] T. Lemoine. “Tubés électroniques hyperfréquences- Technologies, tubes à grilles et klystrons”. In: *Techniques de l’ingénieur* e1620 (2009).

[190] T. Lemoine. “Tubes électroniques hyperfréquences -Tubes à ondes progressives et à champs croisés”. In: *Techniques de l’ingénieur* e1621 (2009).

[191] R.J. Barker, IEEE Nuclear, and Plasma Sciences Society. *Modern microwave and millimeter-wave power electronics*. IEEE Press, 2005.

Reverberation Chambers

[3] D.A. Hill. “Plane wave integral representation for fields in reverberation chambers”. In: *IEEE Transactions on Electromagnetic Compatibility* 40.3 (1998), pp. 209–217.

[4] IEC. *Standard 61000-4-21: Electromagnetic Compatibility (EMC) Part 4: Testing and Measurement Techniques, Sec. 21: Reverberation Chambers*. 2011.

[6] B. Démoulin and P. Besnier. *Les Chambres réverbérantes en électromagnétisme*. Collection Télécom. Hermes Science Publications, 2010.

[45] M. Hoijer. “Maximum power available to stress onto the critical component in the equipment under test when performing a radiated susceptibility test in the reverberation chamber”. In: *Electromagnetic Compatibility, IEEE Transactions on* 48.2 (2006), pp. 372–384.

[46] P. Corona et al. “Use of a Reverberating Enclosure for Measurements of Radiated Power in the Microwave Range”. In: *Electromagnetic Compatibility, IEEE Transactions on* EMC-18.2 (1976), pp. 54–59.

[47] H.-G. Krauthauser. “On the Measurement of Total Radiated Power in Uncalibrated Reverberation Chambers”. In: *Electromagnetic Compatibility, IEEE Transactions on* 49.2 (2007), pp. 270–279.

[48] K. Rosengren et al. “Characterization of antennas for mobile and wireless terminals by using reverberation chambers: improved accuracy by platform stirring”. In: *Antennas and Propagation Society International Symposium, 2001. IEEE*. Vol. 3. 2001, 350–353 vol.3.

[49] H. Mendez H. A. “A new approach to electromagnetic field-strength measurements in shielded enclosures”. In: *Wescon Technical Papers, Western Electronic Show and Convention*. 1968.

[50] H. A. Mendez. “Meaningful EMC Measurements in Shielded Enclosures”. In: *Electromagnetic Compatibility Symposium Record, 1969 IEEE*. 1969, pp. 137–137.

[51] Thomas A. Loughry. “Frequency Stirring: An Alternate Approach to Mechanical Mode-Stirring for the Conduct of Electromagnetic Susceptibility Testing”. In: *Phillips Lab. Kirtland A.F.B. N.M.* (1991).

[52] D.A. Hill. “Electronic mode stirring for reverberation chambers”. In: *Electromagnetic Compatibility, IEEE Transactions on* 36.4 (1994), pp. 294–299.

[53] C.L. Holloway et al. “Reverberation Chamber Techniques for Determining the Radiation and Total Efficiency of Antennas”. In: *Antennas and Propagation, IEEE Transactions on* 60.4 (2012), pp. 1758–1770.

[54] Stephen J. Boyes. “Reverberation Chambers and the Measurement of Antenna Characteristics”. PhD thesis. University of Liverpool, 2013.

[55] David A. Hill. “Electromagnetic Theory of Reverberation Chambers”. In: *NIST, NBS TN-1506* 1506 (1998), p. 60.

[57] D. I. Wu and David C. Chang. *An investigation of a ray-mode representation of the Green’s function in a rectangular cavity*. Vol. 1312. NBS technical note. U.S. Government Printing Office, 1987.

[58] Do-Hoon Kwon, R.J. Burkholder, and P.H. Pathak. “Ray analysis of electromagnetic field build-up and quality factor of electrically large shielded enclosures”. In: *Electromagnetic Compatibility, IEEE Transactions on* 40.1 (1998), pp. 19–26.

[62] Cozza. “Introduction to Reverberation Chambers - Their physics and practical applications”.

[66] B.H. Liu, D.C. Chang, and M.T. Ma. *Eigenmodes and the Composite Quality Factor of a Reverberating Chamber*. NBS Technical Note 1066. National Bureau of Standards, Aug. 1983.

[75] C-T. Tai and P. Rozenfeld. “Different Representations of Dyadic Green’s functions for a Rectangular Cavity”. In: *Microwave Theory and Techniques, IEEE Transactions on* 25 (1976). (Also see a report HDL-TR-1724 by the same authors with the same title, prepared for the U.S. Army Material Command, Harry Diamond Labs, Adelphi, Maryland, December 1975), pp. 597–601.

[77] T. H. Lehman. “A statistical theory of electromagnetic fields in complex cavities”. In: *Interaction Notes, Note* 494 (1993).

[78] E. Amador. “Modèles de compréhension par la théorie des images des phénomènes transitoires et du régime permanent en chambre réverbérante électromagnétique”. PhD thesis. IETR - INSA de Rennes, 2011.

[79] M. L. Crawford and G. H. Koepke. *Design, Evaluation, and Use of a Reverberation Chamber For Performing Electromagnetic Susceptibility/Vulnerability Measurements.* NBS Technical Note 1092. National Bureau of Standards, 1986.

[80] C.L. Holloway et al. “Requirements for an effective reverberation chamber: unloaded or loaded”. In: *Electromagnetic Compatibility, IEEE Transactions on* 48.1 (2006), pp. 187–194.

[82] J.G. Kostas and B. Boverie. “Statistical model for a mode-stirred chamber”. In: *Electromagnetic Compatibility, IEEE Transactions on* 33.4 (1991), pp. 366–370.

[86] C.L. Holloway et al. “On the Use of Reverberation Chambers to Simulate a Rician Radio Environment for the Testing of Wireless Devices”. In: *Antennas and Propagation, IEEE Transactions on* 54.11 (2006), pp. 3167–3177.

[87] J. M. Ladbury. “Monte Carlo simulation of reverberation chambers”. In: *Digital Avionics Systems Conference, 1999. Proceedings. 18th*. Vol. 2. 1999, 10.C.1–1–10.C.1–8 vol.2.

[88] B. Esen. “Quality Factor of Microwave Chambers”. MA thesis. Texas Tech. University, 1996.

[89] D.A. Hill. *Aperture Excitation of Electrically Large, Lossy Cavities*. NIST Technical Note 1361, 1993.

[91] J.M. Dunn. “Local, high-frequency analysis of the fields in a mode-stirred chamber”. In: *Electromagnetic Compatibility, IEEE Transactions on* 32.1 (1990), pp. 53–58.

[93] J. M. Ladbury et al. *Rapid Evaluation of Mode-stirred Chambers Using Impulsive Waveforms*. NIST technical note. U.S. Government Printing Office, 1996.

[94] Robert E. Richardson. *Reverberant Microwave Propagation*. Technical Report 2000-2008. Naval Surface Warfare Center Dahlgreen Div VA, 2008.

[95] A.K. Mitra and T.F. Trost. “Power transfer characteristics of a microwave reverberation chamber”. In: *Electromagnetic Compatibility, IEEE Transactions on* 38.2 (1996), pp. 197–200.

[96] A. K. Mitra. “Some Critical Parameters for the Statistical Characterization of Power Density witinh a Microwave Reverberation Chamber”. PhD thesis. Texas Tech. University, 1996.

[97] D.A. Hill. “A reflection coefficient derivation for the Q of a reverberation chamber”. In: *Electromagnetic Compatibility, IEEE Transactions on* 38.4 (1996), pp. 591–592.

[98] P. Corona, G. Latmiral, and Enrico Paolini. “Performance and Analysis of a Reverberating Enclosure with Variable Geometry”. In: *Electromagnetic Compatibility, IEEE Transactions on* 22.1 (1980), pp. 2–5.

[99] D.A. Hill. "Linear dipole response in a reverberation chamber". In: *Electromagnetic Compatibility, IEEE Transactions on* 41.4 (1999), pp. 365–368.

[100] J. M. Ladbury and D. A. Hill. "An improved model for antennas in reverberation chambers". In: *Electromagnetic Compatibility (EMC), 2010 IEEE International Symposium on*. 2010, pp. 663–667.

[104] C.L. Holloway et al. "Early Time Behavior in Reverberation Chambers and Its Effect on the Relationships Between Coherence Bandwidth, Chamber Decay Time, RMS Delay Spread, and the Chamber Buildup Time". In: *Electromagnetic Compatibility, IEEE Transactions on* 54.4 (2012), pp. 714–725.

[105] E. Genender et al. "Use of reverberation chamber to simulate the power delay profile of a wireless environment". In: *Electromagnetic Compatibility - EMC Europe, 2008 International Symposium on*. 2008, pp. 1–6.

[112] D.A. Hill. "Spatial correlation function for fields in a reverberation chamber". In: *Electromagnetic Compatibility, IEEE Transactions on* 37.1 (1995), pp. 138–.

[161] D.A. Hill and J.M. Ladbury. "Spatial-correlation functions of fields and energy density in a reverberation chamber". In: *Electromagnetic Compatibility, IEEE Transactions on* 44.1 (2002), pp. 95–101.

[164] Liu Huikan. "Spatial correlation functions of fields in a reverberation chamber based on expansion of spherical Bessel functions". In: *Electromagnetic Compatibility, IEEE Transactions on* 48.2 (2006), pp. 427–428.

[173] A. Cozza. "The Role of Losses in the Definition of the Overmoded Condition for Reverberation Chambers and Their Statistics". In: *Electromagnetic Compatibility, IEEE Transactions on* 53.2 (2011), pp. 296–307.

[174] F. Monsef and A. Cozza. "Variability and Confidence Intervals of the Power Measured in a Reverberation Chamber". In: *Electromagnetic Compatibility, IEEE Transactions on* 56.5 (2014), pp. 1238–1241.

[175] J.M. Ladbury et al. *Evaluation of the NASA Langley Research Center mode-stirred chamber facility*. Vol. 1508. NIST technical note. U.S. Government Printing Office, 1999.

[176] M. Hoijer, H.G. Krauthauser, and J. Ladbury. "On Maximum Power Available to Stress Onto the Critical Component in the Equipment Under Test When Performing a Radiated Susceptibility Test in the Reverberation Chamber". In: *Electromagnetic Compatibility, IEEE Transactions on* 50.4 (2008), pp. 1020–1020.

Time-Reversal

[7] A. Cozza. *Stochastic modelling of large cavities - Random and coherent field applications*. Université Paris-Sud, Habilitation à Diriger la Recherche, 2012.

[35] M. Davy et al. "Focusing and amplification of electromagnetic waves by time reversal in an leaky reverberation chamber". In: *Comptes Rendus Physique* 11.1 (2010). Propagation and remote sensing Propagation and Teledection, pp. 37 –43.

[36] A. Derode, A. Tourin, and M. Fink. "Ultrasonic pulse compression with one-bit time reversal through multiple scattering". In: *Journal of applied physics* 85.9 (1999), pp. 6343–6352.

[37] S. K. Hong et al. "Focusing an arbitrary RF pulse at a distance using time-reversal techniques". In: *Journal of Electromagnetic Waves and Applications* 27.10 (2013), pp. 1262–1275.

[38] M. Davy. "Application du retournement temporel en micro-ondes à l'amplification d'impulsons et l'imagerie". PhD thesis. Université Paris 7 - Denis Diderot, 2010.

[39] D. Carsenat and C. Decroze. “UWB Antennas Beamforming Using Passive Time-Reversal Device”. In: *Antennas and Wireless Propagation Letters, IEEE* 11 (2012), pp. 779–782.

[40] S. K. Hong et al. “Single-Feed Beam-Steering of Short Pulses via Time Reversal”. In: *Antennas and Wireless Propagation Letters, IEEE* 13 (2014), pp. 794–797.

[41] T. Fromenteze, C. Decroze, and D. Carsenat. “Miniaturized device for passive microwave UWB beamforming”. In: *Antennas and Propagation (EuCAP), 2014 8th European Conference on*. 2014, pp. 354–358.

[42] T. Fromenteze, C. Decroze, and D. Carsenat. “Waveform Coding for Passive Multiplexing: Application to Microwave Imaging”. In: *Antennas and Propagation, IEEE Transactions on* 63.2 (2015), pp. 593–600.

[43] T. Fromenteze et al. “Computational imaging using a mode-mixing cavity at microwave frequencies”. In: *Applied Physics Letters* 106.19 (2015), pp. –.

[44] W.S. Wall and S.K. Hong. “Improved Time-Reversal-Based Beamforming Using a Self-Biasing Switch”. In: *Antennas and Wireless Propagation Letters, IEEE* 13 (2014), pp. 1337–1340.

[60] G. Montaldo et al. “The time reversal kaleidoscope: a new concept of smart transducers for 3D imaging”. In: *Ultrasonics, 2003 IEEE Symposium on*. Vol. 1. 2003, pp. 42–45.

[81] A. Cozza. “Statistics of the performance of time reversal in a lossy reverberating medium”. In: *Physical Review E* 80.5 (2009), p. 056604.

[106] A. Derode, A. Tourin, and M. Fink. “Limits of time-reversal focusing through multiple scattering: Long-range correlation”. In: *The Journal of the Acoustical Society of America* 107.6 (2000), pp. 2987–2998.

[107] K. J. Haworth et al. “Generalized shot noise model for time-reversal in multiple-scattering media allowing for arbitrary inputs and windowing”. In: *The Journal of the Acoustical Society of America* 125.5 (2009), pp. 3129–3140.

[113] M. Fink et al. “Self focusing in inhomogeneous media with time reversal acoustic mirrors”. In: *Ultrasonics Symposium, 1989. Proceedings., IEEE 1989*. 1989, 681–686 vol.2.

[114] G. Lerosey et al. “Time Reversal of Electromagnetic Waves”. In: *Phys. Rev. Lett.* 92 (19 2004).

[115] G. Lerosey. “Retournement temporel d’ondes électromagnétiques et application à la télécommunication en milieux complexes”. Theses. ESPCI ParisTECH, 2006.

[116] M. Fink. “Time-reversal of ultrasonic fields. Part I: Basic principles”. In: *Ultrasonics, Ferroelectrics, and Frequency Control, IEEE Transactions on* 39.5 (1992), pp. 555–566.

[117] F. Wu, J-L. Thomas, and M. Fink. “Time-reversal of ultrasonic fields. Part II: Experimental results”. In: *Ultrasonics, Ferroelectrics, and Frequency Control, IEEE Transactions on* 39.5 (1992), pp. 567–578.

[118] M. Fink et al. “Time-reversed acoustics”. In: *Reports on Progress in Physics* 63.12 (2000), p. 1933.

[119] J. de Rosny. “Milieux Réverbérant et réversibilité”. PhD thesis. Université Paris VI-Pierre et Marie Cuire, 2000.

[120] Rémi Carminati, Manuel Nieto-Vesperinas, and Jean-Jacques Greffet. “Reciprocity of evanescent electromagnetic waves”. In: *J. Opt. Soc. Am. A* 15.3 (1998), pp. 706–712.

[121] C. Draeger and M. Fink. “One-channel time reversal of elastic waves in a chaotic 2D-silicon cavity”. In: *Physical Review Letters* 79 (1997), p. 407.

[122] G Lerosey et al. “Time reversal of wideband microwaves”. In: *Applied Physics Letters* 88.15 (2006), pp. 154101–154101.

[124] A. Cozza. "Emulating an Anechoic Environment in a Wave-Diffusive Medium Through an Extended Time-Reversal Approach". In: *Antennas and Propagation, IEEE Transactions on* 60.8 (2012), pp. 3838–3852.

[125] H. Moussa, A. Cozza, and M. Cauterman. "Directive wavefronts inside a time reversal electromagnetic chamber". In: *Electromagnetic Compatibility, 2009. EMC 2009. IEEE International Symposium on*. 2009, pp. 159–164.

[126] WA Kuperman et al. "Phase conjugation in the ocean: Experimental demonstration of an acoustic time-reversal mirror". In: *The Journal of the Acoustical Society of America* 103.1 (1998), pp. 25–40.

[127] R. Dubroca et al. "Time reversal-based processing for human targets detection in realistic through-the-wall scenarios". In: *Radar Conference (EuRAD), 2011 European*. 2011, pp. 1–4.

[128] Jean-Louis Thomas, F. Wu, and M. Fink. "Self focusing on extended objects with time reversal mirror, applications to lithotripsy". In: *Ultrasonics Symposium, 1994. Proceedings., 1994 IEEE*. Vol. 3. 1994, 1809–1814 vol.3.

[129] Jean-Louis Thomas and Mathias A Fink. "Ultrasonic beam focusing through tissue inhomogeneities with a time reversal mirror: application to transskull therapy". In: *Ultrasonics, Ferroelectrics, and Frequency Control, IEEE Transactions on* 43.6 (1996), pp. 1122–1129.

[130] M. Fink. "Time reversal and phase conjugation with acoustic waves: industrial and medical applications". In: *Lasers and Electro-Optics, 2005. (CLEO). Conference on*. Vol. 3. 2005, 2334–2335 Vol. 3.

[131] P. Kosmas and C.M. Rappaport. "Time reversal with the FDTD method for microwave breast cancer detection". In: *Microwave Theory and Techniques, IEEE Transactions on* 53.7 (2005), pp. 2317–2323.

[132] Ros Kiri Ing et al. "In solid localization of finger impacts using acoustic time-reversal process". In: *Applied Physics Letters* 87.20, 204104 (2005), pp. –.

[133] C. Hudin, J. Lozada, and V. Hayward. "Localized tactile stimulation by time-reversal of flexural waves: Case study with a thin sheet of glass". In: *World Haptics Conference (WHC), 2013*. 2013, pp. 67–72.

[134] R.K. Ing and M. Fink. "Time recompression of dispersive Lamb waves using a time reversal mirror-application to flaw detection in thin plates". In: *Ultrasonics Symposium, 1996. Proceedings., 1996 IEEE*. Vol. 1. 1996, 659–663 vol.1.

[135] C. Prada et al. "Decomposition of the time reversal operator: Detection and selective focusing on two scatterers". In: *The Journal of the Acoustical Society of America* 99.4 (1996), pp. 2067–2076.

[136] C. Prada and J-L Thomas. "Experimental subwavelength localization of scatterers by decomposition of the time reversal operator interpreted as a covariance matrix". In: *The Journal of the Acoustic Society of America* 114.1 (2003), pp. 235–243.

[137] A. Baussard and T. Boutin. "Time-Reversal RAP-MUSIC Approach". In: *Electromagnetics in Advanced Applications, 2007. ICEAA 2007. International Conference on*. 2007, pp. 141–144.

[138] A. J. Devaney. "Super-resolution Processing of Multi-static Data Using Time Reversal and MUSIC". URL: http://www.ece.neu.edu/faculty/devaney/preprints/paper02n_00.pdf.

[139] S. K. Lehman and A. J. Devaney. "Transmission mode time-reversal super-resolution imaging". In: *The Journal of the Acoustic Society of America* 113.5 (2003), pp. 2742–2753.

[140] Chun H Wang, James T Rose, and Fu-Kuo Chang. "A synthetic time-reversal imaging method for structural health monitoring". In: *Smart Materials and Structures* 13.2 (2004), p. 415.

[141] P. Kyritsi et al. “Time reversal techniques for wireless communications”. In: *Vehicular Technology Conference, 2004. VTC2004-Fall. 2004 IEEE 60th*. Vol. 1. 2004, 47–51 Vol. 1.

[142] G Lerosey et al. “Time reversal of electromagnetic waves and telecommunication”. In: *Radio Science* 40.6 (2005).

[143] W. Zheng, Z Zhao, and Z.-P Nie. “Application of TRM in the UWB through wall radar”. In: *Progress In Electromagnetics Research* 87 (2008), pp. 279–296.

[144] N. Maaref et al. “Electromagnetic imaging method based on time reversal processing applied to through-the-wall target localization”. In: *Progress In Electromagnetics Research M* 1 (2008), pp. 59–67.

[145] J.M.F. Moura and Yuanwei Jin. “Detection by Time Reversal: Single Antenna”. In: *Signal Processing, IEEE Transactions on* 55.1 (2007), pp. 187–201.

[146] Alexander Sutin et al. “Nonlinear detection of land mines using wide bandwidth time-reversal techniques”. In: *Proc. SPIE 6217, Detection and Remediation Technologies for Mines and Minelike Targets XI*. Vol. 6217. 2006, 62171B–62171B–12.

[147] S. K. Hong et al. “Nonlinear Electromagnetic Time Reversal in an Open Semireverberant System”. In: *Phys. Rev. Applied* 2 (4 2014), p. 044013.

[148] Didier Cassereau and Mathias Fink. “Focusing with plane time-reversal mirrors: An efficient alternative to closed cavities”. In: *The Journal of the Acoustical Society of America* 94.4 (1993), pp. 2373–2386.

[149] M. Fink and C. Prada. “Acoustic time-reversal mirrors”. In: *Inverse problems* 17.1 (2001), R1.

[150] Mickaël Tanter, Jean-Louis Thomas, and Mathias Fink. “Time reversal and the inverse filter”. In: *The Journal of the Acoustical Society of America* 108.1 (2000), pp. 223–234.

[151] R Carminati et al. “Theory of the time reversal cavity for electromagnetic fields”. In: *Optics letters* 32.21 (2007), pp. 3107–3109.

[152] J. de Rosny, G. Lerosey, and M. Fink. “Theory of Electromagnetic Time-Reversal Mirrors”. In: *Antennas and Propagation, IEEE Transactions on* 58.10 (2010), pp. 3139–3149.

[154] A. Sarvazyan, L. Fillinger, and L.R. Gavrilov. “Time-reversal acoustic focusing system as a virtual random phased array”. In: *Ultrasonics, Ferroelectrics, and Frequency Control, IEEE Transactions on* 57.4 (2010), pp. 812–817.

[155] Philippe Roux, Benoit Roman, and Mathias Fink. “Time-reversal in an ultrasonic waveguide”. In: *Applied Physics Letters* 70.14 (1997), pp. 1811–1813.

[156] A. Derode, P. Roux, and M. Fink. “Robust Acoustic Time Reversal with High-Order Multiple Scattering”. In: *Phys. Rev. Lett.* 75 (23 1995), pp. 4206–4209.

[157] P. Blomgren, G. Papanicolaou, and H. Zhao. “Super-resolution in time-reversal acoustics”. In: *The Journal of the Acoustical Society of America* 111.1 (2002), pp. 230–248.

[158] Geoffroy Lerosey et al. “Focusing beyond the diffraction limit with far-field time reversal”. In: *Science* 315.5815 (2007), pp. 1120–1122.

[159] Christophe Gomez. “Time-reversal superresolution in random waveguides”. In: *Multiscale Modeling & Simulation* 7.3 (2009), pp. 1348–1386.

[160] H. Ammari, É Bonnetier, and Y. Capdeboscq. “Enhanced Resolution in Structured Media”. In: *SIAM J. Appl. Math.* 70.5 (2009), pp. 1428–1452.

[162] D. Cassereau, F. Wu, and M. Fink. “Limits of self-focusing using closed time-reversal cavities and mirrors-theory and experiment”. In: *Ultrasonics Symposium, 1990. Proceedings., IEEE 1990*. 1990, 1613–1618 vol.3.

[163] C. Draeger and M. Fink. “One-Channel Time Reversal of Elastic Waves in a Chaotic 2D-Silicon Cavity”. In: *Phys. Rev. Lett.* 79 (3 1997), pp. 407–410.

[165] A. Derode, A. Tourin, and M. Fink. “Random multiple scattering of ultrasound. II. Is time reversal a self-averaging process?” In: *Phys. Rev. E* 64 (3 2001), p. 036606.

[166] A. Cozza and F. Monsef. “Multiple-Source Time-Reversal Transmissions in Random Media”. In: *Antennas and Propagation, IEEE Transactions on* 62.8 (2014), pp. 4269–4281.

[167] T. Fromenteze, D. Carsenat, and C. Decroze. “A Precorrection Method for Passive UWB Time-Reversal Beamformer”. In: *Antennas and Wireless Propagation Letters, IEEE* 12 (2013), pp. 836–840.

[168] Gabriel Montaldo et al. “Generation of very high pressure pulses with 1-bit time reversal in a solid waveguide”. In: *The Journal of the Acoustical Society of America* 110.6 (2001), pp. 2849–2857.

[169] C. Draeger and M. Fink. “One-channel time-reversal in chaotic cavities: theoretical limits”. In: *The Journal of the Acoustical Society of America* 105 (1999), p. 611.

[170] C. Draeger, J-C. Aime, and M. Fink. “One-channel time-reversal in chaotic cavities: Experimental results”. In: *The Journal of the Acoustical Society of America* 105.2 (1999), pp. 618–625.

[171] A. Cozza and H. Moussa. “Enforcing deterministic polarisation in a reverberating environment”. In: *Electronics Letters* 45.25 (2009), pp. 1299–1301.

[172] A. Cozza. “Increasing peak-field generation efficiency of reverberation chamber”. In: *Electronics Letters* 46.1 (2010), pp. 38–39.

Statistics

[5] T. H. Lehman and G. J. Freyer. “Characterization of the maximum test level in a reverberation chamber”. In: *Electromagnetic Compatibility, 1997. IEEE 1997 International Symposium on*. 1997, pp. 44–47.

[85] A. Papoulis and S.U. Pillai. *Probability, Random Variables, and Stochastic Processes*. McGraw-Hill series in electrical engineering: Communications and signal processing. Tata McGraw-Hill, 2002.

Acoustics

[56] Heinrich Kuttruff. *Room acoustics*. CRC Press, 2009.

[59] E. N. Gilbert. “Ray statistics in reverberation”. In: *The Journal of the Acoustical Society of America* 83.5 (1988), pp. 1804–1808.

[61] J. Jouhaneau. “Acoustique des salles”. In: *Techniques de l’ingénieur* c3360 (1995).

[63] R. H. Bolt, P. E. Doak, and P. J. Westervelt. “Pulse Statistics Analysis of Room Acoustics”. In: *The Journal of the Acoustical Society of America* 22.3 (1950), pp. 328–340.

[64] W. B. Joyce. “Exact effect of surface roughness on the reverberation time of a uniformly absorbing spherical enclosure”. In: *The Journal of the Acoustical Society of America* 64.5 (1978), pp. 1429–1436.

[65] Trevor J Cox and Peter D’antonio. *Acoustic absorbers and diffusers: theory, design and application*. CRC Press, 2009.

[67] M.R. Schroeder. “Statistical Parameters of the Frequency Response Curves of Large Rooms”. In: *J. Audio Eng. Soc* 35.5 (1987), pp. 299–306.

[68] D-Y. Maa. “Distribution of Eigentoness in a Rectangular Chamber at Low Frequency Range”. In: *The Journal of the Acoustical Society of America* 10.3 (1939), pp. 235–238.

[69] R. H. Bolt. “Frequency Distribution of Eigentones in a Thrre-Dimensional Continuum”. In: *The Journal of the Acoustic Society of America* 10.3 (1939), pp. 228–234.

[72] M. R. Schroeder. “Frequency-Correlation Functions of Frequency Responses in Rooms”. In: *The Journal of the Acoustical Society of America* 34.12 (1962), pp. 1819–1823.

[73] M. R. Schroeder and K. H. Kuttruff. “On Frequency Response Curves in Rooms. Comparison of Experimental, Theoretical, and Monte Carlo Results for the Average Frequency Spacing between Maxima”. In: *The Journal of the Acoustical Society of America* 34.1 (1962), pp. 76–80.

[92] M.R. Schroeder. “New method of measuring reverberation time”. In: *The Journal of the Acoustical Society of America* 37 (1965), p. 409.

[108] J-D Polack. “La transmission de l’énergie sonore dans les salles”. PhD thesis. Univeristé du Maine, 1998.

[109] P. Penna. “Some Statistical properties of reverberation process in diffuse sound fields”. MA thesis. The Acoustics Laboratory, Danmark tekniske højskole, 1993.

[177] C. W. Kosten. “The mean free path in room acoustics”. In: *Acta Acustica united with Acustica* 10.4 (1960), pp. 245–250.

Materials

[101] D.R.J. White and M. Mardiguan. *A handbook series on electromagnetic interference and compatibility*. Vol. 3, pp. 2.10. Don White Consultants, 1988.

[102] T. Y. Otoshi and M.M.. Franco. “The electrical conductivities of steel and other candidate materials for shrouds in a beam-waveguide antenna system”. In: *IEEE Transactions on Instrumentation and Measurement* 45.1 (1996), pp. 77–83.

[103] N. Bowler. “Frequency-Dependence of Relative Permeability in Steel”. In: *AIP Conference Proceedings* 820.1 (2006), pp. 1269–1276.

Amplification and Solid-State Design

[31] R.J. Trew, J.-B. Yan, and P.M. Mock. “The potential of diamond and SiC electronic devices for microwave and millimeter-wave power applications”. In: *Proceedings of the IEEE* 79.5 (1991), pp. 598–620.

[32] R.J. Trew. “SiC and GaN transistors - is there one winner for microwave power applications?” In: *Proceedings of the IEEE* 90.6 (2002), pp. 1032–1047.

[178] K. Song, Y. Fan, and X. Zhou. “Broadband radial waveguide power amplifier using a spatial power combining technique”. In: *IET microwaves, antennas & propagation* 3.8 (2009), pp. 1179–1185.

[179] D.I.L. de Villiers. “Analysis and Design of Conical Transmission Line Power Combiners”. PhD thesis. University of Stellenbosch, 2007.

Other References

[12] D. Månsson. "IEMI and EMC Considerations for Large Systems | Smart Grid Aspects". In: *Progress In Electromagnetics Research Symposium Proceedings, Stockholm* (2013), pp. 1366–1370.

[29] J. H. Booske. "Plasma physics and related challenges of millimeter-wave-to-terahertz and high power microwave generationa)". In: *Physics of Plasmas* 15.5 (2008), pp. –.

[33] R. Poisel. *Modern Communications Jamming: Principles and Techniques*. Artech House, 2011.

[70] H. Weyl. "Über die asymptotische Verteilung der Eigenwerte". In: *Nachrichten der Königlichen Gesellschaft der Wissenschaften zu Göttingen* (1911), pp. 110–117.

[74] J. G. Van Bladel. *Electromagnetic fields*. Vol. 19. John Wiley & Sons, 2007.

[111] H.J. Stöckmann. *Quantum Chaos: An introduciton*. Cambridge University Press, 2007.

[123] R. F. Harrington. *Time-Harmonic Electromagnetic Fields*. Wiley-IEEE Press, 2001.

[192] M. Frater and M. Ryan. *Electronic Warfare for the Digitized Battlefield*. Norwood, MA, USA: Artech House, Inc., 2001.

[193] R. Poisel. *Foundations of Communications Electronic Warfare*. Artech House Electronic Warfare Library. Artech House, 2008.

[194] K.B. Alexander. *Electronic Warfare in Operations: U. S. Army Field Manual FM 3-36*. DIANE Publishing Company, 2012.

Published Paper during the course of this PhD

[184] H. Vallon et al. "Time-Reversed Excitation of Reveberation Chambers : Improving Efficiency and Reliability in the Generation of Radiated Stress". In: *Electromagnetic Compatibility, IEEE Transactions on* to be published (2015).

Published Conference Papers during the course of this PhD

[181] H. Vallon et al. "Effect of loading a mode-stirred chamber with antennas on Q-factor and comparison to theory". In: *General Assembly and Scientific Symposium (URSI GASS), 2014 XXXIth URSI*. 2014, pp. 1–4.

[182] H. Vallon et al. "Étude du gain en puissance du retournement temporel en milieu réverbérant". In: *Journée Nationale Microondes*. 2013.

[183] H. Vallon et al. "Increasing Peak-Power Field Generation Efficiency in Reverberation Chambers". In: *AMEREM*. 73. 2014.

[185] H. Vallon et al. "Améliorer la génération de champs forts grâce au retournement temporel". In: *EMGE*. 2013.

[186] H. Vallon et al. "Etude probabiliste du gain en puissance du retournement temporel en milieu réverbérant". In: *Assemblée Générale GdR Ondes*. 2013.

Submitted Patents during this PhD

[187] H. Vallon et al. "Time Reversal Billard". English and French. Pat. V.Réf. TCSINV14 003 N.Réf. BFF 14P0354. 2014.

[188] H. Vallon et al. “Time-Reversal Omnidirectionnal Device”. English and French. Pat. V.Réf. TCSINV14003 N.Réf. BFF 14P0784. 2014.

List of Figures

Appendix A

HPEM

In this appendix various graphics further presenting the state-of-the-art of high-power microwave devices as well as some general knowledge concerning MVED and Solide-State devices and Electronic Warfare are presented.

An important factor when considering HPM sources is the peak to average levels depending on the duty cycle allowed by the considered technology as it is shown in Figure A.1. The retained technology should take into account this parameter depending on the desired applications.

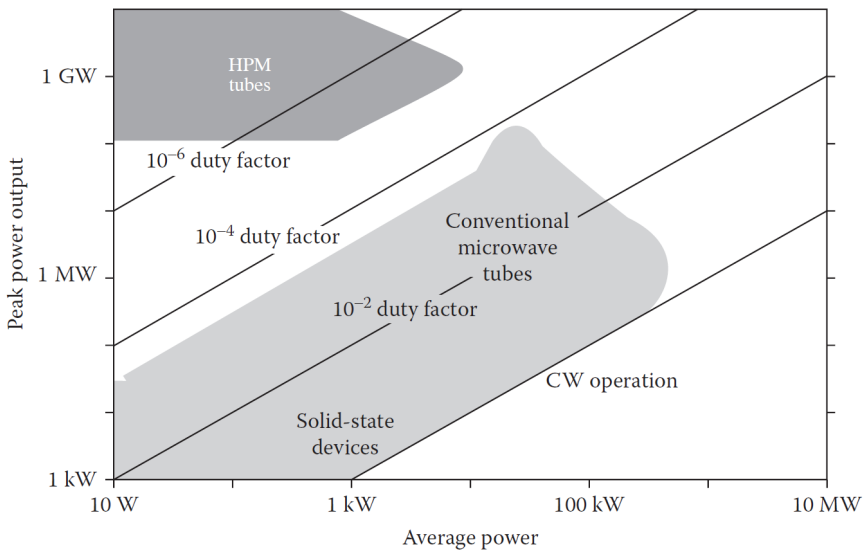

Figure A.1 Peak vs. average power for microwave sources with duty factor [1]

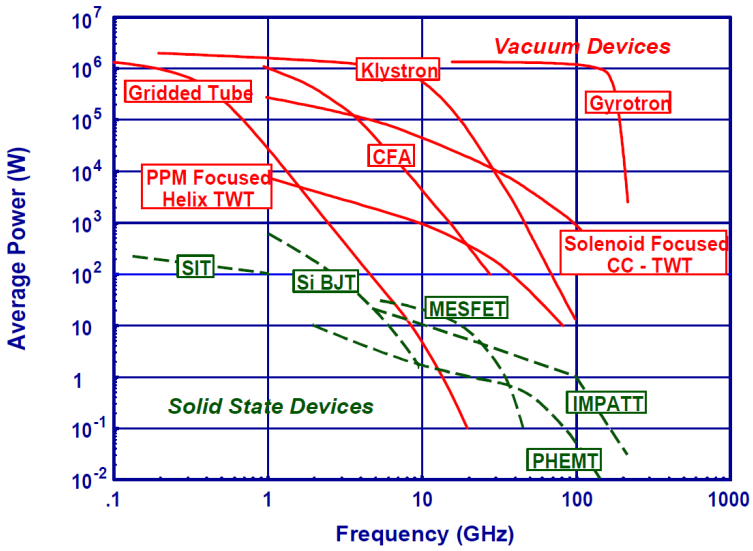

Figure A.2 Source Performance (Average Power) State of the art for various technologies. [189]

Figure A.2 presents a more detailed state-of-the-art of the average power levels that can be obtained in function of frequency and of the technology. Tube technologies still dominate high-power microwave technologies but do not allow the same flexibility as solid-state devices and are most of the times more complex to put in place and heavier.

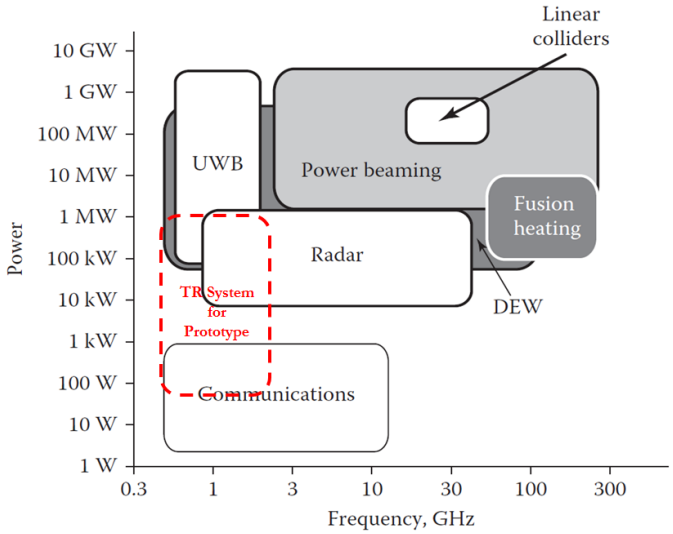

Figure A.3 Domains of HPM applications. "Power" is typically peak-power, but in some cases, such as fusion heating and some directed energy weapons (DEWs), it is average power. Regions are schematic; specific schemes vary widely.

Figure A.3 represents the domains of application of HPM and MPM sources in function of frequency and power levels reached. The considered applications for the time-reversal Amplification System considered during this work is also presented.

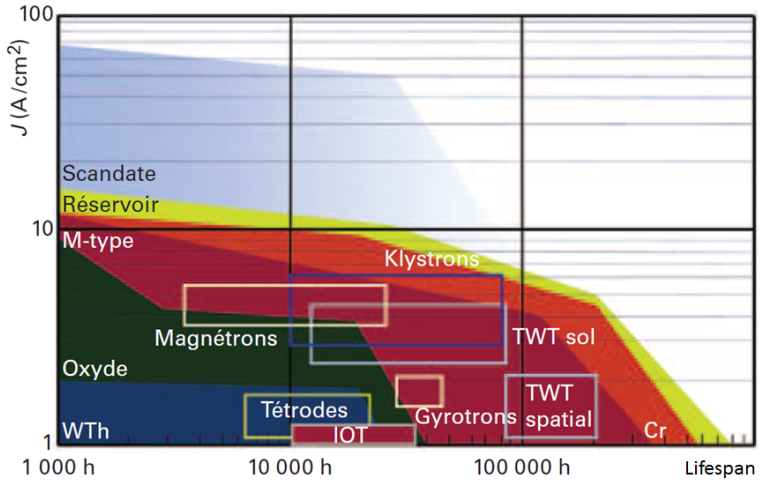

Figure A.4 Lifespan of tube technologies. [189]

Another important figure of merit when considering which technology should be used is the lifespan of a device. As can be seen in Figure A.4 even if for some applications lifespans can span over 100000 hours. Most of tube technologies lifespan seem to be of the order of 10000 hours which just above one year. Another trend is that the higher the power the lower the lifespan. However, for very complex solid-state amplifiers, the lifespan can also be very short.

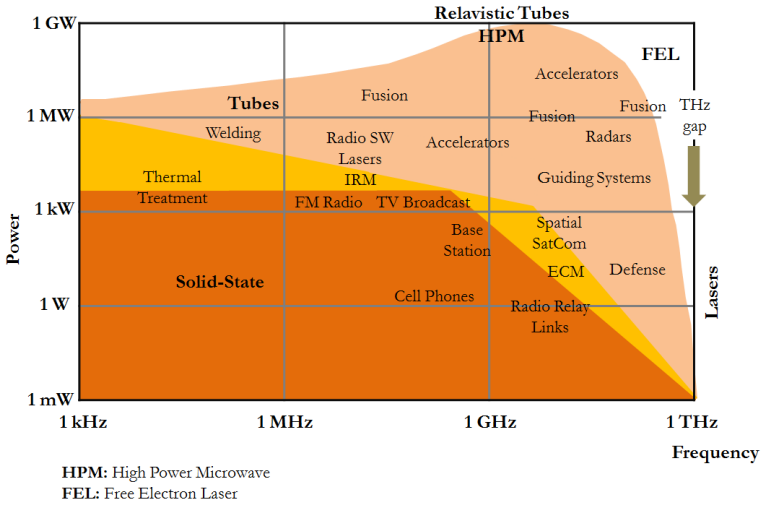

Figure A.5 Applications using solid-state or vacuum technologies. [190]

Figure reveals the trends of solid-state and MVED application fields. As we can see most of the lower-power application fields use solid-state devices only for very high-powers do vacuum technologies still offer better perspective than SSPA. However, with recent novel developments tubes are also getting replaced by solid-state not only because the power levels that are obtainable using solid-state devices have increased further but also because nowadays brute force approach are getting replaced by less powerful but more skilled attack methods. One of the main reasons for this trend the increase number of complex electronics in everyday life.

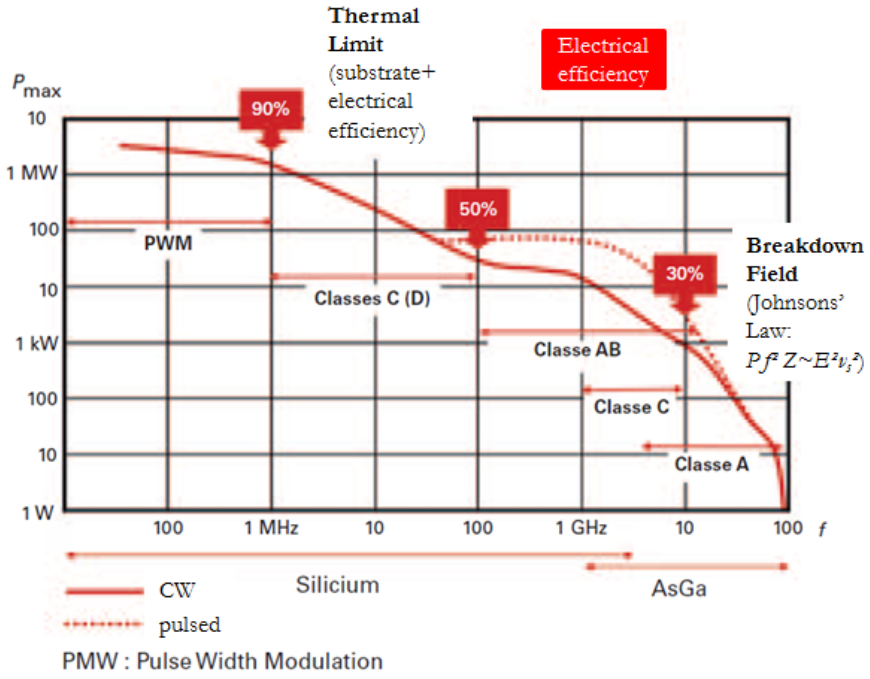

Figure A.6 State of the Arte of Solid-State Power Amplifiers. [190]

Figure A.6 shows a state of the art of the power levels that can be obtained using solid-state power amplifiers depending in which class they are used. This graphic allows to assess how much a TRAS system could benefit from using the solid-state power amplifiers in another class of functioning.

Figure A.7, A.8 and A.9 represent the peak-power limitations of TWT Gyrotrons, Magnetrons and Klystorns technologies and their "current" domain of applications. As we can see almost all the application fields corresponding to TWT could be replaced by solid-state devices enhanced by time-reversal.

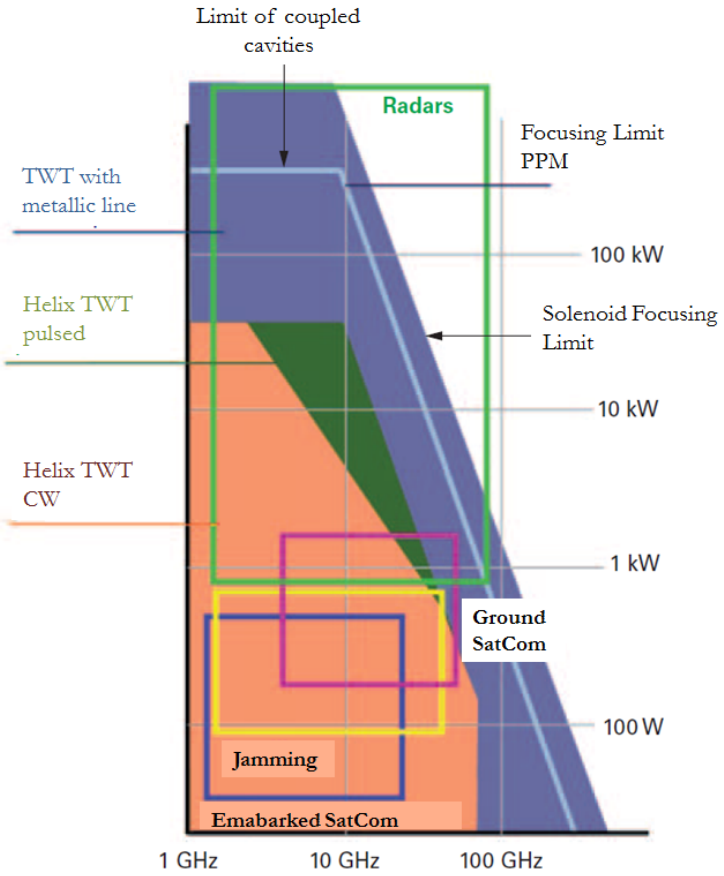

Figure A.7 Peak power of TWT technologies. [190]

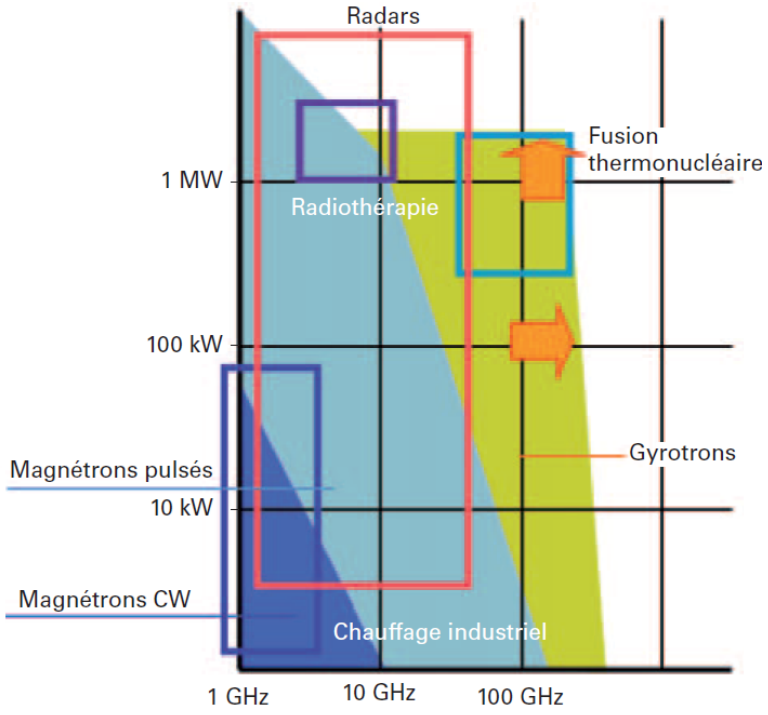

Figure A.8 Peak power of Gyrotron and Magnetron technologies. [190]

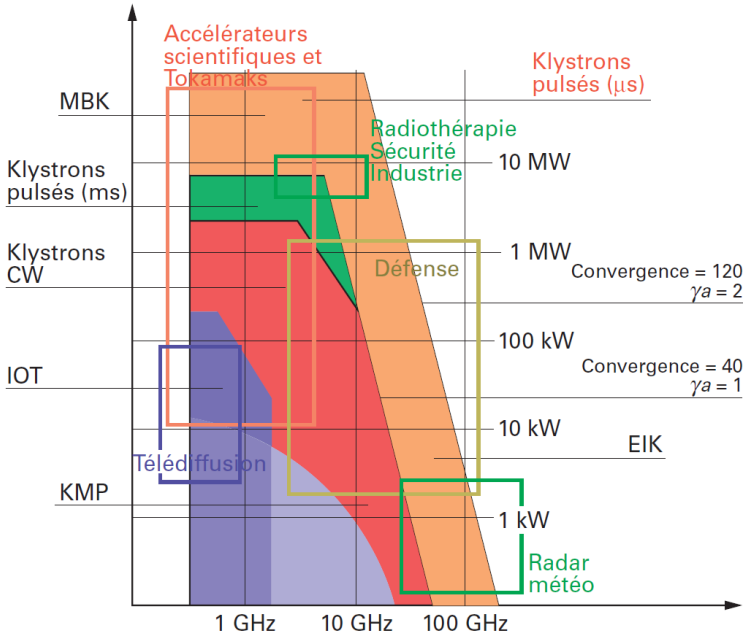

Figure A.9 Peak power of Klystron technologies. [189]

Figures A.10 and A.11 show the physical differences between solid state and Miwcrowave Vacuum Electron Devices. All microwave power electronics operate on the principle of converting the kinetic

energy of an electron stream (electron current) to coherent electromagnetic radiation. In solid-state microwave electronics, the electron stream is sustained by applying a voltage between the emitter and collector electrodes or the source and drain electrodes. This electron stream diffusively drifts through a solid medium (semiconductor). The drifting electrons experience many collisions with the atoms of the semiconductor lattice. As a result of these collisions, the electron stream irretrievably converts a significant fraction of its kinetic energy into waste heat directly inside the device. In MVEDs this problem considerably reduced since the electron stream travels in a sustained vacuum. The electron stream is accelerated by an applied voltage between the anode and the cathode. The only source of heat occurs when the energy left in electron stream collides with the collector. However, contrarily to solid-state devices part of this energy can be recycled. Operation temperature of solid-state devices is also limited to temperatures below 200 °C otherwise some of its components will possibly melt. Vacuum devices are virtually immune to ionizing radiation fluxes, such as one might encounter in space. Finally, the interaction region of a properly designed MVED can withstand much higher electric fields without breakdown than can the materials interior to a solid-state electronic device.

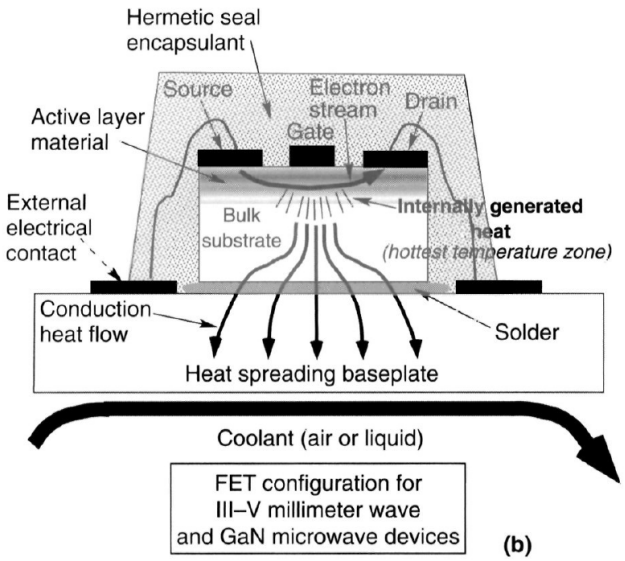

Figure A.10 Illustration of the fundamental physics behind field effect transistor solid-state devices [191].

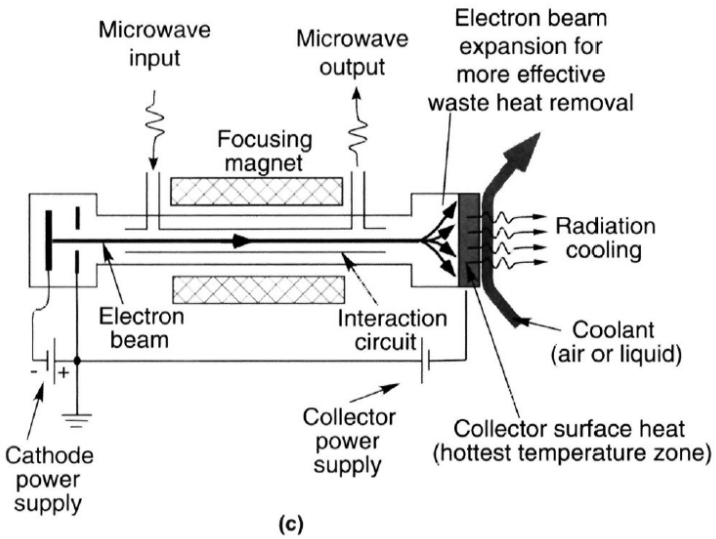

Figure A.11 Illustration of the fundamental physics behind vacuum microwave power electron devices [191].

Finally, Figures A.12 and A.13 give the domain of applications and the three subdivision and their respective definitions of Electronic Warfare. These definitions were important when considering the power-level needed for the time-reversal system to be considered as a viable solution.

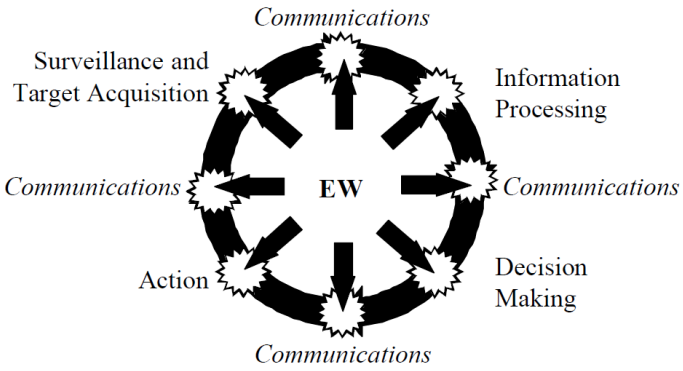

Figure A.12 Domains of EW applications.[192]

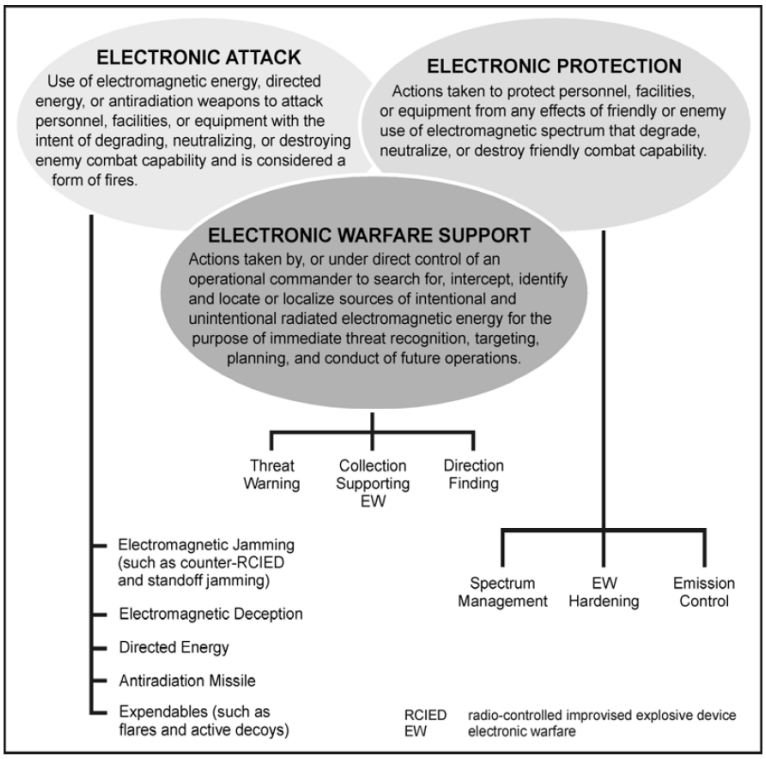

Figure A.13 The three subdivisions of electronic warfare.[193, 194]

Appendix B

Number of points used for frequency averaging

As previously shown, averaging over the number of stirrer positions N_S was insufficient and averaging over a number of frequency N_F was also necessary in order to separate composite quality factor curves. A derivation enabling the evaluation of the number of points needed for the frequency averaging in order to obtain an acceptable separation of the quality factor curves is explained here. A parameter s is fixed underneath which the two curves cannot be considered separated enough. In FigureB.1. The dashed lines represent the measured curves after averaging over stirrer positions and the full line curves correspond to the same curves after averaging over the points represented in the figure.

We therefore want to calculate the integral of the following probability.

$$P\left(\widehat{Q}_2 - \widehat{Q}_8 > s\right) \tag{B.1}$$

Where $\widehat{Q}_2$ and $\widehat{Q}_8$ are the respectivaly the estimators of the quality factors with 2 and 8 antennas in the RC.

In order to express the integral above $\widehat{Q}_8 = x$ is used for conditioning. The equation therefore becomes.

$$P\left(\widehat{Q_2} - \widehat{Q_8} > s \middle| \widehat{Q_8} = x\right) \tag{B.2}$$

The two quality factors being independent variables, the conditioned expression can be simplified in the following product:

$$I = \int_{-\infty}^{+\infty} \int_{x+s}^{+\infty} p\left(\widehat{Q_2} > x + s\right) p\left(\widehat{Q_8} = x\right) dydx \tag{B.3}$$

where p are the probability density functions. S_{21} is proportional to the E-field inside the room. It is a well property of fields inside RCs that they follow a complex gaussian distribution [3]. Therefore quality factors Q which are proportional to $|S_{21}|^2$ follow an expontial law or χ^2_2. These distributions have their mean value μ equal to their standard deviations σ. When averaging over the stirrer positions and frequencies the quality factor distributions will tend towards Gaussian variables with $\widehat{\sigma}_N = \widehat{\mu}/\sqrt{N}$ with $N = N_F N_S$.

The quality factor distributions can therefore be expressed as:

$$f\left(|S_{21}|^2_N\right) = \frac{\sqrt{N}}{\sqrt{2\pi}\mu} \exp\left(-\frac{1}{2}\left(\frac{x-\mu}{\mu/\sqrt{N}}\right)\right)^2 \tag{B.4}$$

The integral terefore becomes:

$$I = \int_{-\infty}^{+\infty}\int_{x+s}^{+\infty} \frac{\sqrt{N}}{\sqrt{2\pi}\widehat{\mu}_2} \exp\left(-\frac{1}{2}\left(\frac{y-\widehat{\mu}_2}{\widehat{\mu}_2/\sqrt{N}}\right)^2\right) \times \frac{\sqrt{N}}{\sqrt{2\pi}\widehat{\mu}_8} \exp\left(-\frac{1}{2}\left(\frac{x-\widehat{\mu}_8}{\widehat{\mu}_8/\sqrt{N}}\right)^2\right) dydx \tag{B.5}$$

The first integral is equal to a complementary error function :

$$\widehat{I} = \frac{1}{2}\sqrt{\frac{N}{2\pi}} \int_{-\infty}^{+\infty} \operatorname{erfc}\left(\sqrt{\frac{N}{2}}\frac{x+s-\widehat{\mu}_2}{\widehat{\mu}_2}\right) \times \frac{1}{\widehat{\mu}_8} \exp\left(-\frac{N}{2}\left(\frac{x-\widehat{\mu}_8}{\widehat{\mu}_8}\right)^2\right) dx \tag{B.6}$$

In order to integrate on the entire space the equation a change in the variables is needed.

$$\begin{cases} \Delta\widehat{Q} = \widehat{\mu}_2 - \widehat{\mu}_8 \\ \eta = \Delta\widehat{Q} + s \\ \xi = \dfrac{x-\widehat{\mu}_8}{\widehat{\mu}_8} \end{cases} \tag{B.7}$$

From the graphic above we also can see the following equality.

$$x + s - \widehat{\mu}_2 = x - \eta - \widehat{\mu}_8 \tag{B.8}$$

By replacing variables in in (B.5) and using the equality above we obtain:

$$\widehat{I} = \frac{1}{2}\sqrt{\frac{N}{2\pi}} \int_{-\infty}^{+\infty} \operatorname{erfc}\left(\sqrt{\frac{N}{2}} \frac{\xi - \eta/\widehat{\mu}_8}{1 + \Delta\widehat{Q}/\widehat{\mu}_8}\right) \exp\left(-\frac{N}{2}\xi^2\right) d\xi \tag{B.9}$$

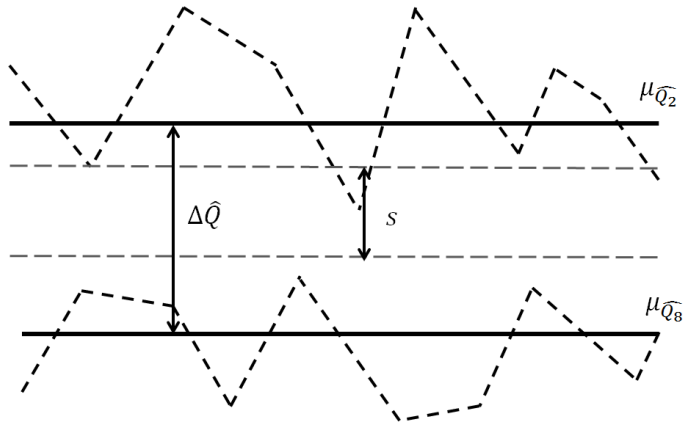

Figure B.1 Mean vs mearuement curves.

The graphics bellow show the possibility to obtain different values of s in function of the number of points.

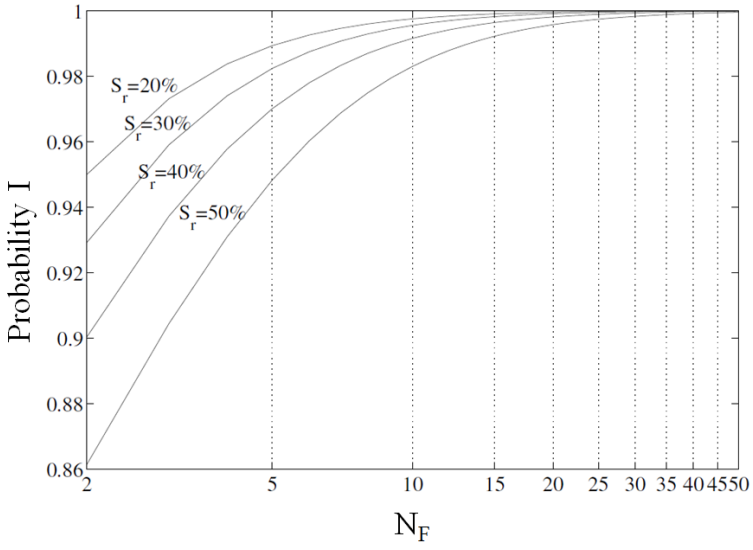

Figure B.2 Probability to obtain a distance between Q-factors estimates greater than 50% the distance between their related means.

Appendix C

IEC 6100-4-21 tables for field uniformity

		Minimum Number of Samples[a] Required for Test Validation[d]	Number of Frequencies[b] Required for Validation
Frequency Range	f_s to $3f_s^c$	12	20
	$3f_s$ to $6f_s$	12	15
	$6f_s$ to $10f_s$	12	10
	Above $10f_s$	12	20/decade

Table C.1 Sampling Requirements in function of frequency.

[a] The minimum number of stirring steps is 12 for all frequencies. For many reverberation chambers it is necessary to increase the number of stirring steps at low frequencies. The maximum number of stirring steps is the number of independent samples that a particular stirrer can provide. This number varies with frequency and must be verified during the commissioning of the room. If the room does not satisfy the requirement of uniformity, the number of stirring steps can be increased up to the number of samples of independent brewer.

[b] Logarithmically Spaced

[c] f_s Lowest Usable Frequency

[d] The stirring sequencing used for validation of the room must be the same as that used for subsequent tests.

Frequency Range in MHz	Standard Deviation Requirement For Test Validity
80 to 100	4dB[a]
100 to 400	4 dB at 100 MHz with linear decrease to 3dB at 400MHz[a]
Above 400	3dB[a]

Table C.2 Field Uniformity Requirement.

[a]Three frequencies per octave may exceed the maximum allowed standard deviation within a proportion of not more than 1dB of the required level.

Focalisation d'une Onde de Forte-Puissance par Retournement Temporel

Mots-clés : Électromagnétisme, Chambre Réverbérantes, Retournement Temporel

Résumé :
L'objectif de la thèse a été de mettre en place des modèles analytiques et statistiques permettant d'évaluer les performances d'un système à retournement temporel pour la génération de fortes puissances. L'apport du retournement temporel en milieu réverbérant a aussi pu être modélisé. En parallèle, des travaux sur l'impact des antennes dans une chambre réverbérante ont été menés afin d'évaluer les performances d'un système ayant plusieurs sorties. Les résultats de thèse ont permis l'élaboration de nouvelles métriques de performances du système. Le développement d'un prototype a nécessité la conception et la réalisation d'amplificateurs, de combineurs radiaux et d'une chambre réverbérante. Les campagnes de mesures ont permis la validation complète des modèles.

Focusing High-Power ElectroMagnetic Waves Using Time-Reversal

Key Words : Electromagnetics, Reverberation Chamber, Time-Reversal

Summary :
The aim of this thesis was to develop analytical and statistical models assessing the performance of a Time-Reversal Amplification System (TRAS). This system allows generating medium to high-power microwaves using a time-reversal technique. The benefits of driving an RC with time-reversed signals were also modelled. Theoretical and experimental work evaluating the impact of antennas in a reverberation chamber was conducted in order to assess the performance of a TRAS system with multiple outputs. The results of this thesis have lead to the development of new metrics evaluating such a TRAS systems performance. The development of a prototype required the design and realization of solid state power amplifiers, broadband radial waveguide and a reverberation chamber. The measurement campaigns that ensued led to the validation of the models developed.